



National Library
of Canada

Bibliothèque nationale
du Canada

Ottawa, Canada
K1A 0N4

TC -

65394

ISBN

0-315-17485-4

21

CANADIAN THESES ON MICROFICHE SERVICE - SERVICE DES THÈSES CANADIENNES SUR MICROFICHE

PERMISSION TO MICROFILM - AUTORISATION DE MICROFILMER

• Please print or type - Écrire en lettres moulées ou dactylographier

AUTHOR - AUTEUR

Full Name of Author - Nom complet de l'auteur

Prakash C. Patnaik.

Date of Birth - Date de naissance

June 4, 1954.

Canadian Citizen - Citoyen canadien

Yes / Oui

No / Non

Country of Birth - Lieu de naissance

India

Permanent Address - Résidence fixe

Bijipur Tota Street-1,
Berhampur, India.

THESIS - THÈSE

Title of Thesis - Titre de la thèse

High Temperature Sulfidation Properties of Fe-Al Alloys

Degree for which thesis was presented
Grade pour lequel cette thèse fut présentée

Ph.D.

Year this degree conferred
Année d'obtention de ce grade

1984

University - Université

McMaster

Name of Supervisor - Nom du directeur de thèse

Dr. W.W. Smeltzer

AUTHORIZATION - AUTORISATION

Permission is hereby granted to the NATIONAL LIBRARY OF CANADA to microfilm this thesis and to lend or sell copies of the film.

L'autorisation est, par la présente, accordée à la BIBLIOTHÈQUE NATIONALE DU CANADA de microfilmer cette thèse et de prêter ou de vendre des exemplaires du film.

The author reserves other publication rights, and neither the thesis nor extensive extracts from it may be printed or otherwise reproduced without the author's written permission.

L'auteur se réserve les autres droits de publication; ni la thèse ni de longs extraits de celle-ci ne doivent être imprimés ou autrement reproduits sans l'autorisation écrite de l'auteur.

ATTACH FORM TO THESIS - VEUILLEZ JOINDRE CE FORMULAIRE À LA THÈSE

Signature

Prakash C. Patnaik

Date

May 30, 1984.

HIGH TEMPERATURE SULFIDATION PROPERTIES
OF Fe-Al ALLOYS

By

© PRAKASH CHANDRA PATNAIK, M.Tech., M.Eng.

A Thesis

Submitted to the School of Graduate Studies
in Partial Fulfilment of the Requirements
for the Degree
Doctor of Philosophy

McMaster University

February 1984

HIGH TEMPERATURE SULFIDATION PROPERTIES
OF Fe-Al ALLOYS

DOCTOR OF PHILOSOPHY (1984)
(Metallurgy and Materials Science)

McMASTER UNIVERSITY
Hamilton, Ontario

TITLE: High Temperature Sulfidation Properties of Fe-Al
Alloys

AUTHOR: Prakash Chandra Patnaik, B.S.Eng. (Hons.)
M.Tech. (I.I.T., Kharagpur)
M.Eng. (McMaster University)

SUPERVISOR: Professor W.W. Smeltzer

NUMBER OF PAGES: xxi, 293

ABSTRACT

The sulfidation properties of Fe-Al alloys containing 6, 9, 18 and 28 atomic percent Al were investigated in alloy/FeS diffusion couples, in sulfur vapour at the dissociation pressure of FeS and in H_2S+H_2 atmospheres at 1173K. The reaction kinetics were determined thermogravimetrically and by layer thickness measurements. The reacted specimens were analyzed using light microscopy, X-ray diffraction and electron metallographic techniques (SEM, EPMA) along with EDAX spectrometry. Particular interest was given to the mode of precipitation and growth of sulfide phases.

Diffusion coupling of Fe-Al alloys with FeS in the form of compacts results in periodic precipitation of sulfide ($FeS+FeAl_2S_4$) bands in the alloy. The thickness of sulfide bands increases with depth satisfying the Jablczynski's relationship for Liesegang type of precipitation processes. The initial stage of sulfide band formation is explained by a model involving precipitation of Al_2S_3 which is subsequently converted to $FeAl_2S_4$. Growth of each sulfide band or layer is supported by rapid diffusion of iron and aluminum in the FeS phase. It is suggested that aluminum depletion from the alloy in front of a sulfide layer ultimately leads to its cessation of growth. A new sulfide band begins to form at a distance ahead of the sulfide layer

where the concentration product for the precipitation of Al_2S_3 is satisfied.

The mode of precipitation of sulfide changes from bands parallel to the original alloy surface to platelets normal to alloy surface when Fe-6, 9 and 18 Al alloys are sulfidized in sulfur vapour supplied by a mixture of Fe and FeS. The acicular internal sulfide precipitates of FeAl_2S_4 and Al_2S_3 in these alloys are elongated in the growth direction. Their growth is interpreted by a model involving enhanced sulfur diffusion along the incoherent interfaces between the internal sulfides and alloy matrix. The alloy composition at which transition from internal to external scale formation of Al_2S_3 occurs, is calculated using available models and compared with the experimental results.

Fe-9 Al alloy sulfidizes parabolically in $\text{H}_2\text{S}+\text{H}_2$ atmospheres giving rise to a scale consisting of an outer Al-doped FeS layer, an inner $\text{FeS}+\text{FeAl}_2\text{S}_4$ layer and Al_2S_3 +alloy internal precipitation zone. The Fe-18 Al alloy is sulfidized by a two-stage kinetics. In the initial stage, growth of $\text{FeS}+\text{FeAl}_2\text{S}_4$ nodules is observed accompanied by internal sulfidation beneath these nodules. The final stage of the reaction curve commences when an inner film of Al_2S_3 forms at the external scale/alloy interface. Models based upon diffusion and the thermochemistry of the sulfidation reactions are advanced to account for the reaction kinetics and sulfide morphologies.

The ternary Fe-Al-S isotherm is determined experimentally and it is used to interpret the scale microstructures which grew by parabolic kinetics.

ACKNOWLEDGEMENTS

The author wishes to express his sincere gratitude to Professor W.W. Smeltzer for his suggestion of this problem and continued guidance throughout the entire course of this work. The interest and encouragement shown by Professor G.R. Purdy and Professor R.B. Anderson, who were both members of the supervisory committee, is gratefully acknowledged. Discussions with Professor J.S. Kirkaldy are also gratefully acknowledged. I am indebted to my wife Pushpa for her limitless help, support and assistance.

Thanks are due to the staff, post-doctoral fellows and graduate students of the Department of Metallurgy and Materials Science. In particular, acknowledgements are due to Messrs. D. Hodgson, T. Bryner and M. Van Oosten for their technical assistance, drafting and photographic work. The thesis was typed with skill and very remarkable patience by Mrs. H. Kennelly, to whom I give special thanks.

The author finally acknowledges the financial support of the Department of Metallurgy and Materials Science in the form of a graduate scholarship and teaching assistantship. Finances for the support of this research were obtained from a research grant to Professor Smeltzer by the Natural Sciences and Engineering Research Council of Canada.

TABLE OF CONTENTS

		<u>PAGE</u>
CHAPTER 1	INTRODUCTION	1
CHAPTER 2	SULFIDATION OF METALS AND ALLOYS	4
	2.1 INTRODUCTION	4
	2.2 THERMODYNAMICS OF METAL-SULFUR SYSTEMS	5
	2.2.1 Pure Metal Sulfidation	5
	2.2.2 Alloy Sulfidation	6
	2.3 KINETICS OF SULFIDATION-	11
	2.4 THEORIES OF ALLOY SULFIDATION	14
	2.4.1 Introduction	14
	2.4.2 Selective Sulfidation	15
	2.4.3 Interface Stability	18
	2.4.4 The Concept of Diffusion Path	21
	2.4.5 Internal Sulfidation	24
	2.4.6 Morphology and Distribution of Internal Sulfide Precipitates	41
CHAPTER 3	LITERATURE REVIEW	51
	3.1 INTRODUCTION	51
	3.2 PROPERTIES OF Fe-Al ALLOYS	51
	3.2.1 Crystal and Defect Structures	51
	3.2.2 Directional Decomposition of ϵ -FeAl	53
	3.2.3 Thermodynamic Properties	54
	3.2.4 Diffusion Properties	54

	<u>PAGE</u>
3.3 PROPERTIES OF Fe-S SYSTEM -	58
3.3.1 Crystal and Defect Structure	58
3.3.2 Thermodynamic Properties	60
3.3.3 Solubility of Sulfur in Iron and Iron Based Alloys	64
3.3.4 Diffusion Properties	65
3.3.5 Kinetics and Mechanism of Iron Sulfidation.	72
3.4 PROPERTIES OF Al-S SYSTEM	74
3.4.1 Crystal and Defect Structure	74
3.4.2 Thermodynamic Properties	77
3.4.3 Diffusion Properties	79
3.4.4 Kinetics of Sulfidation	79
3.5 PROPERTIES OF Fe-Al-S SYSTEM	79
3.5.1 Crystal and Defect Structure	79
3.5.2 Thermodynamic Properties	79
3.5.3 Diffusion Properties	79
3.5.4 Sulfidation Properties	80
3.6 SUMMARY	80
CHAPTER 4 EXPERIMENTAL PROCEDURES AND TECHNIQUES	82
4.1 INTRODUCTION	82
4.2 SPECIMEN PREPARATION AND ANALYSIS	82
4.3 SULFIDATION APPARATUS	85
4.4 SULFIDATION PROCEDURE	88
4.5 CALCULATION OF SULFUR PRESSURE	92

	<u>PAGE</u>
4.6 EXPERIMENTAL TECHNIQUES USED FOR ANALYZING THE SULFIDATION PRODUCTS	96
4.6.1 Optical Metallography	96
4.6.2 Scanning Electron Metallography	96
4.6.3 X-ray Analysis	97
4.6.4 Electron Probe Microanalysis	97
4.7 DETERMINATION OF THE Fe-Al-S PHASE DIAGRAM	98
CHAPTER 5 EXPERIMENTAL RESULTS	103
5.1 INTRODUCTION	103
5.2 PERIODIC PRECIPITATION OF SULFIDES IN FeS/Fe-Al ALLOY DIFFUSION COUPLE	104
5.2.1 Sulfidation Kinetics	104
5.2.2 Sulfide Morphological Development	108
5.3 SULFIDATION OF Fe-Al ALLOYS IN SULFUR VAPOUR AT THE DISSOCIATION PRESSURE OF FeS	143
5.3.1 Sulfidation Kinetics	143
5.3.2 Sulfide Morphological Development in Subscales and Scales	147
5.3.3 Sulfide Scale Formation on the Fe-28 a/o Al Alloy	154
5.4 SULFIDATION PROPERTIES OF Fe-Al ALLOYS IN H ₂ S-H ₂ ATMOSPHERES	156
5.4.1 Sulfidation Kinetics	156
5.4.2 Sulfide Morphological Development	159
5.5 INERT MARKER MEASUREMENTS	168

	<u>PAGE</u>
5.6 PHASE IDENTIFICATION	174
5.6.1 Electron Probe Microanalyses	174
5.6.2 X-ray Analyses	184
5.6.3 X-ray Energy Dispersive Analyses	190
5.6.4 Summary	195
5.7 PHASE EQUILIBRIA IN Fe-Al-S SYSTEM at 1173K	195
5.7.1 Metallography	197
5.7.2 X-ray Analyses	199
5.7.3 Electron Probe Microanalyses	199
CHAPTER 6 ANALYSIS AND DISCUSSION OF EXPERIMENTAL RESULTS	206
6.1 INTRODUCTION	206
6.2 THERMOCHEMISTRY OF Fe-Al-S SYSTEM AND ITS TERNARY ISOTHERM AT 1173K	208
6.3 PERIODIC PRECIPITATION OF SULFIDES IN FeS/Fe-Al ALLOY DIFFUSION COUPLES	215
6.3.1 Introduction	215
6.3.2 Calculation of the First Pre- cipitation Distance in the Alloy and the Mechanism of Periodic Precipitation	217
6.3.3 Diffusion Model for the Growth of a Sulfide Band	231
6.3.4 Conclusions	238

	<u>PAGE</u>
6.4 SULFIDATION OF Fe-Al ALLOYS IN S ₂ VAPOUR AT THE DISSOCIATION PRESSURE OF FeS	240
6.4.1 Introduction	240
6.4.2 Internal Precipitation of FeAl ₂ S ₄ and its Formation in the External Scale	241
6.4.3 Internal Sulfidation Model	245
6.4.4 Formation of the Protective Al ₂ S ₃ Scale	252
6.4.5 Conclusions	256
6.5 SULFIDATION PROPERTIES OF Fe-Al ALLOYS IN H ₂ S-H ₂ ATMOSPHERES	257
6.5.1 Introduction	257
6.5.2 Sulfidation Mechanisms and Models	259
6.5.3 Correlation of Sulfidation Scaling Models to the Fe-Al-S Isotherm	269
6.5.4 Conclusions	273
CHAPTER 7 SUMMARY	275
REFERENCES	278
APPENDIX I THERMOCHEMISTRY OF IRON AND ALUMINUM SULFIDES	287

LIST OF FIGURES

<u>FIGURE</u>		<u>PAGE</u>
2.1 (a)	Ratio of the non-Henrian to that of Henrian sulfur solubility as a function of solute mole fraction for various values of interaction parameter.	10
2.1 (b)	Variation and shape of sulfur solubility curves as a function of N_B for positive and negative values of interaction parameter.	12
2.2	Interface stability model.	16
2.3	Diffusion paths and their plot on the ternary A-B-S isotherm with corresponding schematic scale microstructures.	23
2.4	Steady-state concentration profiles for internally sulfidized A-B alloy.	29
2.5 (a)	Concentration profiles of solute B and sulfur in the underlying alloy of a BS_V scale.	33
2.5 (b)	The product $N_B \cdot N_S^V$ as a function of distance in the underlying alloy.	33
2.6	Ternary oxidation model.	36
2.7 (a)	The critical fraction of B in the alloy, N_B^{O*} , for exclusive external oxidation as a function of k_p/D_{BB} and ϵ_O^B .	40
2.7 (b)	The oxygen solubility curves with the diffusion paths superimposed for an alloy of $N_B^O = 0.17$.	40
2.8	Schematic representation of Liesegang bands.	45
2.9 (a)	Microstructure of periodic precipitation of GaAs in silver.	48
2.9 (b)	Periodic precipitation of water bubbles in silver.	48
3.1	Fe-Al phase diagram	52

<u>FIGURE</u>		<u>PAGE</u>
3.2	Fe and Al activities in Fe-Al system at 1173K.	55
3.3	Variation of chemical diffusion coefficient (D) with Al concentration (94).	57
3.4	Fe-S phase diagram.	59
3.5	Fe-S phase diagram in the Fe _{1-x} S region (108).	61
3.6	Plot of H ₂ S/H ₂ vs. 1/T for Fe-S system (112).	63
3.7	Temperature dependence of the sulfur solubility in iron (118).	66
3.8	Temperature dependence of the chemical diffusivity of iron sulfide (126).	71
3.9	Al-S phase diagram (77).	76
4.1	Schematic kinetic assembly using H ₂ -H ₂ S atmospheres.	86
4.2	A cross-section through the die used for making FeS/Fe-Al alloy diffusion couples.	89
4.3	X-ray diffraction pattern of commercial iron sulfide.	91
4.4	Internal sulfidation set-up:	93
4.5	Heating schedule for the preparation of FeAl ₂ S ₄ and determination of ternary isotherm.	101
5.1	Parabolic plots of sulfidation zone thickness vs. time in the FeS/Fe-Al alloy diffusion couples.	106
5.2	Plot of parabolic rate constant vs. alloy composition for FeS/Fe-Al alloy diffusion couples.	107
5.3	Optical photomicrograph of FeS/Fe-1 Al alloy diffusion couple.	109
5.4	Optical photomicrographs of FeS/Fe-6 and 9 Al alloy diffusion couples.	110, 111

<u>FIGURE</u>		<u>PAGE</u>
5.5	Relation between sulfide thickness and its depth of formation.	113
5.6	Plots of X_n vs. X_{n-1} for FeS/Fe-6 and 9 Al alloy diffusion couples.	116,118
5.7	Plots of ΔSULF_n vs. X_n for FeS/Fe-6 and 9 Al alloy diffusion couples.	120,122
5.8	Plots of X_n vs. X_{n-1} for FeS/Fe-6, 9, 18 and 28 Al alloy diffusion couples.	125-130
5.9	Plots of ΔSULF_n vs. X_n for FeS/Fe-6, 9, 18 and 28 Al alloy diffusion couples.	132-137
5.10	Plot of spacing coefficient k as a function of alloy aluminum content.	138
5.11	Cross-section of sulfidation zone in the FeS/Fe-6 and 9 Al alloy diffusion couples.	141
5.12	Photomicrograph of the alloy sulfidation zone sectioned parallel and normal to alloy surface in FeS/Fe-6 Al diffusion couple.	142
5.13	Parabolic plots of internal sulfidation depth vs. time in S_2 vapour for Fe-6, 9 and 18 Al alloys.	145
5.14	Parabolic plots of weight gain vs. time in S_2 vapour for Fe-6, 9 and 18 Al alloys	146
5.15	Cross-section of internal sulfidation zones of (a,c) Fe-6 Al and (b) Fe-9 Al alloys in S_2 vapour.	148
5.16	Cross-section of internal sulfidation zone for Fe-18 Al alloys in S_2 vapour.	149
5.17	Cross-section of Fe-9 Al alloy showing the morphology of internal sulfide precipitates at various depths.	150
5.18	Cross-section of internal sulfidation zone near the alloy and external scale/alloy interfaces for Fe-6, 9 and 18 Al alloys.	152
5.19	Cross-section of internal sulfidation zone revealing the intersulfide spacings for Fe-6, 9 and 18 Al alloys.	153

<u>FIGURE</u>		<u>PAGE</u>
5.20	Cross-section of the only sulfide scale (Al_2S_3) formed on Fe-28 Al alloys in S_2 vapour.	155
5.21	Linear plots of sulfidation kinetics of Fe-Al alloys in $\text{H}_2\text{S-H}_2$ atmospheres.	157
5.22	Parabolic plot of sulfidation kinetics of Fe-Al alloys in $\text{H}_2\text{S-H}_2$ atmospheres.	158
5.23	Photomicrograph of the scale and subscale regions of Fe-9 Al alloy sulfidized in $\text{H}_2\text{S-H}_2$ atmospheres at $p_{\text{S}_2} = 10^{-1}$ Pa.	161
5.24 (a)	Photomicrograph of the scale cross-section on the Fe-18 Al alloy at $p_{\text{S}_2} = 10^3$ Pa.	162
5.24 (b)	SEM micrograph of the outer surface of the scale on the Fe-18 Al alloy at $p_{\text{S}_2} = 10^2$ Pa.	162
5.25	Photomicrographs of the scale cross-sections (a) and (b) emphasizing the interface regions between the alloy and inner layer of external scale on Fe-18 Al alloy at $p_{\text{S}_2} = 10^2$ Pa.	164
5.26	Photomicrograph of the interface region between the external scale and alloy at $p_{\text{S}_2} = 10$ Pa for Fe-18 Al alloy.	165
5.27 (a)	Linear plots of sulfide layer thicknesses vs. time on the Fe-18 Al alloy in $\text{H}_2\text{S-H}_2$ atmospheres, $p_{\text{S}_2} = 10^2$ Pa.	166
5.27 (b)	Parabolic plots of sulfide layer thicknesses on the Fe-18 Al alloy in $\text{H}_2\text{S-H}_2$ atmospheres, $p_{\text{S}_2} = 10^2$ Pa.	167
5.28	SEM micrograph of the nodular sulfides on Fe-18 Al alloys at $p_{\text{S}_2} = 10$ Pa.	169
5.29	Photomicrographs of sulfide nodules (a), (c) and (d) at $p_{\text{S}_2} = 10^2$ Pa and (b) at $p_{\text{S}_2} = 10$ Pa.	170
5.30	Micrographs of the inner layer of external scale of Fe-18 Al alloys at $p_{\text{S}_2} = 10$ Pa.	171
5.31	Photomicrograph showing the position of a Pt marker above the sulfidation zone in FeS/Fe-9 Al diffusion couple.	172

<u>FIGURE</u>		<u>PAGE</u>
5.32	Photomicrographs showing the position of a Pt marker at the outer and inner layer interface of Fe-9 and 18 Al alloys at $p_{S_2} = 10$ Pa.	173
5.33	Microprobe traces for iron, aluminum and sulfur in FeS/Fe-9 Al alloy diffusion couple.	175,177
5.34	Microprobe traces for iron and aluminum in the sulfidation zone of Fe-9 Al alloy sulfidized in S_2 vapour.	179
5.35	Microprobe scans across the scale on the Fe-18 Al alloy at $p_{S_2} = 10^2$ Pa.	181
5.36	Microprobe scans across the inner two-phase layer of the external scale on Fe-18 Al alloy at $p_{S_2} = 10^2$ Pa.	181
5.37	Microprobe scans across the scale on the Fe-18 Al alloy at $p_{S_2} = 10^2$ Pa.	182
5.38	Microprobe scans for a) Fe, Al and (b) Fe,S in the internal sulfidation zone ahead of the innermost layer of Fe-18 Al alloy at $p_{S_2} = 10$ Pa.	183
5.39	X-ray diffraction pattern of sulfides from sulfidation zone of FeS/Fe-Al alloy diffusion couples.	187
5.40	X-ray diffraction pattern of the sulfides in the internal sulfidation zone of (a) Fe-9 Al alloy and (b) external scale of Fe-28 Al alloy.	189
5.41	X-ray diffraction pattern of sulfides from Fe-18 Al alloy sulfidized in H_2S-H_2 atmospheres at $p_{S_2} = 10$ Pa.	191
5.42	Overall compositions of Fe, Al and S considered for analysis of the Fe-Al-S isotherm at 1173K.	196
5.43	Optical photomicrographs revealing the various two-phase and three-phase equilibria.	198

<u>FIGURE</u>		<u>PAGE</u>
5.44	X-ray diffraction pattern of the various equilibrated phases in the pellets.	200
6.1	Experimentally determined ternary Fe-Al-S isotherm at 1173K.	209
6.2	Plot of sulfur activity vs. aluminum atom fraction at 1173K.	214
6.3 (a)	Concentration profiles of aluminum and sulfur in Fe-6 Al alloy.	221
6.3 (b)	Concentration products of aluminum and sulfur in Fe-6 Al alloy as a function of distance.	222
6.4	Schematic concentration profiles of Al and S and Fe during the precipitation and growth of sulfide phases in FeS/Fe-Al alloy diffusion couples.	224
6.5	Verification of relationship between sulfide thickness and alloy composition.	230
6.6	Cross-section of sulfidation zone during the precipitation and growth of sulfide phases for (a) FeS/Fe-6 Al and (b) FeS/Fe-18 Al alloy diffusion couples.	232
6.7	Schematic model for the growth of a sulfide band in FeS/Fe-Al alloy diffusion couples.	234
6.8	Concentration profiles for Al in front of a growing sulfide band for various periods of time.	237
6.9	Plot of apparent permeability vs. alloy aluminum content.	244
6.10	Schematic diagram of the internal sulfidation model in S ₂ vapour at the dissociation pressure of FeS.	246
6.11	Plot of the ratio of apparent permeability to that in pure iron as a function of alloy Al content.	250

<u>FIGURE</u>		<u>PAGE</u>
6.12	Variation of critical atom fraction of aluminum in the alloy as a function of interaction parameter.	255
6.13	Schematic model for scale growth on Fe-9 Al alloys in H_2S-H_2 atmospheres at $p_{S_2} = 10^{-1}$ Pa.	260
6.14	Schematic models for scale growth on Fe-18 Al alloys in H_2S-H_2 atmospheres at $10 \text{ Pa} \leq p_{S_2} \leq 10^2 \text{ Pa}$.	263
6.15	Isothermal section of a phase diagram A-B-S relevant to alloy sulfidation.	270
6.16	Diffusion paths and corresponding schematic scale microstructures on Fe-9 and 18 Al alloys.	272

LIST OF TABLES

<u>TABLE</u>		<u>PAGE</u>
2-1	Diffusion parameters and mode of precipitation in solid systems.	50
3-1	Phases in the Fe-S system.	58
3-2	Summary of sulfur diffusivity in iron.	67
3-3	Iron and sulfur self diffusion in $Fe_{1-x}S$ (108).	69
3-4	Summary of crystal structures of Al_2S_3 (149).	75
3-5	Thermodynamic data for Al_2S_3 formation.	78
4-1	Chemical analyses of iron and aluminum.	83
4-2	Chemical analyses of Fe-Al alloys	85
4-3	Chemical analysis of iron sulfide.	90
4-4	Chemical analyses of iron, aluminum and sulfur used for phase diagram determination.	99
5-1	Kinetic results for FeS/Fe-Al diffusion couples.	105
5-2	Tabulation of X_n , X_{n-1} for FeS/Fe-6 and 9 Al alloy diffusion couples.	115,117
5-3	Tabulation for $\Delta Sulf_n$, ΔMe_n and X_n for FeS/Fe-6 and 9 Al alloy diffusion couples.	119,121
5-4	Tabulation of experimental results for FeS/Fe-6 and 9 Al alloy diffusion couples.	123
5-5	Tabulation of X_n and X_{n-1} for FeS/Fe-6, 9, 18 and 28 Al alloy diffusion couples.	124
5-6	Tabulation of $\Delta Sulf_n$, ΔMe_n and X_n for FeS/Fe-6, 9, 18 and 28 Al alloy diffusion couples.	131
5-7	Tabulation of experimental results for FeS/Fe-6, 9, 18 and 28 Al alloy diffusion couples.	139
5-8	Kinetic results for Fe-Al alloys sulfidized in S_2 at $p_{S_2}^{diss.}$ (Fe/FeS).	144

<u>TABLE</u>		<u>PAGE</u>
5-9	Inter sulfide spacings for Fe-6, 9 and 18 Al alloys sulfidized in S ₂ at p _{S₂} ^{diss.} (Fe/FeS).	154
5-10	Parabolic reaction rate constants for Fe-Al alloys and their comparison with pure iron at 1173K.	160
5-11	Intensity, d spacings and (hkl) indices of Fe _{1-x} S.	185
5-12	Intensity, d spacings and (hkl) indices of FeAl ₂ S ₄ .	185
5-13	Intensity, d spacings and (hkl) indices of Al ₂ S ₃ .	186
5-14	EDAX point analysis on Fe-6 Al alloy.	193
5-15	EDAX point analysis on Fe-9 Al alloy.	193
5-16	EDAX point analysis on the sulfide band in the FeS/Fe-6 Al alloy diffusion couple.	193
5-17	EDAX point analysis on the sulfide band in FeS/Fe-9 Al alloy diffusion couple.	193
5-18	EDAX point analysis on the external scale on Fe-18 Al alloy in S ₂ vapour.	194
5-19	EDAX point analysis in the internal sulfidation zone of Fe-9 Al alloy in S ₂ vapour.	194
5-20	EDAX analysis in the internal sulfidation zone of Fe-9 Al alloy in S ₂ vapour.	194
5-21	Summary of metallographic observations in equilibrium experiments.	197
5-22	Electron probe microanalyses of Fe-Al alloys.	202
5-23	Electron probe microanalyses of equilibrated phases in the Fe-Al-S system.	203

<u>TABLE</u>		<u>PAGE</u>
6-1	The thermodynamic activity of Al in Fe-Al alloys (89,90).	211
6-2	Sulfur activity for the alloy- Al_2S_3 equilibrium.	212
6-3	Diffusion parameters and mode of precipitation in FeS/Fe-Al alloy diffusion couples.	228
6-4	Apparent permeabilities as a function of alloy aluminum content.	243
I-1	Free energy of formation of Fe_{1-x}S .	288
I-2	Free energy of formation of Al_2S_3 .	293

CHAPTER 1
INTRODUCTION

Development of high temperature corrosion resistant alloys is of considerable importance because of the present focus on development of more efficient high temperature combustion and energy conversion systems, including fluidized bed coal combustors, coal gasifiers and gas turbines. These alloys constitute a major fraction of the structural components that are exposed to corrosive atmospheres at elevated temperatures. Typical operating temperatures of reactors used for coal-gasification (1123 - 1273K) lead to severe corrosion of reactor materials^(1,2,3).

On the other hand, petrochemical industries have been presented with the problem of high temperature sulfur corrosion in a number of their processes due to the presence of sulfur in the crude oil. During the processing of crude oil, sulfur is released primarily as hydrogen sulfide. Quite often stainless steels and Inconels are used to obtain useful life times for petroleum processing vessels (with operating temperatures 473 to 873K)^(4-6,9) and gasifiers respectively. It is therefore of considerable interest to develop less expensive sulfur resistant Fe-based alloys at the temperature of concern.

Oxidation resistance in a number of metals and alloys has been achieved at elevated temperatures by incorporating Al

which selectively oxidizes to form a continuous, adherent and slow growing oxide-film. The use of Al as an external coating to achieve such properties is also well known⁽⁷⁾. Similarly, past studies have shown that in sulfur and H_2S-H_2 atmospheres Al addition to iron reduces the sulfidation rate of pure iron by two orders of magnitude in the range of temperatures from 774K to 973K⁽⁸⁻¹¹⁾.

The objective of the present research is to study the sulfidation properties of Fe-Al alloys at 1173K in sulfur and H_2S-H_2 atmospheres. The growth of multilayered scales (usually observed in H_2S-H_2 atmospheres) is not well understood because the corrosion processes are generally complex owing to growth of sulfide solid solutions and multicomponent compounds with concurrent sulfur diffusion in the alloy and internal sulfidation. The latter phenomenon is very important since precipitation of sulfide compounds in the alloy causes a loss of the alloying component. Therefore, this investigation includes detailed studies on the modes of external sulfide scale formation and precipitation of the internal sulfides, particularly at low sulfur pressures corresponding to the FeS dissociation pressure in order to understand more completely the sulfidation properties of Fe-Al alloys. Results concerning the Fe-Al alloy-sulfur system with respect to phase diagrams, sulfide defect structures and diffusion obtained in the present and past investigations are used to interpret the sulfidation mechanisms of Fe-Al alloys containing 1 to 28 a/o Al with models describing the precipitation

and growth of sulfide phases.

A brief description of the present state of knowledge on the sulfidation properties of metals and alloys is presented in the next chapter. This is followed by a literature review of the relevant systems, chapter 3. Several techniques have been used to obtain and collate the necessary data involving specimen preparations, chemical analyses, sulfidation procedures, inert marker technique, metallographic preparations, optical microscopy, X-ray diffraction and electron metallography (SEM, EPMA, EDAX). These techniques and procedures are described in chapter 4. The experimental results are presented in chapter 5 under seven sub-headings: periodic precipitation of sulfides in FeS/Fe-Al alloy diffusion couples, sulfidation of Fe-Al alloys in S_2 vapour at the dissociation pressure of FeS, sulfidation of Fe-Al alloys in H_2S-H_2 atmospheres, inert marker results, phase identification and phase equilibria in the Fe-Al-S system. Finally, the thermochemistry of Fe-Al-S system and the Fe-Al-S isotherm is presented in chapter 6 along with scale growth models to rationalize the experimental results.

CHAPTER 2

SULFIDATION OF METALS AND ALLOYS

2.1 INTRODUCTION

Elementary sulfur and its compounds constitute a major problem of corrosion in many essential branches of modern industry. Although sulfur and oxygen are elements of the same group of the periodic table, environments containing sulfur or its compounds are generally aggressive than oxygen containing environments. First, the degree of disorder of the crystal lattice of sulfides exceeds considerably the disorder of corresponding oxides, in consequence, the mobility of reactants in sulfide scales is many times higher than in oxide scales. For example Cr_2S_3 is reported to have compositions ranging from $\text{CrS}_{1.30}$ (or even lower sulfur content) to $\text{CrS}_{1.54}^{(76)}$. For Cr_2O_3 the deviation from stoichiometry is so small that it has not as yet been accurately determined. In addition, the eutectic temperatures for metal-sulfide systems are considerably lower compared to the eutectic temperatures for corresponding oxide systems. Catastrophic corrosion, caused by the formation of a liquid corrosion product, appears therefore in sulfur or H_2S environments at lower temperatures than in oxygen atmospheres. Also the dissociation pressures of sulfides are high compared to oxides and commonly lead to a relatively high sulfur partial

pressure at a scale/alloy interface which favours rapid internal corrosion. The reaction kinetics in both these cases differ in magnitude and in the nature of rate controlling steps. However, the theories of metal and alloy oxidation are in general applicable to corresponding sulfidation reactions.

Theories of sulfidation and general results for metal-sulfur and alloy-sulfur systems are outlined in this chapter. More comprehensive reviews relating to specific metal-sulfur and alloy-sulfur systems are presented by Stafford⁽²²⁾ and Young⁽²³⁾. For the detailed aspects of oxidation, the reader is referred to several standard works⁽¹²⁻¹⁹⁾ and recent reviews^(20,21).

2.2 THERMODYNAMICS OF METAL-SULFUR SYSTEMS

2.2.1 Pure Metal Sulfidation

A consideration of elementary thermodynamic principles provides an initial guideline to establish the likelihood of forming a sulfide from a metal in a given sulfidizing environment (sulfur or H₂S). If the reaction is of type



the driving force for reaction is the free energy change,

$$\Delta G = \Delta G^{\circ} - RT \ln (p_{S_2})^{\frac{1}{2}} \quad (2.2)$$

Here, ΔG = free energy of reaction (2.1)

ΔG° = standard free energy of reaction (2.1)

R = universal gas constant

If ΔG is negative, the reaction occurs spontaneously.

When H_2S is the reaction species, the reaction would be



The free energy change is given by

$$\Delta G = \Delta G^\circ + RT \ln \frac{P_{H_2}}{P_{H_2S}} \quad (2.4)$$

The standard free energy of formation values, reaction (2.1), are generally reported in the literature. The standard free energy change for reaction (2.3) can be obtained by adding the ΔG° of reaction (2.1) and (2.5) since the free energy change is



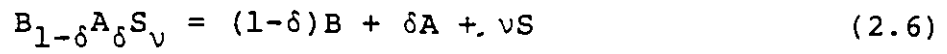
independent of the reaction path. References (22) and (24) describe the standard free energy of formation versus temperature diagrams for the formation of various sulfides.

2.2.2 Alloy Sulfidation

When an alloy AB is sulfidized, the sulfides may produce a solid solution or they may be completely or partly immiscible, producing simple or multiphase scales. If element A does not sulfidize (being noble) and B sulfidizes producing BS

then, account is made for the activities of BS and B in the alloy.

Consider the formation of a sulfide containing negligible concentration of the solvent metal (A). The sulfide-alloy equilibrium may therefore be written as



where B, A and S refer to alloy compositions and A is the solvent metal such that its concentration in the sulfide is small ($\delta \ll 1$). Accordingly for a constant activity of the sulfide $B_{1-\delta}A_{\delta}S_{\nu}$

$$\ln K = \ln a_B^{1-\delta} a_A^{\delta} a_S^{\nu} = \ln N_B^{1-\delta} N_A^{\delta} N_S^{\nu} + \ln \gamma_B^{1-\delta} \gamma_A^{\delta} \gamma_S^{\nu} \quad (2.7)$$

where K is the equilibrium constant. If dissolved sulfur concentration in the solvent metal A is very small, the activity coefficients in Eqn. (2.7) can be expressed according to the Wagner formalism

$$\ln \gamma_B = \ln \gamma_B^O + \epsilon_{B^S}^S N_S + \epsilon_{B^B}^B N_B \quad (2.8)$$

$$\ln \gamma_S = \ln \gamma_S^O + \epsilon_{S^S}^S N_S + \epsilon_{S^B}^B N_B \quad (2.9)$$

$$\ln \gamma_A = 0 \quad ; \quad N_A \approx 1 - N_B \quad (2.10)$$

Upon substituting Eqns. (2.8), (2.9) and (2.10) in (2.7), the equilibrium constant can be expressed in terms of solubilities,

activity coefficients and interaction parameters,

$$\begin{aligned} \ln K = & \ln N_B^{1-\delta} \cdot N_A^\delta N_S^v + (1-\delta)(\ln \gamma_B^O + \epsilon_{B N_S}^S + \epsilon_{B N_B}^B) \\ & + v(\ln \gamma_S + \epsilon_{S N_S}^S + \epsilon_{S N_B}^B) . \end{aligned} \quad (2.11)$$

The sulfur solubility curve for the alloy is then defined by

$$\frac{d \ln K}{d N_B} = 0 . \quad (2.12)$$

A distinction between Henrian and non-Henrian solution behaviour is essential when coupling thermodynamic and diffusional parameters to interpret reaction kinetics. Smeltzer and Whittle⁽²⁵⁾ have used such an analysis to define the conditions for external scale formation of BS scale and external scale formation accompanied by internal sulfidation. Equation (2.7) for the sulfide equilibrium reaction assuming the sulfide to be essentially pure BS_v becomes for Henrian (H) and non-Henrian (NH) behaviour

$$\ln K = \ln (\gamma_{B N_B}^O)_H (\gamma_{S N_S}^O)_H^v \quad (2.13)$$

$$\begin{aligned} \ln K = & \ln (\gamma_{B N_B}^O)_{NH} (\gamma_{S N_S}^O)_{NH}^v + (\epsilon_{B N_S}^B + v \epsilon_{S N_B}^B) N_B \\ & + (\epsilon_{S N_S}^B + v \epsilon_{S N_S}^S) N_S \end{aligned} \quad (2.14)$$

where the activity coefficients were defined in Eqns. (2.8) - (2.10). Since the sulfur solubility is usually very small

(~ 10 - 1000 ppm), $N_S \ll 1$, and if the solute element (B) in the binary alloy exhibits Henrian behaviour ($\epsilon_B^B = 0$), (2.13) and (2.14) yield

$$\frac{(N_S)_{NH}}{(N_S)_H} = \exp(-\epsilon_{S^B}^{N_B}) \quad (2.15)$$

If the Henrian activity coefficient is known, an equilibrium constant can be defined

$$K_H = \frac{K}{\gamma_B^O (\gamma_S^O)^{\nu}} \quad (2.16)$$

such that

$$(N_S)_{NH} = \left(\frac{K_H}{N_B}\right)^{1/\nu} \exp(-\epsilon_{S^B}^{N_B}) \quad (2.17)$$

Expressions (2.16) and (2.17) allow, in principle, a comparison of the sulfur solubilities for Henrian and non-Henrian solution behaviour in a binary alloy.

Figure 2.1(a) represents the ratio of the non-Henrian sulfur solubility to that of Henrian sulfur solubility as given by equation (2.15). In this case component B is the less-noble alloying element in the solid solvent A. As can be seen, positive values of the interaction coefficient ϵ_S^B decrease the solubility, the decrease being more pronounced, the larger the interaction coefficient. The converse is found when $\epsilon_S^B < 0$, the sulfur solubility increasing with larger negative values of ϵ_S^B .

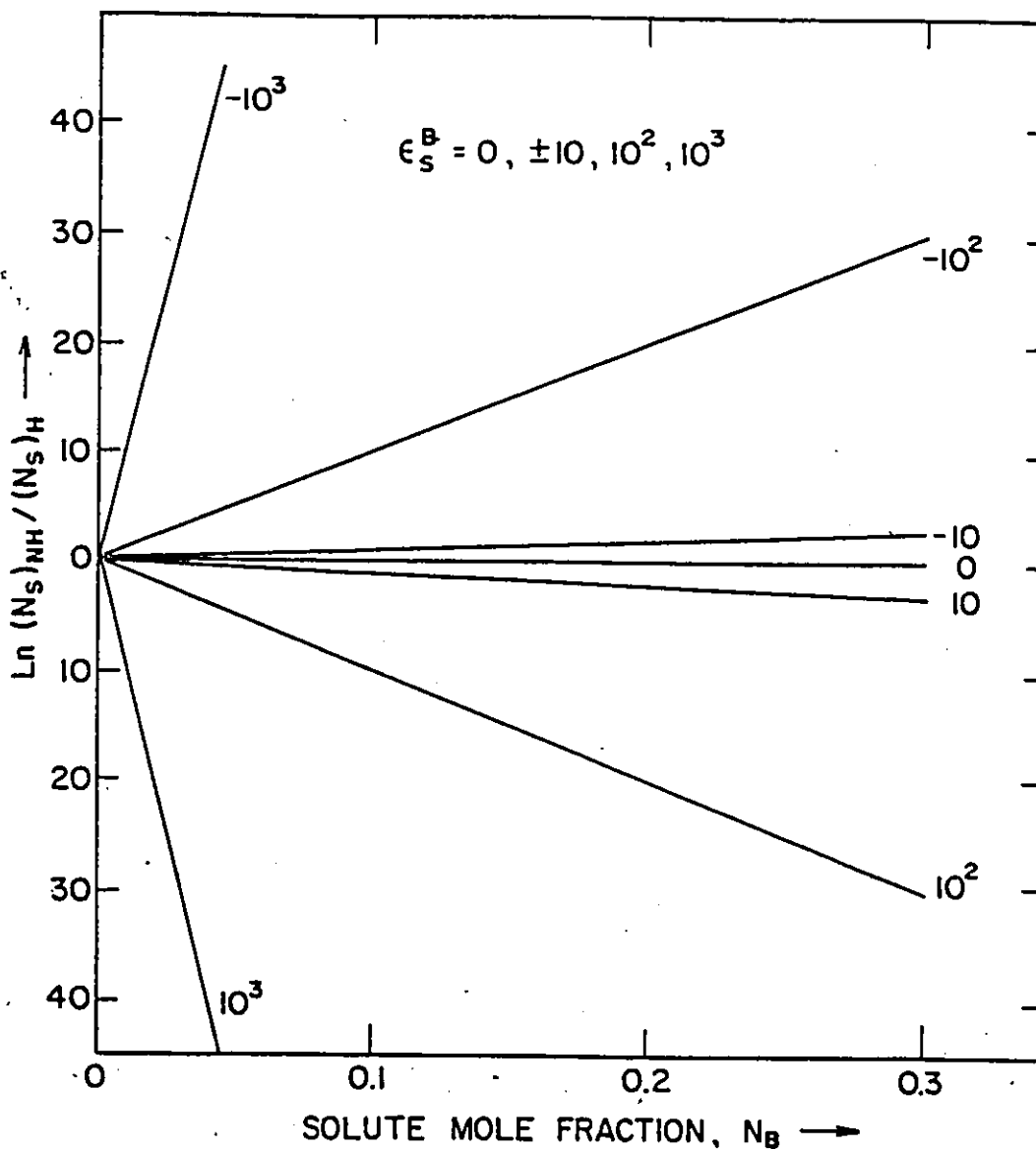


Fig. 2.1(a) Ratio of the non-Henrian to that of Henrian sulfur solubility as a function of solute mole fraction for various values of interaction parameter.

Figure 2.1(b) illustrates the variation and shape of the sulfur solubility curves for different negative values of ϵ_S^B . These solubility curves exhibit minima of larger sulfur concentrations which occur at smaller values of N_B with larger negative values of ϵ_S^B . Application of the sulfur solubility curves is discussed in a greater detail in section 2.4 of this chapter.

2.3 KINETICS OF SULFIDATION

Thermodynamics cannot in general predict the extent of reaction in finite time. The corrosion product eventually covers the metal surface and subsequent reaction is controlled by the physicochemical properties of the scale. Thus for the proper understanding of the observed reaction rate equation, it is important to know the scale morphology and the diffusivity of various species through the scale. Sulfidation of a pure metal or alloy often takes place in different stages; gas adsorption, nucleation and growth of sulfide particles, sulfide film and scale formation. For detailed descriptions of the gas adsorption, nucleation and growth stages, the reader is referred to the works by Germer⁽²⁶⁾, Rama Subramanian⁽²⁷⁾ and Evans⁽²⁸⁾.

In most cases, sulfide scales exhibit parabolic growth behaviour. Other growth relationships like linear, asymptotic and logarithmic are also observed depending on the type of rate control and occurrence of additional processes such as film spalling and short circuit diffusion of reactants in the sulfide scale. For the growth of sulfide scale, Wagner⁽²⁹⁾ has formu-

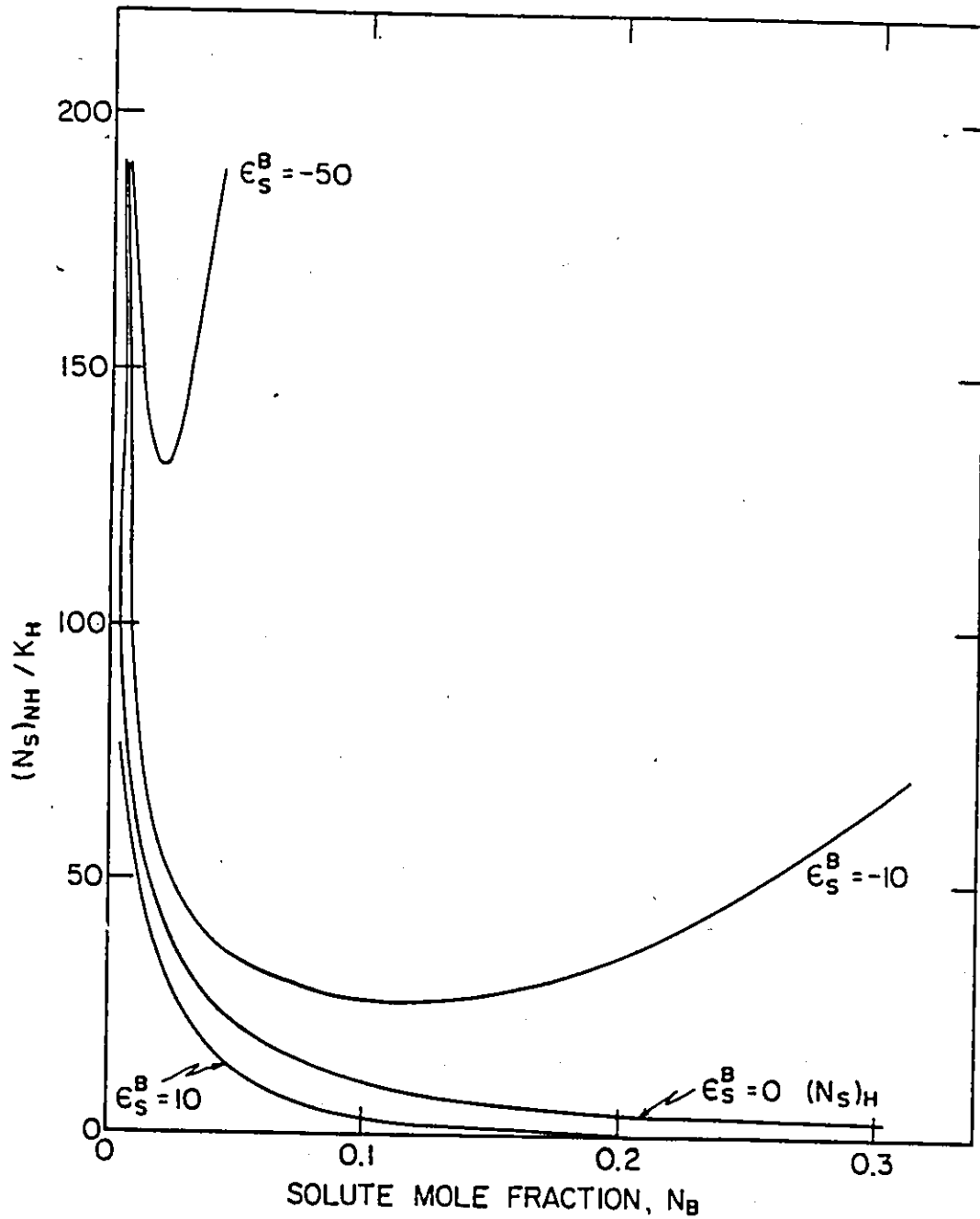


Fig. 2.1(b) Variation and shape of sulfur solubility curves as a function of solute mole fraction for positive and negative values of interaction parameter.

lated a quantitative theory for parabolic growth which has since been tested in many systems and by several investigators. He postulated that the diffusing species in the sulfide scales are ions and electrons which migrate independently. The prerequisite for an ionic species to be mobile is that its sublattices contain point defects such as interstitial ions and vacancies. Reactions at the sulfide-gas and sulfide-metal interfaces are considered to be sufficiently rapid for local equilibrium to be established at these interfaces. The expressions for the rate constant k_r involving diffusion coefficient is given by

$$k_r = C_i \int_{a_s^{(m)}}^{a_s^{(s)}} (D_M \frac{z_M}{z_S} + D_S) d \ln a_S \quad (2.18)$$

where, $C_i = z_S C_S$ is the concentration of sulfur ions in the sulfide in equivalents per cubic centimeter and a_s is the activity of sulfur. D_S and D_M are the self-diffusion coefficients of the metal and non-metal respectively. The superscripts (m) and (s) refer to the sulfide-metal and sulfide-gas interface respectively.

In Wagner's parabolic oxidation theory it is assumed that the oxide is homogenous and does not contain any structural irregularities such as pores, grain boundaries or dislocations. These types of defects give rise to paths of rapid diffusion for reactants which results in non-parabolic oxidation as observed and discussed by several investigators including Evans⁽¹⁴⁾,

Smeltzer et al. (30), Irving (31) and Perrow et al. (32).

2.4 THEORIES OF ALLOY SULFIDATION

2.4.1 Introduction

Sulfidation properties of alloys are more important in practical terms. It is necessary accordingly to develop at least a comprehensive understanding of the mechanisms involved in order to predict their reaction rates and to design alloys that are more sulfidation resistant.

When an alloy AB in which A is the more noble and B is the less noble metal, is sulfidized, the sulfides may produce a sulfide solid solution or they may be completely or partly immiscible, producing simple or multiphase scales. For a detailed classification on the different types of sulfidation and scale morphologies, the reader is referred to the work by Wood (23).

Most alloys are thermodynamically unstable in a sulfidizing atmosphere. The level of sulfidation rate is generally achieved by the formation of a scale which acts as a diffusion barrier to the reactants. The concentration of ionic defects in the sulfides of this scale which effect transport must be low, and the sulfides must remain stoichiometric.

Concentration of point defects in a semi-conducting sulfide (AS) is affected by the addition of sulfide of hetero-valent metal (B_2S_3) if it forms a solid solution. If dissolution of the metal (of higher valence) sulfide produces vacancy and holes, diffusivity of A will increase. However, if inter-

stitial diffusion of metal ions is predominant, diffusivity of A will decrease, since the concentration of metal interstitials is reduced. Similarly, predictions can be made for the addition of lower valent sulfides. Thus, one has a choice of alloying the parent metal to control the sulfidation. However, this has a limited use because conditions such as simultaneous sulfidation and good mutual solid solubility of the sulfides must be satisfied.

2.4.2 Selective Sulfidation

a) Neglecting internal sulfidation, mutual solubilities of sulfides and assuming the formation of a p-type sulfide BS in which B diffuses by a vacancy mechanism and electrons by positive holes, Wagner⁽³⁴⁾ showed that the diffusion controlled growth of BS (Fig. 2.2) on the alloy AB followed a parabolic rate lower than that on the pure metal B as given by

$$\frac{k}{k_0} = \frac{p_a^{1/n} - p^{1/n}}{p_a^{1/n} - p_0^{1/n}} \quad (2.19)$$

where k and k_0 are the parabolic rate constants for BS growing on the alloy and pure B respectively, p_a is the sulfur pressure, p and p_0 are the dissociation pressures of sulfide in equilibrium with the alloy and pure B, respectively. n is a constant, usually in the range of 3 to 6, determined by the defect equilibrium established locally within the sulfide BS. Selective sulfidation takes place in alloys for which the sulfides of the

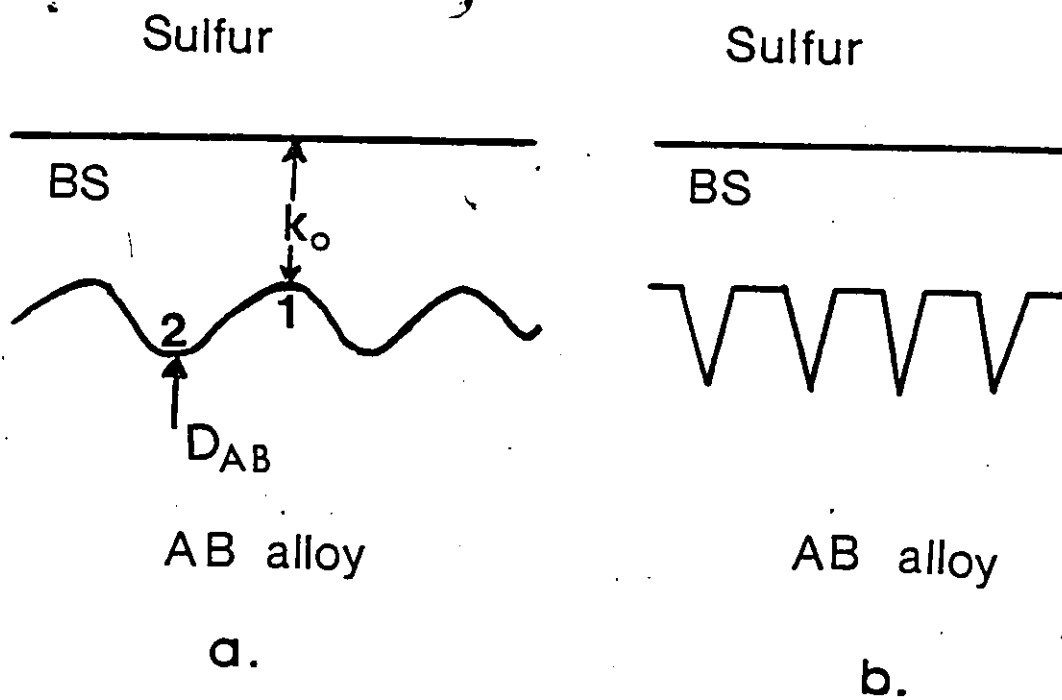


Fig. 2.2 a. Interface stability model of the wave, decays if diffusion through the sulfide is slow and grows if diffusion through the alloy is slow.

b. Fully developed alloy spikes.

alloying components show a great difference in stability; for example, iron alloys with aluminum and chromium. The occurrence of preferential sulfidation is dependent not only on the alloying element but also on the alloy composition, reaction atmosphere and temperature.

b) The case where both A and B form sulfides was also examined by Wagner⁽³⁵⁾ with further assumptions that BS exhibited a lower dissociation pressure than AS, diffusion of B in BS was slower than that of A in AS, and BS formed the stable protective scale. For BS to form alone initially and to be retained, the alloy must be rich in B and diffusion of B in the alloy must be rapid enough to avoid its depletion at the alloy surface. It is desirable to know the minimum concentration of B required for exclusive formation of the highly protective scale BS. This minimum value of concentration is found by setting the diffusive flux equal to the rate of consumption as follows:

$$N_B^{(\text{min.})} = \frac{V}{Z_B M} \left(\frac{\pi k_0}{D_{AB}} \right)^{\frac{1}{2}} \quad (2.20)$$

where V is the molar volume of the alloy, Z_B is the valence of the B ions, D_{AB} is inter diffusion coefficient of B, k_0 is the parabolic rate constant for the growth of BS on B under the given sulfur pressure and M is atomic weight of sulfur. Several systems have been found to agree with this expression^(34,35).

2.4.3 Interface Stability

Wagner ⁽³⁵⁾ suggested that if the interdiffusion in the alloy is fast compared with the rate at which B is consumed by scale growth ($D_{AB} \gg k_0$), B cannot be depleted in the alloy to any great extent. A ripple in the alloy-sulfide interface develops rapidly at the advanced position shown in Fig. 2.2 and labelled 1, because the concentration gradient through the sulfide is steeper at that point. Hence the ripple decays and a planar interface tends to be restored.

However, when diffusion in the alloy is much slower, the sulfide growth rate k drops well below k_0 . Ripples in the alloy-sulfide interface now grow more rapidly at deepest positions, labelled 2, because the steepest concentration gradient in the alloy exists at such points. Thus instability of the planar interface is favoured by slow intermetallic diffusion and an easy diffusion through the sulfide.

Wagner ⁽³⁶⁾ found that the necessary condition of a planar interface is given by

$$\frac{N_B}{1-N_B} \frac{(D/V_a)_{\text{alloy}}}{(D^*/V_s)_{\text{sulfide}}} < 1 \quad (2.21a)$$

where N_B is the mole fraction of B in the bulk alloy, D^* is the self diffusion coefficient of cation in the sulfide at the alloy interface, V_a and V_s are the respective molar volume of alloy and sulfide phases and D is the interdiffusion coefficient in the alloy. The spikes are favoured by dilute B and small

diffusivity in the alloy relative to the sulfide. The more extended tips of the alloy spikes tend to spherodize and may give rise to isolated particles embedded in the external scale as observed in the oxidation of Fe-Ni alloys by Wulf et al. (37). The above criterion is limited under the assumption that sulfur solubility in the alloy and of the more noble alloy component in the sulfide are negligible.

Coates and Kirkaldy (38) have analyzed the interface stability for the general case of isothermal ternary systems. It was assumed that the diffusion coefficients are not a function of concentration, (and that the off-diagonal diffusion coefficients were negligible. The deduced criterion involves diffusion coefficients in the single phase regions of the diffusion couple and parameters related to the ternary isotherm. The general stability criterion was tested through comparison with the results of earlier treatments of related problems and was utilized to establish criteria for (i) interfaces in diffusion bonded materials, (ii) interfaces associated with isothermal systems in which solid alloys are in contact with liquid metals, (iii) oxide-metal interfaces during oxidation of alloys and (iv) precipitate-matrix interfaces in ternary systems.

More recently Whittle et al. (39) derived the stability criteria for the growth of a nearly stoichiometric oxide $(BA)_2O$ on a binary AB alloy. It was assumed that the diffusion coefficients in the alloy were independent of concentration

(alloy is sufficiently dilute with respect to B and O) and that oxygen diffused much more rapidly than metal. Application of linear perturbation theory under these limiting approximations, proved the following. If oxygen diffusion in the alloy occurs predominantly down its own gradient (no cross diffusional effect), the stability criterion for a planar interface is

$$\frac{N_B^{I*} D_{OO}^I + 2(N_B^{I*} - N_B^{I*}) \sqrt{D_{BB}^I D_{OO}^I}}{N_B^{I*} D_{BB}^I + N_B^{II*} D_B^{II*} (V^I/V^{II})} > 1 \quad (2.21b)$$

This criterion becomes in the case of oxygen diffusion in the alloy occurring predominantly from its interaction with the metal gradient

$$\frac{N_B^{I*} V^{II} D_{BB}^I}{N_B^{II*} V^I D_B^{II*}} \left\{ 1 - N_B^{I*} \epsilon_O^B \frac{D_{OO}^I}{D_{BB}^I} \right\} > 1 \quad (2.21c)$$

In these expressions, D , N and V represent self-diffusion coefficients, mole fractions and molar volumes of the alloy and oxide phases denoted by superscript I and II, respectively. Asterisks on these parameters refer to values at a planar alloy-oxide interface. B and O refer to the selectively oxidized metal component and oxygen. N_B^{I*} is the initial concentration of B and ϵ_O^B is the Wagner interaction coefficient between oxygen and B in the alloy.

2.4.4 The Concept of Diffusion Paths

Referring to Onsager's phenomenological multicomponent diffusion theory, as applied by Kirkaldy⁽⁴⁰⁾, the following expressions, which are similar to Fick's second law, can be derived to relate the concentrations of the two independent components in a ternary system

$$\frac{\partial N_1}{\partial t} = \frac{\partial}{\partial x} \left(D_{11} \frac{\partial N_1}{\partial x} \right) + \frac{\partial}{\partial x} \left(D_{12} \frac{\partial N_2}{\partial x} \right) \quad (2.22a)$$

and

$$\frac{\partial N_2}{\partial t} = \frac{\partial}{\partial x} \left(D_{21} \frac{\partial N_1}{\partial x} \right) + \frac{\partial}{\partial x} \left(D_{22} \frac{\partial N_2}{\partial x} \right) \quad (2.22b)$$

Assuming parabolic growth, a parametric substitution

$$x = \lambda t^{1/2} \quad (2.22c)$$

may be used to transform equations 2.22(a) and (b) to ordinary differential equations. The solutions are given by equations in the form

$$N_B = N_B(\lambda) \quad (2.23a)$$

and

$$N_S = N_S(\lambda) \quad (2.23b)$$

where the solute metal (B) and sulfur (S) are chosen arbitrarily as the two independent components. λ can be eliminated from the last two equations to obtain the distribution

$$N_B = N_B(N_S) \quad (2.23c)$$

This relationship can be plotted on the pertinent A-B-S isotherm and the locus obtained is termed the "virtual diffusion path". This path is unique for a given terminal composition and a given set of experimental conditions e.g., constant temperature and pressure. This diffusion path concept is a very compact means of representing ternary diffusion behaviour, especially in multiphase systems.

Kirkaldy and Brown⁽⁴¹⁾ have developed seventeen useful theorems relating to the construction of diffusion paths in ternary multi-phase systems. The path obtained by plotting the relation (2.23c) is defined as a virtual diffusion path because it is calculated on the assumption that all the interfaces are planar and stable and that there is no internal precipitation. Using the virtual diffusion path in conjunction with a knowledge of the thermodynamic and diffusion parameter of the system, one can find whether or not to expect the morphological breakdown or internal sulfidation. To describe the actual configuration one must take into account these phenomena and solve the diffusion equations with a re-formulated set of boundary conditions. A relationship of the form of eqn. 2.23(c) then obtained is referred to as the actual diffusion path.

Figure 2.3 shows a ternary isothermal section of a hypothetical phase diagram (A-B-S) on which two possible diffusion paths and corresponding schematic microstructures are shown. The system is assumed to only contain one sulfide BS_v and element A is considered noble. Path (1) enters into the two-

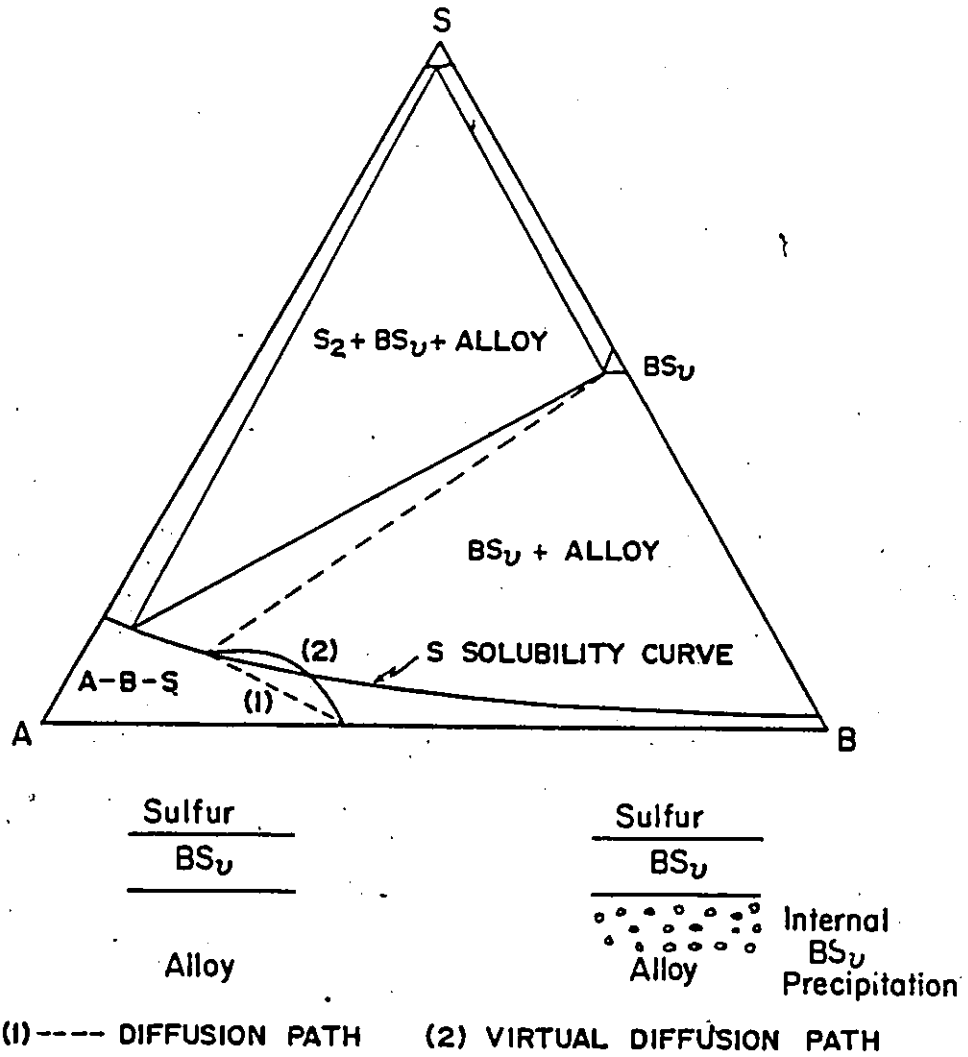


Fig. 2.3 Plot of diffusion paths on the ternary A-B-S isotherm and the corresponding schematic scale microstructures.

phase region coinciding with a tie line and accordingly, a planar interface is exhibited between the sulfide and alloy. Path (2) crosses tie lines in a two-phase region which implies the existence of a constitutionally super saturated zone in front of the planar alloy/sulfide interface. Relief of this super-saturation can occur through morphological break-down of the planar alloy/sulfide interface and/or through internal precipitation of sulfide within the alloy phase adjacent to the interface. The oxidation behaviour of Ni-Fe and Ni-Cr alloys have been interpreted by Dalvi and Coates⁽⁴²⁾ using the diffusion path concept.

2.4.5 Internal Sulfidation

The internal sulfidation of alloys is held to occur through dissolution of atomic sulfur into the base metal at its surface (in the absence of scale) or at the metal-scale interface. The dissolved sulfur diffuses inwards through the metal matrix containing some previously precipitated internal sulfide particles. At an advancing reaction front which remains essentially parallel to the external surface, the inward diffusion of sulfur and the outward diffusion of the alloying element continuously provide sulfur and alloying element concentrations in excess of those corresponding to the solubility product of the alloying element sulfide. Repeated nucleation with accompanying growth of sulfide particles results and the reaction front continues to advance inwards at a decreasing rate which is calculable if this simple model is assumed to hold.

On the basis of this model, the following conditions form a necessary criterion for the occurrence of internal sulfidation in a binary alloy during its isothermal sulfidation at a constant sulfur pressure.

(i) The free energy of formation (per mole of sulfur) for the solute metal sulfide in the bulk alloy must be more negative than the free energy of formation of the lowest sulfide of the base metal.

(ii) To achieve the required activity of dissolved sulfur at the reaction front, the pure solvent metal must exhibit a significant solubility and diffusivity for atomic sulfur.

(iii) The solute metal content of the bulk alloy must be lower than that required to cause the transition from internal to external sulfidation.

(iv) A surface layer formed in the preparation of the alloy surface must not prevent sulfur dissolution into the metal. Therefore, an alloy which satisfies conditions (i) and (ii) may be prevented from undergoing internal sulfidation by intentionally preventing the fulfilment of conditions (iii) and (iv).

Various features of internal oxidation behaviour have been described by Rhines et al. (43,44), Darken (45), Bohm and Kahlweit (46), Wagner (47) and Rapp (48,49,50). The formalism given by Rapp (50) is used in this text. If diffusion control is maintained, the depth ξ , of the internal sulfidation zone, is a parabolic function of time, 't', and may be expressed as:

$$\xi = 2\gamma(D_S t)^{\frac{1}{2}} \quad (2.24)$$

while the velocity of the reaction front motion $d\xi/dt$ is given by:

$$\frac{d\xi}{dt} = \gamma \left(\frac{D_S}{t} \right)^{\frac{1}{2}} \quad (2.25)$$

where D_S is the diffusivity of sulfur in the base metal and γ is a dimensionless parameter. By application of Fick's second law to one-dimensional sulfur diffusion in the base metal and assuming that previously precipitated particles do not interfere with sulfur diffusion,

$$\frac{\partial N_S}{\partial t} = D_S \frac{\partial^2 N_S}{\partial x^2} \quad (2.26)$$

which may be solved for the following boundary conditions,

$$N_S = N_S^{(S)} \quad \text{for } x = 0, t > 0 \quad (2.27)$$

$$N_S = 0 \quad \text{for } x \geq \xi, t > 0 \quad (2.28)$$

where N_S is the mole fraction of sulfur in the base metal, $N_S^{(S)}$ is the mole fraction of sulfur at the external surface and x is the distance from the external surface. Analogously, the solution of the diffusion for the less noble alloying element B, namely

$$\frac{\partial N_B}{\partial t} = D_B \frac{\partial^2 N_B}{\partial x^2} \quad (2.29)$$

is obtained with boundary conditions

$$N_B = N_B^{(0)}, \quad \text{for } x > 0, \quad t = 0 \quad (2.30)$$

$$N_B = 0 \quad \text{for } x \leq \xi, \quad t > 0 \quad (2.31)$$

where N_B is the mole fraction of B at x and $N_B^{(0)}$ is the mole fraction of B in the alloy.

Wagner⁽⁴⁷⁾ has obtained the following solutions of Eqns. (2.26) and (2.29) for the given boundary conditions as

$$N_S = N_S^{(S)} \left(1 - \frac{\text{erf}[x/2(D_S t)^{1/2}]}{\text{erf}(\gamma)} \right) \quad (2.32)$$

$$N_B = N_B^{(0)} \left(1 - \frac{\text{erfc}[x/2(D_B t)^{1/2}]}{\text{erfc}(\gamma \phi^{1/2})} \right) \quad (2.33)$$

where $\phi = D_S/D_B$, erf is the error function and erfc is complementary error function and x is the distance from outer surface of the alloy. The mass balance within the internal sulfidation zone can be used to find an expression for γ . At the precipitation front,

$$\lim_{\epsilon \rightarrow 0} \left[D_S \frac{\partial N_S}{\partial x} \Big|_{x=\xi-\epsilon} = -v D_B \frac{\partial N_B}{\partial x} \Big|_{x=\xi+\epsilon} \right] \quad (2.34)$$

where v is the number of sulfur ions per B ion in the sulfide BS_v . It can be shown that

$$\frac{N_S^{(S)}}{v N_B^{(0)}} = \frac{\exp(\gamma^2) \text{erf} \gamma}{\phi^{1/2} \exp(\gamma^2 \phi) \text{erfc}(\gamma \phi^{1/2})} \quad (2.35)$$

from which γ can be determined knowing $N_S^{(S)}$, $N_B^{(O)}$, v and ϕ . Two limiting approximations exist. For $\gamma \ll 1$ and $\gamma \phi^{1/2} \gg 1$ which is equivalent to

$$\frac{D_B}{D_S} \ll \frac{N_S^{(S)}}{N_B^{(O)}} \ll 1,$$

Eqn. (2.24) may be simplified to

$$\xi = \left[\frac{2N_S^{(S)} D_S t^{1/2}}{v N_B^{(O)}} \right] \quad (2.36)$$

Equation (2.36) is expected to hold under conditions where the movement of the precipitation front is completely determined by sulfur diffusion in the metal (Fig. 2.4).

In a second limiting case, if $\gamma \ll 1$ but $\gamma \phi^{1/2} \ll 1$, conditions which are equivalent to

$$\frac{N_S^{(S)}}{N_B^{(O)}} \ll \frac{D_B}{D_S} \ll 1, \quad \text{then}$$

and

$$\xi = \frac{N_S^{(S)}}{v N_B^{(O)}} (\pi \phi D_S t)^{1/2} \quad (2.37)$$

In this case, the rate of outward diffusion of the alloying element, as well as inward sulfur diffusion are important in determining the sulfidation kinetics (Fig. 2.4).

A further parameter used in the description of internal

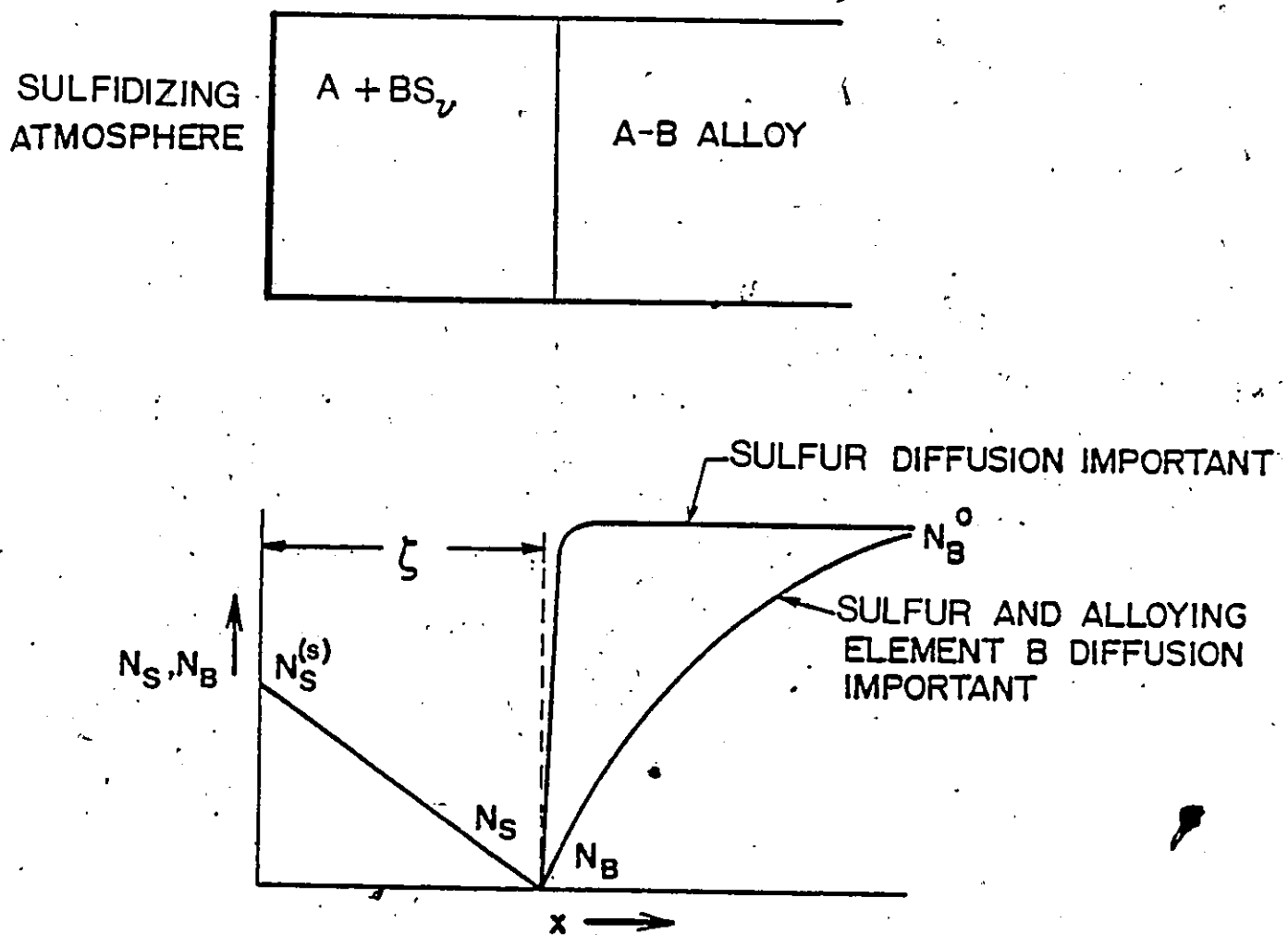


Fig. 2.4 Steady-state concentration profiles for internally sulfidized A-B alloy.

sulfidation process is the enrichment factor, α . Rapp⁽⁵⁰⁾ defined α as follows:

$$\alpha = f/N_B^{(0)} \quad (2.38)$$

where f is the mole fraction of solute B present as the sulfide BS_V in the internal sulfidation zone. From the derivation by Wagner⁽⁴⁷⁾, it can be shown that the fraction of solute enrichment in the zone of internal sulfidation, α , is given by

$$\alpha = [\pi^{1/2} \gamma \phi^{1/2} \exp(\gamma^2 \phi) \operatorname{erfc}(\gamma \phi^{1/2})]^{-1} \quad (2.39)$$

Under the limiting conditions yielding equation (2.36) and Fig. (2.4), a negligible enrichment occurs. For the second case, where Eqn. (2.37) and Fig. (2.4) are valid, an enrichment of solute as BS_V in the sulfidized zone and a depletion of solute from the unsulfidized alloy will result, especially when $N_S^{(S)}$ and ϕ are relatively small.

In most practical applications of high temperature alloys, the internal sulfidation zone forms beneath an external sulfide scale. Expressions describing the kinetics of internal sulfidation in combination with a parabolically thickening external scale have been derived by Rhines et al.⁽⁴³⁾ and Maak⁽⁵¹⁾. The latter author solved the diffusion equations for sulfur at $x < \xi$ and for the solute element B at $x < \xi$ where x is the position co-ordinate of the metal scale interface to obtain the concentration profiles:

$$N_S = N_S^{(S)} \frac{\text{erf}(\gamma) - \text{erf}[x/2(D_S t)^{1/2}]}{\text{erf}(\gamma) - \text{erf}(k_p/2D_S)^{1/2}} \quad (2.40)$$

$$N_B = N_B^{(O)} \left\{ 1 - \frac{\text{erfc}[x/2(D_B t)^{1/2}]}{\text{erfc}(\gamma\phi^{1/2})} \right\} \quad (2.41)$$

For the usual case that $\gamma \ll 1$ and $x \ll \xi$,

$$\frac{\xi(\xi-x)}{2t} = \frac{N_S^{(S)} D_S}{N_B^{(O)} v} F[\xi/2(D_B t)^{1/2}] \quad (2.42)$$

where the auxiliary function F is defined as

$$F(\eta) = \pi^{1/2} \eta \exp(\eta^2) \text{erfc}(\eta) \quad (2.43)$$

in which η is given by

$$\eta = \xi/2(D_B t)^{1/2} \quad (2.44)$$

Depths of internal oxidation zones below a parabolically thickening external scale have been measured for copper-based alloys by Maak⁽⁵¹⁾ and Rapp⁽⁵⁰⁾.

Bohm and Kahlweit⁽⁴⁶⁾ have made a detailed analysis of sulfide nucleation and growth at the internal sulfidation front. They derived the following equation for the number of precipitates per unit volume as a function of the distance from the surface x .

$$Z(x) = \beta \left(\frac{N_S^{(S)}}{x} \right)^3 \quad (2.45)$$

where β is a function of D_S/D_B , $N_B^{(O)}$, K_{sp} and $N_S^* \cdot N_B^*$ (the critical concentration product necessary to form a nucleus of critical size). From equation (2.45) one predicts that:

(a) the number of precipitates per unit volume for a given $N_S^{(S)}$ depends inversely on the cube of the distance of precipitation site from the external surface.

(b) The number of precipitates per unit volume at a given x varies directly as the cube of the oxygen mole fraction at the metal surface.

Wagner⁽⁵²⁾ utilized the solutions of diffusion equations for sulfur and alloying element B to obtain an expression for the product $N_B N_S^V$ at any point. The gradient of this product is related to the diffusion parameters in the alloy, the bulk alloy composition, composition of the alloy at the scale/alloy interface and the rate of thickening of the external scale. The following parameter for the alloy was evaluated,

$$g_S = \left(\frac{\partial \ln(N_B \cdot N_S^V)}{\partial x} \right)_{x=X} \quad (2.46)$$

where X is the co-ordinate of scale-alloy interface. Figure 2.5(a) shows concentrations of solute B and sulfur in the underlying alloy. At the scale-alloy interface, the alloy is saturated with respect to the sulfide BS , i.e. the product $N_B N_S^V$ equals to the solubility product K_{sp} at $x = X$ (Fig. 2.5(b)). Thus one has the following cases:

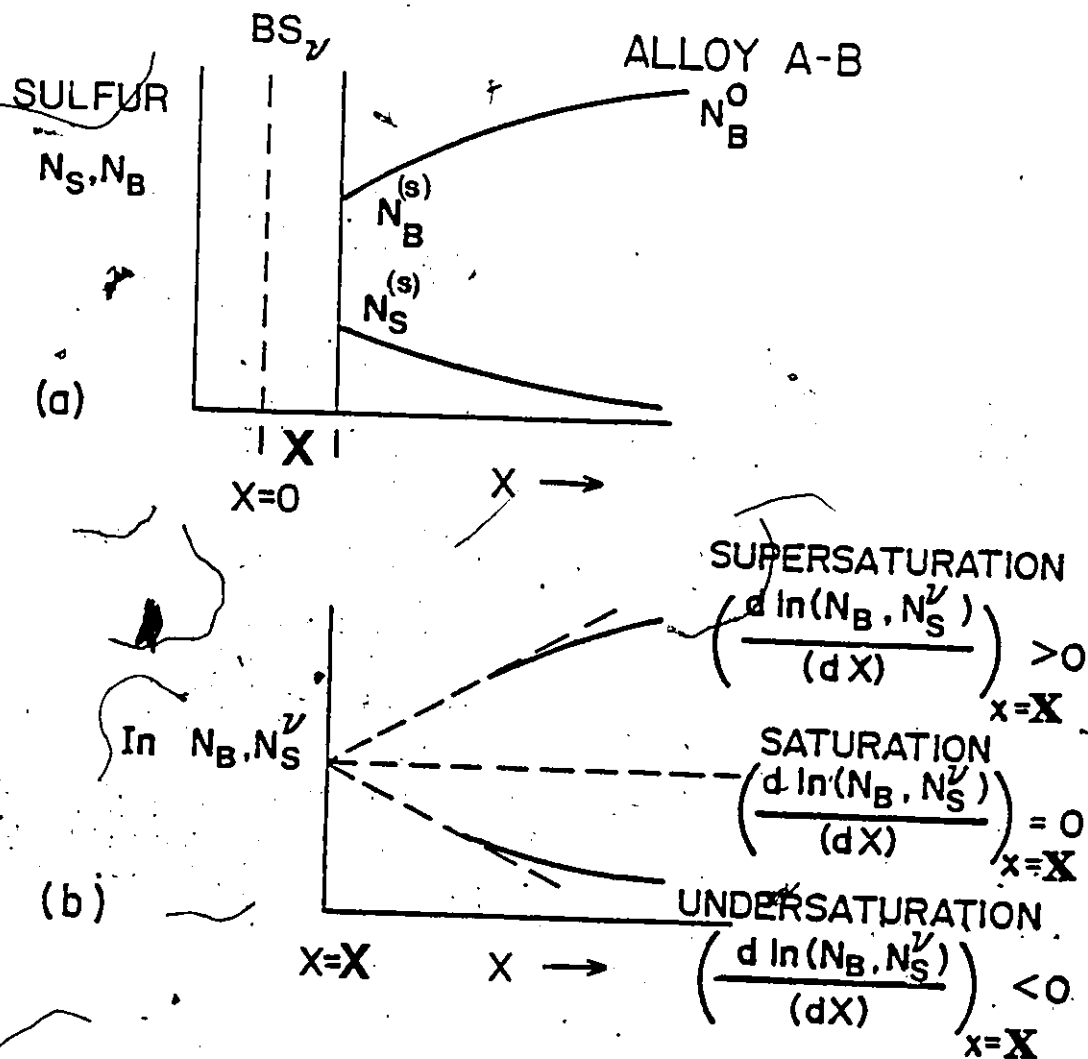


Fig. 2.5 a) Cross-section showing concentration of solute B and sulfur in the underlying alloy.

b) The product $N_B \cdot N_S^V$ as a function of distance in the underlying alloy demonstrating three possibilities (Ref. 54).

a) If the value of g_s in Eqn. (2.46) is negative, the alloy next to scale is undersaturated with respect to sulfide BS_v and no internal sulfidation can occur.

b) If conversely g_s is positive, the alloy next to scale is supersaturated with respect to sulfide BS_v and internal sulfidation may occur. Accordingly the limiting condition for possible internal sulfidation is $g_s > 0$.

Wagner⁽⁵²⁾ has applied the criterion $g_s > 0$ to the oxidation of Cu-Pd alloys and obtained a value of about 2600 for g_s indicating that the condition for internal oxidation was satisfied.

A criterion to define the limiting alloy composition for prevention of depletion of the alloying element by internal sulfidation is of significant importance when considering sulfidation heat-resistant alloys. Wagner⁽⁵²⁾ has placed forward the following criterion: internal sulfidation occurs if diffusion causes the product of the metal and sulfur concentrations to exceed the solubility product of the sulfide at a distance in the alloy behind the scale/alloy interface. He was able to show that the critical solute alloying element atom fraction N_B^{O*} required for exclusive scale growth is

$$N_B^{O*} \geq \frac{F(u) + \frac{1}{v} \left(\frac{D_S}{D_B}\right)^{\frac{1}{2}} u \pi^{\frac{1}{2}}}{1 + \frac{1}{v} \left(\frac{D_S}{D_B}\right)^{\frac{1}{2}} u \pi^{\frac{1}{2}}} \quad (2.47)$$

where v is given by the formula BS_v , $u = (k_p/2D_B)^{1/2}$ and $F(u) = \pi^{1/2} \cdot u \cdot \exp u^2 \cdot \operatorname{erfc}(u)$. Atkinson⁽⁵³⁾ recently demonstrated that Eqn. (2.47) predicted in good agreement with experiment that 0.05 atom fraction of Si should impart SiO_2 film growth on Fe-Si alloys at 773K.

Smeltzer and Whittle⁽⁵⁴⁾ completed a treatment of this problem using a ternary diffusion approach. The diffusion model is given in Fig. 2.6. The ternary oxide $B_{1-\delta}A_\delta O_v$ was assumed to correspond closely with the composition of the binary oxide ($\delta \ll 1$) and the oxygen solubility was considered to exhibit a minimum. Oxygen was considered as the only component diffusing on both its own and on the metal gradient.

The flux equations for the conditions in fig. 2.6 are

$$j_B = -D_{BB} \frac{\partial N_B}{\partial x} \quad (2.48)$$

$$j_O = -D_{OO} \left(\frac{\partial N_O}{\partial x} + \epsilon_{ON_O}^B \frac{\partial N_B}{\partial x} \right) \quad (2.49)$$

where the dilute solution approximation for oxygen diffusing interstitially has been substituted for the off-diagonal diffusion coefficient D_{OB} :

$$D_{OB} = D_{OO} \epsilon_{ON_O}^B \quad (2.50)$$

Assuming D_{OO} and D_{BB} concentration independent then divergence of the fluxes may be written as:

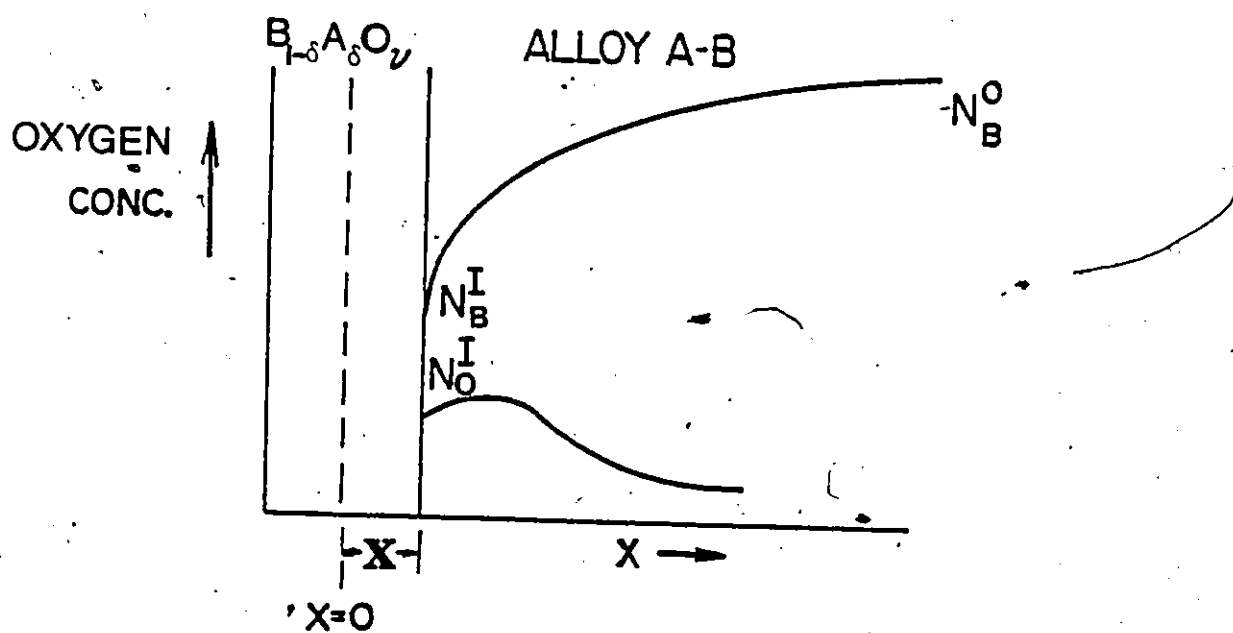


Fig. 2.6 Ternary oxidation model⁽⁵⁴⁾.

$$\frac{\partial N_B}{\partial t} = \frac{\partial}{\partial x} \left(D_{BB} \frac{\partial N_B}{\partial x} \right) = D_{BB} \frac{\partial^2 N_B}{\partial x^2} \quad (2.51)$$

$$\begin{aligned} \frac{\partial N_O}{\partial t} &= \frac{\partial}{\partial x} \left\{ D_{OO} \left(\frac{\partial N_O}{\partial x} + \epsilon_{O^B}^B \frac{\partial N_B}{\partial x} \right) \right\} \\ &= D_{OO} \frac{\partial^2 N_O}{\partial x^2} + D_{OO} \epsilon_{O^B}^B \frac{\partial}{\partial x} \left(N_O \frac{\partial N_B}{\partial x} \right) \end{aligned} \quad (2.52)$$

The solution to equation (2.51) is:

$$N_B = N_B^O - (N_B^O - N_B^I) \frac{\operatorname{erfc}(x/2\sqrt{D_{BA}t})}{\operatorname{erfc}(\sqrt{k_p/2D_{BA}})} \quad (2.53)$$

where N_B^I is the atom fraction B at the scale/alloy interface, k_p is the corrosion constant related by

$$x = \sqrt{2k_p t} \quad (2.54)$$

to the position of actual alloy surface X (Fig. 2.6) at any time.

The solution for the oxygen profile is given by

$$\begin{aligned} N_O &= \frac{D_{OB}}{D_{OO}} (N_B^O - N_B^I) \frac{\operatorname{erfc}(x/2\sqrt{D_{BB}t})}{\operatorname{erfc}(k_p/2D_{BB})^{1/2}} \\ &+ N_O^I \frac{\operatorname{erfc}(x/2\sqrt{D_{OO}t})}{\operatorname{erfc}(k/2D_{OO})^{1/2}} \\ &- \frac{D_{OB}}{D_{OO}} (N_B^O - N_B^I) \frac{\operatorname{erfc}(x/2\sqrt{D_{OO}t})}{\operatorname{erfc}(k_p/2D_{OO})^{1/2}} \end{aligned} \quad (2.55)$$

where N_O^I is the mole fraction of oxygen at the alloy/scale interface, which is also the oxygen solubility limit for an alloy of composition N_B^I .

The condition for internal oxidation to occur is

$$\left(\frac{dN_O}{dN_B}\right)_{x=X}^{DP} \geq \left(\frac{dN_O}{dN_B}\right)_{x=X}^{Sol} \quad (2.56)$$

where the gradient of the diffusion path (DP) at $x = X$ is given by

$$\left(\frac{dN_O}{dN_B}\right)_{x=X}^{DP} = \left(\frac{\partial N_O}{\partial x} / \frac{\partial N_B}{\partial x}\right)_{x=X} \quad (2.57)$$

The gradient of the oxygen solubility curve at $x = X$ with N_B^I and N_O^I as the interfacial oxygen and solute concentrations is obtained from equations (2.8) - (2.10) and (2.12) as:

$$\left(\frac{dN_O}{dN_B}\right)_{x=X}^{Sol.} = - \frac{N_O^I}{N_B^I} \left(\frac{1 + N_B^I \epsilon_B^B + v N_A^I \epsilon_O^B}{v + N_O^I \epsilon_O^B + v N_O^I \epsilon_O^O} \right) \quad (2.58)$$

Using eqns. (2.64), (2.65), (2.68) and (2.69) in (2.67), a limiting bulk atom fraction of the solute, N_B^{O*} , in the alloy was defined above which internal oxidation does not occur. N_B^{O*} satisfies,

$$\begin{aligned} \epsilon_O^B (N_B^{O*})^2 + \left\{ \frac{1-F(u)}{F(u)} \left[1 + \left(\frac{D_{OO}}{D_{BB}} \right)^{\frac{1}{2}} \frac{u}{v} \pi^{\frac{1}{2}} \right] - \epsilon_O^B [1+F(u)] \right\} N_B^{O*} \\ + \left\{ \epsilon_O^B F(u) - (1-F(u)) - \left(\frac{D_{OO}}{D_{BB}} \right)^{\frac{1}{2}} \frac{1-F(u)}{F(u)} \frac{u}{v} \pi^{\frac{1}{2}} \right\} = 0 \end{aligned} \quad (2.59)$$

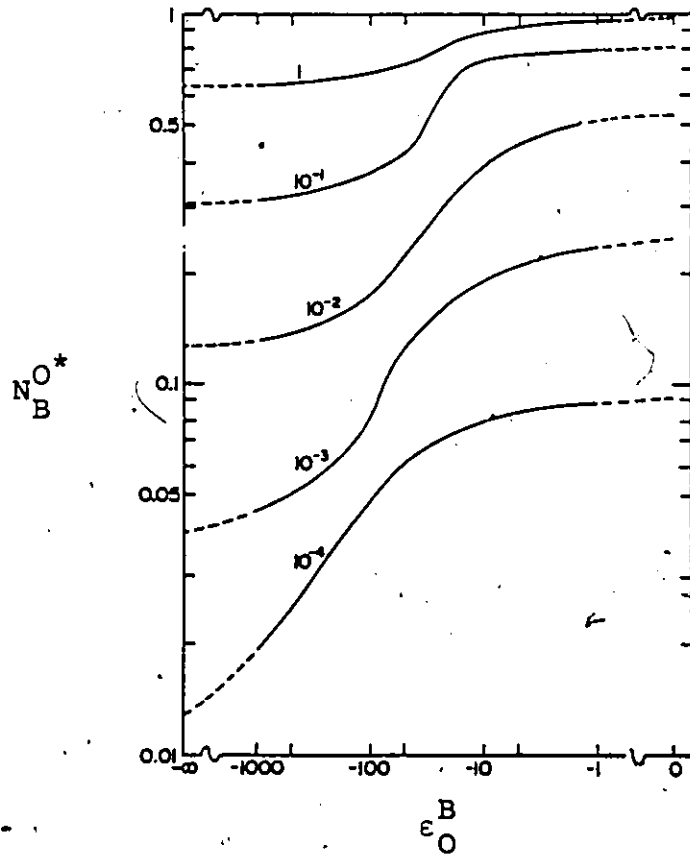
where, ϵ_O^B is the Wagner interaction coefficient of oxygen and B in the alloy. In case of ideal behaviour, when $\epsilon_O^B = 0$, Eqn. (2.59) reduces to (2.47).

Any test of the application of predictions from this model suffers from these extreme limitations: the lack of oxygen or sulfur solubility data in solid binary alloys, of ternary interaction parameters and of ternary A-B-O or A-B-S phase diagrams. However, Eqn. (2.59) was used to evaluate $N_B^{O^*}$ as a function of ϵ_O^B for $D_{OO}/D_{BB} = 100$ and several values of k_p/D_{BB} as shown in Fig. 2.7(a). $N_B^{O^*}$ of each calculated curve ranges between two limiting extremes dependent on ϵ_O^B . Thus $N_B^{O^*}$ is markedly affected by non-ideal oxygen solution behaviour especially within a range of value $-1000 < \epsilon_O^B < -10$. The influence of non-ideal oxygen solution behaviour on both its solubility and virtual diffusion paths is illustrated by the plots in Fig. 2.7(b). The solubility curves exhibit minima of larger oxygen concentration at smaller N_B as ϵ_O^B becomes more negative. For the diffusional cases considered, the alloying element is prevented from internally oxidizing when $\epsilon_O^B = -100$. The alloy is internally oxidized for $\epsilon_O^B < -100$: the diffusion paths cut into the two-phase alloy+oxide field because the slope of the virtual diffusion path is of larger magnitude at its contact point with the solubility curve.

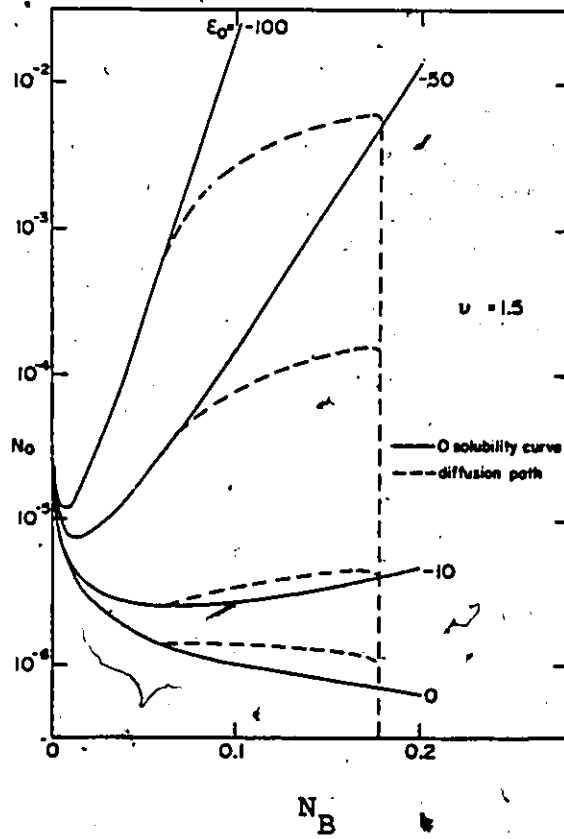
Analysis of the internal oxidation problem by concepts of ternary diffusion is of recent origin. Lesychyn⁽⁵⁵⁾ has investigated the transition from internal to external oxidation for Ag-Zn alloys: this transition to exclusive growth of a ZnO film at 823K occurs at 0.28 atom fraction of Zn. Equation (2.47) predicts the unreasonable value of $N_{Zn}^{O^*} = 0.9$ whilst

Fig. 2.7 a) The critical atom fraction of B in the alloy, N_B^{O*} for exclusive external oxidation as a function of k_p/D_{BB} and ϵ_O^B , $D_{OO}/D_{BB} = 100$.

b) The oxygen solubility curve according to Eq. (2.17) with $K_H = 10^{-10}$, $k_p = 10^{-12}$ and $\nu = 1.5$ with diffusion paths superimposed for an alloy of $N_B^O = 0.178$.



a.



b.

Eqn. (2.59) predicts a value corresponding to the experimental value if $\epsilon_0^{\text{Zn}} = -500$. It therefore appears that measurements on the non-ideal oxygen or sulfur solution behaviour and determinations of oxygen-metal or sulfur-metal interaction coefficients are essential for a more complete description and understanding of internal oxidation or sulfidation. Recently, Gesmundo et al. (56) used a quasi-chemical approach and derived a value of -3884 for ϵ_0^{Al} in Cu-Al alloys at 1173K. Ozturk et al. (57) have used the surface excess thermodynamic approach for Fe-Cr alloys in oxygen atmosphere and derived a value of -87 for ϵ_0^{Cr} at 1313K as compared to -8.6 at liquid iron temperature 1873K.

2.4.6 Morphology and Distribution of Internal Sulfide Precipitates

The previously discussed classical description of internal sulfidation defines general precipitation of the sulfide of the selectively sulfidized element as small polyhedral or acicular particles at a volume fraction small enough not to interfere with diffusion. It is recognized, however, that several other types of precipitation modes may compete and even completely suppress the above type of general precipitation.

One mode of internal sulfidation encompasses cellular and discontinuous precipitation whereby the sulfur saturated parent alloy phase (α) decomposes to the solute-depleted but structurally identical phase (α') and a sulfide precipitate phase (β). That is, $\alpha \rightarrow \alpha' + \beta$ by growth of parallel $\alpha' + \beta$ lamel-

lae into α . In discontinuous precipitation, lateral segregation of the alloying element occurs by diffusion along a boundary separating α' from α . Another mode involves eutectic or eutectoid decomposition whereby the sulfur supersaturated liquid or solid parent phase (γ) transforms into two new phases ($\alpha+\beta$). Thus $\gamma \rightarrow \alpha+\beta$ by growth of parallel lamellae of two sulfides into the γ phase.

Examples of this type of behaviour are seen in the oxidation of γ Ni-Al⁽⁵⁸⁾ alloys and sulfidation of Ni-Mo⁽⁵⁹⁾ and Ni-Al⁽⁶⁰⁾ alloys. Oxidation of γ Ni-Al alloys containing 2 to 8 a/o Al in the range 1073 to 1473K leads to growth of a duplex scale containing layers of NiO, NiO+NiAl₂O₄ and an Al depleted alloy region containing oxide cylindrical rods which extend right across the internal oxidation zone. These rods consist of NiAl₂O₄ and Al₂O₃, the latter oxide accounting for ~ 35% of the innermost rod length⁽⁶¹⁾. In this case, a boundary in the alloy at the reaction front for lateral diffusion of metal did not occur. The growth of the oxide rods is controlled by simultaneous outward aluminum and inward oxygen diffusion to the reaction front.

An internal sulfidation zone in Ni-Mo alloys exhibits cellular morphology arising from discontinuous precipitation. The internal MoS_x precipitates grow as regularly spaced plates into the alloy and a sharply defined boundary existed in the alloy at the reaction front. The sulfidation kinetics were linear. In the sulfidation of γ Ni-Al alloys at 973K in H₂S/H₂

atmospheres, the kinetics were linear and the reaction products were formed in three distinct layers: a NiS or Ni₃S₂ layer, an Al₂S₃-Ni₃S₂ lamellar layer and an innermost Al-Ni-S liquid layer. The latter two layers comprise the subscale which migrates inwards by diffusional and segregation processes of internal sulfidation. The lamellar layer in this case results from a cooperative precipitation process involving transformation of the Ni-Al-S liquid into two solid phases Al₂S₃ and Ni₃S₂.

Substantial deviation from the classical interpretation of internal oxidation has been observed by Whittle⁽⁶²⁾, Shida⁽⁶³⁾, Wood⁽⁶⁴⁾ and Stott et al.⁽⁶⁵⁾. Two types of internal penetration were observed: a relatively uniform penetration of internal oxidation through the alloy grains, and an enhanced penetration, especially at lower temperatures, along alloy grain boundaries. Whittle et al.⁽⁶²⁾ have described the kinetics of uniform type of internal oxidation and attempted to analyze the discrepancies between the observed rates and those anticipated from the classical theory outlined in the previous section, in terms of a model based on enhanced inward penetration of oxygen at the incoherent interfaces between oxide particles and alloy matrix within the internal oxidation zone.

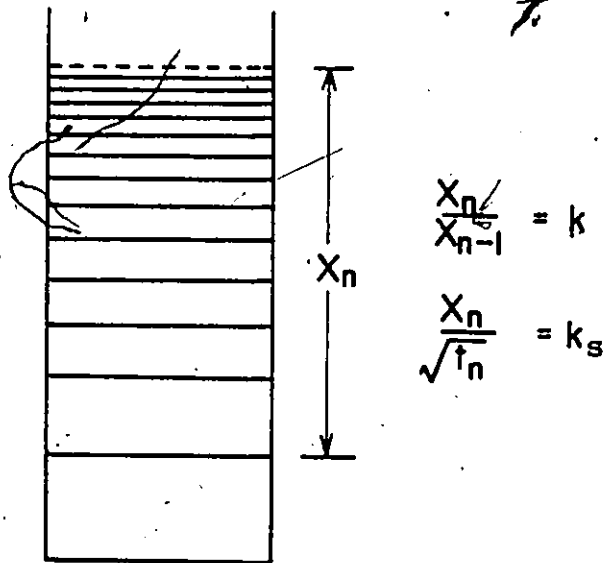
Extensive studies on the Ag-Cd system⁽⁶⁶⁾ have shown that internal oxidation of these alloys containing small amounts of certain metallic impurities such as Al, Be, Mg, Sc and Y leads to periodic precipitation of oxides as Liesegang bands. The

classical description of periodic precipitation was first given by R.E. Liesegang in colloidal systems and it is now classified as "Liesegang Phenomenon" (67). This phenomenon is observed, when, in a test tube one concentrated aqueous solution containing A ions is kept on top of another dilute gelatin solution with a second electrolyte containing B ions. The ions diffuse into the gelatin and react to form an insoluble precipitate $A_{\nu_A} B_{\nu_B}$. The precipitate forms discontinuous bands of homogeneous precipitation as shown in Fig. 2.8 by the two kinetic relationships (Eqns. 2.60 and 2.61) which have been proven to be valid by several investigators (68,69).

$$\frac{x_n}{x_{n-1}} = k \quad (2.60)$$

$$\frac{x_n}{\sqrt{t_n}} = k_s \quad (2.61)$$

Equation (2.60) defines the ratio of distances of n^{th} and $(n^{\text{th}}-1)$ band to be a constant k , known as Jablczynski's spacing coefficient (70) and Eqn. (2.61) defines the parabolic dependence of the distance of n^{th} band formation with time t_n . From these observations Ostwald (71) suggested that the precipitation is not an equilibrium process but occurs only when a certain critical value K_n^* of the concentration product $K_n = [A]^{\nu_A} \cdot [B]^{\nu_B}$ has been attained, at which point $A_{\nu_A} B_{\nu_B}$ precipitates until K_n reaches an equilibrium value for the solubility product. More recently,



Jablczynski's relationship $\frac{X_n}{X_{n-1}} = k$

$k \rightarrow$ Spacing coefficient

Fig. 2.8 Schematic representation of Liesegang bands.

Wagner⁽⁶⁸⁾ and Prager⁽⁶⁹⁾ completed approximate calculations for the distance of consecutive precipitation bands based upon an analysis of the diffusion processes. There has been numerous publications in the literature dealing with Liesegang phenomenon in colloidal systems where these mathematical analyses^(68,69) have been used successfully.

In the internal oxidation of Ag-Cd alloys containing Be, Al, Mg and Y, the CdO particles were found to be distributed in the form of bands satisfying the Jablczynski's relationship in the presence of the oxides of the ternary alloying element (MgO, Al₂O₃, etc.). Van Rooijen et al.⁽⁷²⁾ used a model of internal oxidation in ternary alloys to predict band spacing as a function of temperature, Cd concentration and concentration of the third element in good agreement with the experimental results.

The diffusional analysis for sulfidation of alloys by Kirkaldy⁽⁴⁰⁾ has shown that the sulfur concentration in the internal sulfidation zone can be expressed by

$$\frac{\partial N_S}{\partial t} = D_S \frac{(1 - \frac{D_B m}{D_S n})}{(1 - \frac{m}{n})} \frac{\partial^2 N_S}{\partial x^2} = D_{\text{eff}} \frac{\partial^2 N_S}{\partial x^2} \quad (2.62)$$

where N_S and N_B are the sulfur and alloying element concentrations

D_S and D_B are sulfur and alloying element diffusivities

$\frac{1}{m} = \frac{dN_S}{dN_B}$, slope of the solubility curve

$$n = \frac{N_B - N_B^{BS}}{N_S - N_S^{BS}}, \quad N_S^{BS} \text{ and } N_B^{BS} \text{ are concentrations of sulfur and alloying element in the BS sulfide, and}$$

D_{eff} is the effective diffusion coefficient.

It is possible that D_{eff} in Eqn. (2.62) can take negative values, thus implying the possibility of periodic spatial distribution in N_S and therefore a periodic precipitation of sulfide BS in the alloy. Equation (2.62) is a non-linear differential equation (since m and n are strong functions of concentrations) the solutions of which could correspond to the Liesegang phenomenon (67).

There have been a few other investigations on periodic precipitation in solid systems. Gerrard et al. (73) investigated the counter diffusion of Al and As in copper at 1173K using a Cu-1.5 As/Cu-8Al diffusion couple and observed periodic precipitation of AlAs in the Cu-8Al alloy. Chenot (74) observed periodic precipitation of GaAs in Ag-As alloys at 973K using a Ag-10Ga/Ag-6As diffusion couple. Gallium diffused into the Ag-As alloy to react with As forming GaAs precipitates in the form of bands parallel to the Ag-Ga/Ag-As couple interface (Fig. 2.9 (a)).

Extensive work on Liesegang phenomenon was completed by Klueh and Mullins (75) by annealing oxygen saturated silver single crystals in hydrogen at 1073K; hydrogen diffused into silver and reacted with the dissolved oxygen to form water vapour bubbles as precipitates. Under certain conditions the bubbles formed in the form of bands which obeyed the Jablczyn-

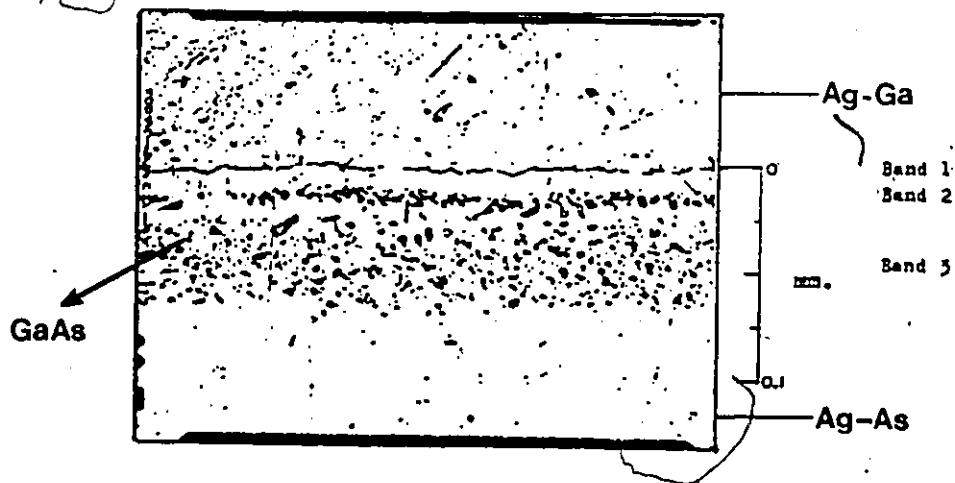


Fig. 2.9 (a) Microstructure of periodic precipitation of GaAs in Silver (74).

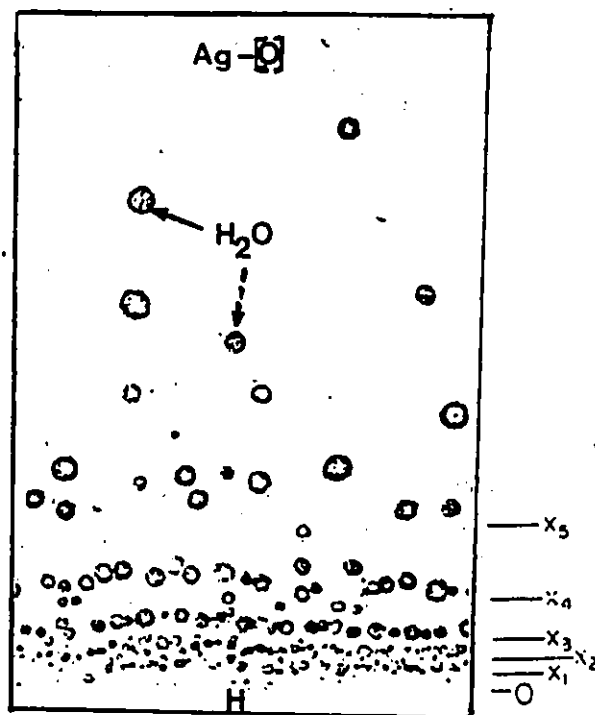


Fig. 2.9 (b) Periodic precipitation of water bubbles in silver (75).

ski's relationship (Fig. 2.9 (b)). They modified the Wagner's mathematical analysis of periodic precipitation and the spacing coefficient calculated from this more precise analysis compared well with that found experimentally. Table 2-1 summarizes the mode of precipitation and the diffusion parameters in solid systems. The distribution of precipitates in the subscale zone of an alloy has been analyzed by Laflamme and Morral⁽¹⁶⁸⁾ and Ohriner and Morral⁽¹⁶⁹⁾ using the diffusional approach by Kirkaldy⁽⁴⁰⁾. Two limiting cases of subscale formation have been identified. In one case the amount of precipitate is constant across the subscale zone and precipitation occurs at the subscale matrix interface. In the other case, precipitation occurs continuously through the subscale as the subscale forms. Treatment of the second limiting case results in an error function distribution for the amount of precipitate across the subscale zone⁽¹⁶⁸⁾.

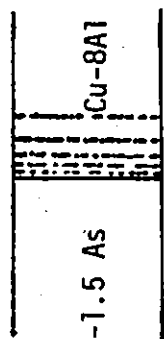
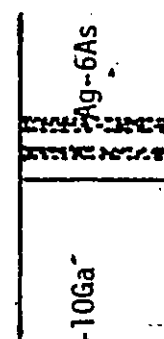
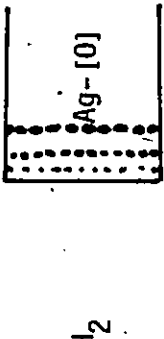
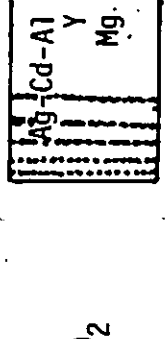
Reference	Temp. (K)	Couple	Outer Reactant	Inner Reactant	Precipitates	Diffusion Parameters
73	1173	Cu-1.5 As 	As	Al	AlAs	$D_{As} = 6.9 \times 10^{-9} \text{ cm}^2/\text{s}$ $D_{Al} = 1.7 \times 10^{-9} \text{ cm}^2/\text{s}$ $\frac{D_{As}}{D_{Al}} = 4$
74	973	Ag-10Ga 	Ga	As	GaAs	$D_{Ga} = 6 \times 10^{-10} \text{ cm}^2/\text{s}$ $D_{As} = 3 \times 10^{-10} \text{ cm}^2/\text{s}$ $\frac{D_{Ga}}{D_{As}} = 2$
75	1073	H ₂ 	H	O	H ₂ O	$D_H = 8.4 \times 10^{-5} \text{ cm}^2/\text{s}$ $D_O = 2.1 \times 10^{-5} \text{ cm}^2/\text{s}$ $\frac{D_H}{D_O} = 4$
72	1073	O ₂ 	O	Cd Al or Mg	CdO + Al ₂ O ₃ or MgO	$D_O = 2.1 \times 10^{-5} \text{ cm}^2/\text{s}$ $\left. \begin{matrix} D_{Al} \\ D_{Mg} \end{matrix} \right\} \text{ not known.}$

Table 2-1 Diffusion parameters and mode of precipitation in solid systems.

CHAPTER 3

LITERATURE REVIEW

3.1 INTRODUCTION

Stainless steels are not immune to corrosion in H_2S-H_2 atmospheres, although the rate of scaling is reasonably low at temperatures less than 500K. Therefore intensive research is being carried out presently to develop steels with alloying elements such as Al, Cr and Mn for resistance to high temperature H_2S-H_2 attack. This chapter reviews the available data on iron-aluminum, iron-sulfur and aluminum-sulfur binary systems and the Fe-Al-S ternary system which will be useful later in designing the experiments and to analyze the experimental results.

3.2 PROPERTIES OF Fe-Al ALLOYS

3.2.1 Crystal and Defect Structures

The Fe-Al phase diagram (Fig. 3.1) is well established (77,78). Unlike other f.c.c. metals aluminum is a ferrite (α) stabilizer, the atomic radius being 12% larger than iron. Miscibility with α -Fe extends to more than 50 a/o Al. Within this b.c.c. region there are two super lattices exhibiting wide solubility limits. In Fe-Al, CsCl (B2) structure, Fe occupies the cube corners and Al the centres and in Fe_3Al , the BiF_3 (DO_3) structure, Al occupies alternate cube centres. Fe_3Al undergoes

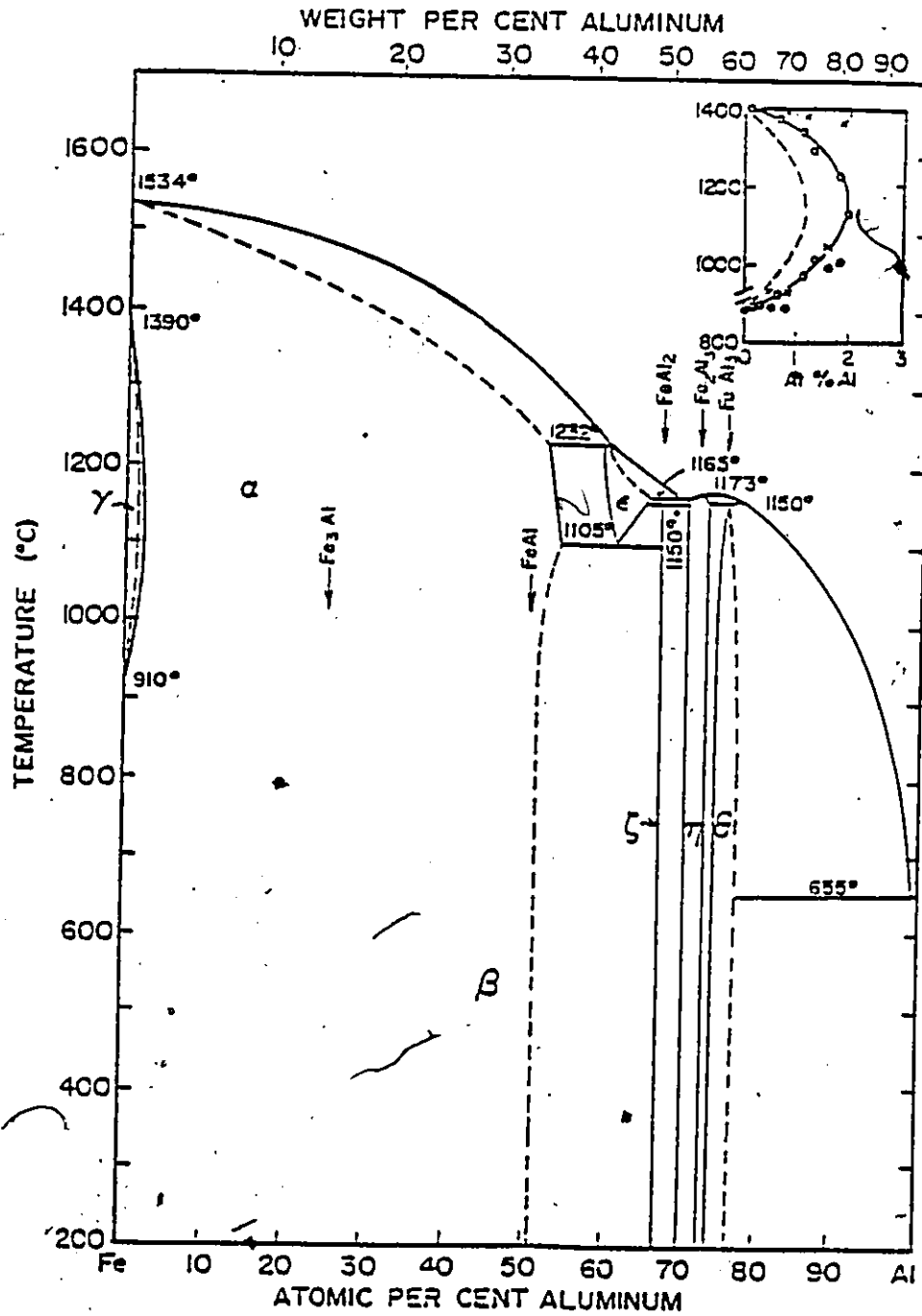


Fig. 3.1 Fe-Al system (78).

disorder at 813K. Lihl and Ebel⁽⁷⁹⁾ determined the phase boundaries of the disordered α +ordered FeAl (β_2) two phase field up to 1073K. These phase boundaries were extrapolated to high temperature by Schiermann et al.⁽⁸⁰⁾ and recently reviewed by Chang and Neumann⁽⁸¹⁾. Four intermediate phases are formed in Fe-Al system: ϵ (Fe₂Al₃) cubic forms peritectically at 1504K which decomposes eutectoidally at about 1367K, ζ (FeAl₂) has a rhombohedral structure, η (Fe₂Al₅) has an orthorhombic structure, θ (FeAl₃) has a monoclinic structure. Solid solubility of Fe in Al based on lattice parameter measurements⁽⁸²⁾ has been found to be 0.052 wt% Fe at 928K, 0.006% at 773K.

Solid solubility in γ Fe is very restricted, less than 1 a/o Al at 1423K according to Rocquet et al.⁽⁸³⁾ and the (γ + α)/ α phase boundary extends to 2a/o Al. The lattice parameter of alloys in the range 0 - 50 a/o Al and structural changes connected with order-disorder transformation were studied by Bradley et al.⁽⁸⁴⁾.

3.2.2 Directional Decomposition of ϵ -FeAl

The ϵ -FeAl phase which has been suggested to be b.c.c. with 16 atoms per unit cell is formed peritectically at about 1503K. The FeAl-FeAl₂ eutectoid, as most eutectoids, has a lamellar morphology⁽⁸⁵⁾. The unit cell and the lattice parameter of FeAl₂ have been studied by Bastin et al.⁽⁸⁶⁾.

3.2.3 Thermodynamic Properties

The activity of Al and Fe in solid Fe-Al alloys has been determined by various workers^(78,87-90). Heats of formation for these alloys have been determined calorimetrically by Kubaschewski and Dench⁽⁹¹⁾. Radcliffe et al.⁽⁸⁸⁾ determined thermodynamic properties of Fe-Al alloys between 1173K and 1273K by electromotive force measurements, using a molten chloride electrolyte. Figure 3.2 represents plots of the activity of Fe and Al vs. Al atom fraction at 1173K. The activity of aluminum in these alloys shows a strong negative deviation from Raoult's law at low concentrations which increases markedly above 40 a/o Al.

3.2.4 Diffusion Properties

The diffusion in the α -phase of the Fe-Al system has been investigated by Sato⁽⁹²⁾, Hirano et al.⁽⁹³⁾, Nishida et al.⁽⁹⁴⁾ and Akuezie et al.⁽⁹⁵⁾. Sato⁽⁹²⁾ has studied the diffusion of Al in α -iron at 1123K and obtained the following result.

$$\begin{aligned}\bar{D} &= 8.2 \times 10^{-10} \text{ cm}^2/\text{s} \\ D_{\text{Al}} &= 9.7 \times 10^{-10} \text{ cm}^2/\text{s} \\ D_{\text{Fe}} &= 1.73 \times 10^{-10} \text{ cm}^2/\text{s} .\end{aligned}$$

A detailed investigation on interdiffusion in the α -solid solution phase in the range of temperature 1073-1373K was made by Nishida et al.⁽⁹⁴⁾. The chemical diffusivity, \bar{D} , was found to

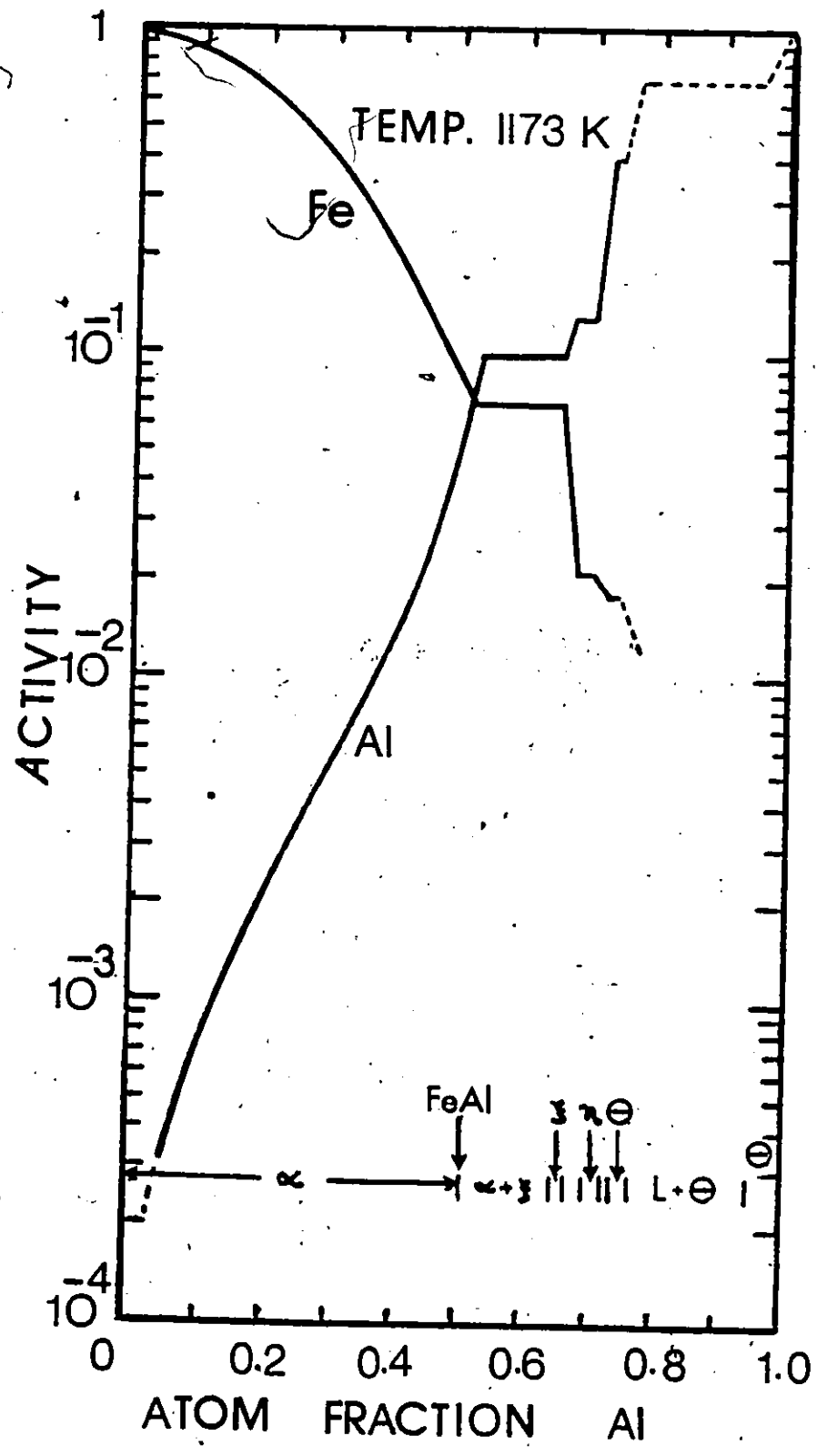


Fig. 3.2 Fe and Al activities in Fe-Al system at 1173K (88).

be strongly dependent upon Al concentration and it showed a peak value at a concentration of Al corresponding to the order-disorder boundary (Fig. 3.3).

The interdiffusion results obtained by Akuezue and Whittle⁽⁹⁵⁾ showed general agreement with those obtained by Nishida⁽⁹⁴⁾ and Hirano⁽⁹³⁾. The former workers found the activation energy for the interdiffusion process to fall within the range 196-230 KJ.mole⁻¹ and these energy appeared to depend systematically on composition, decreasing from 217 KJ.mole⁻¹ at 10 a/o Al to a minimum of 196 KJ.mole⁻¹ at 23 a/o Al, and increasing again to a maximum of 230 KJ.mole⁻¹ at about 31 a/o Al.

Ryabov et al.⁽⁹⁶⁾ reported the following values for diffusion coefficients of Fe⁵⁵ in Fe-Al compounds at 1223K as determined by a thin-layer radioactive tracer technique.

Fe in FeAl ₃	$D \sim 1.25 \times 10^{-10} \text{ cm}^2/\text{s}$
FeAl ₅	$D \sim 20 \times 10^{-10} \text{ cm}^2/\text{s}$
FeAl ₂	$D \sim 0.63 \times 10^{-10} \text{ cm}^2/\text{s}$
FeAl	$D \sim 6.3 \times 10^{-10} \text{ cm}^2/\text{s}$
Fe ₃ Al	$D \sim 20 \times 10^{-10} \text{ cm}^2/\text{s}$

Fellner et al.⁽⁹⁷⁾ have measured the chemical diffusion coefficient \tilde{D} in the low and intermediate temperature range for the 25 a/o Al α -solid solution phase. In the range 473 to 673K,

$$\tilde{D} = 6.5 \times 10^{-11} \exp(-2658 \text{ K/T})$$

while from 673 to 873K

$$\tilde{D} = 6.6 \times 10^{-6} \exp(-10466 \text{ K/T}) .$$

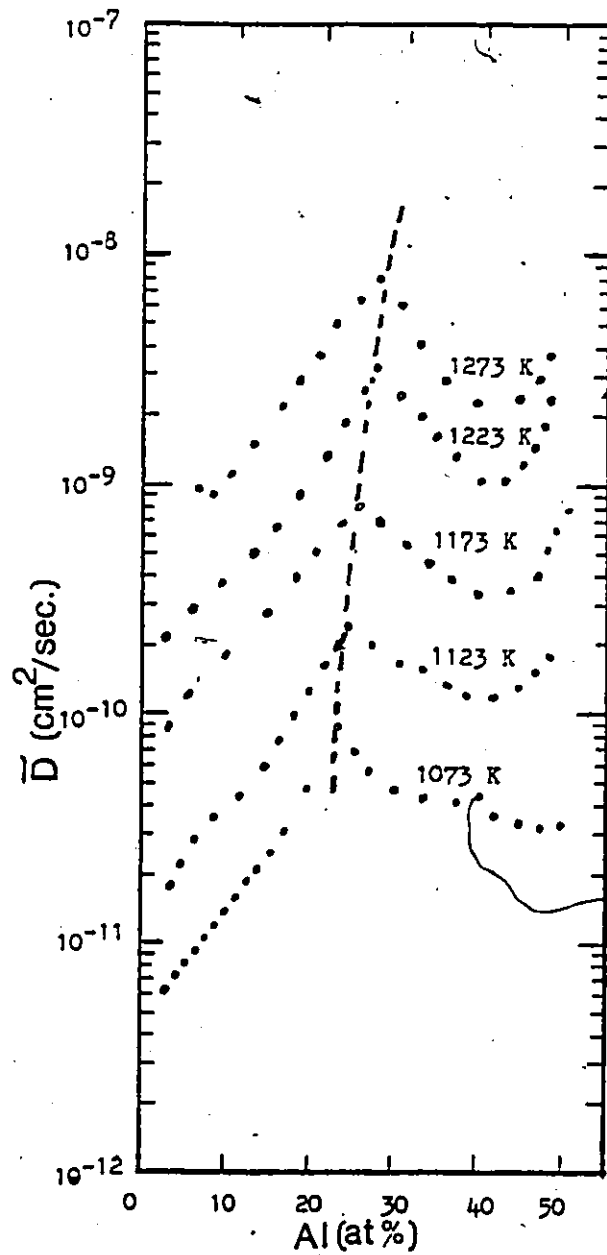


Fig. 3.3 Variation in chemical diffusion coefficient (\bar{D}) with Al concentration (94).

3.3 PROPERTIES OF Fe-S SYSTEM

3.3.1 Crystal and Defect Structure

The Fe-S phase diagram of (Fig. 3.4) is well established⁽⁷⁷⁾. The different phases and their crystal structures are tabulated in Table 3-1. At least three room temperature ferrous sulfide phases have been long recognized: stoichiometric FeS, known as troilite (T); the pyrrhotite, hexagonal $Fe_{1-x}S$ (H), and monoclinic $Fe_{1-x}S$ (M). Additional phases have been identified between (H) and (M)^(98,99). The FeS_2 phase

Table 3-1

Phase	Formula	Symmetry
ζ	FeS (Troilite)	Hexagonal
ϵ	$Fe_{1-x}S$ (Pyrrhotite)	Hexagonal
ϵ'	$Fe_{1-x}S$ (Pyrrhotite)	Monoclinic
η	FeS_2 (Pyrite)	Cubic
	FeS_2 (Marcasite)	Orthorhombic

decomposed on heating at 1 atm pressure and 970K. The troilite (T) phase is stoichiometric, whereas the hexagonal pyrrhotite due to the presence of Fe vacancies (NiAs structure) exhibits nonstoichiometry ranging up to 25 atomic percent. Its nonstoichiometry or phase extent as a function of sulfur activity and temperature have been the subject of many recent investigations⁽¹⁰⁰⁻¹⁰⁴⁾.

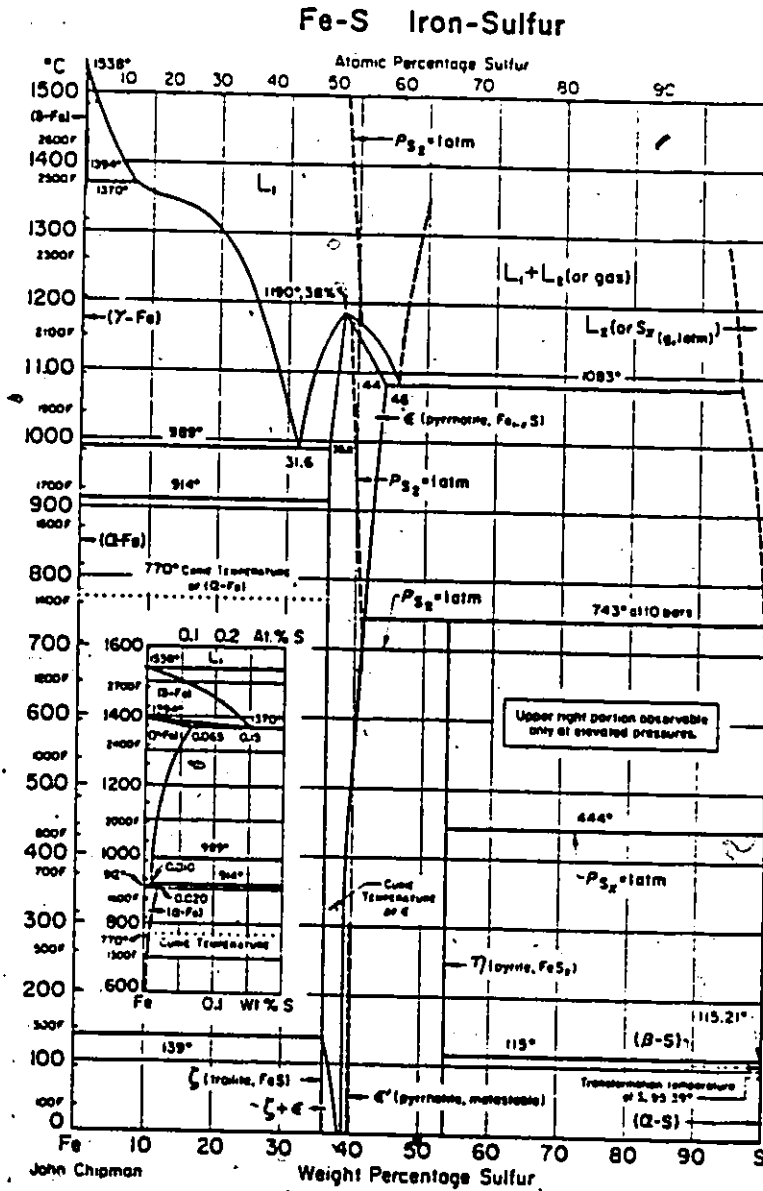


Fig. 3.4 Phase diagram of Fe-S. (17)

Iron sulfide is a metallic-type electrical conductor at temperature exceeding 411K⁽¹⁰⁵⁾, and the magnitude of the conductivity is practically independent of sulfur activity⁽¹⁰⁶⁾. A point defect model for this solid based on the existence of interacting iron vacancies exhibiting strong repulsive forces has been advanced by Libowitz⁽¹⁰³⁾ to account for the dependence of non-stoichiometry on sulfur activity and temperature. It has been suggested also that different types of defects can exist near stoichiometry, namely Frenkel defects or iron in sulfur sites⁽¹⁰⁴⁾, but direct experimental evidence for their existences has not been found to the present⁽¹⁰⁷⁾.

The phase diagram⁽¹⁰⁸⁾ for Fe_{1-x}S and several sulfide phases is represented in Fig. 3.5. The Fe_{1-x}S sulfur-rich boundary is moved to increasingly higher sulfur pressure as the temperature is increased. The dotted lines represent the variation of non-stoichiometry with temperature at several sulfur pressures.

3.3.2 Thermodynamic Properties

The standard heat of formation of FeS has been obtained by numerous workers and summarized in reference (109). The effect of composition on the standard heat of formation of Fe_{1-x}S has been determined by Ariya et al.⁽¹¹⁰⁾. Gronvold et al.⁽¹¹¹⁾ determined the heat capacity of Fe_{1-x}S and determined the standard entropies $S_{298}^{\circ} = 60.35 \text{ J/mole.K}$.

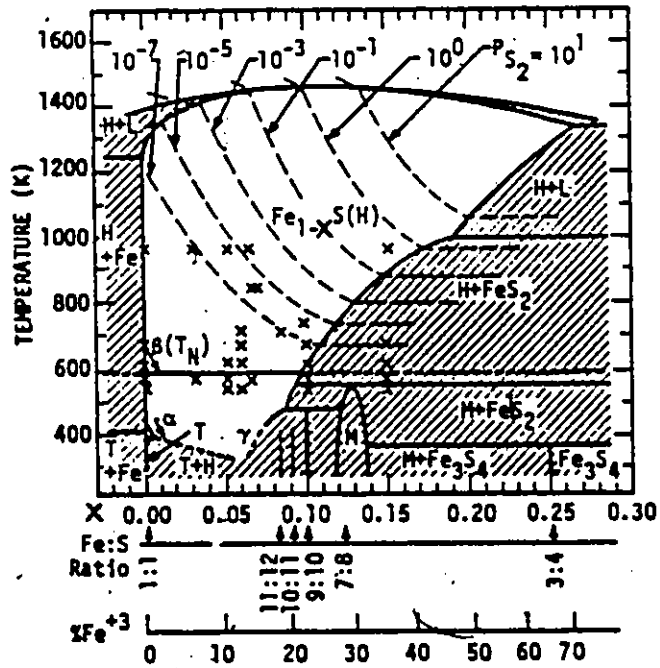


Fig. 3.5 Fe-S phase diagram in the Fe_{1-x}S region (108).

Rosenqvist⁽¹¹²⁾ has determined the free energy of formation of FeS between 773 and 1261K (eutectic temperature) by using a mixture of H₂ and H₂S. The equilibrium diagram for Fe-H₂S/H₂ system in Fig. 3.6 is drawn by Rosenqvist⁽¹¹²⁾. The heavy curves correspond to different two-phase equilibria, and the slope of these curves corresponds to the heat of corresponding reaction, eg.,



The fine curves correspond to constant compositions within a homogeneous phase, and the slope of these curves corresponds to the heat of solution of sulfur referred to H₂S as reference, eg.



This type of diagram (Fig. 3.6) is quite useful in anticipating the reaction products at a given temperature and H₂S/H₂ ratio.

The dissociation pressures of FeS over a range of temperature has been described by McCabe et al.⁽¹¹³⁾ and by Nagamori et al.⁽¹⁰¹⁾. In the region of temperature from 1073 to 1373K, the pressure temperature relationship is given by⁽¹¹¹⁾

$$\log P_{\text{S}_2} = -1.528 \times \frac{10^4}{T} + 5.48 \quad (3.3)$$

Jacob et al.⁽¹¹⁴⁾ have reviewed the Fe-S binary system and established the standard free energy for the reaction,

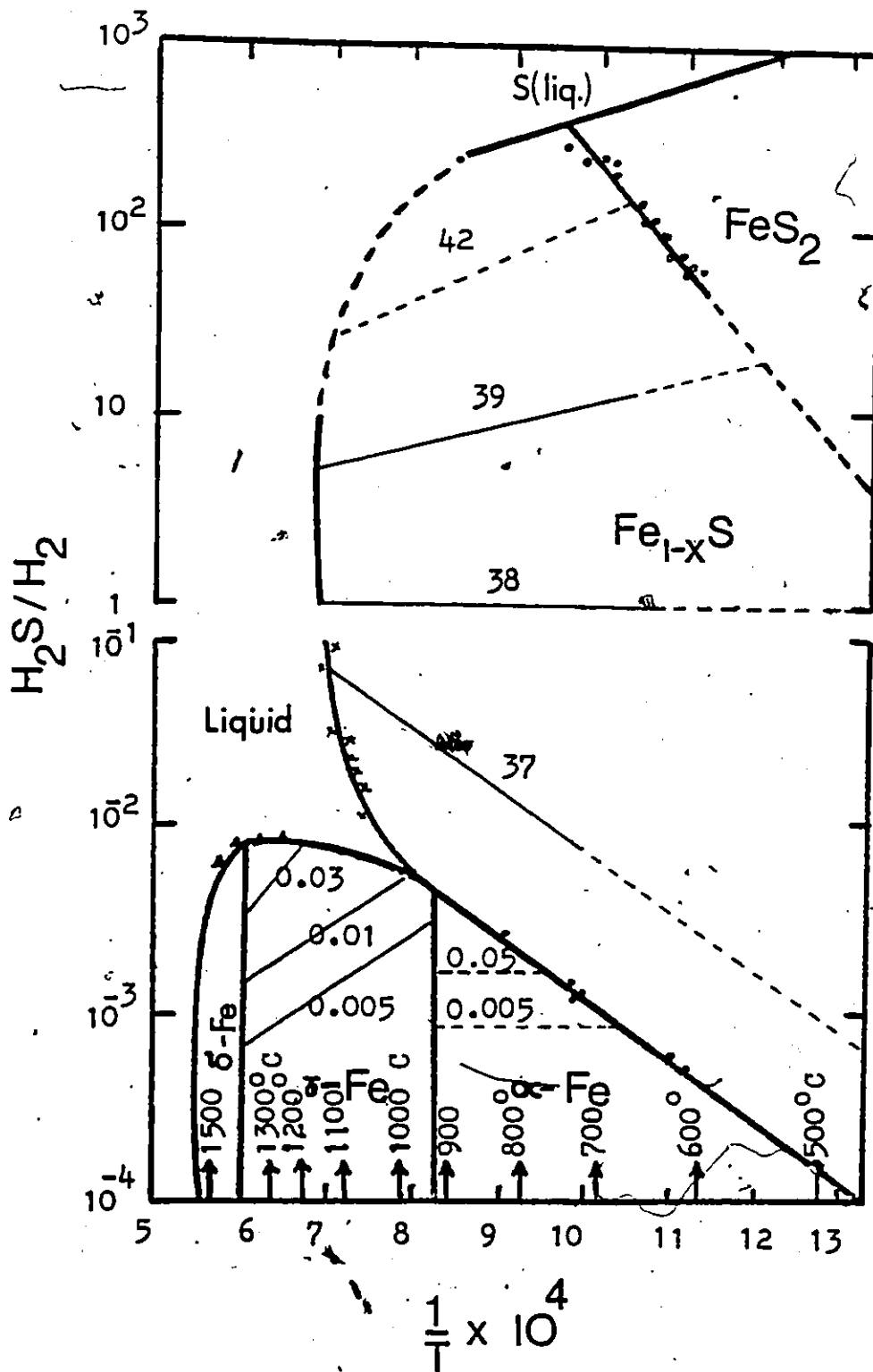
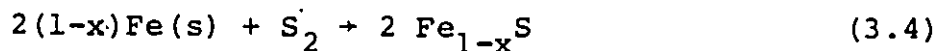


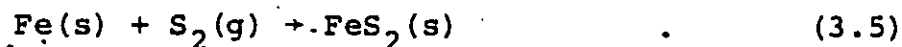
Figure 3.6 Plot of H_2S/H_2 vs. $1/T$ for the system Fe-S (112).



$$\Delta G^\circ = -303,000 + 108.2 T (\pm 3000) \text{ J/mole of } \text{S}_2$$

which compares well with the data obtained by Sudo⁽¹¹⁵⁾, Richardson et al.⁽¹¹⁶⁾ and Nagomori et al.⁽¹¹¹⁾.

The compound FeS_2 can exist in one of two forms (marcasite at low temperatures) and pyrite at high temperature) with a transformation temperature of about 635K. FeS_2 decomposes around 980K, yielding a monosulfide and elemental sulfur. The thermodynamic properties of FeS_2 have been reported in reference (129). The standard free energy of formation of FeS_2 is given by



$$\Delta G^\circ = -334,700 + 240.5 T (\pm 800) \text{ J/mole}$$

3.3.3 Solubility of Sulfur in Iron and Iron-based Alloys

Solubility of sulfur in α -Fe has been measured by various workers^(112,117-119). Ainslie et al.^(117,118) obtained the sulfur solubility values by equilibrating single crystal and polycrystalline sheet specimens to H_2 - H_2S atmospheres containing radioactive sulfur. The solubility of S in pure α -iron of grain size 0.11 ± 0.02 mm was measured to be

$$\text{wt } \% \text{ S} = 7.85 \times 10^3 \exp(-48900/RT) \quad (3.6)$$

$$\log(\text{wt } \% \text{ S}) = -\frac{6320}{T} + 3.89 \quad (3.7)$$

in the temperature range 923-1183 K. The sulfur solubility in single crystal specimens was found to be lower than in polycrystalline specimens. Herrnstein et al. (118) have measured the sulfur solubility in both single and polycrystalline iron but did not find any significant difference in values in the temperature range 1023 to 1173K. They obtained the solubility-temperature relationship as

$$\log(\text{wt } \% \underline{S}) = -\frac{3800}{T} + 1.44 \quad (3.8)$$

The variation of sulfur solubility values with temperature by various co-workers is presented in Fig. 3.7.

There has been a limited number of investigations on the effect of alloying additions on the solubility of sulfur in solid iron (118,120). Turkdogan et al. (122) determined the sulfur solubility in Fe-Mn alloys over the temperature range 1273-1600K. Increasing Mn alloy concentration resulted in a decreasing sulfur solubility. A large number of results have been accumulated on the influence of alloying elements on the sulfur solubility in liquid iron at temperatures ranging from 1823-1873K (121).

3.3.4 Diffusion Properties

Results for sulfur diffusion in single and polycrystals of α and γ -Fe are tabulated in Table 3-2 (117-120). Ainslie et al. (117) measured the S diffusivity in single and polycrystals of Fe by using a radioactive S^{35} . Sulfur segregation at α -iron grain boundaries has been studied by Ainslie et al. (119).

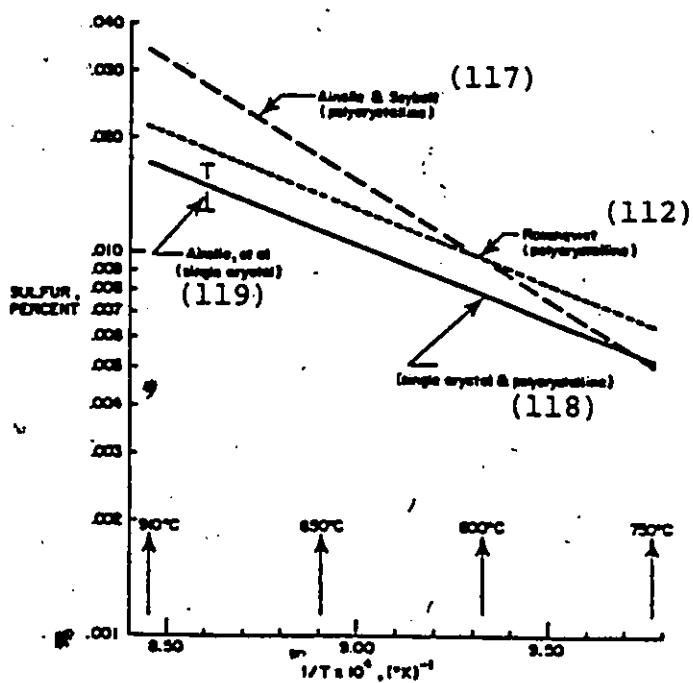


Fig. 3.7 Temperature dependence of the solubility of sulfur in iron (118).

Table 3-2

Summary of Sulfur Diffusivities in Iron

Reference	Technique	Phase and Material	Temp. range K	$D = D_0 \exp(-Q/RT)$	$D_S^Y(1173K)$ *	$D_S^\alpha(1173K)$ *
Ainslie (1960)	Radioactive S^{35}	α -Fe Single Crystal	973-1173	$D_S^\alpha = 1.68 \exp(-48900/RT)$		1.29×10^{-9}
117, 119		α -Fe-Si Polycrystal	1173-1573	$D_S^{\alpha Fe-Si} = 2.68 \exp(-49700/RT)$		1.47×10^{-9}
Siebel (1964)	Radioactive S^{35}	α -Fe Polycrystal	1123-1173	$D_S^\alpha = 1.35 \exp(-48400/RT)$		1.29×10^{-9}
123		γ -Fe Polycrystal	1173-1733	$D_S^\gamma = 2.42 \exp(-53400/RT)$	2.7×10^{-10}	
Kononyuk (1967)	Sulfurized specimens sectioned and analyzed chemically	α -Fe Polycrystal	1173	-		1.3×10^{-9}
124		α -Fe Polycrystal	1173	-		1.6×10^{-9}
Herrnstein (1967)	Internal Sulfidation of Ferritic Fe-Mn alloys	γ -Fe Polycrystal	1423-1523	$D_S^\gamma = 1.8 \times 10^{-2} \exp(-38500/RT)$	1.15×10^{-9}	
118		α -Fe-Mn Polycrystal	1023-1173	$D_S^\alpha = 1.68 \exp(-42800/RT)$		1.8×10^{-8}
Mang (1970)	Changes of electrical resistance of sulfurized Fe foil	α -Fe Polycrystal	973-1173	$D_S^\alpha = 2.7 \exp(-49000/RT)$		2×10^{-9}
125		γ -Fe Polycrystal	1173-1273	$D_S^\gamma = 0.5 \exp(-50000/RT)$	2.4×10^{-10}	

* in cm^2/s

suggesting that the polycrystals of iron contain 50 to 100 percent more sulfur than single crystals, and the excess sulfur in the polycrystals is found to be concentrated at the grain boundaries. Using transmission electron microscopy, they observed that the grain boundaries of sulfurized iron were associated with very high density dislocation networks which were not observed in sulfur free iron. These networks are thought to form when sulfur, having first entered the specimens by preferential diffusion along grain boundaries diffuses from the grain boundaries laterally into the grains by a substitutional mechanism⁽¹¹⁹⁾. In view of the size (0.127 nm) of sulfur atoms in comparison to iron (0.126 nm), the activation energy values (Table 3-2) and X-ray structural measurements, Herrnstein et al.⁽¹¹⁸⁾ have suggested that sulfur diffuses in iron substitutionally.

Diffusional investigations on FeS are rather limited. Until 1974 iron and sulfur diffusivities were inferred from the scaling kinetics. Condit et al.⁽¹⁰⁸⁾ in 1974, using the radiotracer technique, demonstrated that iron diffusion occurs by a vacancy mechanism at rates dependent on the crystallographic direction, $D_c = 1.8 D_a$, (c - prismatic direction, a - Basal direction). Furthermore they found that sulfur diffuses at rates several orders of magnitude lower than for iron (Table 3-3). Fryt et al.⁽¹²⁶⁾ have determined the chemical diffusivity and non-stoichiometry as a function of sulfur activity and temperature.

TABLE 3-3 (a)

Iron self diffusion in Fe_{1-x}S in cm^2/s (108)

Temperature K	Iron deficit x	D_a a-axis	D_c c-axis
550	0.003	9.6×10^{-13}	1.7×10^{-12}
570	0.003	1.6×10^{-12}	6.1×10^{-12}
625	0.003	1.2×10^{-11}	2.2×10^{-11}
723	0.060	5.9×10^{-10}	1.2×10^{-9}
861	0.066	6.3×10^{-9}	8.3×10^{-9}
970	0.031	1.5×10^{-8}	4.3×10^{-8}

TABLE 3-3 (b)

Sulfur self diffusion in Fe_{1-x}S in cm^2/s (108)

Temperature K	Iron deficit x	D_a a-axis	D_c c-axis
1168	0.065	3.2×10^{-12} *	
1223	0.065	6.4×10^{-12} *	
1270	0.052	2.2×10^{-9}	1.22×10^{-9}
1330	0.098	8.4×10^{-9}	

* Orientation not determined.

Using the interrupted sulfidation kinetics method originally developed by Rosenberg⁽¹²⁷⁾, Fryt et al.⁽¹²⁶⁾, calculated the chemical diffusion coefficient and found it to be independent of the degree of nonstoichiometry at a given temperature. Its temperature dependence was given as

$$\tilde{D}(\text{cm}^2/\text{s}) = (6.7 \pm 2.0) \times 10^{-2} \exp\left(-\frac{30900 \pm 600}{RT}\right) \quad (3.9)$$

Figure 3.8 shows the variation of \tilde{D} with temperature. Using a point defect model involving a large repulsive interaction between iron vacancies to interpret their results, Fryt et al.⁽¹²⁶⁾ obtained a correlation yielding an expression to evaluate the self diffusion coefficient of iron from the chemical diffusivity and obtained good agreement with iron tracer diffusivity in the a-direction obtained by Condit et al.⁽¹⁰⁸⁾.

Danielwski⁽¹²⁸⁾ has studied the diffusional properties of Fe in Fe_{1-x}S . Using the tracer diffusivity results by Condit et al.⁽¹⁰⁸⁾, they evaluated the parabolic rational rate constant for iron sulfidation and found satisfactory agreement with the published results. However, at high sulfur pressures, experimental values of this sulfidation rate constant differed from predicted values. This discrepancy was attributed to the dependence of the iron diffusion coefficient for iron sulfide on crystal orientation⁽¹²⁹⁾.

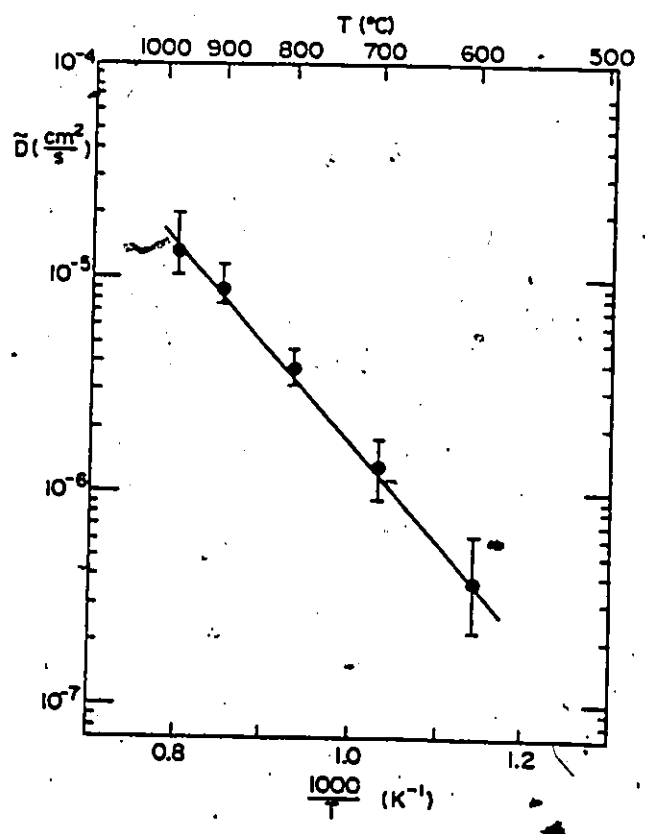


Figure 3.8 Temperature dependence of the chemical diffusivity of iron sulfide (126).

3.3.5 Kinetics and Mechanism of Fe Sulfidation

The kinetics of iron sulfidation have been intensively investigated (130-139). These kinetics have been shown to be parabolic at sulfur pressures in the range 13 to 66.6 Pa at temperatures in the range 673-1073K. Hauffe and Rahmel (132) and Meussner et al. (133) have demonstrated that the growth of FeS occurred by outward diffusion of Fe ions via cation vacancies in the FeS lattice. Although scale growth involves iron migration by iron vacancies in $Fe_{1-x}S$, the sulfur pressure dependence is unusual in that the parabolic rate constants show a $p_{S_2}^{1/n}$ dependence where n ranges from 3 to 7.

Two general features have prevented a rigorous comparison of calculated and measured parabolic sulfidation rates. These were the dependence of the value of the iron self-diffusion coefficient on the directionality in NiAs structure of $Fe_{1-x}S$ (108) and the fact that the scales exhibit a texture with the preferred growth direction dependent on sulfur pressure (126,129). Fryt et al. (140) systematically examined the sulfidation kinetics of iron over a wide range of sulfur activity $10^{-6} < p_{S_2} < 10^3$ Pa. They calculated the parabolic scaling rate constants in relation to the scale texture, the iron self-diffusion coefficient and the defect structure of iron sulfide using the Wagner equation for scaling by iron diffusion and the Libowitz point defect model involving a strong repulsive interaction between the iron vacancies. The expression yielding the parabolic rational rate constant is given by

$$k_r = \frac{\tilde{D}\Delta x}{\bar{v}} \quad (3.10)$$

where

$$\tilde{D} = (6.7 \pm 2.0) \times 10^{-2} \exp\left(-\frac{20,900 \pm 600}{RT}\right)$$

and

$$x = p_{S_2}^{1/2} \exp - \frac{\mu_{FeS} + qV_{Fe} + 4\xi V_{Fe} x(2-x)}{RT} \quad (3.11)$$

\tilde{D} = chemical diffusion coefficient in $Fe_{1-x}S$

x = Non-stoichiometry in FeS

μ_{FeS} = Free energy of formation of stoichiometric FeS

qV_{Fe} = Free energy of formation of Fe vacancies with respect to pure solid iron.

ξV_{Fe} = Free energy of interaction between iron vacancies.

The predicted values for these rate constants were found to be in good agreement with the experimental results⁽¹⁴⁰⁾. They also found that the sulfur pressure dependence of k_r (varying from $p_{S_2}^{1/3}$ to $p_{S_2}^{1/7}$) is not accidental but directly arises from the predicted influence of sulfur pressure and temperature on stoichiometry caused by the strong repulsive interaction between iron vacancies. The activation energy for parabolic sulfidation varies with the sulfur pressure ranging from 6.9×10^4 and 8.4×10^3 Joules/mole at $p_{S_2} = 10^{-3}$ Pa respectively.

Sulfidation of pure iron in H_2S/H_2 atmospheres often leads to a duplex layer growth at temperatures less than 873K. According to marker measurements it is suggested that sulfur can be supplied to the iron substrate by perforations resulting from dissociation of the inner part of the outer layer of iron sul-

vide⁽¹⁴¹⁻¹⁴³⁾. Several kinetic equations involving the growth of a two-layer scale on iron in H_2S/H_2 atmospheres have been described by Haycock and Dravenicks et al.⁽¹³⁰⁾.

3.4 PROPERTIES OF Al-S SYSTEM

3.4.1 Crystal and Defect Structure

In the Al-S system, Hansen and Anderko⁽⁷⁷⁾ have reported that $AlS(S)$ and $Al_2S_3(S)$ exist and Ficalora et al.⁽¹⁴⁴⁾ have identified $AlS(g)$, $Al_2S_2(g)$ and $Al_2S(g)$ in the vapour phase.

The structure of Al_2S_3 has been investigated by Flahaut^(145,146), who reported three structural modifications, each of which is hexagonal. Later studies showed that it can also have a cubic defect spinel structure when prepared with either 2% As substituted for Al⁽¹⁴⁷⁾, or when prepared at high temperature and pressure⁽¹⁵⁰⁾. A tetragonal defect spinel structure has also been reported upon synthesis at high temperature and pressure⁽¹⁴⁸⁾. This structural information is collected in Table 3-4⁽¹⁴⁹⁾.

A hypothetical Al-S phase diagram is given by Hansen et al.⁽⁷⁷⁾ which is based on the cooling curve results and examination of sulfidation products at various temperatures (Fig. 3.9). Al_2S_3 melts at 1373K. The solubility of sulfur in Al ranges from 1 a/o at 973K to 5 a/o at 1173K.

TABLE 3.4

Summary of Crystal Structures of Al_2S_3 (149)

Description	Crystal System	Density* (gms/cm ³)	Lattice Parameters	Comments	References
α - Al_2S_3	Hexagonal	$\rho_x = 2.33$ $\rho_m = 2.32$	$a_0 = 6.423$ $c_0 = 17.83$ $c_0/a_0 = 2.776$	Stable at room temp. and 1 atm pressure	145, 146
β - Al_2S_3	Hexagonal	$\rho_x = 2.55$ $\rho_m = 2.5$	$a_0 = 3.579$ $c_0 = 5.829$ $c_0/a_0 = 1.629$	Stable in the presence of Al_4C_3 1273-1373K	145, 146
γ - Al_2S_3	Hexagonal-Rhombohedral	$\rho_x = 2.37$ $\rho_m = 2.36$	$a_0 = 6.47$ $c_0 = 5.829$ $c_0/a_0 = 2.669$ $a_R = 6.86$ $a_R = 56^\circ 16'$	Stable from 1273-1373K 1 atm	146
Tetragonal defect spinnel	Tetragonal	-	$a_0 = 7.026$ $c_0 = 29.819$ $c_0/a_0 = 4.244$	Prepared at 2-65 Kbar 1273-1473K	148
Cubic defect spinnel	Cubic	$\rho_x = 2.71$	$a_0 = 9.94$	Prepared at 40 Kbar 673K	150
Cubic defect spinnel	Cubic	$\rho_x = 2.78$ $\rho_m = 2.80$	$a_0 = 9.93$	2% As substituted for Al	147

* ρ_x is calculated density; ρ_m is the measured density.

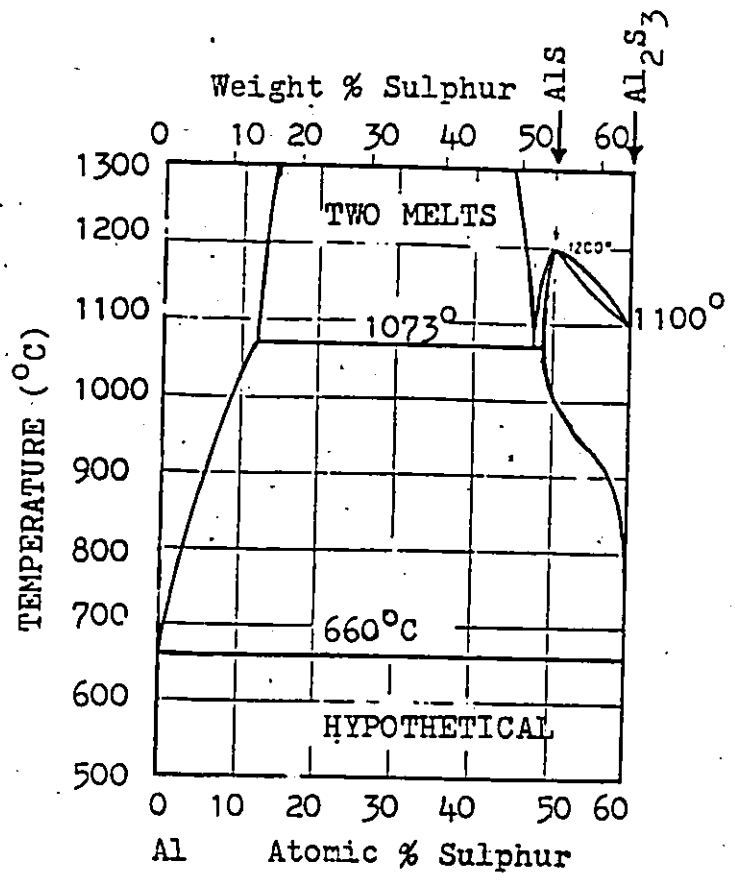


Fig. 3.9 Al-S phase diagram (77).

3.4.2 Thermodynamic Properties

The reported values for heat of formation of Al_2S_3 show wide divergence⁽¹⁰⁹⁾ varying from $-5 \times 10^5 \pm 4000$ Joule/mole of Al_2S_3 to $-9.2 \times 10^5 \pm 5000$ Joule/mole of Al_2S_3 . Recently Ferrante et al.⁽¹⁵¹⁾ determined the low temperature heat capacity which yielded a standard entropy value $S_{298}^{\circ} = 116.93 \pm 0.2$ Joule K^{-1} mole $^{-1}$. The standard enthalpy of formation for the following reaction at 298K.



was obtained as

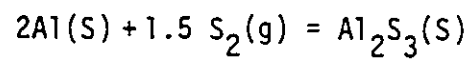
$$\Delta H_{f298}^{\circ} = 6.5 \times 10^5 \pm 4000 \text{ Joule mole}^{-1}.$$

These results with the published data for pure aluminum and sulfur were used by the above authors to obtain a complete set of thermodynamic data for Al_2S_3 from 0 to 900K at appropriate temperature intervals (Table 3-5). The heat capacity of Al_2S_3 in the range of 298-1300K is reported to be⁽¹⁰⁹⁾

$$C_p = [24.42 + 8.62 \times 10^{-3} T] \times 4.187 \text{ Joule mole}^{-1} \text{ K}^{-1} \quad (3.13)$$

AlS is extremely unstable and decomposes in air. Al_2S_3 , being a salt of very weak base and weak acid, hydrolyses slowly in moist air, generating H_2S and $\text{Al}(\text{OH})_3$ or perhaps $\text{Al}_2\text{O}_3 \cdot \text{Al}_2\text{S}_3 \cdot \text{H}_2\text{O}$ ⁽¹⁵²⁾.

Table 3-5
Thermodynamic Data for the Reaction



T, K	$\Delta H_{\text{f}}^{\circ}$ KJ mole ⁻¹	$\Delta G_{\text{f}}^{\circ}$ KJ mole ⁻¹
100	-843.617	-816.063
200	-842.943	-786.205
298.15	-844.371	-761.083
300	-844.354	-759.726
400	-843.299	-731.674
500	-941.926	-703.914
600	-840.456	-676.443
700	-838.999	-649.223
800	-837.638	-622.200
900	-836.433	-595.362

3.4.3 Diffusion Properties

The diffusional properties of the sulfide phases in Al-S system are not reported in the literature.

3.4.4 Sulfidation Kinetics

Sulfidation kinetics of pure aluminum are not reported in the literature.

3.5 PROPERTIES OF Fe-Al-S SYSTEM

3.5.1 Crystal and Defect Structure

The existence of a ternary compound of composition FeAl_2S_4 is reported by several authors^(146,153,154). Nishida and Narita⁽¹⁵⁴⁾ have reported its structure to be hexagonal with lattice parameters as $a_0 = 0.3659 \pm 0.0004$ nm and $c_0 = 3.617 \pm 0.003$ nm and found good agreement with the lattice parameters obtained by Flahaut⁽¹⁴⁶⁾.

3.5.2 Thermodynamic Properties

The thermodynamic properties of Fe-Al-S solid system are not known. At 1823K in liquid iron, sulfur solubility is decreased by the addition of aluminum⁽¹⁵⁵⁾. The activity coefficient of sulfur in liquid Fe-Al alloy containing 5 a/o Al is found to be 3.2 at 1823K and the Wagner interaction coefficient ϵ_S^{Al} has a typical value of 6.7⁽¹²¹⁾.

3.5.3 Diffusion Properties

Diffusion results for phases in the Fe-Al-S system are not reported in the literature.

3.5.4 Sulfidation Properties

Strafford et al. (156,157) have studied the sulfidation properties of Fe based alloys containing Ni, Co, Cr and Al in sulfur vapour and H_2S-H_2 atmospheres at temperatures 773 to 1273K. They observed approximately linear kinetics for Fe-5 wt. % Al alloy in these atmospheres. Fe-Al alloys exhibited a substantially lower reaction rate relative to pure iron. The scale was composed of an outer $Fe_{1-x}S$ layer and an inner layer containing a mixture of $Fe_{1-x}S$ and Al_2S_3 .

High temperature corrosion behaviour of Fe-Al alloys was also investigated by Nishida et al. (10,153) in sulfur vapour at 10^5 Pa over the temperature range 773 to 1173K. The reaction rate constant decreased with increasing Al alloy contents. Subsequent work by Nishida et al. (153) on Fe-2% C-Al alloys (Al up to 25 wt. %) has shown an increase in corrosion rate upon small additions of Al to Fe-2 wt.% C. However, additions of aluminum more than 7 to 8 wt.% increased the corrosion resistance of the alloy markedly.

3.6 SUMMARY

Sulfidation behaviour of pure iron, both in sulfur and H_2S-H_2 atmospheres is well established and determined by diffusional controlled growth of iron sulfide. However, the sulfidation behaviour of pure aluminum is not reported in the literature. A limited amount of work on binary Fe-Al alloys demonstrated that the reaction kinetics are initially parabolic in sulfur

vapour and linear in H_2S+H_2 atmospheres. However, the established beneficial effect of aluminum additions to the corrosion resistance of iron in sulfur and H_2S bearing atmospheres demands additional investigation. A thorough literature search does not reveal any useful data on the defect structure and diffusion properties of the sulfides in the Al-S and Fe-Al-S systems which can be used to rationalize the observations and experimental results to be obtained in this investigation.

CHAPTER 4

EXPERIMENTAL PROCEDURES AND TECHNIQUES

4.1 INTRODUCTION

A variety of experimental techniques was used for preparation and analyses of materials, sulfidizing the specimens and characterization of sulfidation products. These techniques include argon arc melting, annealing and homogenization, chemical analyses, kinetics of sulfidation and inert marker measurements. For characterization of sulfidation products optical microscopy, x-ray diffraction, electron microprobe and EDAX spectrometries have been used.

4.2 SPECIMEN PREPARATION AND ANALYSIS

Iron (99.99% purity) and aluminum (99.98% purity) used in this investigation were obtained from Materials Research Corporation and Johnson Matthey Chemicals Ltd., respectively. The certified chemical analyses of these metals are given in Table (4-1). Chunks of each metal were mechanically cleaned and accurately weighed to yield alloys with nominal compositions of 1, 6, 9, 18 and 28 a/o Al. The total weight of each batch was approximately 40 gms. The alloys were prepared by melting in an electric arc furnace with non-consumable W electrodes in an argon atmosphere gettered of oxygen by titanium. An alloy

Table 4-1
Certified Chemical Analyses of Iron and Aluminum
in ppm

Impurities	Iron	Aluminum
C	18	-
Cu	30	< 1
Si	50	-
Cr	30	-
Mo	30	-
Mg	< 10	10
Ca	< 10	-
Ti	< 10	-
S	40	-
Al	60	By difference
Fe	By difference	2

sample was remelted several times to obtain a homogenous composition and finally cast as a small ingot (of size 6 cm in length and approximately 1 cm in diameter) in a horizontal mold with a water-cooled copper hearth.

The alloy ingots containing 6, 9, 18 and 28 a/o Al were annealed at 1473K for 12h in a furnace equipped with a continuous argon (ultra pure) flow system. The annealing temperature for the 1 a/o Al alloy was chosen at 1173K to avoid the gamma loop and the two phase $\alpha+\gamma$ regions. To remove oxygen from the incoming argon and furnace atmosphere, zirconium chips were introduced at the gas entrance side of the horizontal furnace tube. After annealing the alloys were mounted on iron blocks using cold setting epoxy resin and hardener. They were cut into small buttons approximately 3 to 5 mm thick and 10 mm in diameter using silicon carbide cutting blades. The samples were then polished on all sides through a series of silicon carbide papers (200, 320, 400 and 600 grit) using water as a lubricant. A vacuum anneal (at 1173K for 18h) was then given by placing the samples in an alumina tube, sealed in a quartz tube under vacuum to relieve the internal stresses introduced during cutting and polishing. Final polishing was carried out on napless cloths impregnated with 6 μm and then 1 μm diamond paste with kerosene as the lubricant. The samples were finally washed with petroleum ether and methyl alcohol and then dried with acetone.

The metallography of polished alloy specimens was examined using optical microscopy. The average grain size of any alloy was usually large; it varied from 0.1 mm to about 0.8 mm for alloys with 1, 6, 9, 18 and 28 a/o Al. The alloy homogeneity was insured using EPMA. The actual aluminum contents were determined by wet chemical analyses using a Perkin-Elmer Atomic Absorption spectro-photometer (Table 4-2):

Table 4-2

Chemical Analyses of Fe-Al Alloys

Nominal Composition at. %	Actual Compositions, %	
	at.% Al	wt.% Al
Fe-1 Al	0.95	0.46
Fe-6 Al	5.84	2.91
Fe-9 Al	8.77	4.44
Fe-18 Al	18.2	9.7
Fe-28 Al	27.83	15.6

4.3 SULFIDATION APPARATUS

The apparatus used for the sulfidation experiments is shown schematically in Fig. 4.1. In the author's previous work (M. Eng. thesis) ⁽¹⁵⁸⁾ this assembly was used to obtain the kinetics by measuring the weight gain of the specimen using a McBain balance. Some of the Fe-Al alloy sulfidation kinetics using this assembly and their mode of sulfidation will be

Figure 4/1 Kinetic Assembly

1. Inlet for H₂
2. Inlet for H₂S and H₂S + H₂ mixtures
3. Mixing Bulb
4. Oxygen inlet
5. Matheson rotameters
6. Vacuum pump
7. Gas sampler
8. Helium channel
9. Mercury manometer
10. By-pass channel
11. H₂ + H₂S inlet to the furnace
12. Mullite tube
13. Specimen
14. Target
15. Spring chamber
16. Molybdenum wire
17. Motor
18. Spring
19. Cathetometer
20. Platinum wire
21. Furnace
22. Thermocouple
23. Exhaust channel
24. Absorption flask filled with caustic soda.

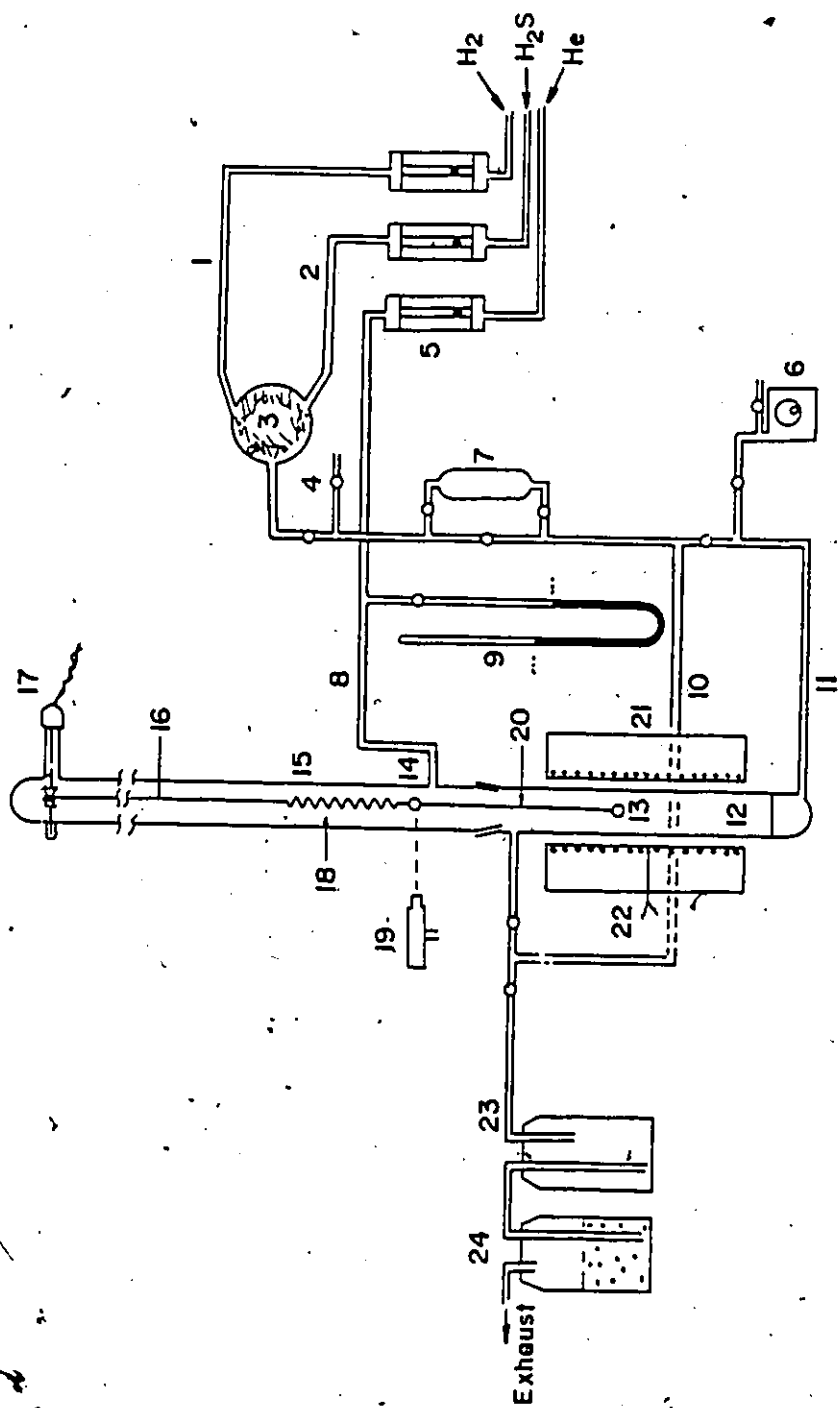


Fig. 4.1 Schematic kinetic assembly using H_2S-H_2 atmosphere.

referred to in the experimental results section of this thesis. The details of this assembly have also been described elsewhere⁽¹⁵⁸⁾. In essence, the McBain balance consists of a winch with positioning forks, a spring (18) connected to the winch by a molybdenum wire (16) and a target (14) attached to the bottom of the spring. The sample (13) is suspended from the target by means of a Pt wire. During the reaction, the extension of the spring is followed through the target movement by a cathetometer (19). Helium gas is used to purge the upper portion of the reaction chamber, thus avoiding condensation of sulfur in the spring chamber (15). From the spring calibration, cathetometer data are converted to weight gain by the specimen. To control the sulfur partial pressure a mixture of hydrogen sulfide and hydrogen gas was used. The spring material was an alloy of Fe-Ni-Cr-Ti known as Elinvar-Extra⁽¹⁵⁸⁾.

In the present work, alloys of Fe-Al containing 1, 6, 9, 18 and 28 at/o Al were sulfidized by diffusion coupling of these alloys with FeS and subsequent annealing in evacuated quartz capsules at 1173K. Alloys sulfidized in this manner ensures proper equilibrium sulfur activities at the interfaces between various phases. Also, this method avoids the use of dynamic flow of sulfidizing species. Particularly for Fe-Al alloys in the low sulfur pressure range, the residual oxygen in the flowing gas can form oxides such as Al_2O_3 . In another set-up, alloys were sulfidized at the dissociation pressure of FeS fixed by a mixture of Fe and FeS in a quartz capsule.

4.4 SULFIDATION PROCEDURE

Figure 4.2 represents a cross-section through the die used for making diffusion couples. FeS of 99.99% purity (Table 4-3) was obtained from Cerac Incorporated, Wisconsin. Typically, the iron sulfide was $\text{Fe}_{0.914}\text{S}$ (Pyrrhotite) of hexagonal structure. Extra small peaks in the X-ray diffraction pattern (Fig. 4.3) of this material suggested the presence of FeS (Troilite) which is also of hexagonal structure. Alloys were embedded in the Fe sulfide powder and compressed at a pressure of 5.9×10^8 Pa ($6\text{t}/\text{cm}^2$) in the cylindrical tool steel (SPS-245) die as shown in Fig. 4.2. The cylindrical couples thus obtained were 20 mm in height and 15 mm in diameter. The alloy sample thickness varied from 3 to 5 mm. In some instances, a 50 μm Pt marker was spot welded onto the alloy surface at several places prior to making a diffusion couple. The couples were annealed at 1173K in evacuated (1 to 2 Pascals) quartz glass capsules, by placing the tubes in the furnace hot zone maintained at the test temperature ($\pm 2^\circ\text{C}$), for various periods of time and then quenched in air and, in some instances, in water. Thin-walled quartz capsules tended to explode while cooling in air. Therefore thick-walled capsules having 2 mm wall thickness were used. Diffusion couples after annealing treatment were sectioned, polished and then analyzed for metallography, compositional and structural analyses.

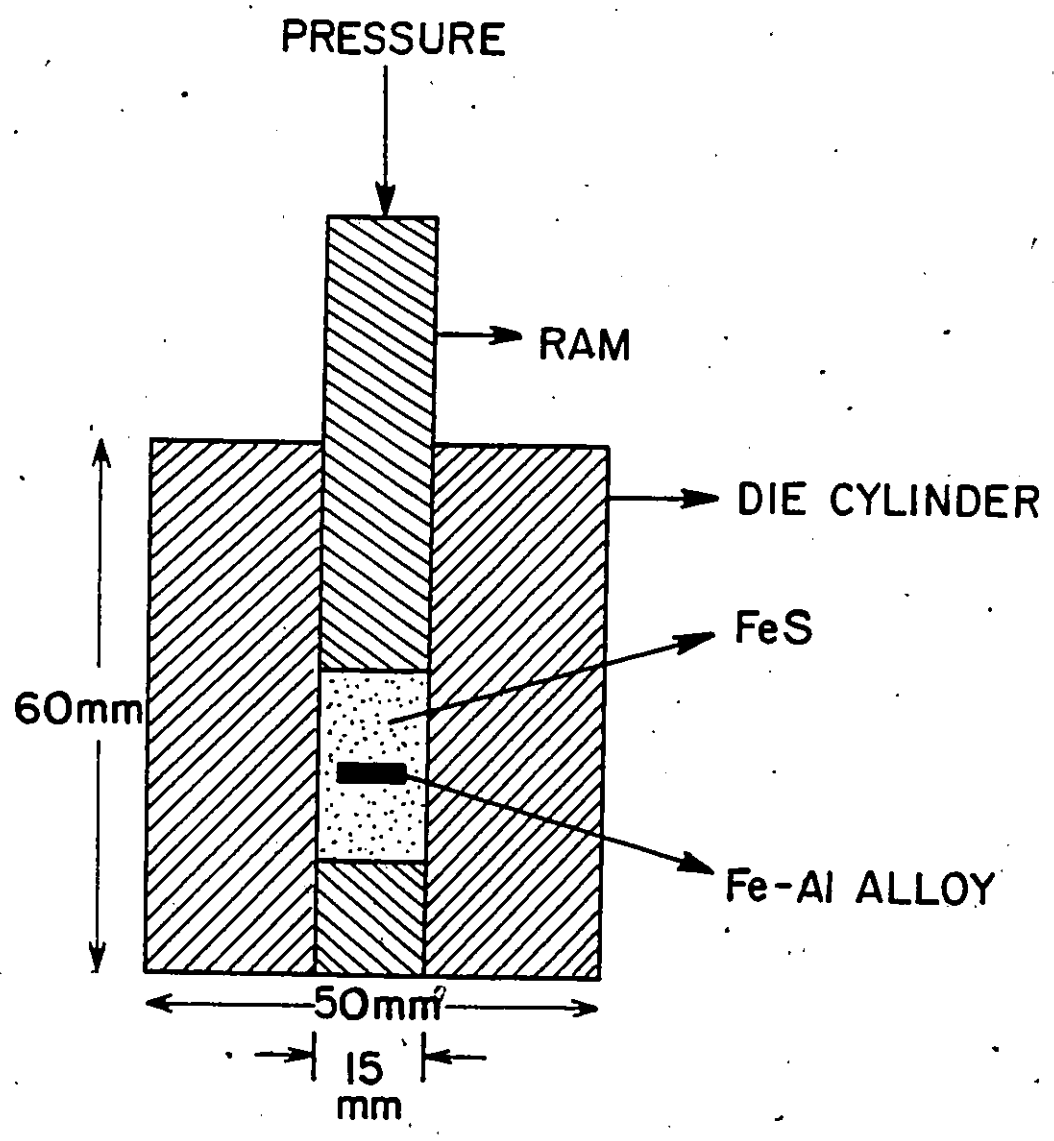


Fig. 4.2 A CROSS-SECTION THROUGH THE DIE USED FOR MAKING DIFFUSION COUPLES

Table (4-3)

Certified Chemical Analysis of $\text{Fe}_{0.9}\text{S}$ in ppm

Impurities	Amount by ppm
Ag	10
Al	10
Mg	10
Mn	10
Mo	10
Si	70
Ti	10

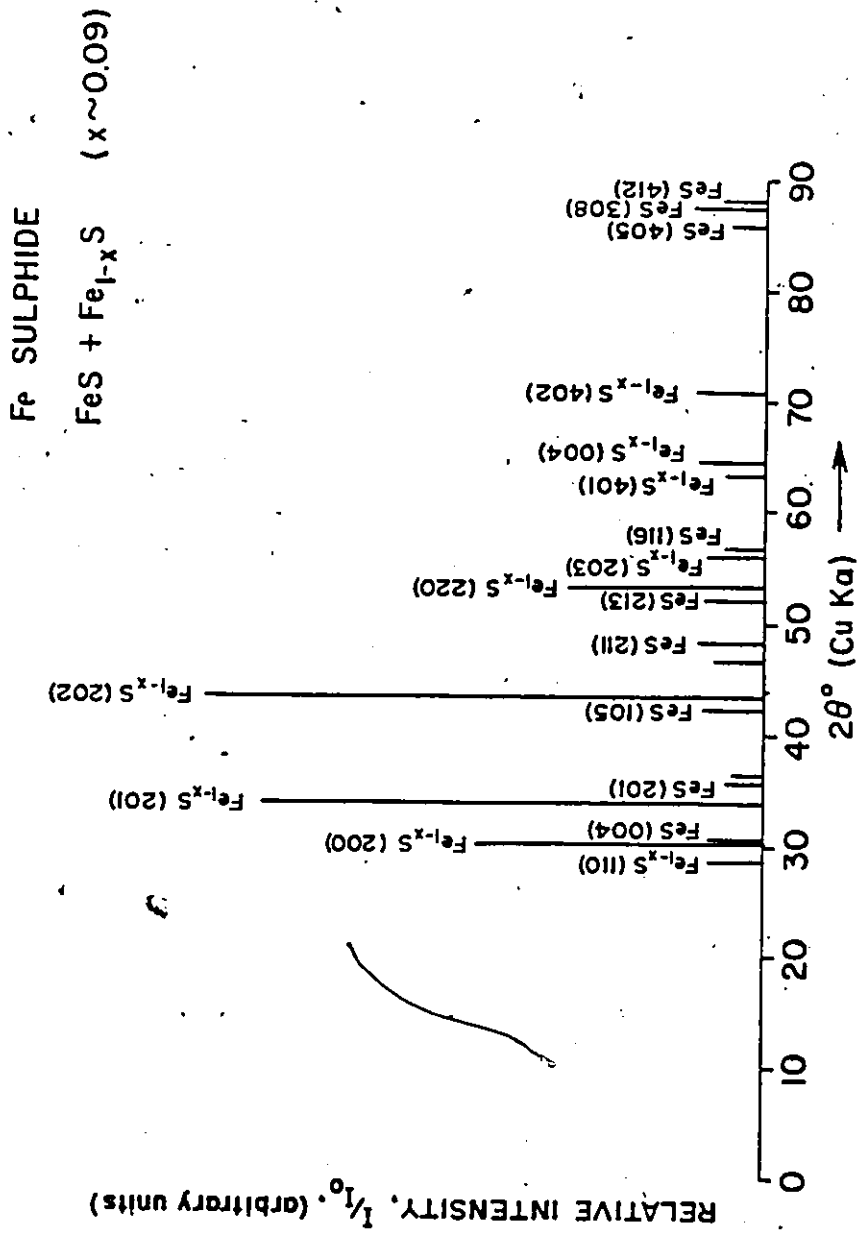


Fig. 4.3 X-ray diffraction pattern of commercial high purity iron sulfide.

Sulfidation of 6, 9, 18 and 28 a/o Al alloys was also carried out at the dissociation pressure of FeS in quartz capsules to study the internal sulfidation kinetics, and the mode of precipitation of sulfides in the alloy. The sulfur activity was maintained at the dissociation pressure of FeS by a mixture of Fe and FeS. The amount of FeS powder taken in the Fe+FeS mixture was enough to sulfidize completely the less noble alloying element, i.e., Al in the alloy samples. The alloy samples were suspended in an alumina tube by means of Pt wires as shown in Fig. 4.4. The quartz tubes were evacuated (1 to 2 Pascals) and then annealed for various periods of time. The sulfidized alloy specimens were sectioned, polished and then investigated by metallographic, compositional, and structural methods.

4.5 CALCULATION OF SULFUR PRESSURE

The sulfur pressure in quartz capsules was calculated from the dissociation pressure of FeS at 1173K. From the free energy change of reaction (4.1) (Appendix I),



$$\Delta G^\circ = -303,000 + 108.2 T \quad (\pm 3000) \text{ Joules/mole of } \text{S}_2$$

$$\text{AT } 1173\text{K}, p_{\text{S}_2}^{\text{diss.}} = \exp \frac{\Delta G^\circ}{RT} = 1.44 \times 10^{-8} \text{ atm} = 1.45 \times 10^{-3} \text{ Pa.}$$

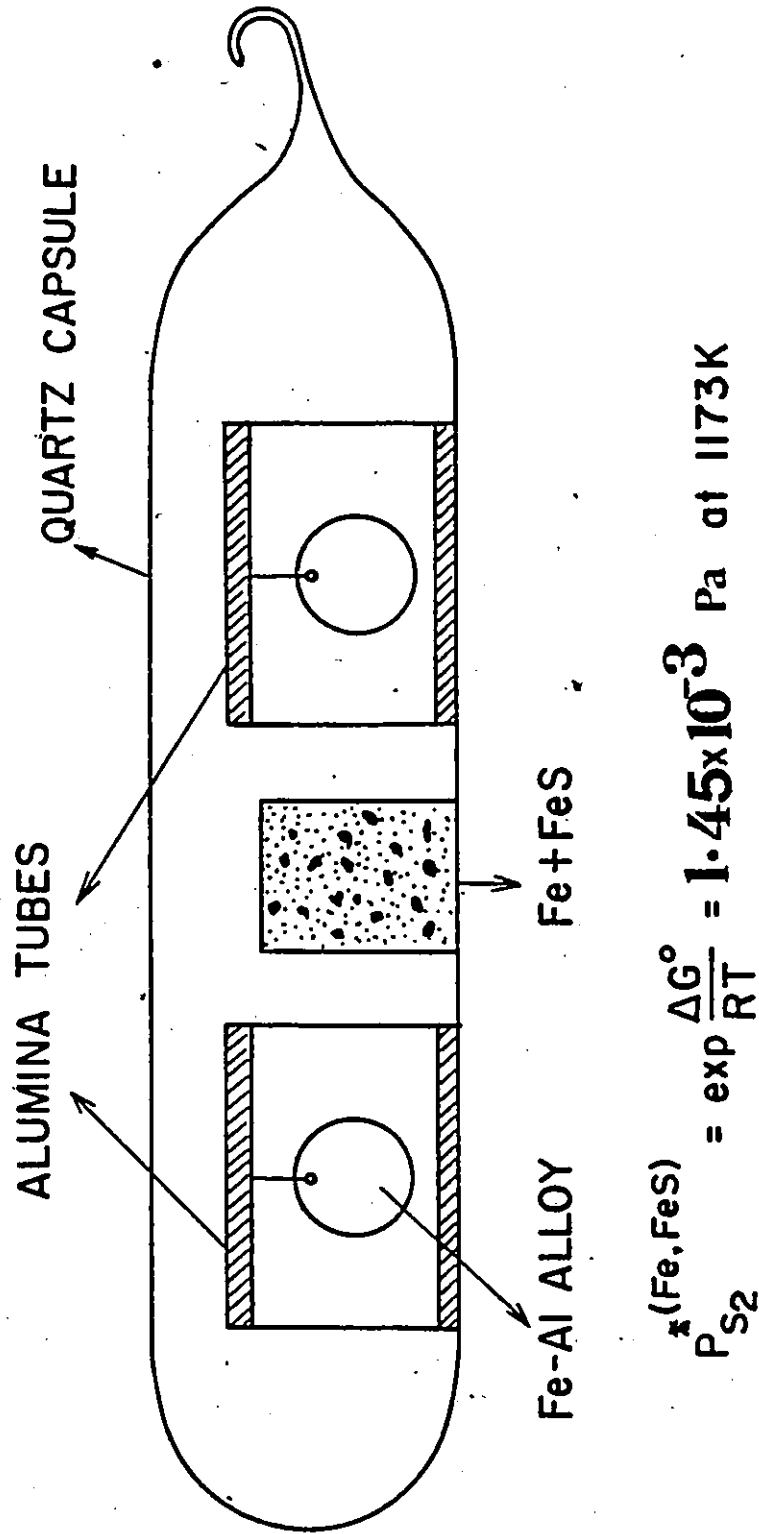
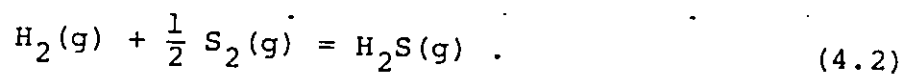


Fig. 4.4 Internal sulphidation set-up.

The sulfur pressure in H_2S-H_2 atmosphere is calculated as follows. In essence when H_2S and H_2 gases are mixed at room temperature and this atmosphere heated to 1073 to 1373K, several gaseous species such as S , S_2 , S_4 , S_6 , S_8 and HS form. Among these only the species S_2 and HS reach substantial concentrations at temperatures 1073 to 1373K and p_{S_2} ranging from 10^3 Pa to 10^{-3} Pa⁽²⁴⁾. Considering $p_{H_2}^o + p_{H_2S}^o = 1$ atmosphere at room temperature and the reaction (4.2),



Nagamori et al. (101) have derived a relation between p_{H_2S} , p_{S_2} and K_1 (equilibrium constant for reaction 4.2), neglecting the species HS . The relation is given by

$$*n_{H_2S}^o = \frac{2K_1 n_{S_2}^{3/2} + 2n_{S_2} (1+n_{S_2})^{1/2} + K_1 n_{S_2}^{1/2}}{K_1 n_{S_2}^{1/2} + (1+n_{S_2})^{1/2}} \quad (4.3)$$

where, $n_{S_2} = p_{S_2} / (1-p_{S_2})$ and is the equilibrium mole number of S_2 species at high temperature. The value of K_1 calculated from the free energy data⁽²⁴⁾ is given by Eqns. (4.4) and (4.5).

$$\Delta G^o(4.2) = -RT \ln K_1 = -180720 + 98.8 T \text{ Joules/mole of } H_2S \quad (4.4)$$

$$K_1 = \exp\left(\frac{18072 - 98.8 T}{RT}\right) \quad (4.5)$$

From Eqn. (4.3) through (4.5), for a known value of K_1 (at a specific temperature), the partial pressure of sulfur p_{S_2} was calculated for various values of p_{H_2S} using a computer programme. At a particular temperature, p_{S_2} increases with increase in p_{H_2S} .

In the sulfidation assembly shown in Fig. 4.1, calibrations of flow rates were made by the soap-bubble method for various gases (helium, pure H_2 , H_2S+H_2 mixtures of various proportions). The flow rate of a gas was calibrated against the float height in the rotameter. A total flow rate of 750 c.c/min was found to vary linearly with the rotameter readings in most of the cases. Hence, for a particular p_{S_2} , the corresponding p_{H_2S} was taken from the computed table to calculate the flow rate of pure H_2 and H_2S or a H_2S+H_2 mixture. For a low value of p_{S_2} , pure hydrogen was generally blended with a mixture of H_2+H_2S of low H_2S content. From the rotameter calibrations, the flow rates of various gases were converted to rotameter readings.

Another method was used to check the validity of the above calculation. Since sulfur is produced from the dissociation of H_2S by the reaction,



the equilibrium constant K is given by (4.7)

$$K = \frac{p_{S_2}^{1/2} \cdot p_{H_2}}{p_{H_2S}} \quad (4.7)$$

Knowing $K = \exp\left(-\frac{180720+98.8 T}{RT}\right)$ and the p_{H_2}/p_{H_2S} ratio, p_{S_2} was calculated. At a total flow rate of 750 c.c./min., the ratio of H_2/H_2S flow rates corresponded to the ratio of p_{H_2}/p_{H_2S} .

4.6 EXPERIMENTAL TECHNIQUES USED FOR ANALYZING THE SULFIDATION PRODUCTS

4.6.1 Optical Metallography

The sulfidized specimens were cold mounted vertically in epoxy resin contained within 25 mm diameter plastic rings. Some specimens were vacuum impregnated with cold mounting epoxy to fill the open pores in the scale or at the alloy-scale interface caused by scale separation before mounting them in the resins encased in plastic rings. They were polished in cross-section on silicon carbide papers of 200, 320, 400 and 600 grit using kerosene as the lubricant. The microstructures of specimens were examined and photomicrographs were taken using a Zeiss microscope. To obtain good contrast between the scale and alloy structures, polarized light was used. Thicknesses of internal sulfidation zones were measured with the help of a calibrated cross-wire eye-piece attached to the microscope.

4.6.2 Scanning Electron Metallography

Scanning electron microscopy (SEM) was used to study the morphological features of a sulfide scale. The samples mounted in the cold epoxy resin were coated with carbon by vapour deposition to allow uniform electron conduction and to avoid electrical charge build up. An energy dispersive X-ray analyzer attached to the Cambridge model electron microscope

was used to identify the elements and their distribution in various parts of the scale. Results from EDAX analyser were interpreted by comparing the X-ray counts from the sample to that of a set of standards as described later.

4.6.3 X-ray Analysis

The X-ray analysis^{Sy} of the constituents of the sulfidation product was carried out using a Philips X-ray diffractometer. Samples from the scale were crushed into powder in a mortar and mounted on a glass slide by compacting it under sufficient pressure to cause cohesion and smoothing of the surface. Specimens with an external sulfide layer were mounted directly on a glass slide for reflection X-ray diffraction analyses. For powder samples, sodium chloride was used as the standard to correct for any deviation in 'd' spacings. A voltage of 30 KV and 20 mA (CuK_α radiation) was used throughout in this investigation. The results (relative peak intensities and 'd' spacings or diffraction angle 2θ) obtained from the samples were compared to those results from prepared standards and in ASTM tables. ✓

4.6.4 Electron Probe Microanalysis

A Cameca electron microprobe was used to identify the composition of phases in the scale, composition gradients across the alloy and the scale, and equilibrium compositions in phases prepared for the Fe-Al-S isotherm analysis. Operating

conditions were 16 and 20 KV acceleration voltages and 85 to 95 nano-ampere specimen currents. Pure Al (99.998%) and Fe-Al alloys containing 1, 6, 9, 18 and 28 a/o Al were used as standards to analyze aluminum in the sulfide phases and in the alloy. Pure Fe (99.99%) was used as a standard for Fe in the alloys. FeS was used both as a standard to analyze Fe in sulfide phases and sulfur in the alloy and sulfide scales. Corrections were applied for background, atomic number and absorption. For analysis of the ternary Fe-Al-S isotherm, standards of FeAl_2S_4 and Al_2S_3 were prepared using pure Fe, Al and S.

It was difficult to obtain composition of fine size precipitates by EPMA due to the limitation of the probe size. Therefore, several profiles of Fe, Al and S were made by scanning the probe beam continuously in different directions to show the distribution of the fine particles.

4.7 DETERMINATION OF THE Fe-Al-S PHASE DIAGRAM

A number of the ternary phases in the Fe-Al-S system were synthesized from the elements. The starting materials of 99.99% Fe and Al, 99.999% S were obtained from Cerac, Incorporated. The certified chemical analyses of these materials are given in Table (4-4). Several overall compositions were chosen. In each case, the elements were thoroughly mixed, compressed to a pellet and then placed in a high purity (99.9%) alumina crucible which was sealed in a quartz tube under vacuum (1 to 2 Pa). This method avoided a direct reaction between Al in the

Table 4-4

Certified Chemical Analyses of Fe, Al and S
in ppm.

Impurities	Fe	Al	S
Ca	10	< 10	-
Cr	10	40	-
Cu	70	10	-
Ga	10	-	-
Mg	10	10	-
Mn	10	30	-
Mo	70	-	-
Ni	100	-	-
Si	-	10	-
Sn	-	10	-
Fe	By difference	-	-
Cl	-	-	< 1
Na	-	-	< 1
S	-	-	By difference

pellet and SiO_2 in the quartz, and contamination of SiO_2 in the sample was minimal. The contamination of SiO_2 in the sample mix has been found to be as high as 30 wt.% elsewhere (154).

Previous workers using Al and S to obtain high purity Al_2S_3 (149) in quartz ampoules have encountered explosions while determining a suitable heating schedule. This behaviour was due to the autocatalytic nature of Al sulfidation by which the exothermic sulfidation reaction increased the sulfur pressure in the ampoule. With an increased sulfur pressure, the reaction rate increases, releasing more heat. This led to excessive sulfur pressures and rupturing of the quartz tube. This problem was not encountered in our present experiments perhaps due to the rapid reaction between Fe and S. However, for a successful experiment a combination of slow and step heatings were used.

Figure 4.5 shows a typical heating schedule of the samples in the quartz ampoules. Initially it was heated for 2 days in steps at 423K and 509K (total p_{S_x} at 509 K = 10^3 Pa) to permit combination of the sulfur and metals. All the samples contained 35 a/o S with varying amounts of Fe and Al. The completeness of reaction between sulfur and the metals was indicated by the absence of visible sulfur in the quartz tube. After approximately 240 hours at 1173K the ampoules were quenched. The quenched samples were mounted for metallographic examination. In addition to metallography, X-ray diffraction

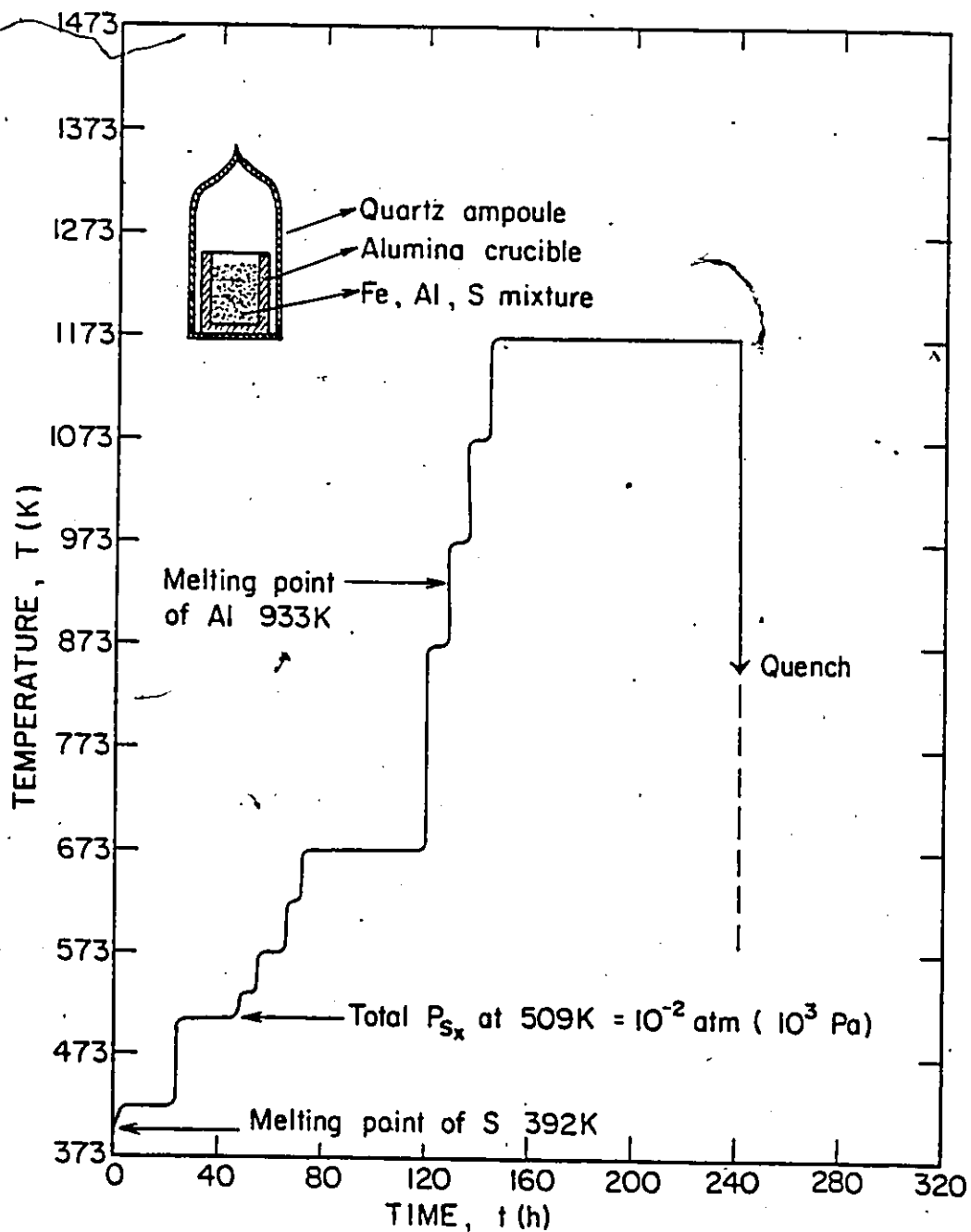


Fig. 4.5 Heating schedule for the preparation of FeAl_2S_4 and determination of Fe-Al-S ternary isotherm.

was also employed to identify the various crystalline phases present in each sample. The compositions of various phases were determined using the electron microprobe with the binary alloys and synthetic sulfides of known compositions as standards.

CHAPTER 5

EXPERIMENTAL RESULTS

5.1 INTRODUCTION

The experimental results can be conveniently divided into six sections. Sulfidation behaviour of alloys containing 1, 6, 9, 18 and 28 a/o Al at 1173K by compacting with FeS is presented in section 5.2. Kinetics were measured by sulfide layer thicknesses as a function of exposure time. When these alloys were sulfidized by S_2 vapour fixed at the dissociation pressure of FeS, transition from internal to external sulfidation occurred at 28 a/o Al in the alloy (section 5.3). Increasing the sulfur pressure by H_2S-H_2 mixtures resulted in development of complex sulfide morphologies, at sulfur partial pressures ranging from 1 Pa to 10^3 Pa (section 5.4). Results from inert Pt marker measurements are presented in section 5.5. Phase identifications were carried out using electron microprobe, X-ray diffraction and X-ray energy dispersive analyses. These results are compiled in section 5.6. Results from the phase equilibria in Fe-Al-S ternary system are presented in section 5.7.

5.2 PERIODIC PRECIPITATION OF SULFIDES IN FeS/Fe-Al ALLOY DIFFUSION COUPLES

5.2.1 Sulfidation Kinetics

Sulfidation kinetics of alloys containing 6, 9, 18 and 28 a/o Al coupled to FeS were obtained by measuring the sulfidation zone thicknesses since the subscales grew uniformly on these alloys. The sulfidation zone consists of alternate layers of metal and sulfides in the form of bands parallel to the original alloy surface. The layer thicknesses were measured by examining polished cross-sections of specimens in an optical microscope equipped with a calibrated eye-piece. Several measurements were taken on a single specimen to perform statistical analyses. The standard errors (σ/\sqrt{N}) were calculated from the standard deviation (σ) and the number of measurements (N). The kinetic results were reproducible within the standard errors of the measurement as will be shown later.

Table (5-1) summarizes the kinetic results which are shown in Fig. 5.1 by parabolic plots. The penetration depths given in the table and shown in this figure are for the total product layer consisting of alternate alloys and sulfide bands. It is evident from this figure that sulfidation kinetics of the alloys containing up to 28 a/o are parabolic. The parabolic rate constants $k_s (= x/\sqrt{t})$ increase with increasing aluminum content in the alloy (Fig. 5.2). Reproducibility of these measurements have been presented by two sets of results in Fig. 5.2. A straight line was drawn with these points and a correlation coefficient of 0.98 has been obtained. This shows a

Table (5-1)
Kinetic Results for FeS/Fe-Al Diffusion Couples

Alloy composition (atom %)	Time of Reaction (s)	Thickness of Product layer (μm)	Standard error in the measurements	Parabolic rate constant k_s ($\mu\text{m}/\text{s}^{1/2}$)
Fe-6Al	1800	146	± 5	3.5 ± 0.1
	3600	198	± 7	
	5400	265	± 6	
Fe-9Al	1800	229	± 4	5.7 ± 0.2
	3600	350	± 9	
	5400	416	± 8	
Fe-18Al	1800	270	± 15	6.7 ± 0.3
	3600	358	± 20	
	5400	520	± 22	
Fe-28Al	1800	424	± 12	10.2 ± 0.2
	3600	591	± 14	
	5400	742	± 14	

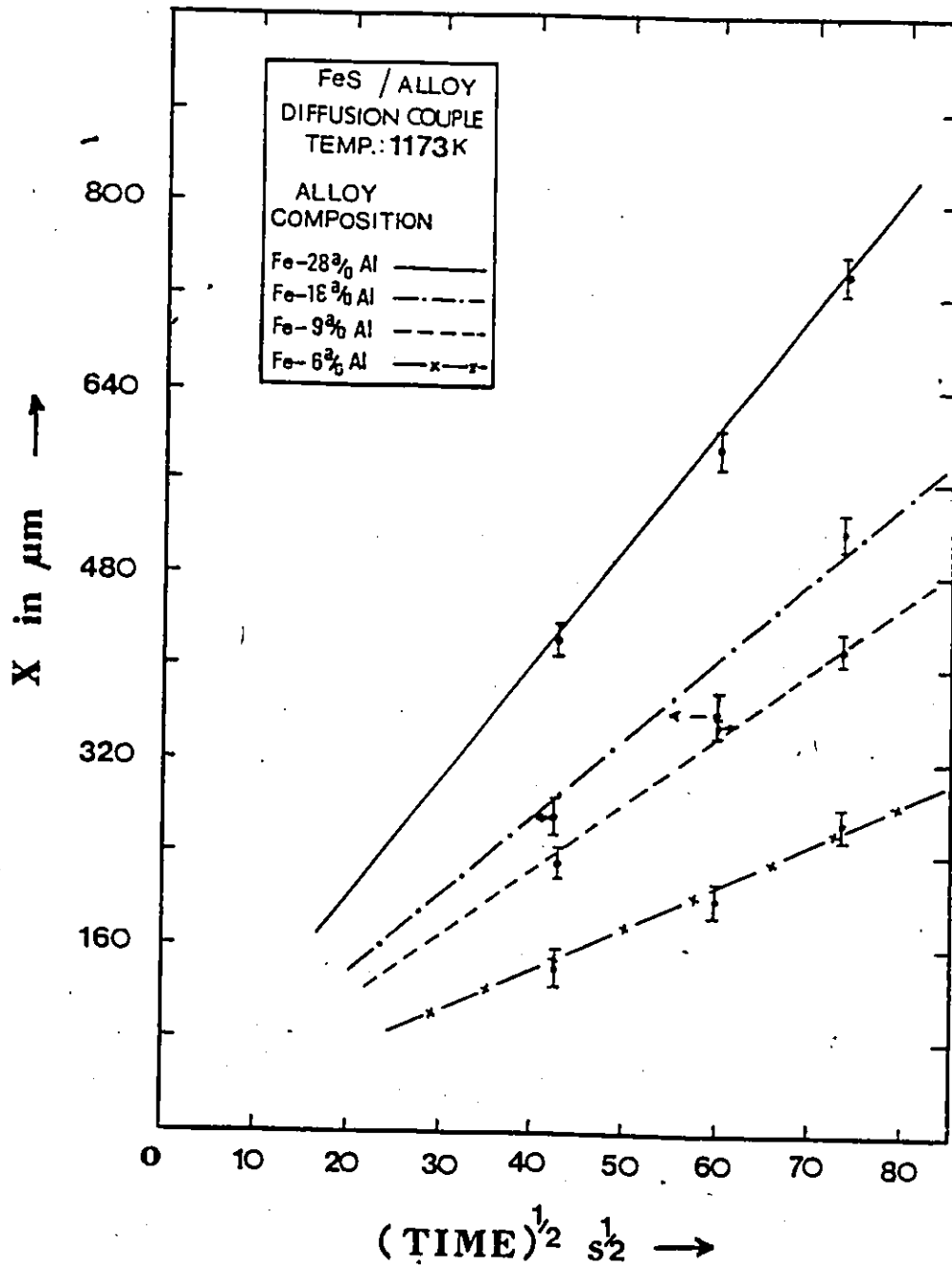


Fig. 5.1 Parabolic plots of sulfidation zone thickness vs. time for Fe-6, 9, 18 and 28 Al alloys in the FeS/alloy diffusion couples.

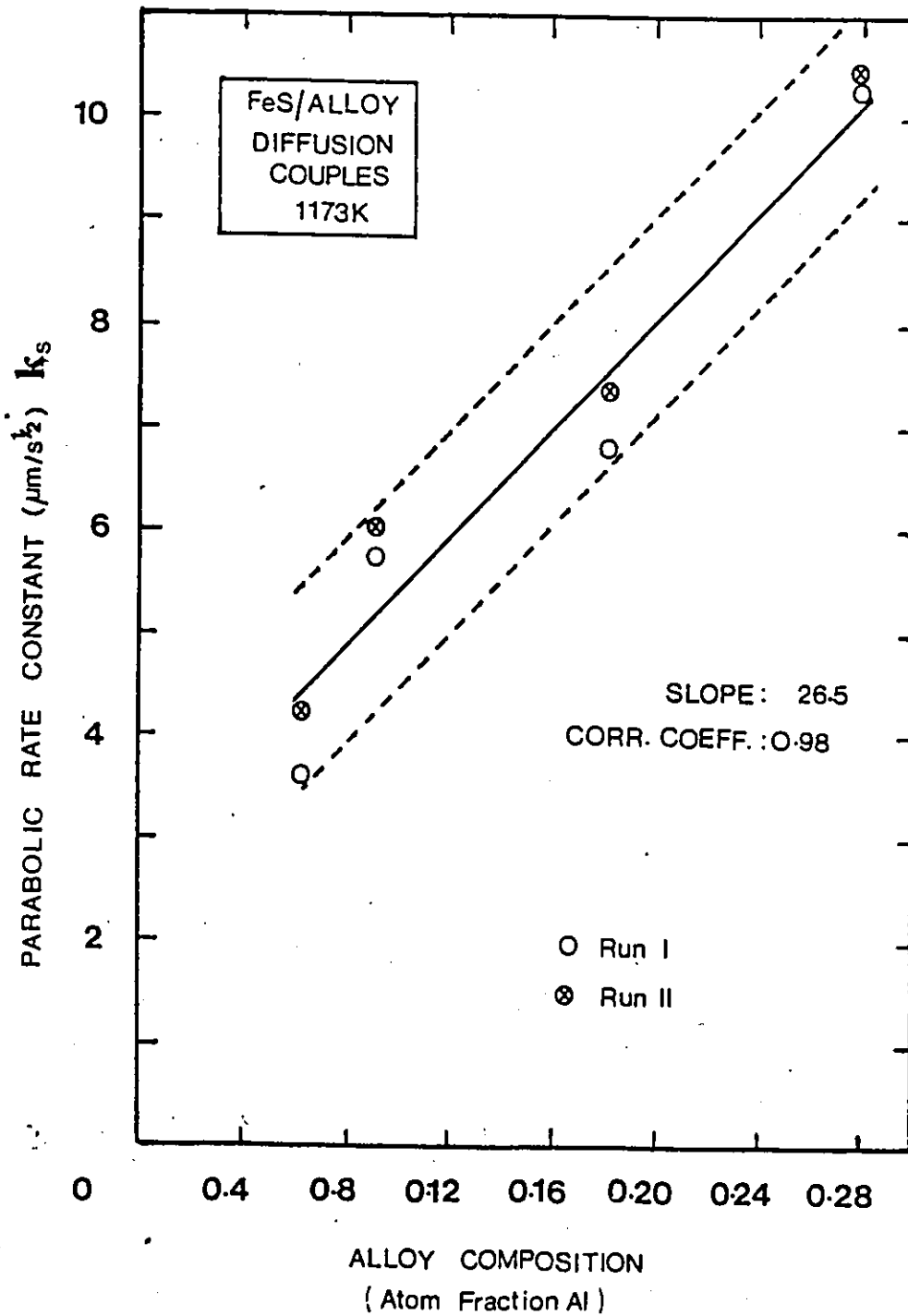


Fig. 5.2 Plot of parabolic rate constant vs. alloy composition for FeS/Fe-Al alloy diffusion couples.

linear relationship between the parabolic rate constant and alloy composition. The dotted lines show the scatter band in which these data points fall. Fe-1 Al alloys sulfidized in this manner did not exhibit reaction product layers but showed general internal precipitation of sulfide particles as shown in Fig. 5.3.

5.2.2 Sulfide Morphological Development

Diffusion coupling of alloys containing 6 to 28 Al in contact with FeS resulted in the periodic precipitation of sulfide bands in the alloy. Experiments were initially carried out with diffusion couples containing Fe-6 Al and Fe-9 Al alloys annealed for 10800 and 7200 s, respectively, at 1173K. These results will be first presented. For a comprehensive study of this phenomenon and to definitively demonstrate the effect of alloy composition, alloys containing 6, 9, 18 and 28 a/o Al were coupled with FeS and annealed for 1500 s in evacuated quartz capsules, at 1173K.

Figures 5.4(a) and (b) show polished cross-sections of the diffusion couples from the first set of measurements. In these figures, the position x is the original FeS/alloy interface obtained from auxiliary calculations considering the molar volumes of alloy and sulfides. The sulfidation zone consists of alternate dark and bright bands or layers which are more distinct towards the subscale/alloy interface. The bright bands are alloy depleted of aluminum; the dark bands consist of a mixture of two sulfides, FeS and FeAl_2S_4 . The most remarkable feature il-

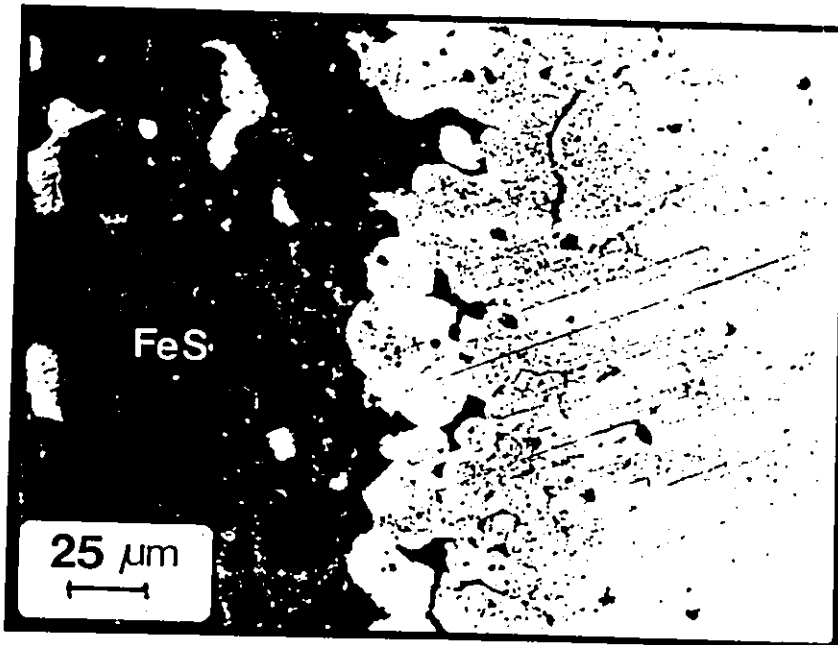
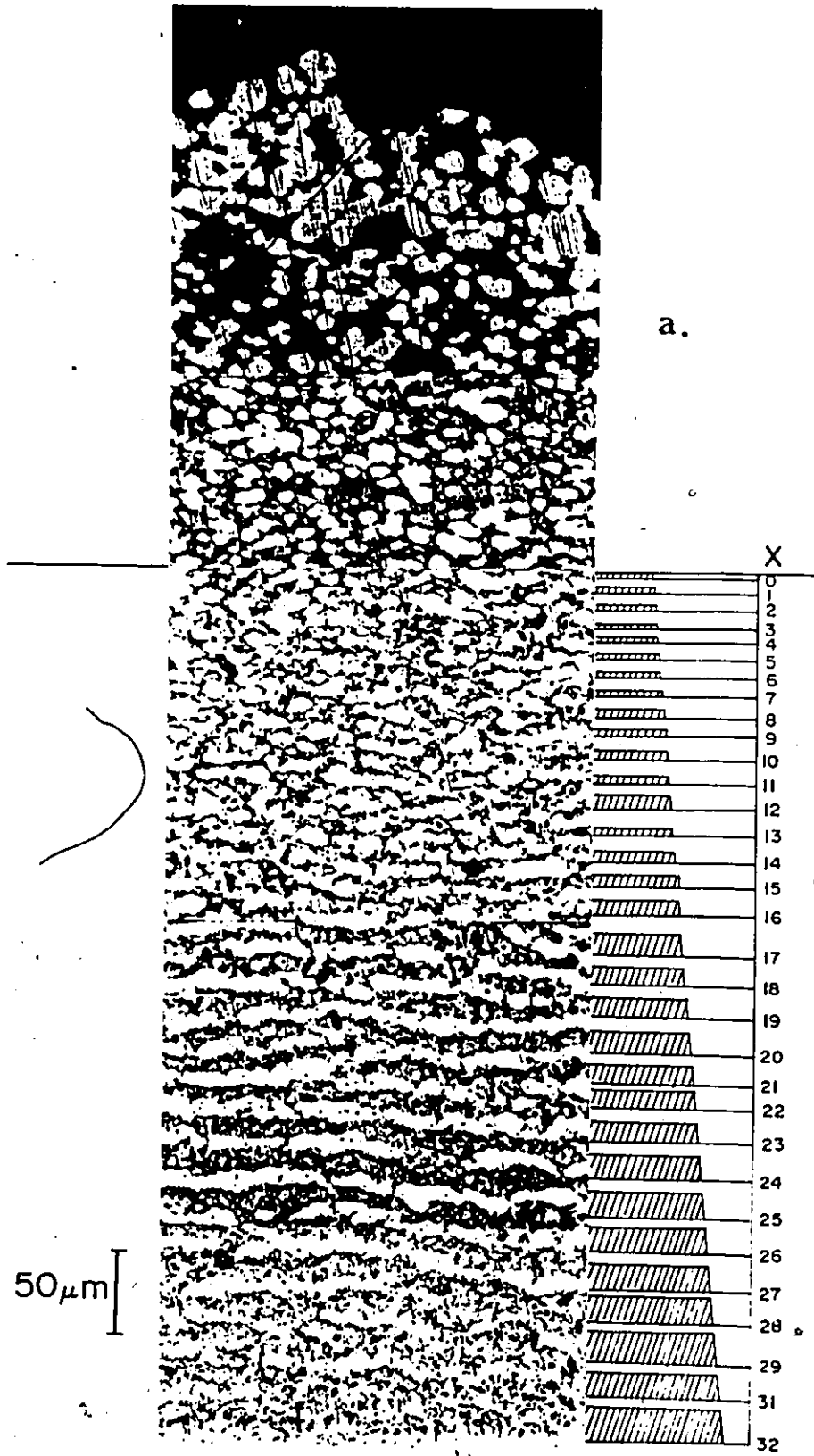
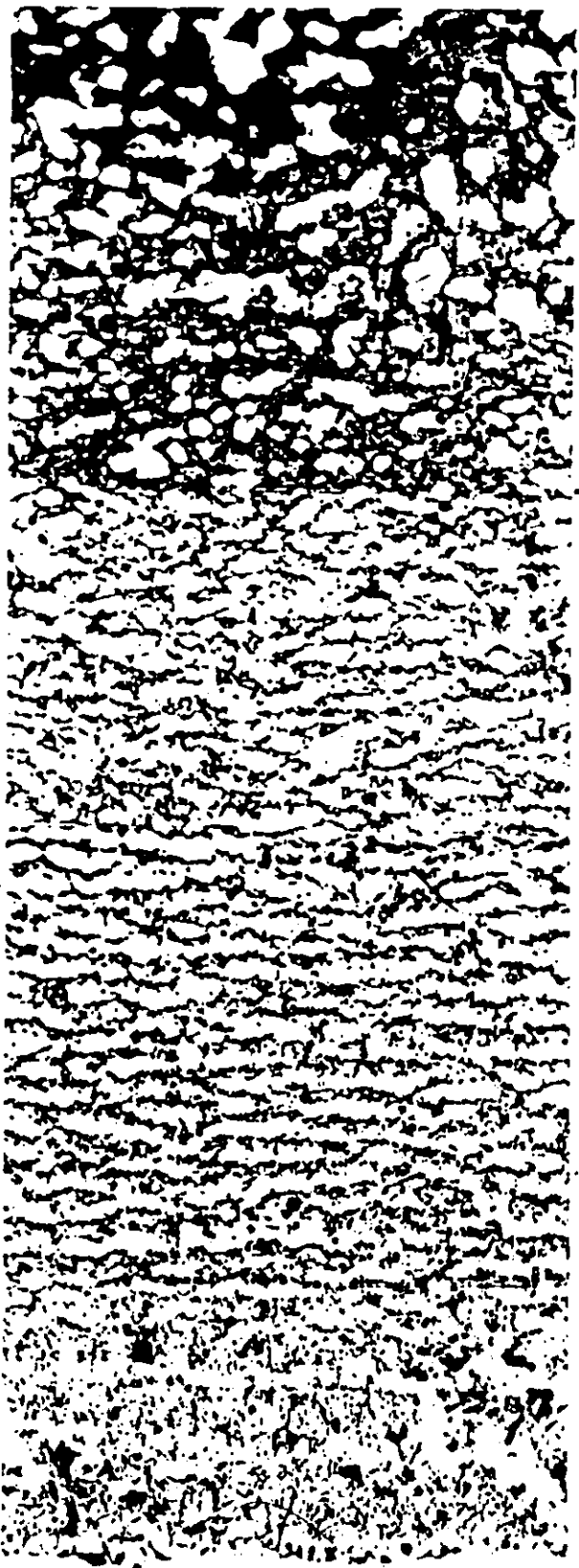


Fig. 5.3 Optical photomicrograph showing the cross-section of a FeS/Fe-1 Al alloy diffusion couple annealed for 43200 s (12 h) at 1173K.

- Fig. 5.4 a) Optical photomicrograph showing cross-section of the FeS/Fe-6 Al alloy diffusion couple annealed for 10800 s at 1173K.
- b) Optical photomicrograph of the cross-section of the FeS/Fe-9 Al alloy diffusion couple annealed for 7200 s at 1173K.





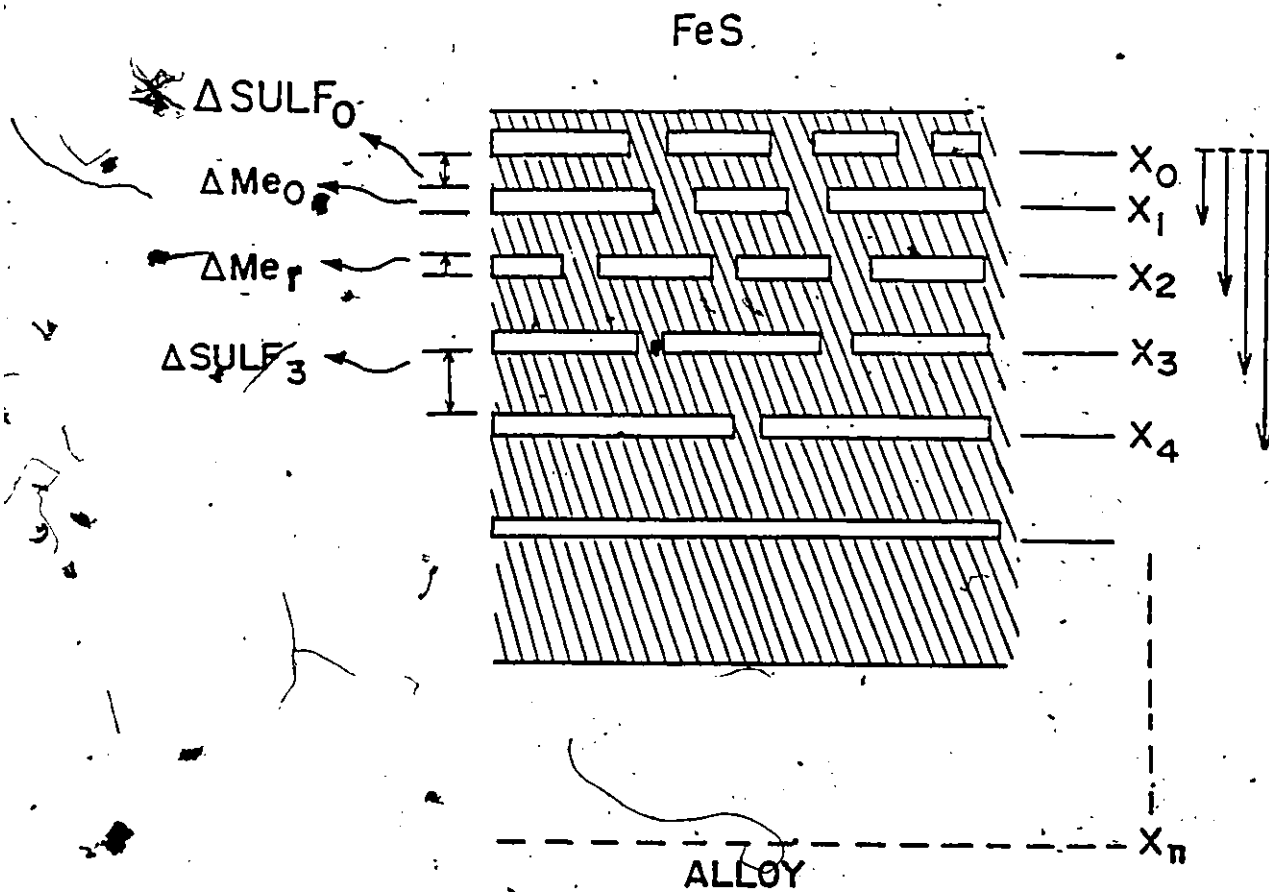
50 μm

X

b.

illustrated in these micrographs is that the thickness of a dark sulfide band increases with depth from the original FeS/alloy interface towards the sulfidation zone/alloy interface. The thicknesses of the bright metallic bands were measured and tabulated. In spite of the difficulty in measuring their thicknesses, it is found that the thicknesses of metallic bands remain constant with their respective standard deviation values as tabulated in Tables 5-3, 5-6.

To correlate this morphology of periodic precipitates with the classical Liesegang type of precipitation, a schematic is shown in Fig. 5.5 in which ΔMe_n and $\Delta SULF_n$ ($n \geq 1$), denote the band thicknesses of metal and sulfides ($FeS + FeAl_2S_4$) respectively. X_n denotes the beginning of formation of n^{th} sulfide band. Using the Jablczynski's relationship (Eqn. 2.60) for Liesegang precipitation^(67,70), $X_n/X_{n-1} = k$ (spacing coefficient constant), a relationship is given in this figure to relate the sulfide thickness $\Delta SULF_n$ and depth X_n . Tables 5-2(a) and (b) show the measurements of X_n and X_{n-1} , and their plots are shown in Figs. 5.6(a) and (b) for Fe-6 and 9 Al alloys, respectively. Measurements of $\Delta SULF_n$ and ΔMe_n with depth X_n are tabulated in Tables 5-3(a), (b) and plots of $\Delta SULF_n$ vs. X_n are shown in Figs. 5.7(a) and (b) for Fe-6 and 9 Al alloys respectively. The latter plots are linear because the thickness of the metal band ΔMe_n was smaller than $\Delta SULF_n$ and its average value within the experimental measurement was constant. Each determination of X_n and $\Delta SULF_n$ was taken from a mean of ten independent measure-



$$\frac{X_{n+1}}{X_n} = \frac{X_n}{X_{n-1}} = k, \quad n \geq 1, \quad X_0 = \text{ORIGINAL ALLOY/FeS INTERFACE.}$$

$$X_1 = X_0 + \Delta \text{SULF}_0 + \Delta \text{Me}_0$$

$$X_2 = X_1 + \Delta \text{SULF}_1 + \Delta \text{Me}_1$$

$$X_3 = X_2 + \Delta \text{SULF}_2 + \Delta \text{Me}_2$$

$$X_{n+1} = X_n + \Delta \text{SULF}_n + \Delta \text{Me}_n$$

$$\underline{\Delta \text{SULF}_n = (k-1) X_n - \Delta \text{Me}_n}$$

Fig. 5.5 Relation between sulfide thickness and its depth of formation.

ments. Standard errors were calculated for each determined data point from the standard deviation and these errors are shown clearly by error bars in Figs. 5.7(a) and (b). Table 5-4 represents a summary of results and evaluated parameters obtained for the diffusion couples containing Fe-6Al and Fe-9Al alloys using the following equations.

$$\frac{X_n}{X_{n-1}} = k \quad (5.1)$$

$$\Delta\text{SULF}_n = (k-1)X_n - \Delta\text{Me}_n \quad (5.2)$$

$$\frac{X_n}{\sqrt{t_n}} = k_s \quad (5.3)$$

Results obtained for diffusion couples of the above and all other alloys annealed for 1500 s are tabulated in a similar manner as above (Tables 5-5(a)-(d) and 5-6(a)-(d)) and plotted in Figs. 5-8(a)-(d) and 5-9(a)-(d). Table 5-7 summarizes these experimental results and the parameters determined from all of the presented results. In general it is observed that the depth of penetration or the corrosion product layer thickness increases with increasing Al content in the alloy whereas the spacing coefficient is independent of alloy composition (Fig. 5.10). The numbers of sulfide bands increased with increasing Al content in these alloys. Linear plots of X_n vs. X_{n-1} and ΔSULF_n vs. X_n satisfy the experimental measurements with reasonable correlation coefficients (Tables 5-5 to 5-6).

No. of Bands	X_n (μm)	X_{n-1} (μm)	No. of Bands	X_n (μm)	X_{n-1} (μm)
1	12.3	3.75	23	335	315.5
2	22.3	12.3	24	357.5	335
3	32.5	22.3	25	380	357.5
4	40.3	32.5	26	400.8	380
5	50.8	40.3	27	423.8	400.8
6	62.3	50.8	28	442.5	423.8
7	72.5	62.3	29	467.5	442.5
8	85.5	72.5	30	487.5	467.5
9	95	85.5	31	512.5	487.5
10	110	95			
11	125	110			
12	139.5	125			
13	154	139.5			
14	170	154			
15	185	170			
16	202	185			
17	225	202			
18	243	225			
19	262.5	243			
20	283.8	262.5			
21	302.5	283.8			
22	315.5	302.5			

FeS/ALLOY DIFFUSION COUPLE
 ALLOY: Fe-6Al
 TEMPERATURE: 1173K
 ANNEALING TIME: 10800 s

FROM X_n vs X_{n-1} PLOT
 SLOPE = 1.03
 CORRELATION COEFF. = 0.999

Table 5.2(a) Tabulation of X_n and X_{n-1} as defined by Fig. 5.5 for FeS/Fe-6Al diffusion couple.

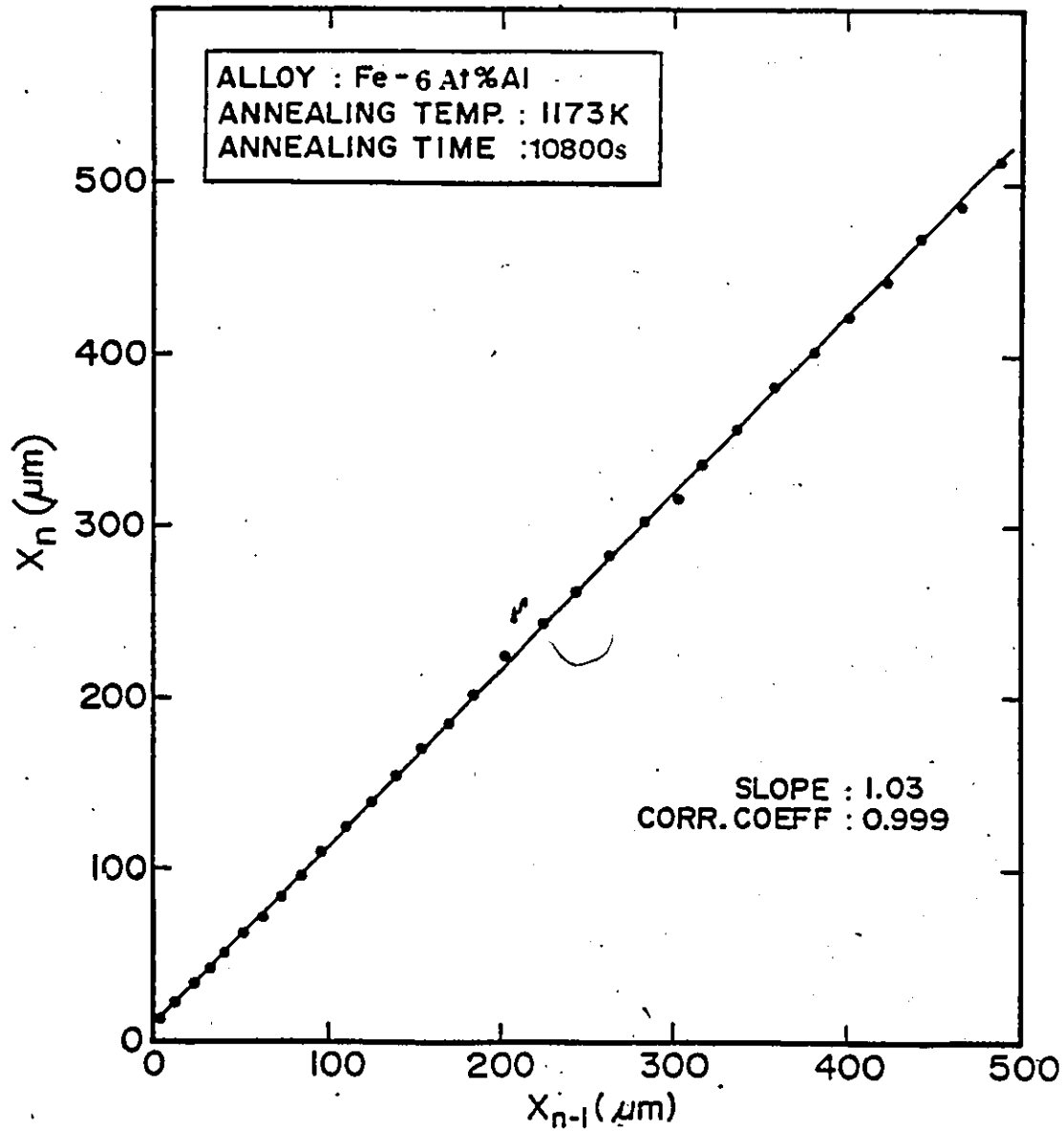


Fig. 5.6(a) Plot of X_n vs. X_{n-1} for FeS/Fe-6 Al alloy diffusion couple.

No. of Bands	X_n (μm)	X_{n-1} (μm)
1	18.3	4.8
2	32.9	18.3
3	48.8	32.9
4	63.4	48.8
5	78.0	63.4
6	97.6	78.0
7	114.6	97.6
8	136.6	114.6
9	163.4	136.6
10	195.1	163.4
11	240.2	195.1

FeS/ALLOY DIFFUSION
 COUPLE
 ALLOY: Fe-9Al
 TEMPERATURE: 1173K
 ANNEALING TIME: 7200 s
 FROM X_n vs. X_{n-1}
 PLOT
 SLOPE = 1.14
 CORR. COEFF. = 0.998

Table 5-2(b). Tabulation of X_n and X_{n-1} as defined by Fig. 5.5 for FeS/Fe-9 Al diffusion couple.

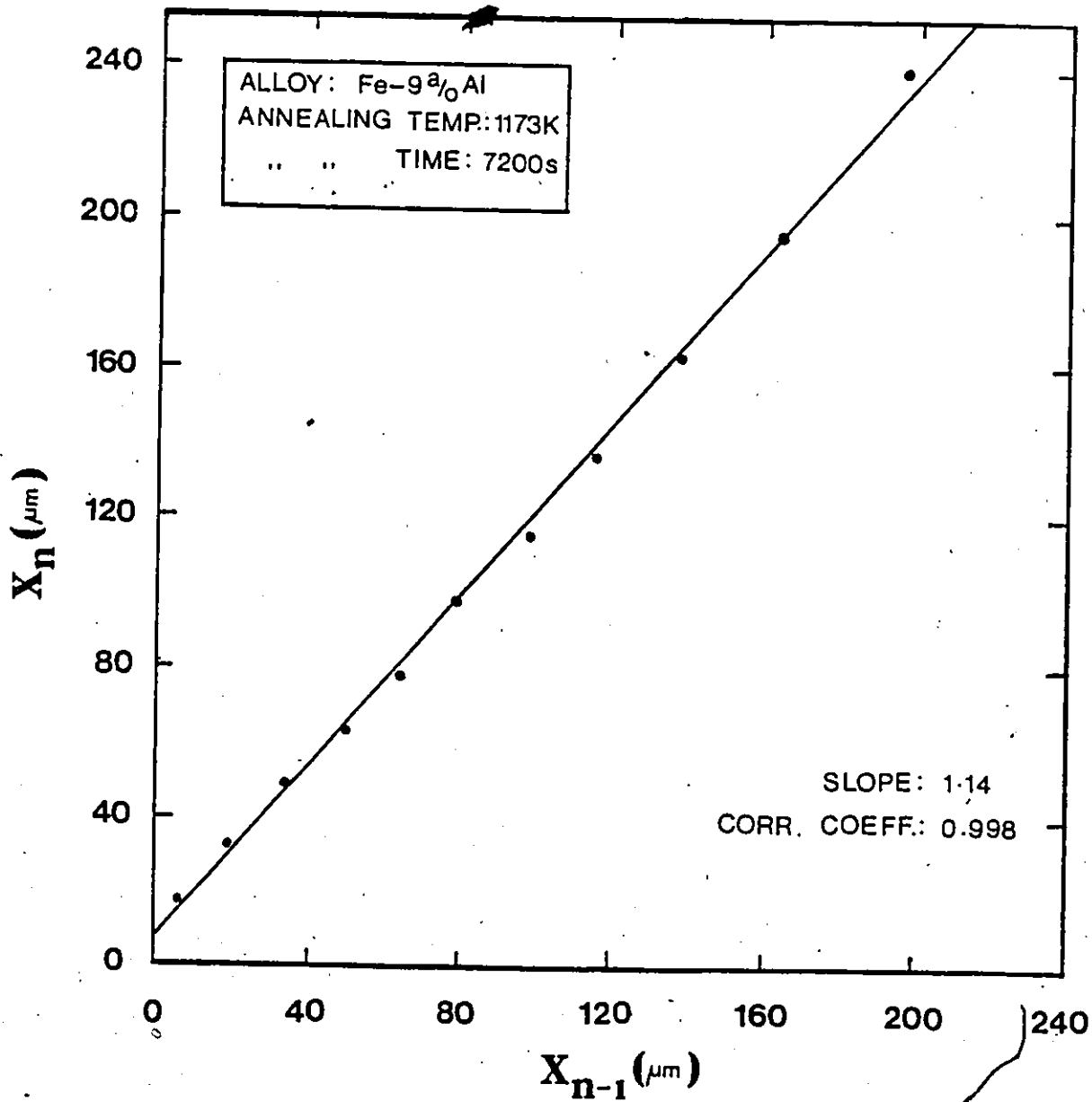


Fig. 5.6(b) Plot of X_n vs. X_{n-1} for FeS/Fe-9 Al alloy diffusion couple.

No. of Bands	X_n (μm)	ΔSULF_n (μm)	ΔMe_n (μm)	No. of Bands	X_n (μm)	ΔSULF_n (μm)	ΔMe_n (μm)
1	12.3	3.0	7.2	24	357.5	15.5	7.0
2	22.5	3.7	6.3	25	380	16.0	4.8
3	32.5	2.9	5.0	26	400.8	15.8	7.1
4	40.3	2.6	7.9	27	423.7	16.2	3.6
5	50.8	4.7	6.8	28	442.5	16.8	7.2
6	62.3	4.6	5.6	29	467.5	20.8	3.2
7	72.5	4.5	7.5	30	487.5	17.1	7.9
8	85.5	5.5	5.5	31	512.5	23.4	6.2
9	95	5.3	9.7				
10	110	6.0	9.0				
11	125	5.3	9.2				
12	139.5	9.2	5.3				
13	154	5.8	10.2				
14	170	7.4	7.6				
15	185	7.9	9.1				
16	202	9.2	10.8				
17	225	13.2	5.8				
18	243	11.0	8.5				
19	262.5	11.3	10.0				
20	283.8	13.4	5.3				
21	302.5	12.1	6.9				
22	315.5	11.0	8.5				
23	335	13.7	8.8				

FeS/ALLOY DIFFUSION COUPLE
ALLOY: Fe-6Al
TEMP.: 1173K
ANNEALING TIME: 10800 s

Mean $\Delta\text{Me}_n = 7.20 \mu\text{m}$
Standard Deviation ± 1.88

From ΔSULF_n vs. X_n PLOT

SLOPE = 0.036
CORR. COEFF. = 0.07

Table 5-3(a) Tabulation of X_n , ΔSULF_n and ΔMe_n for FeS/Fe-6Al Diffusion couples.

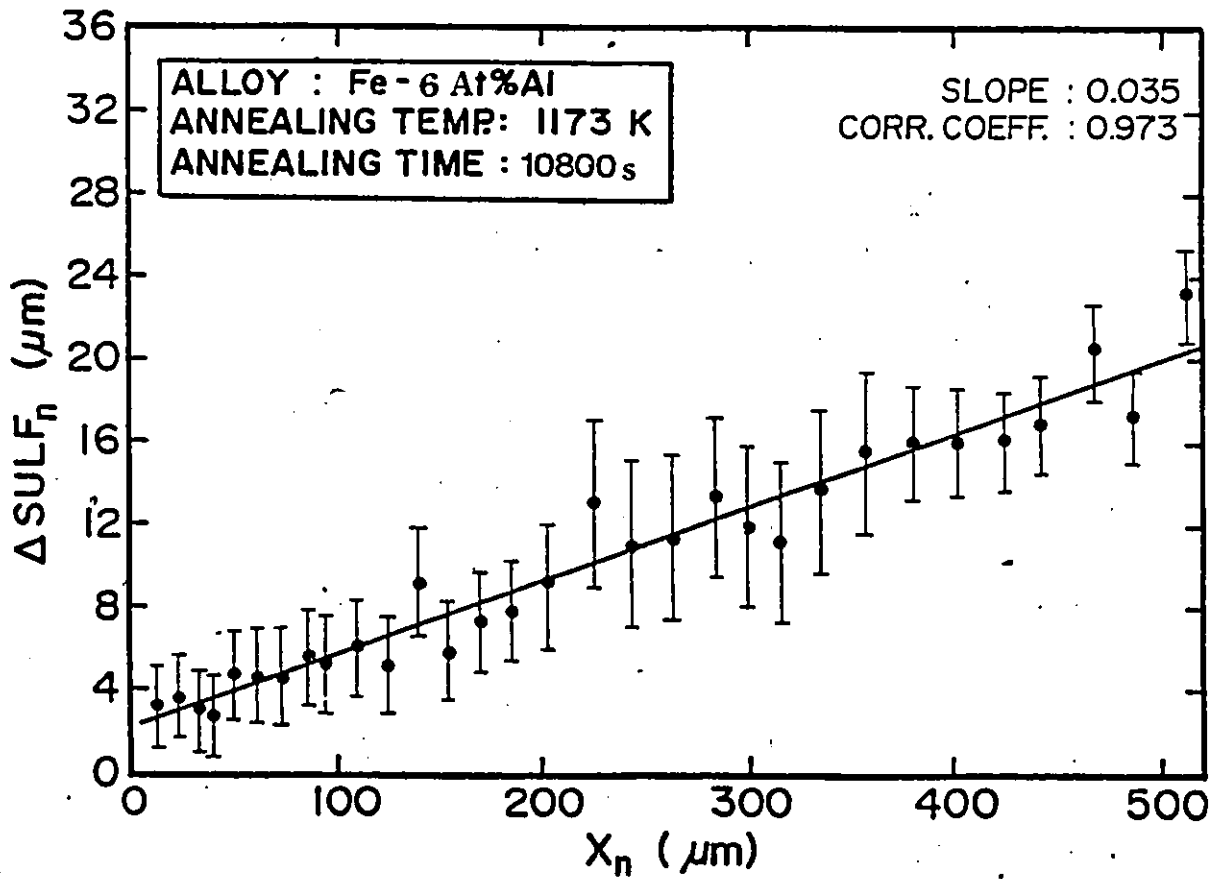


Fig. 5.7(a) Plot of sulfide thickness ΔSULF_n vs. depth X_n for FeS/Fe-6Al alloy diffusion couple.

No. of Bands	X_n (μm)	ΔSULF_n (μm)	Me_n (μm)	
1	18.3	5.5	9.1	
2	32.9	5.9	10	FeS/ALLOY DIFFUSION
3	48.8	7.0	7.6	COUPLE
4	63.4	7.5	7.1	ALLOY: Fe-9Al
5	78.0	8.7	8.9	TEMP.: 1173K
6	97.6	10.7	6.3	ANNEALING TIME: 7200 s
7	114.6	13.0	8.4	
8	136.6	16.2	9.8	Mean $\Delta\text{Me}_n = 9.01 \mu\text{m}$
9	163.4	18.7	12	Standard Deviation = ± 1.52
10	195.1	25.4	9.7	
11	240.2	35.0	10.1	FROM ΔSULF_n vs. X_n PLOT

CORR. COEFF. = 0.973

Table 5-3(b) Tabulation of sulfide band thicknesses (ΔSULF_n) and metal band thicknesses (ΔMe_n) vs. depth X_n for FeS/Fe-9Al diffusion couples.

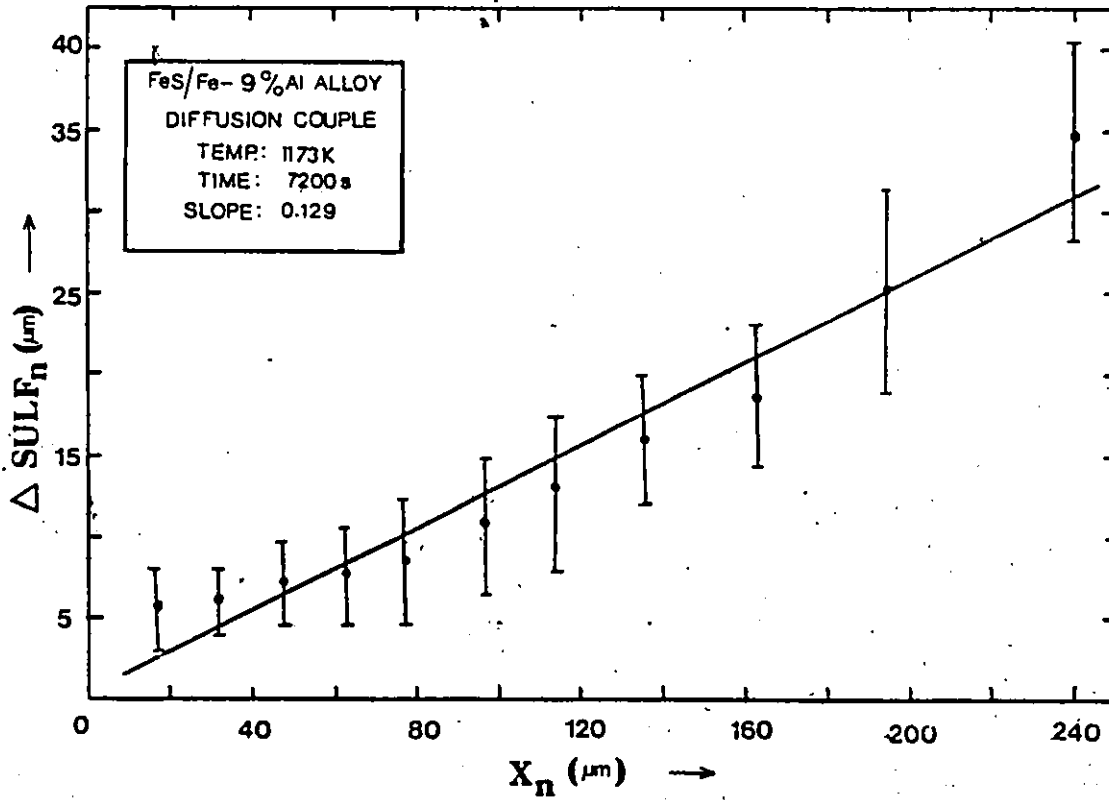


Fig. 5.7(b) Plot of sulfide thickness ΔSULF_n vs. depth X_n for FeS/Fe-9Al diffusion couple.

Experi- mental parameter	Alloy	
	Fe-6Al	Fe-9Al
Annealing time	10800 s	7200 s
Spacing coefficient $\frac{X_n}{X_{n-1}} = k$	1.03	1.145
Correlation Coefficient of X_n vs. X_{n-1}	0.999	0.998
Metal Band Thicknesses (μm) and standard deviation	7.2 $\sigma = \pm 1.88$	9.01 $\sigma = \pm 1.51$
ΔSULF_n (maximum μm)	23.4	35
Penetration Rate k_s MAXM.IN $\mu\text{m}/\text{s}^{1/2}$	7.9	8.6

Table 5-4. Tabulation experimental results of FeS/Fe-6 and 9Al alloy diffusion couples.

Table 5-5(a)

No. of Bands	X_n (μm)	X_{n-1} (μm)	
1	13.2	3.8	
2	22.9	13.2	
3	30.5	22.9	FeS/ALLOY DIFFUSION COUPLE
4	37.8	30.5	
5	46.8	37.8	ALLOY: Fe-6Al
6	57.3	46.8	TEMP.: 1173K
7	68.7	57.3	ANNEALING TIME: 1500 s
8	82.0	68.7	
9	95.0	82.0	FROM X_n vs. X_{n-1} PLOT
10	106.1	95.0	
11	118.3	106.1	SLOPE = 1.04 CORR. COEFF. = 0.999

Table 5-5(b)

No. of Bands	X_n (μm)	X_{n-1} (μm)	
1	11.8	4.4	
2	17.9	11.8	FeS/ALLOY DIFFUSION COUPLE
3	24.6	17.9	
4	30.8	24.6	ALLOY: Fe-9Al
5	36.5	30.8	TEMP.: 1173K
6	47.7	36.5	ANNEALING TIME: 1500 s
7	57.5	47.7	
8	66.9	57.5	FROM X_n vs. X_{n-1} PLOT
9	79.9	66.9	SLOPE = 1.06
10	94.2	79.9	CORR. COEFF. = 0.99

Table 5-5. Tabulation of X_n and X_{n-1} for a) Fe-6Al and b) Fe-9Al FeS/alloy diffusion couples.

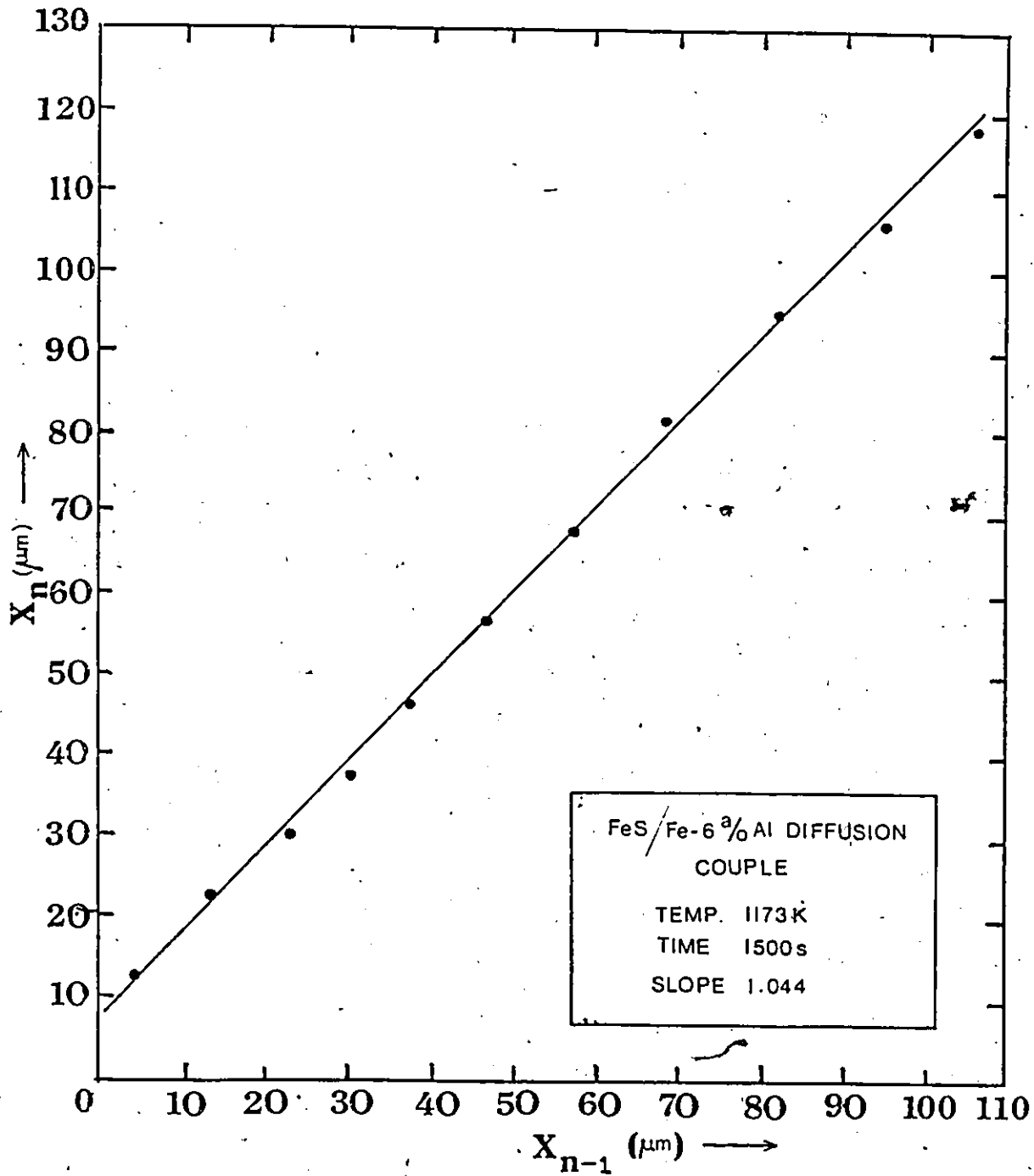


Fig. 5.8(a) Plot of X_n vs. X_{n-1} for FeS/Fe-6Al alloy diffusion couple.

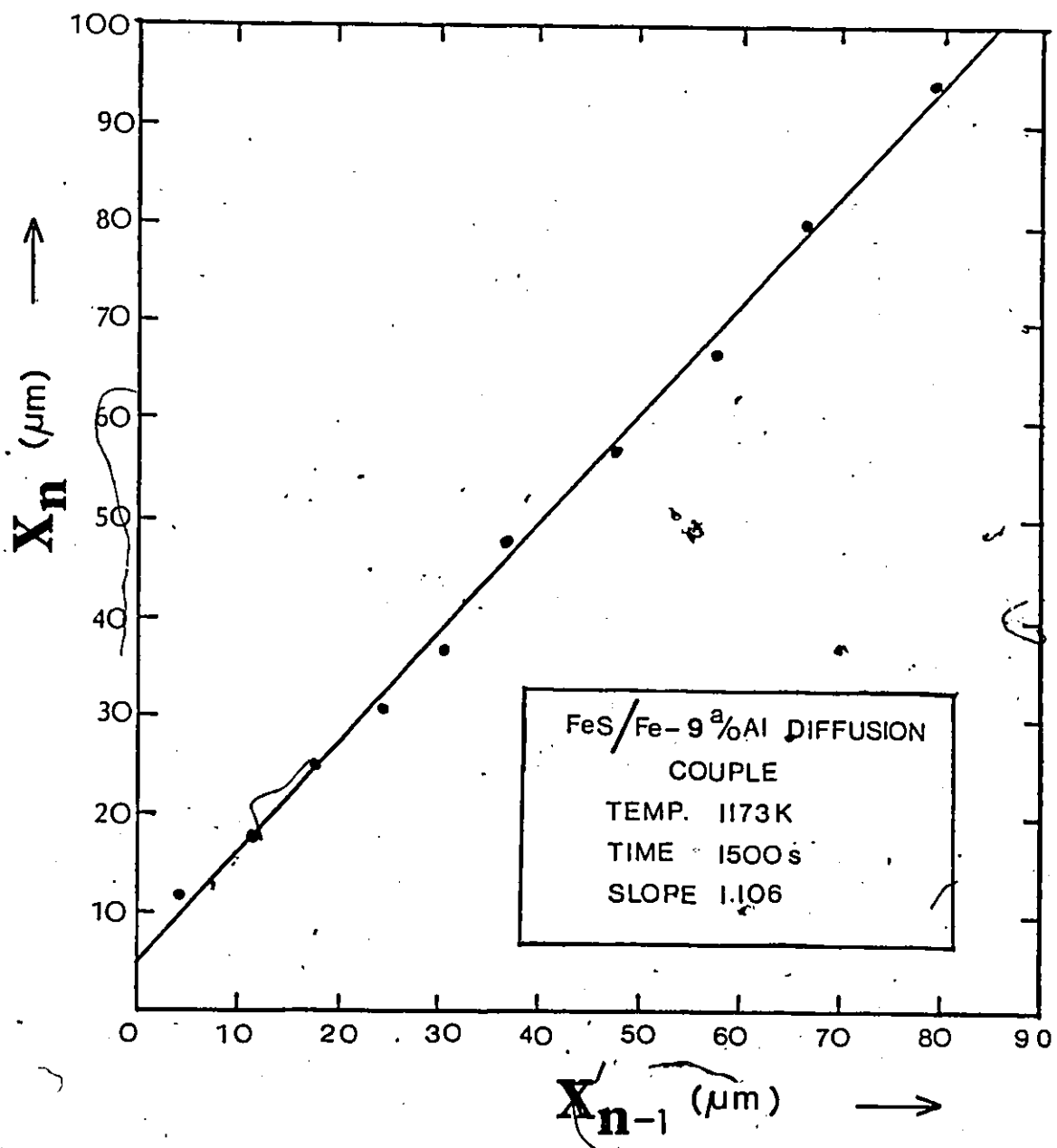


Fig. 5.8(b) Plot of X_n vs. X_{n-1} for FeS/Fe-9Al alloy diffusion couple.

No. of Bands	X_n (μm)	X_{n-1} (μm)	No. of Bands	X_n (μm)	X_{n-1} (μm)
1	9.2	2.88	29	199.6	191.4
2	15.4	9.2	30	205.8	199.6
3	24.8	15.4	31	214.0	205.8
4	34.6	24.8	32	221.1	214.0
5	40.4	34.6	33	227.7	222.1
6	45.4	40.4	34	234.6	227.7
7	51.9	45.4	35	243.3	234.6
8	59.6	51.9	36	250.9	243.3
9	64.6	59.6	37	258.6	250.9
10	71.2	64.6	38	264.5	258.6
11	74.9	71.2	39	270.2	264.5
12	80.8	74.9	40	278.3	270.2
13	90.4	80.8	41	286.5	278.3
14	99.8	90.4			
15	107.7	99.8			
16	117.3	107.7			
17	126.9	117.3			
18	134.6	126.9			
19	140.4	134.6			
20	144.3	140.4			
21	149.0	144.3			
22	154.8	149.0			
23	159.6	154.8			
24	163.5	159.6			
25	167.3	163.5			
26	174.9	167.3			
27	182.7	174.9			
28	191.4	182.7			

FeS/ALLOY DIFFUSION COUPLE

ALLOY: Fe-18 a/o Al
TEMPERATURE: 1173K
ANNEALING TIME: 1500 s

FROM X_n vs. X_{n-1} PLOT

SLOPE = 1.008
CORRELATION COEFF. = 0.999

Table 5-5(c) Tabulation of X_n and X_{n-1} for FeS/Fe-18Al diffusion couple.

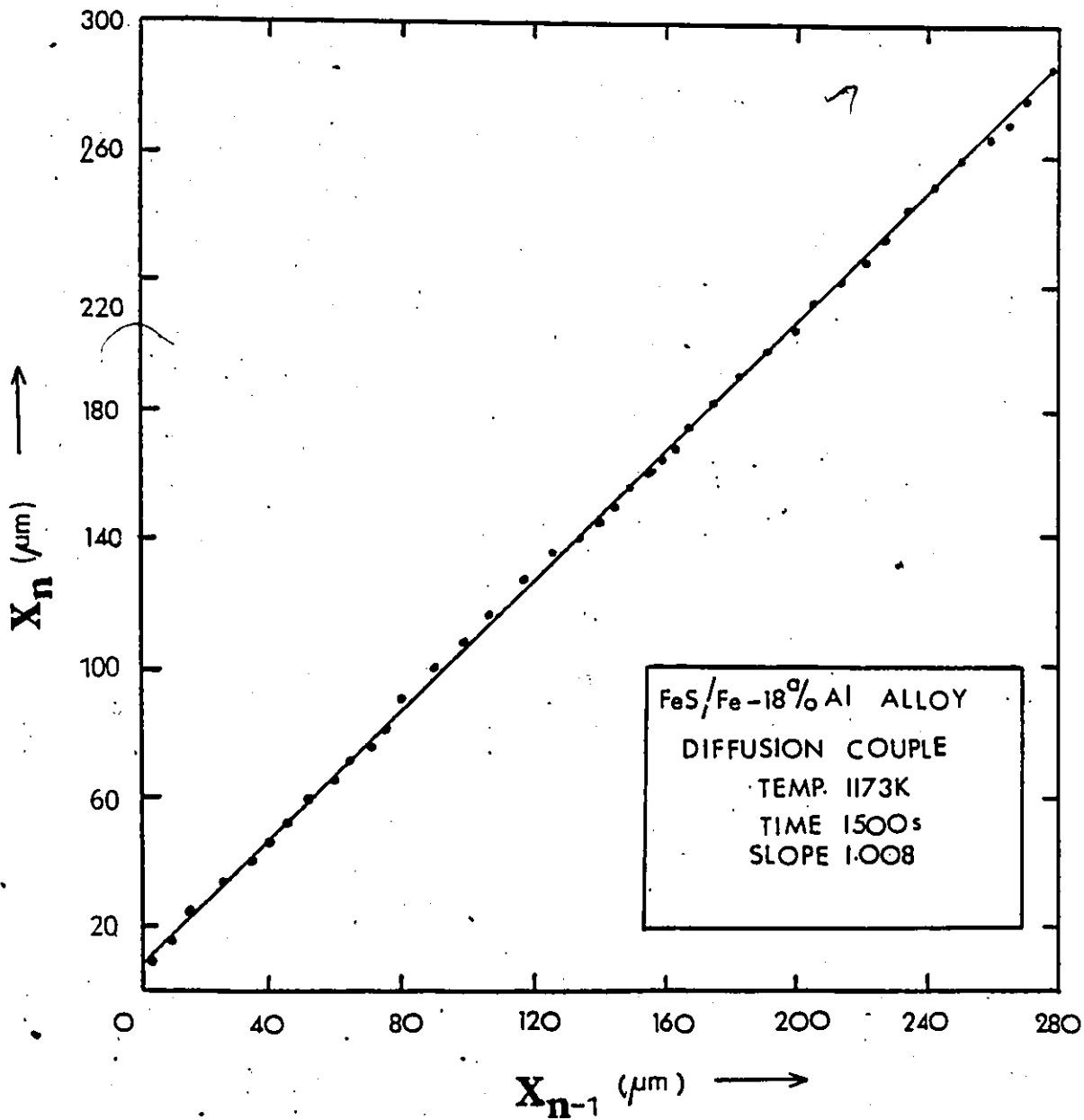


Fig. 5.8(c) Plot of X_n vs. X_{n-1} for FeS/Fe-18Al alloy diffusion couple.

No. of Bands	X_n (m)	X_{n-1} (m)	No. of Bands	X_n (m)	X_{n-1} (m)
1	10.6	2.3	26	253.8	243.3
2	17.9	10.6	27	265.8	253.8
3	28.8	17.9	28	278.8	265.8
4	36.5	28.3	29	293.7	278.8
5	43.3	36.5	30	307.2	293.7
6	53.8	43.3	31	320.7	307.2
7	64.0	53.9	32	335.2	320.7
8	74.0	64.0	33	349.7	335.2
9	82.7	74.0	34	366.0	349.7
10	90.9	82.7	35	383.4	366.0
11	99.9	90.9	36	399.9	383.4
12	108.7	99.9			
13	119.2	108.7			
14	128.8	119.2			
15	140.4	128.8			
16	152.9	140.4			
17	163.5	152.9			
18	174.0	163.5			
19	184.6	174.0			
20	194.2	184.6			
21	203.6	194.2			
22	211.5	203.6			
23	221.1	211.5			
24	232.7	221.1			
25	243.3	232.7			

FeS/ALLOY DIFFUSION
COUPLE
ALLOY: Fe-28 a/o Al
TEMPERATURE: 1173K
ANNEALING TIME: 1500 s
FROM X_n vs. X_{n-1} PLOT
SLOPE = 1.109
CORRELATION COEFF: 0.96

Table 5.5(d) Tabulation of X_n and X_{n-1} for FeS/Fe-28Al diffusion couple.

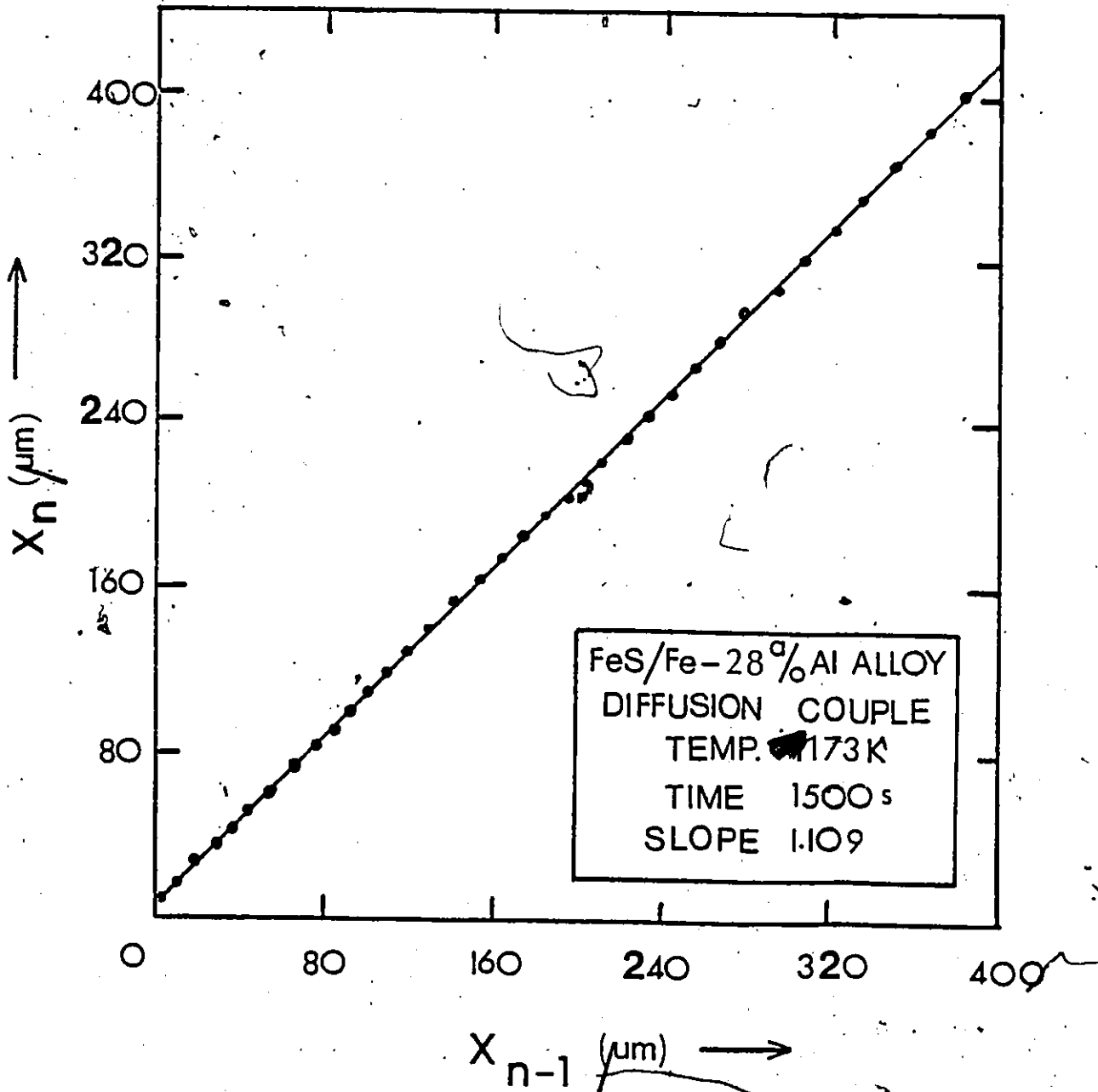


Fig. 5.8(d) Plot of X_n vs. X_{n-1} for FeS/Fe-28Al alloy diffusion couple.

Table 5-6 (a)

No. of Bands	X_n (μm)	ΔSULF_n (μm)	ΔMe_n (μm)	
1	13.2	4.4	5.3	
2	22.9	4.5	3.1	FeS/ALLOY DIFFUSION
3	30.5	5.6	2.7	COUPLE
4	37.8	4.8	4.2	ALLOY: Fe-6Al
5	46.8	5.9	4.6	TEMP.: 1173K
6	57.3	7.5	3.9	ANNEALING TIME: 1500 s
7	68.7	7.6	5.8	Mean $\Delta\text{Me}_n = 4.05 \mu\text{m}$
8	82.1	7.8	5.1	Standard deviation = ± 0.98
9	95.0	9.2	2.9	FROM ΔSULF_n vs. X_n PLOT
10	106.1	8.8	3.4	
11	118.3	9.7	3.6	CORR. COEFF. = 0.96

Table 5-6 (b)

No. of Bands	X_n (μm)	ΔSULF_n (μm)	ΔMe_n (μm)	
1	11.8	3.9	2.2	FeS/ALLOY DIFFUSION
2	17.9	2.9	3.8	COUPLE
3	24.6	3.8	2.4	ALLOY: Fe-9Al
4	30.8	2.7	3.0	TEMP.: 1173K
5	36.5	3.7	4.5	ANNEALING TIME: 1500 s
6	47.7	7.5	3.3	Mean $\Delta\text{Me}_n = 3.85 \mu\text{m}$
7	57.5	6.9	2.5	Standard deviation = ± 1.32
8	66.9	6.7	5.3	
9	79.9	9.4	5.6	FROM ΔSULF_n vs. X_n PLOT
10	94.2	10.2	5.9	
				CORR. COEFF. = 0.92

Table 5-6. Tabulation of X_n , ΔSULF_n and ΔMe_n for FeS/Fe-6Al (a) and FeS/Fe-9Al (b) diffusion couples.

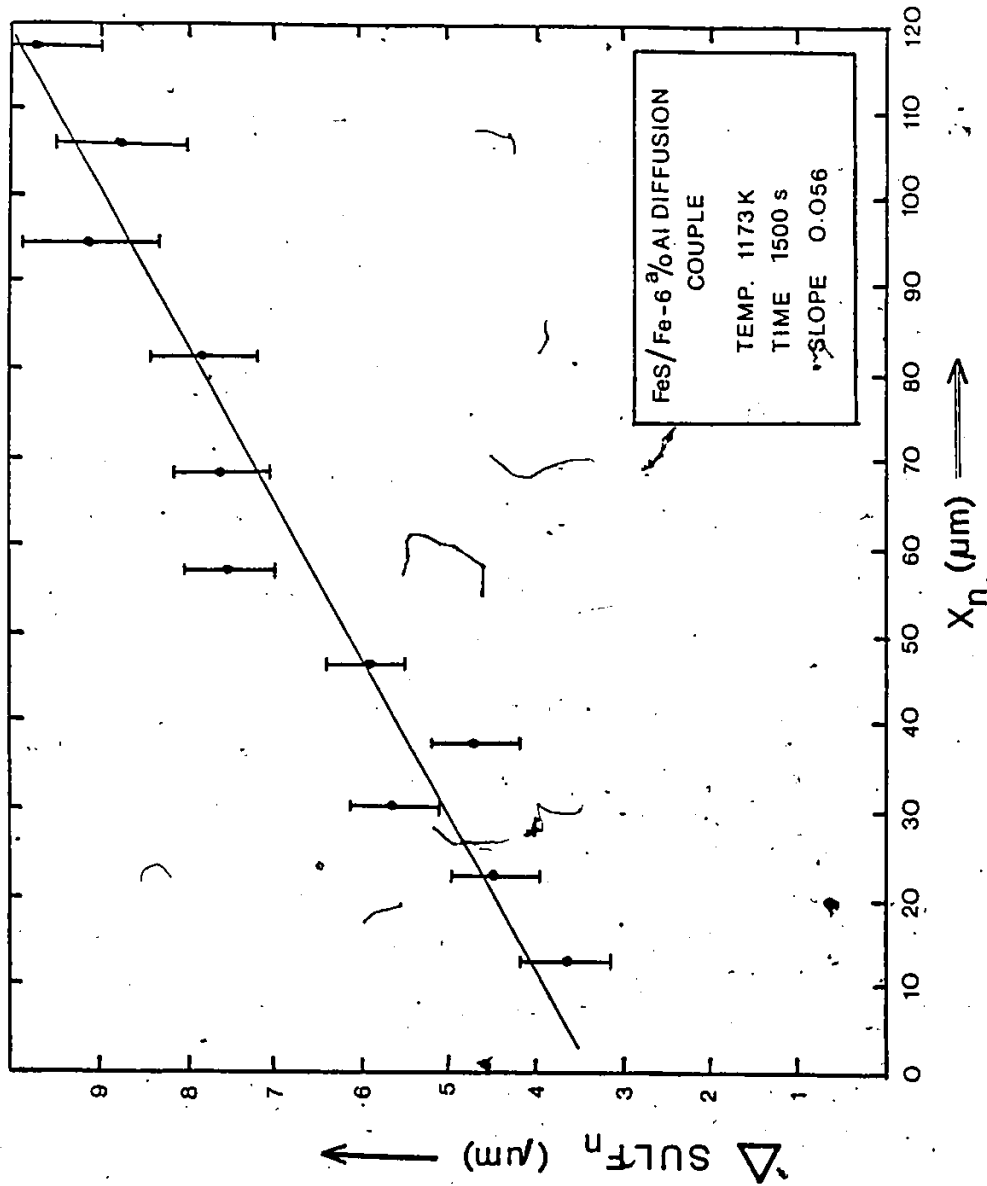


Table 5.9(a). Plot of sulfide thickness ΔSULF_n vs. depth X_n for FeS/Fe-6Al alloy diffusion couple.

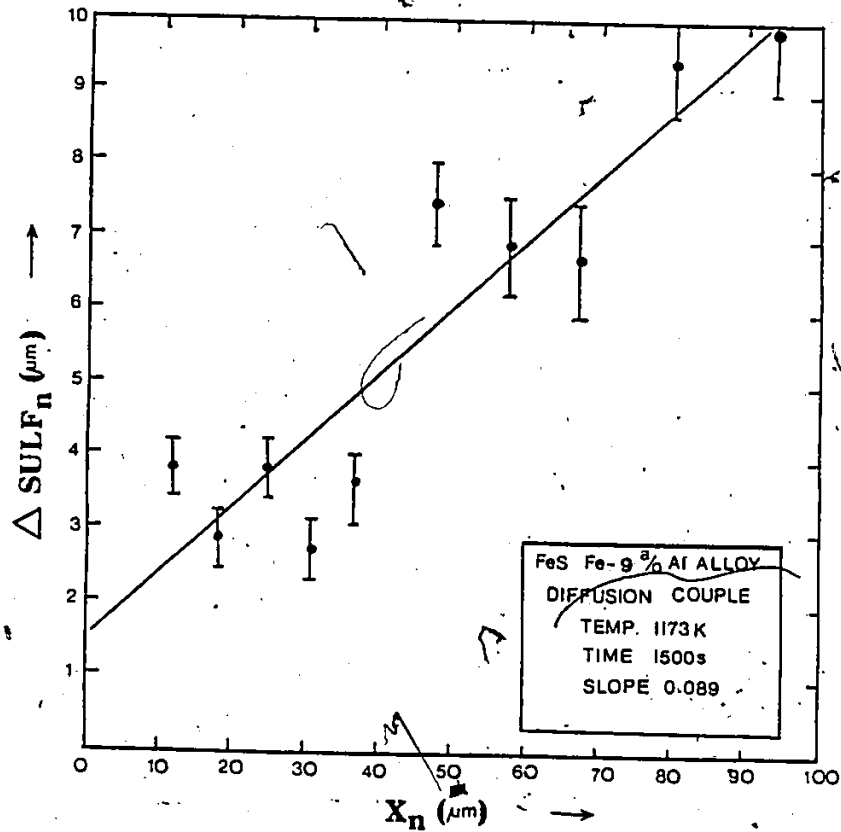


Fig. 5.9(b) Plot of sulfide thickness ΔSULF_n vs. depth X_n for FeS/Fe-9Al alloy diffusion couple.

No. of Bands	X_n (μm)	ΔSULF_n (μm)	ΔMe_n (μm)	No. of Bands	X_n (μm)	ΔSULF_n (μm)	ΔMe_n (μm)
1	9.2	3.8	2.4	27	182.7	3.8	4.9
2	15.4	3.7	4.7	28	191.4	5.6	2.6
3	24.8	4.2	5.6	29	199.6	5.7	2.5
4	34.6	5.8	4.0	30	205.8	3.8	4.4
5	40.4	2.9	2.1	31	214.0	5.6	1.5
6	45.4	3.3	3.2	32	221.1	4.8	1.1
7	51.9	4.2	3.5	33	227.7	4.2	2.7
8	59.6	4.0	2.8	34	234.6	5.8	2.9
9	64.6	2.7	3.9	35	243.3	5.8	1.9
10	71.2	2.5	1.2	36	250.9	6.2	1.5
11	74.9	1.9	4.0	37	258.6	6.3	1.6
12	80.8	2.3	6.7	38	264.5	4.8	1.9
13	90.4	4.0	5.4	39	270.2	5.6	2.5
14	99.8	4.2	3.7	40	278.3	6.7	1.5
15	107.7	5.8	3.8	41	286.5	7.7	1.7
16	117.3	4.4	5.2	FeS/ALLOY DIFFUSION COUPLE ALLOY: Fe-18A1 TEMP.: 1173K ANNEALING TIME: 1500 s Mean $\Delta\text{Me}_n = 3.01 \mu\text{m}$ Standard deviation = ± 1.38 FROM ΔSULF_n vs. X_n PLOT CORR. COEFF. = 0.93			
17	126.9	4.4	3.3				
18	134.6	4.2	1.6				
19	140.4	3.1	1.8				
20	144.3	1.9	2.8				
21	149.0	2.1	3.7				
22	154.8	3.1	1.7				
23	159.6	3.7	1.2				
24	163.5	2.1	1.7				
25	167.3	2.7	3.9				
26	174.9	3.3	4.5				

Table 5-6(c) Tabulation of X_n , ΔSULF_n and ΔMe_n for FeS/Fe-18A1 diffusion couple.

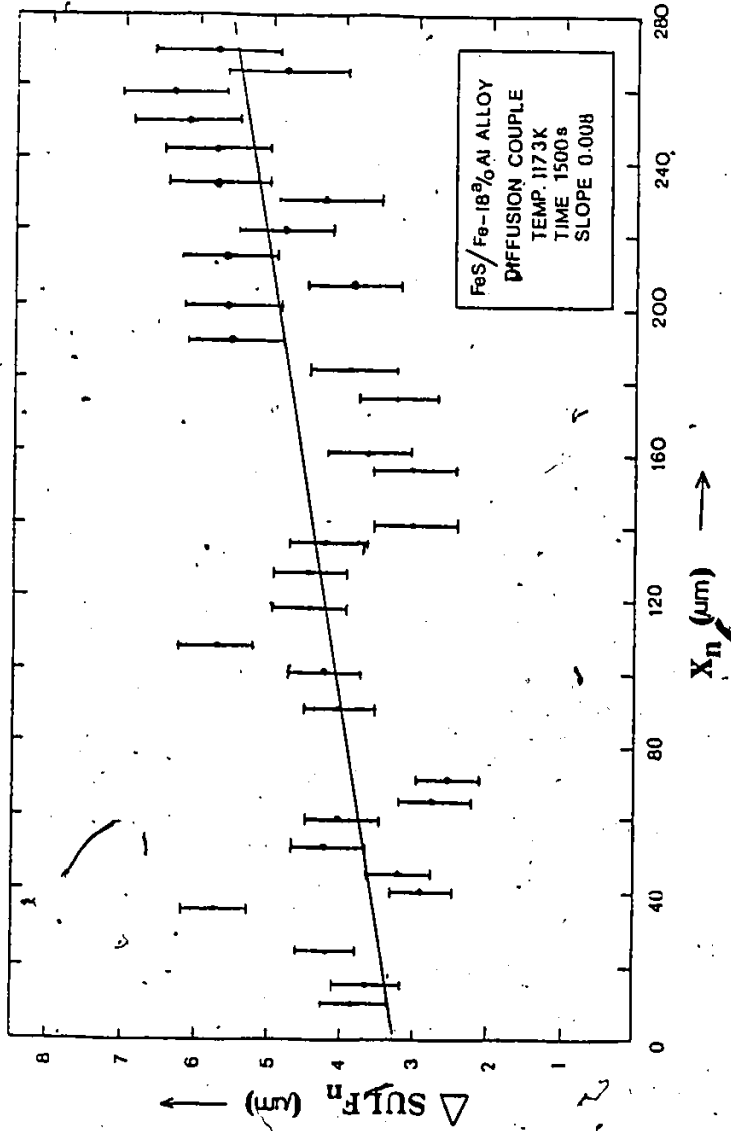


Fig. 5.9(c) Plot of sulfide thickness ΔSULF_n vs. depth X_n for FeS/Fe-18Al alloy diffusion couple.

No. of Bands	X_n (μm)	ΔSULF_n (μm)	ΔMe_n (μm)	No. of Bands	X_n (μm)	ΔSULF_n (μm)	ΔMe_n (μm)
1	10.6	3.8	3.5	27	265.8	9.6	3.4
2	17.9	3.7	6.2	28	278.8	9.8	3.1
3	28.8	6.2	2.5	29	293.7	11.3	2.2
4	36.5	5.4	1.5	30	307.2	11.5	2.0
5	43.9	3.8	5.7	31	320.7	11.7	2.8
6	53.8	5.9	4.3	32	335.2	11.7	2.8
7	64.0	6.2	3.8	33	349.7	11.9	3.4
8	74.0	7.3	1.4	34	366.0	11.4	4.8
9	82.7	4.9	3.3	35	383.4	14.6	1.9
10	90.9	5.6	3.4	36	399.9	15.5	2.1
11	99.9	5.8	3.0				
12	108.7	7.7	2.8				
13	119.2	7.5	2.1				
14	128.8	7.7	3.9				
15	140.4	8.8	3.7				
16	152.9	9.6	1.0				
17	163.5	7.7	2.8				
18	174.0	6.7	2.9				
19	184.6	7.7	1.9				
20	194.2	7.7	1.7				
21	203.6	7.8	1.1				
22	211.5	7.3	2.1				
23	221.1	6.7	3.9				
24	232.7	9.2	1.4				
25	243.3	7.7	2.8				
26	253.8	9.6	2.4				

FeS/ALLOY, DIFFUSION COUPLE
 ALLOY: Fe-28A1
 TEMP.: 1173K.
 ANNEALING TIME: 1500 s

Mean $\Delta\text{Me}_n = 2.87 \mu\text{m}$
 Standard deviation = ± 1.17

FROM ΔSULF_n vs. X_n PLOT

CORR. COEFF. = 0.92

Table 5-6(d) Tabulation of X_n , ΔSULF_n and ΔMe_n for FeS/Fe-28A1 alloy diffusion couple.

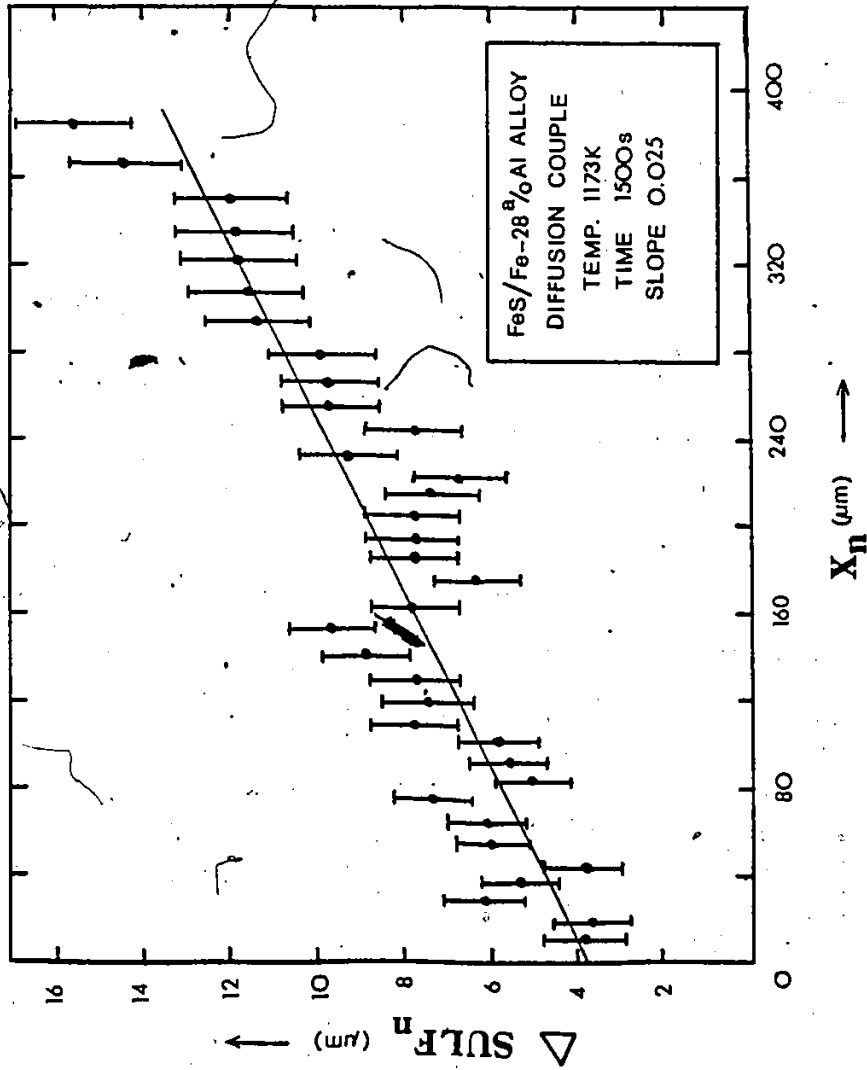


Fig. 5.9(d) Plot of sulfide thickness ΔSULF_n vs. depth X_n for FeS/Fe-28Al alloy diffusion couple.

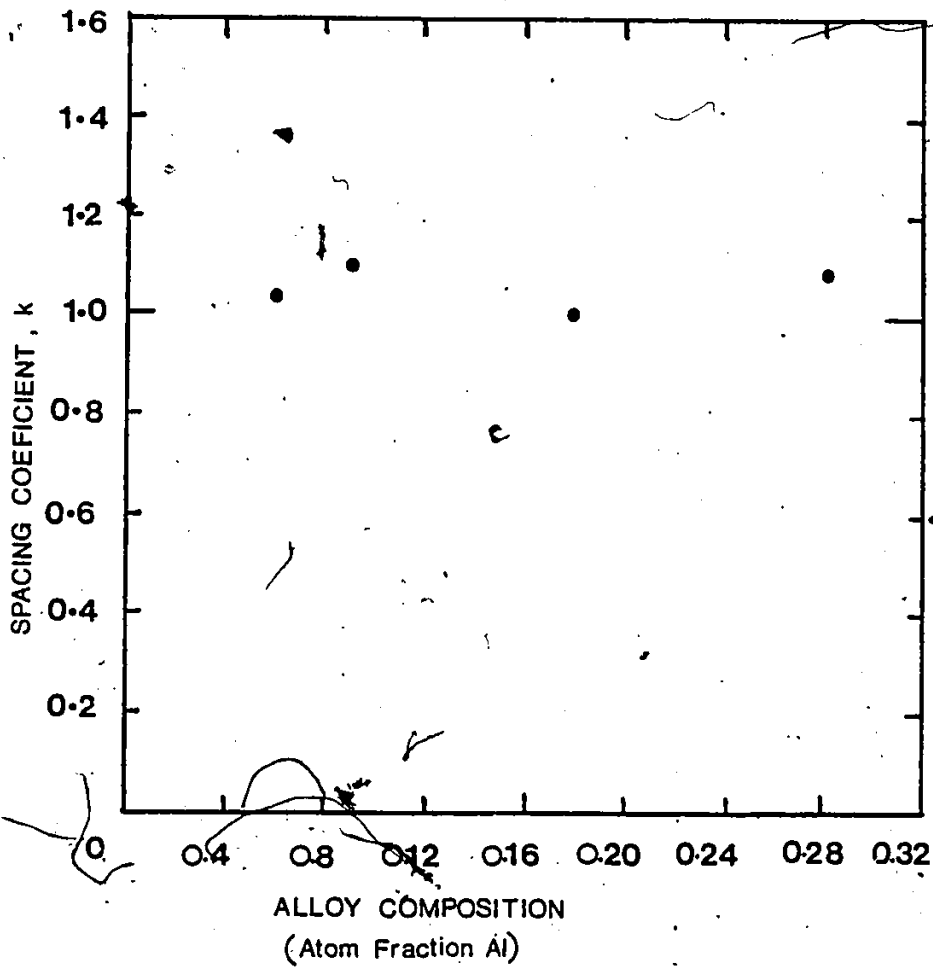


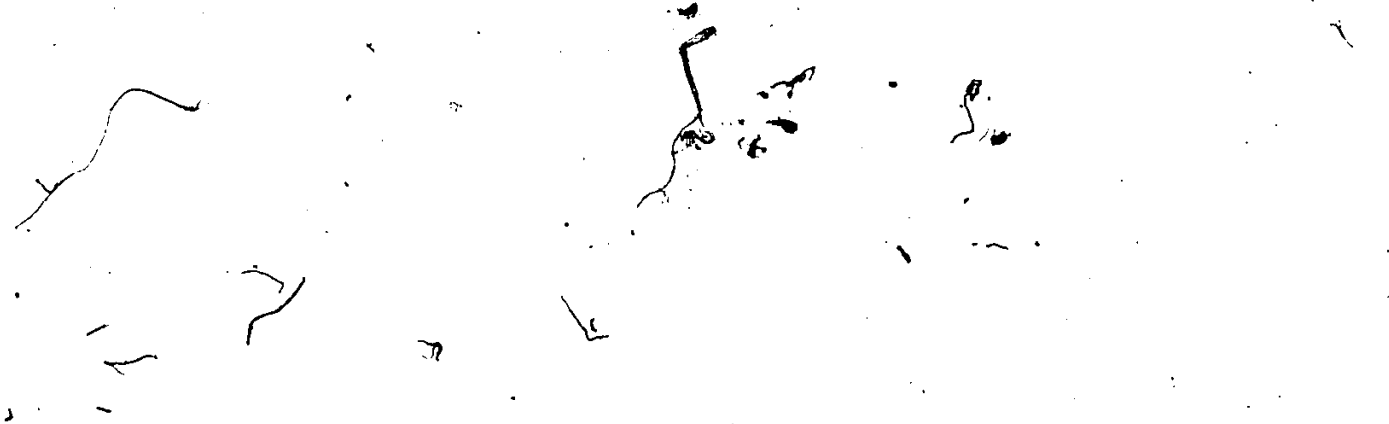
Fig. 5.10 Plot of spacing coefficient k as a function of alloy aluminum content.


Experimental Parameters	Alloy Composition			
	Fe-6 a/o Al	Fe-9 a/o Al	Fe-18 a/o Al	Fe-28 a/o Al
Annealing time seconds	1500	1500	1500	1500
Average number of sulfide bands	10	12	36	43
Spacing Coeff. $k_n = \frac{X_n}{X_{n-1}}$	1.044	1.106	1.008	1.109
Correlation coeff. of X_n vs. X_{n-1}	0.999	0.998	0.999	0.999
Slope of ΔSULF_n vs. X_n	0.056	0.089	0.008	0.025
Average metal band thicknesses (μm) and their standard dev.	4.05 $\sigma = \pm 0.98$	3.85 $\sigma = \pm 1.32$	3.0 $\sigma = \pm 1.38$	2.87 $\sigma = \pm 1.17$
ΔSULF_n (maximum) in μm	9.2 ± 0.5	10.6 ± 0.8	12.4 ± 1.0	15.1 ± 1.1
Average Penetration Depth in μm	167	232	287	391
Rate Constant $X_n/t^{1/2}$ in $\mu\text{m}/\text{s}^{1/2}$	4.2 ± 0.2	6.0 ± 0.3	7.4 ± 0.3	10 ± 0.2

Table 5-7. Tabulation of experimental results for FeS/Fe-6,7,18 and 28 Al alloy diffusion couples.

Each sulfide band of these diffusion couples consists of two phases, FeS and FeAl_2S_4 (grey and dark colorations, respectively, under optical microscope). This is evident from the micrographs shown in Figs. 5-11(a) and (b). Generally, the FeAl_2S_4 particles tend to be randomly distributed in the FeS phases, but at some positions they appear as semi-continuous lateral array of precipitates.

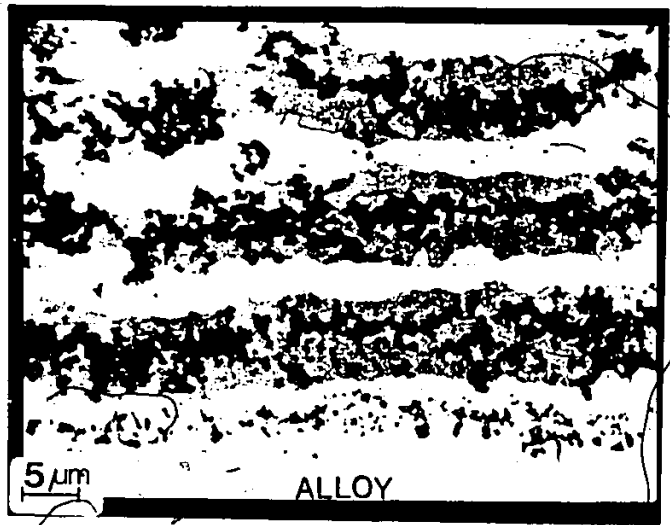
Figure 5.12 shows micrographs of a FeS/Fe-6Al diffusion couple, sectioned parallel (Fig. 5.12(a)) and normal (Fig. 5.12(b)) to the alloy surface. Continuous networks of the metallic bands are depicted in Fig. 5.12(a). A general distribution of FeAl_2S_4 precipitates in the FeS phase of the sulfide bands is also evident. The micrograph in Fig. 5.12(b) also illustrates that the average thicknesses of sulfide bands increased with depths whereas on an average the metallic band thicknesses remained the same. It is clear from the micrographs of Fig. 5.11(a) and (b) depicting the last sulfide band and the alloy substrate within its vicinity that the sulfide is initially precipitated by a mode of internal sulfidation. Also, the metal bands tend to become more discontinuous at distances extending outward from the innermost sulfide interface. The metal actually appears as discrete particles in the sulfide matrix at $x=0$ as very close to the FeS-Fe reaction pellet interface (Fig. 5.4).

- 
- The top half of the page contains several hand-drawn sketches. On the left, there are two wavy, irregular lines. In the center, there is a more complex sketch showing a vertical line with several horizontal and diagonal branches extending from it. To the right, there is a simple loop-like shape. These sketches appear to be preliminary drawings or annotations related to the figures described in the text.
- Fig. 5.11 a) Optical photomicrograph showing the cross-section of the sulfidation zone in the FeS/Fe-6Al alloy diffusion couple.
- b) Optical photomicrograph of the cross-section of the alloy sulfidation zone in the FeS/Fe-9Al diffusion couple.

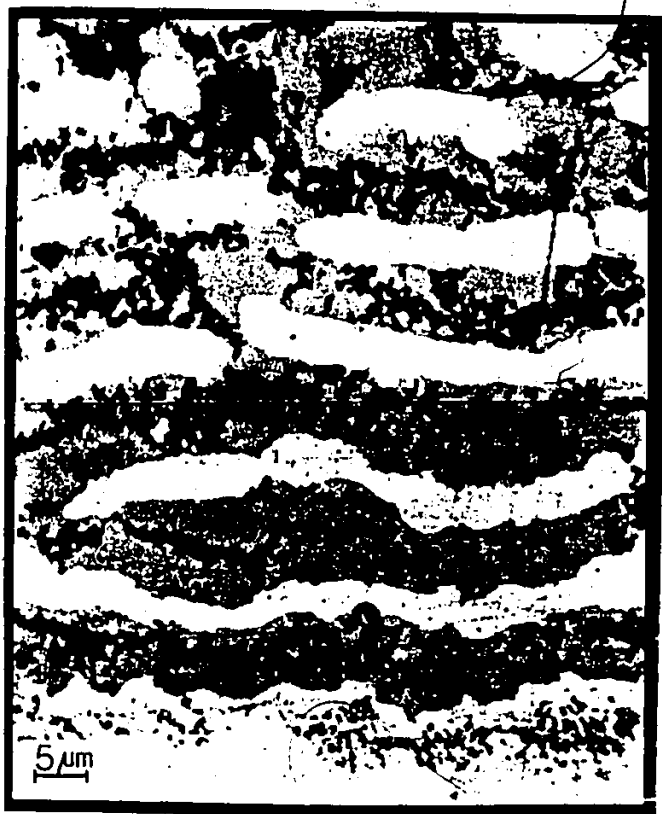


The bottom left of the page features a hand-drawn sketch of a wavy, irregular line, similar to the ones in the top left. This sketch is likely related to the figure described in the text below.

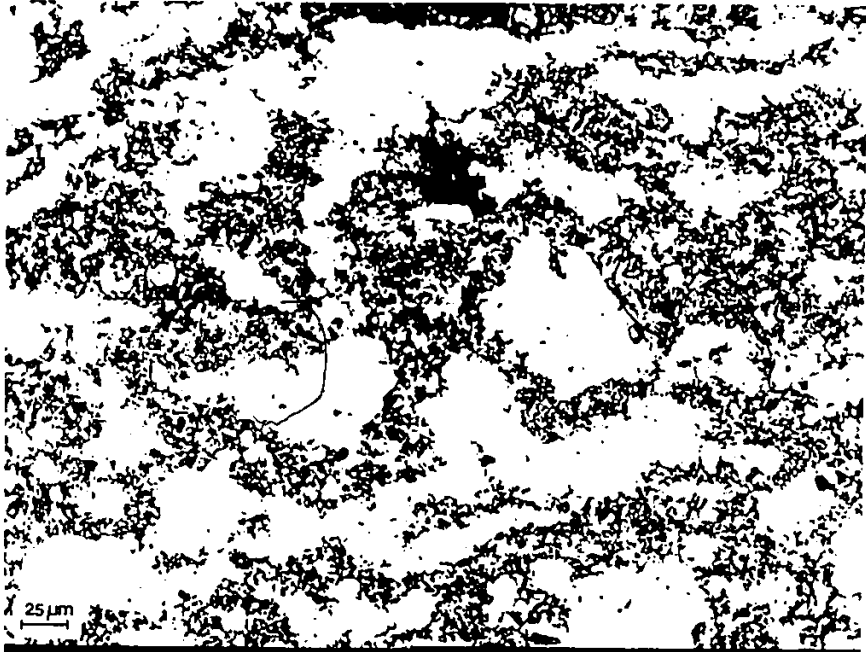
Fig. 5.12 Optical photomicrograph of the alloy sulfidation zone in the FeS/Fe-6 Al diffusion couple, sectioned a) parallel and b) normal to the alloy surface.



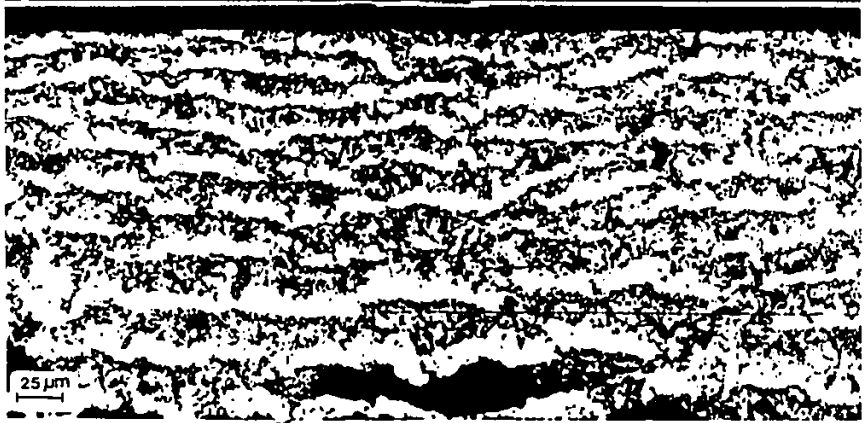
a.



b.



(a)



(b)

5.3 SULFIDATION OF Fe-Al ALLOYS IN SULFUR VAPOUR AT DISSOCIATION PRESSURE OF FeS

Fe-Al alloys containing 6, 9, 18 and 28 a/o Al were sulfidized in S_2 vapour at the dissociation pressure of FeS. The experimental assembly has been described in section 4.4. The reason for using such an assembly was to avoid the formation of FeS during the sulfidation of these alloys. Sulfidized alloys were prepared for metallographic examination. Alloys containing 6 a/o aluminum sulfidized internally, whereas Fe-9Al and Fe-18Al alloys sulfidized both internally and externally. The alloy containing 28 a/o Al when sulfidized at 1173K, only yielded an external scale.

5.3.1 Sulfidation Kinetics

Sulfidation kinetics of Fe-6, 9 and 18Al at 1173K were determined by measuring the depths of uniform internal sulfidation zones as well as the sulfur uptake. Figure 5.13 shows the depths of internal sulfidation, measured from the external surface, as a function of time for various Fe-Al alloys (Table 5-8). The standard errors are indicated by the size of each data point in the Figs. 5.13 and 5.14. The linear plots obtained by a regression analysis correspond to parabolic reaction kinetics. A significant point in this figure, is that the depths of internal sulfidation in the alloys after corresponding exposures decreased with aluminum content up to 9 a/o Al. The alloy containing 18 Al exhibited the largest penetration depth of internal sulfidation. This is also indicated in Table (5-8)

Table 5-8
Kinetic results for Fe-Al alloy sulfidation in S_2 (Fe/FeS)

Alloy Composition	Time of Reaction (seconds)	Thickness of I.S. zone (μm)	Parabolic Rate Constants k_p ($\mu\text{m}/\text{s}^2$)
Fe-6 a/o Al	7200	602.6	7.35
	14400	881.6	
	21600	1080.2	
Fe-9 a/o Al	3600	416.7	5.09
	7200	605.2	
	21600	752.1	
Fe-18 a/o Al	3600	507.1	8.45
	7200	715.8	
	9000	814.6	

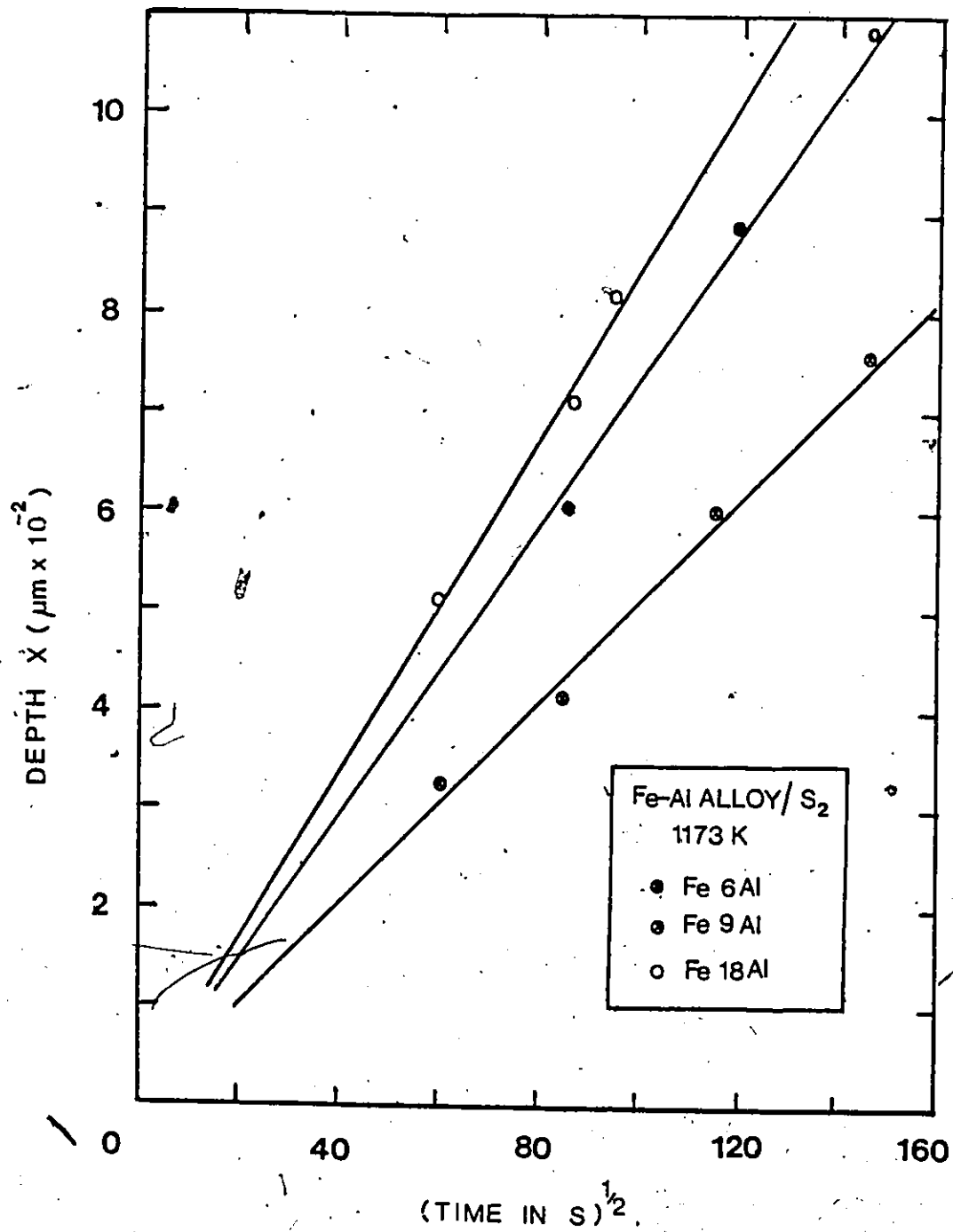


Fig. 5.13 Parabolic plots of internal sulfidation depth vs. time for Fe-6, 9 and 18 Al alloys in S_2 vapour at the dissociation pressure of FeS .

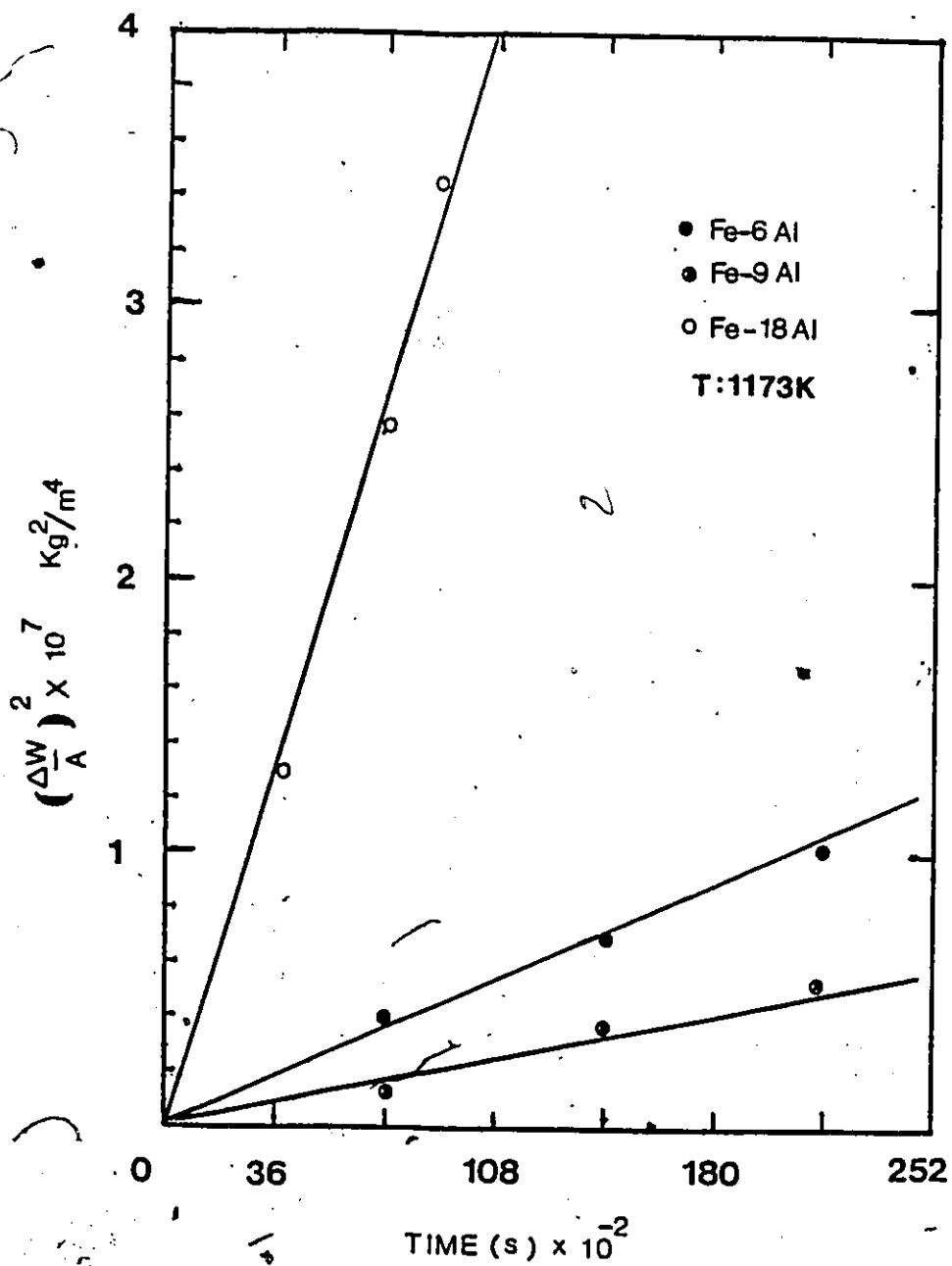


Fig. 5.14 Parabolic plots of weight gain vs. time for Fe-6, 9 and 18 Al alloys in S_2 vapour at the dissociation pressure of FeS .

by the corresponding parabolic rate constants obtained from Fig. 5.13. Parabolic fit has also been obtained for the sulfur uptake as a function of time for these alloys as shown in Fig. 5.14. An external scale on the Fe-9 Al alloy was only observed at isolated small areas over the alloy surface for sulfidation times up to 2.16×10^4 seconds. The external scale on the Fe-18 Al alloy which sulfidized both internally and externally was continuous and it grew at the rate of $8.9 \times 10^{-2} \text{ } \mu\text{m/s}^{1/2}$.

5.3.2 Scale Morphological Development

The internal sulfide precipitates formed in the Fe-6, 9 and 18 Al alloys were acicular in morphology. These acicular precipitates were largely oriented to the surface of the alloy with exceptions of some alloy grains in which they were oriented at an angle less than 90° to the alloy surface. Figures 5.15(a), (b), (c) and 5.16(a), (b) illustrate these features. The advancing front of an internal sulfidation zone was quite uniform, although slight irregularities were found occasionally at the corners of the specimens. No intergranular sulfidation was observed in any of the three alloys exposed at 1173K.

Figures 5.17(a), (b) and (c) show transverse sections of the internal sulfides at various depths from the surface of the alloy containing 9 a/o Al. Section (b) is closer to the external surface whereas sections (a) and (c) are closer to the internal sulfidation front/alloy interface. As illustrated in the transverse sections (a) and (b), the sulfides exhibit a

Fig. 5.15 Optical photomicrographs of the cross-section of internal sulfidation zones of (b,c) Fe-6 Al and (a) Fe-9 Al alloys in S_2 vapour.

Fig. 5.16 Optical photomicrographs of the cross-section of internal sulfidation zone for Fe-18 Al alloy in S_2 vapour.

Fig. 5.17 Optical photomicrographs of Fe-9 Al alloy showing the morphology of internal sulfide precipitates at various depths taken in cross-section. Sections (a) and (c) are closer to alloy/internal sulfidation front whereas section (b) is closer to the external surface.

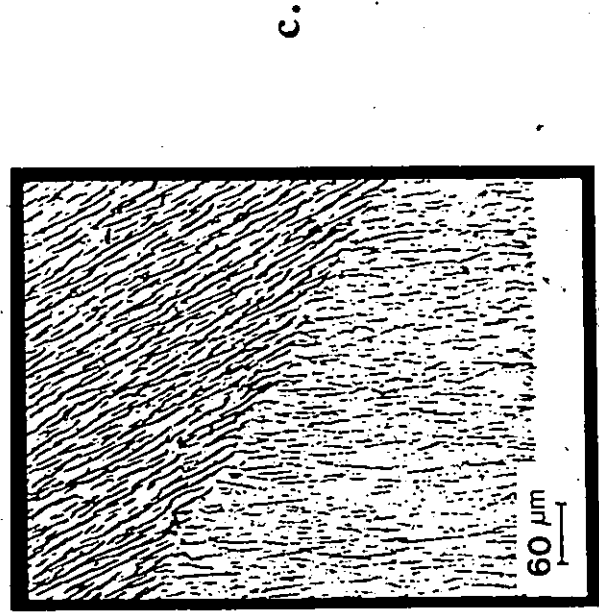
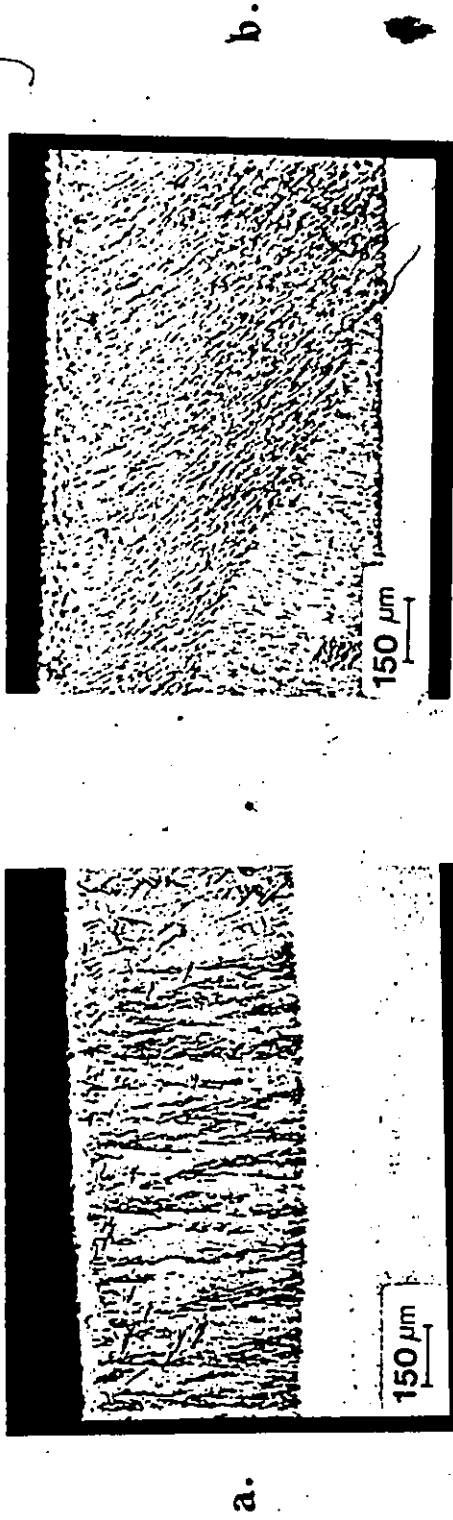
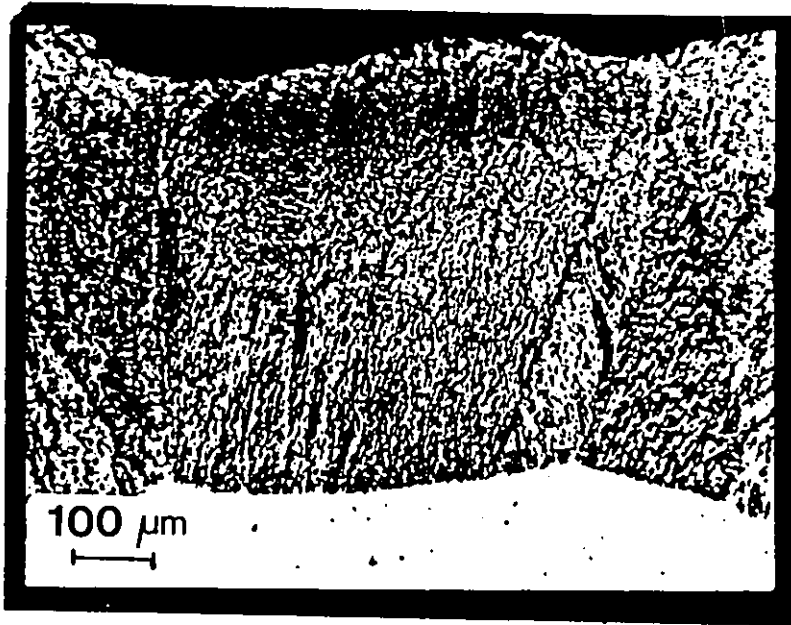


Fig. 5.15 a. Fe-9%Al/S₂

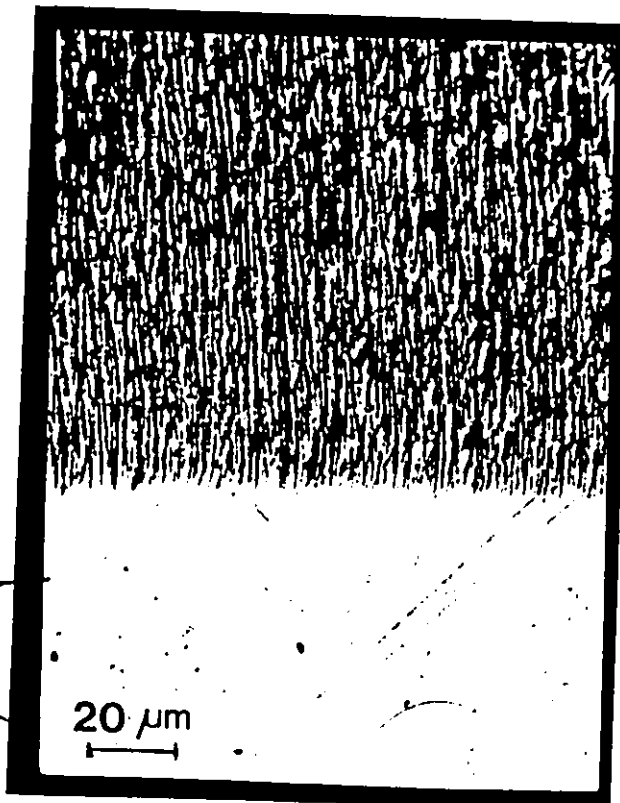
b.} Fe-6%Al/S₂

c.} Temp.: 1173K

Fig. 5.16



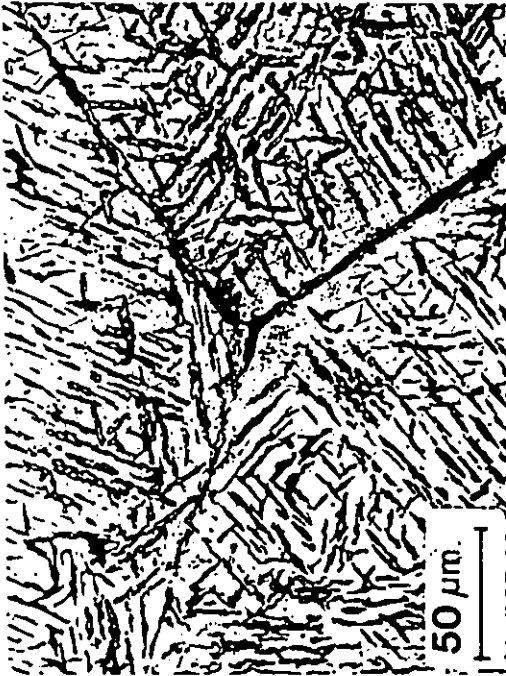
a.



b.

Fig. 5.17

a.



c.



b.

platelet morphology oriented in several crystallographic directions. Furthermore, sulfides existing deeper into the alloy near the advancing front appear to contain more than one phase, one enveloping the other (sections (a) and (c)). The sulfide precipitates exhibit thicknesses ranging from 0.5 to 2 μm , widths ranging from 10 to 20 μm and lengths several hundred microns. In all the alloys, the platelike internal sulfide precipitates extended either from right below the gas/alloy interface, or from the external scale/subscale interface (Fig. 5.18).

The center to center spacings of internal sulfides were measured for various alloys. It is evident from Figs. 5.19(a), (b) and (c) for alloys containing 6, 9 and 18 a/o Al, that the inter-lamellar spacing between the platelets decreases with increasing aluminum content in the alloy. Table 5-9 presents the variation of this spacing with alloy composition. Measurements of inter-lamellar spacings were performed at various depths in the internal sulfidation zone for each alloy. Accordingly the spacing values presented in Table 5-9 are averages of several measurements. Sulfide platelets in Fe-6 Al alloys were thicker than those in the Fe-9 and 18 Al alloys. The thickness of these sulfide platelets, moreover, varied slightly in different grains of a given alloy.

Fig. 5.18 Optical photomicrographs showing the cross-section of the internal sulfidation zone near the alloy and external scale/alloy interfaces for a) Fe-6 Al, b) Fe-9 Al and c) Fe-18 Al alloys sulfidized in S_2 vapour.

Fig. 5.19 Optical photomicrographs revealing the cross-section of internal sulfide precipitates and their spacings for a) Fe-6 Al, b) Fe-9 Al and c) Fe-18 Al alloys sulfidized in S_2 vapour.

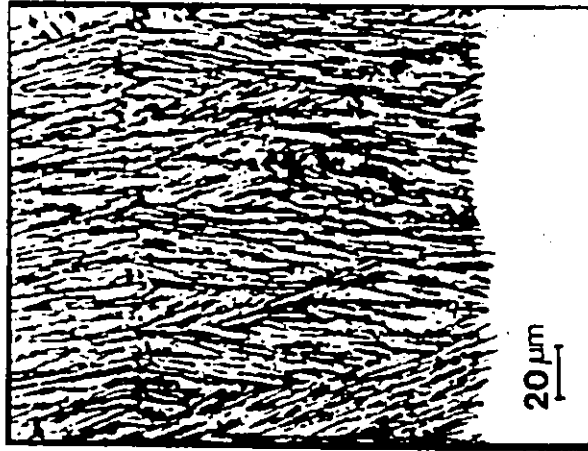
b.



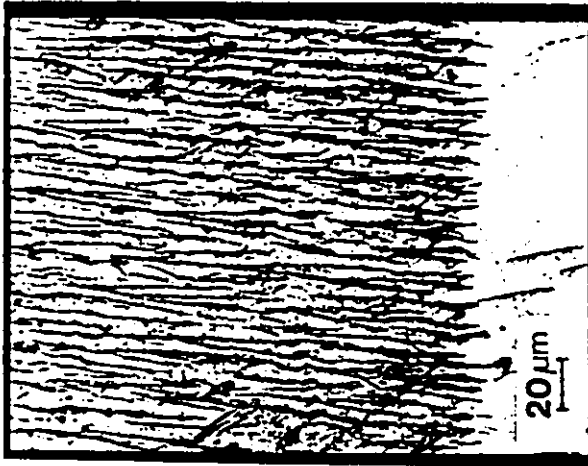
c.



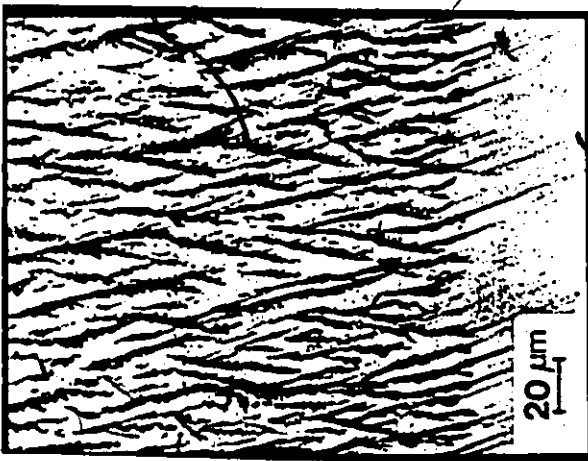
a.



c.



b.



a.

Table 5-9

Inter sulfide spacings for Fe-6, 9 and 18 Al alloys

Alloy Composition	Time of Sulfidation(s)	Spacing μm
Fe-6 Al	14400	7.9 \pm 0.5
Fe-9 Al	14400	3.8 \pm 0.6
Fe-18 Al	14400	2.6 \pm 0.5

5.3.3 External Scale Formation on the Fe-28 Al Alloy

An external scale without any associated internal sulfidation were observed to grow on the Fe-28 Al alloy. A scale was compact and adherent at the reaction temperature but it spalled off the alloy during cooling of the quartz capsules. Figure 5.20 shows a photomicrograph of the external scale identified as Al_2S_3 . The separation of this scale from the alloy substrate is evident in this micrograph. This scale grew at a rate of $7.2 \times 10^{-2} \mu\text{m}/\text{s}^{1/2}$. Since Al_2S_3 is very reactive to atmospheric moisture, precautions were taken to protect the specimens from moisture particularly during handling for various analyses.

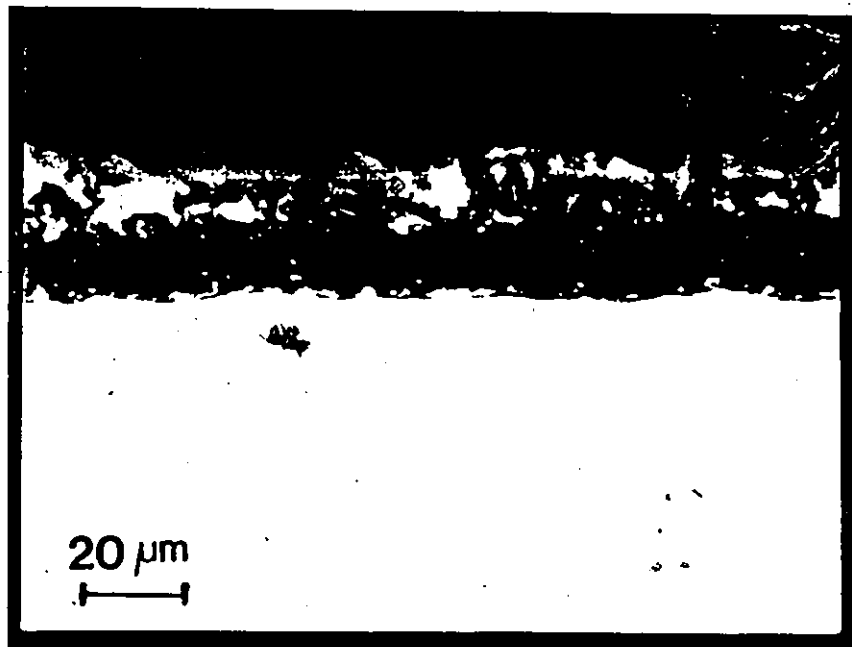


Fig. 5.20 Optical photomicrograph of the cross-section of the only sulfide scale (Al_2S_3) formed on Fe-28 Al alloys in S_2 vapour.

5.4 SULFIDATION PROPERTIES OF Fe-Al ALLOYS IN H₂S-H₂ ATMOSPHERES

Fe-Al alloys containing 9 and 18 a/o Al were sulfidized at various sulfur pressures using H₂S-H₂ atmospheres at a total pressure of 10⁵ Pa. A detailed investigation was carried out on the sulfidation properties of the Fe-18 Al alloys at 1173K and sulfur pressures ranging from 1 to 10³ Pa. A weight gain by the sample was not detected within the minimum limits of measurement in atmospheres at and lower than $P_{S_2} = 10^{-1}$ Pa for exposures up to 18 hours.

5.4.1 Sulfidation Kinetics

The sulfidation kinetics of Fe-9 and 18 Al were determined thermo-gravimetrically using a McBain balance described earlier in chapter 4. The results, weight gain per unit area of the specimen vs. sulfidation time, are shown in Fig. 5.21 for $10^3 \geq P_{S_2} \geq 1$ Pa. The alloy containing 9 a/o Al was exposed at $P_{S_2} = 10^{-1}$ Pa. The kinetic results are presented according to parabolic co-ordinates in Fig. 5.22. From these plots, one concludes that the kinetic curves for the Fe-18 Al at sulfur pressures of 10² Pa and 10 Pa, consist of three distinct regions. Following a brief initial period (2000 seconds), the kinetic curves represent two different rates given by k_1 , k_2 and k'_1 , k'_2 respectively. The transition from one rate to the other took place at shorter times at higher sulfur pressure. The distinct sections of the reaction curves represented by limiting tangents when the sulfidation kinetics are plotted

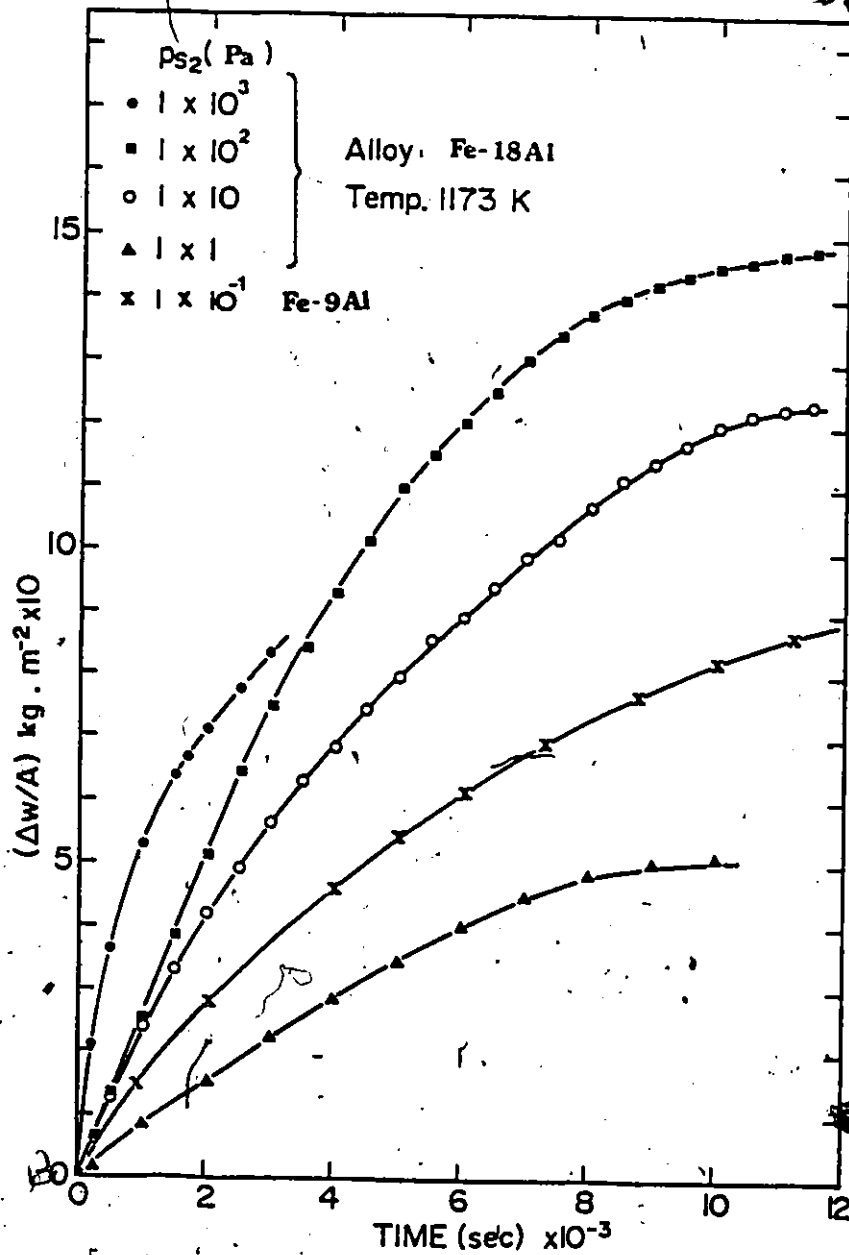


Fig. 5.21 Linear plots of sulfidation kinetics of Fe-Al alloys in H_2S-H_2 atmospheres.

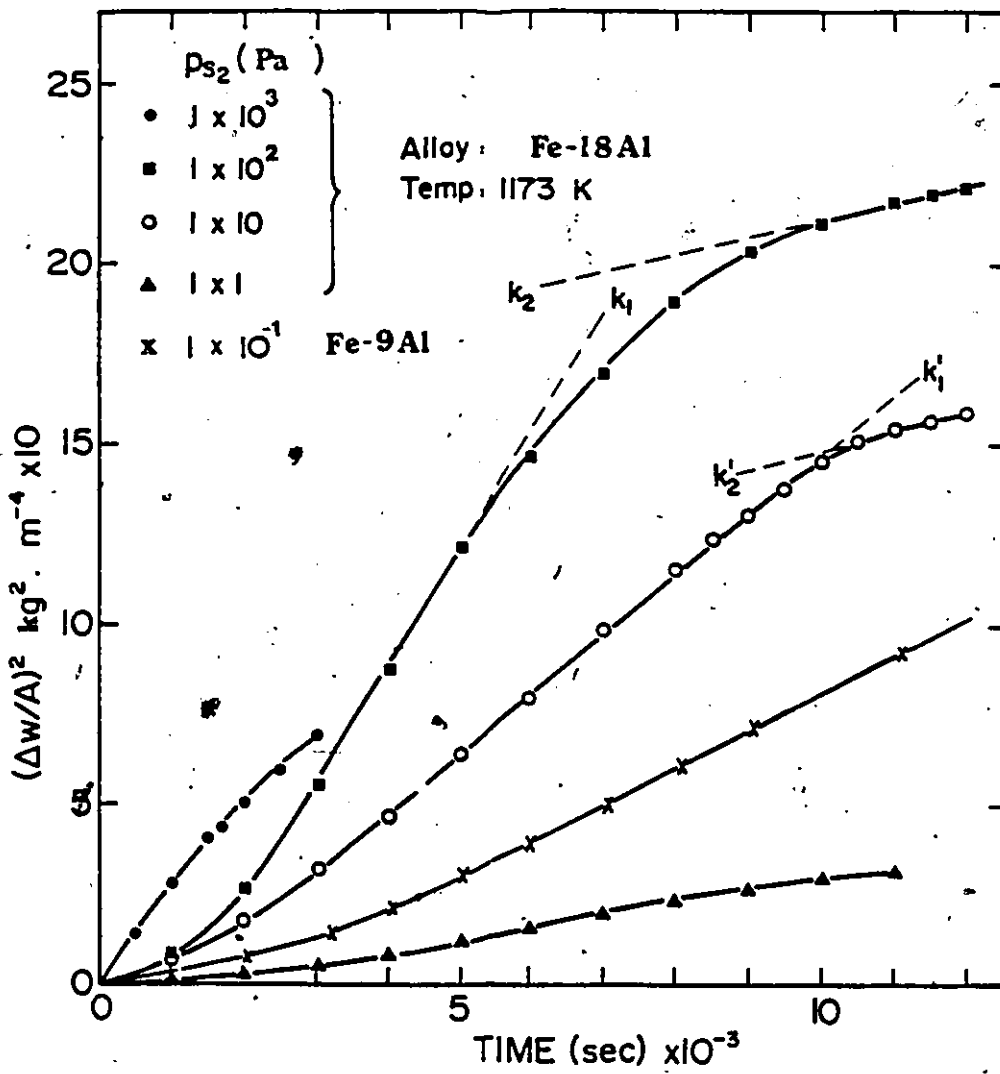


Fig. 5.22 Parabolic plot of sulfidation kinetics of Fe-Al alloys in H_2S-H_2 atmospheres.

in parabolic coordinates are described as representing parabolic rates. The rate constants determined from the slopes of these tangents are designated as parabolic reaction rate constants (Table 5-10).

In summary, the sulfidation kinetics of the Fe-Al alloys are complex. In the H_2S-H_2 atmospheres at $P_{S_2} = 10^2$ Pa and 10 Pa, the parabolic rate constants k_2 for the Fe-18 Al alloy were of similar magnitude and an order of magnitude less than the parabolic rate constants k_1 (Table 5-10). Decreasing sulfur pressure led to lower alloy sulfidation rates. At $P_{S_2} = 10^{-1}$ Pa, the Fe-9 Al alloy sulfidized parabolically but sulfidation of the Fe-18 Al alloy could not be detected within the sensitivity of the McBain balance.

5.4.2 Sulfide Morphological Development

The reaction product layers formed on the Fe-9 Al alloy at $P_{S_2} = 10^{-1}$ Pa are shown in cross-section in Fig. 5.23(a), (b) and (c). The micrographs illustrate three distinct regions. The external scale is comprised of two regions: an outer layer composed of a single bright sulfide phase (region 1) and an inner layer composed of two sulfides existing as alternate bright and dark phases (region 2). The internal sulfidation zone (region 3) is composed of a dark sulfide phase extending into the alloy substrate. Needle or platelet type of sulfide precipitates is observed in region 3. Figure 5-24(a) shows an optical photomicrograph of the scale on the Fe-18 Al alloy at $P_{S_2} = 10^3$ Pa and Fig. 5.24(b) shows a scanning electron micro-

Table 5-10

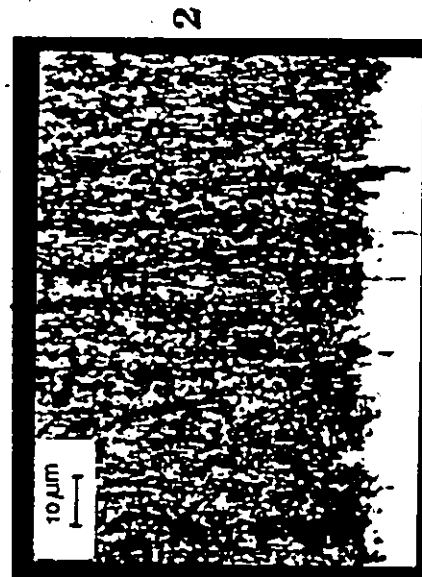
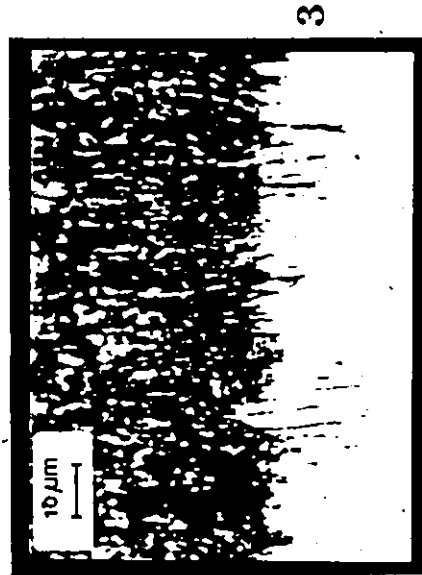
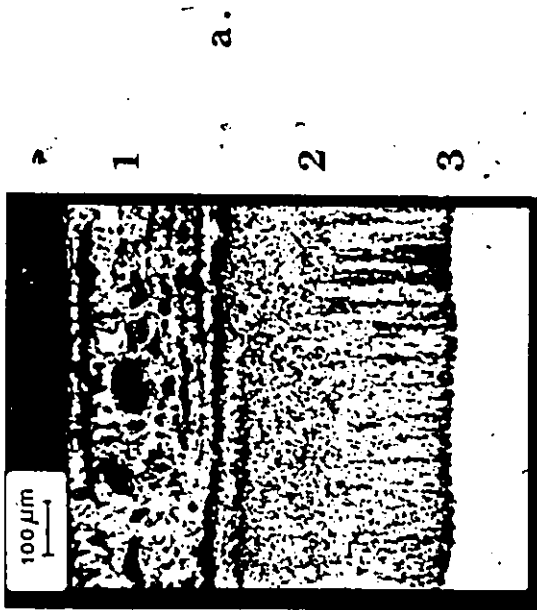
Parabolic reaction rate constants for Fe-Al alloys
and their comparison with pure iron at 1173K

Alloy	P_{S_2} in Pa	k_1^*	k_2^*	k_p^*	Ref.
Pure Fe	36			2.3×10^{-4}	140.
Pure Fe	6.3			1.9×10^{-4}	140.
Fe-9 Al	10^{-1}			8.9×10^{-5}	This work.
Fe-18 Al	1			2.9×10^{-5}	This work
	10	1.6×10^{-4}	4.9×10^{-5}		This work
	10^2	3.3×10^{-4}	4.9×10^{-5}		This work
	10^3			2.4×10^{-4}	This work

* in $\text{kg}^2 \text{m}^{-4} \text{s}^{-1}$.

Fig. 5.23 Optical photomicrographs of the scale and sub-scale regions of Fe-9 Al alloy sulfidized in H_2S-H_2 atmospheres at $p_{S_2} = 10^{-1}$ Pa.

Fig. 5.24 a) Optical photomicrograph of the scale cross-section on the Fe-18 Al alloy at $p_{S_2} = 10^3$ Pa.
b) SEM micrograph of the outer surface of the scale formed at $p_{S_2} = 10^2$ Pa on the Fe-18 Al alloy.



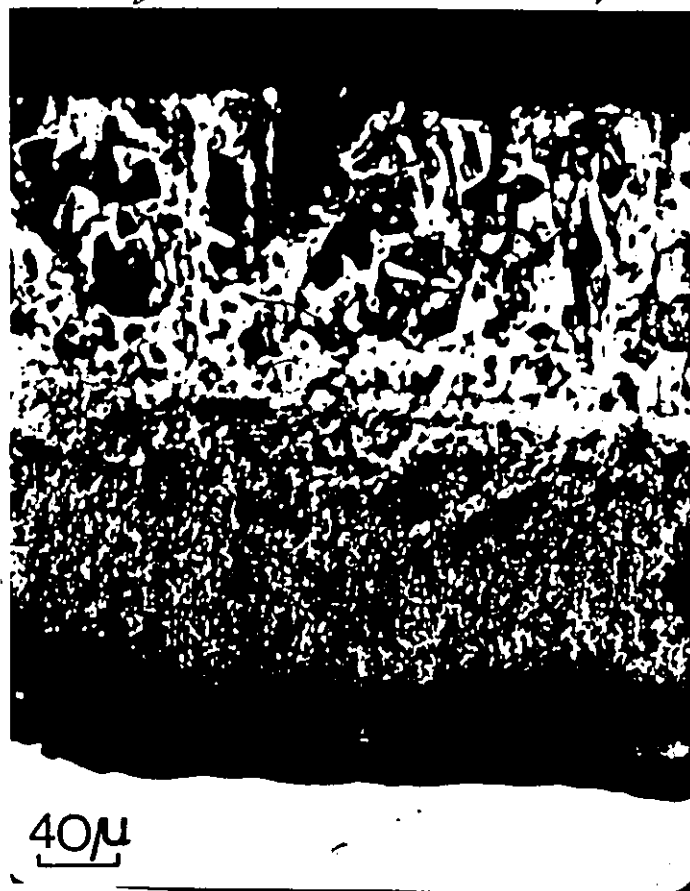
b.

c.

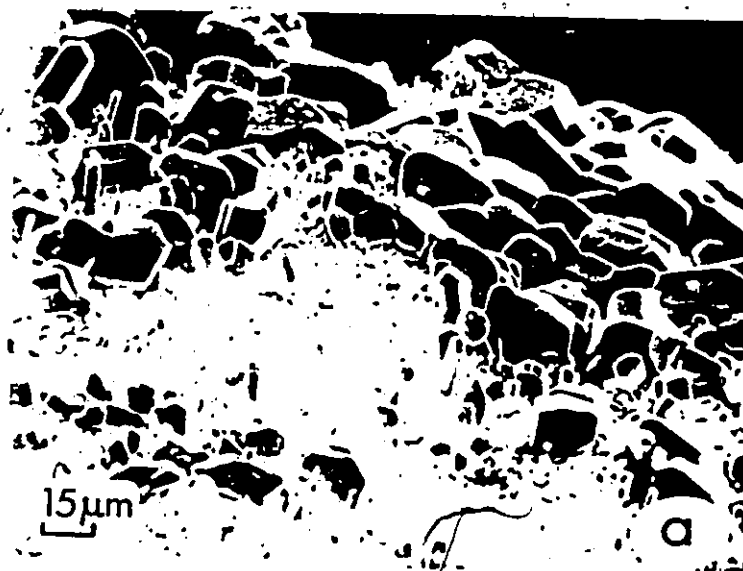
3

2

a.



b.



graph of the outer surface of the scale formed at $p_{S_2} = 10^2$ Pa. Regions, 1, 2 and 3 will be shown subsequently to contain FeS, FeS+FeAl₂S₄ and FeAl₂S₄+Al₂S₃, respectively.

In order to study the corrosion mechanism, the Fe-18 Al alloy was subjected to different times of reaction at 1173K and $p_{S_2} = 10^2$ Pa. Optical micrographs of the scale cross-sections in Fig. 5.25(a) and (b) emphasize the interfacial region between the alloy and the inner layer of the external scale for up to 900 seconds of reaction. There are sulfide platelets extending into the alloy from the sulfides in the inner layer of the external scale. After a longer time (10800 seconds) a continuous film appeared at the advancing front of the external scale and needles or platelets of a sulfide extended from the continuous film into the alloy. A similar feature was also observed at $p_{S_2} = 10$ Pa (Fig. 5.26). It will be shown that the platelet sulfides in the inner layer are composed of FeAl₂S₄ and the small platelets extending into the alloy from the FeAl₂S₄ platelets and the continuous film region (3) are Al₂S₃.

Measurements of layer thicknesses in the external scale formed on the Fe-18 Al alloy sulfidized for various time periods at $p_{S_2} = 10^2$ Pa are shown in Fig. 5.27(a). Parabolic plots of the results given in Fig. 5.27(a) are shown in Fig. 5.27(b). These plots exhibit two stages of parabolic kinetics as observed from the weight gain measurements (Fig. 5.22).

The growth of sulfide nodules was observed on the Fe-18 Al alloy at $p_{S_2} = 10$ Pa. These nodules nucleated at isolated

Fig. 5.25 Optical photomicrographs of the scale cross-sections (a) and (b) emphasizing the interface regions between the alloy and inner layer of external scale at $p_{s_2} = 10^2$ Pa for Fe-18 Al alloy.



40μ

b. 15 Minutes



40μ

a. 5 Minutes

2

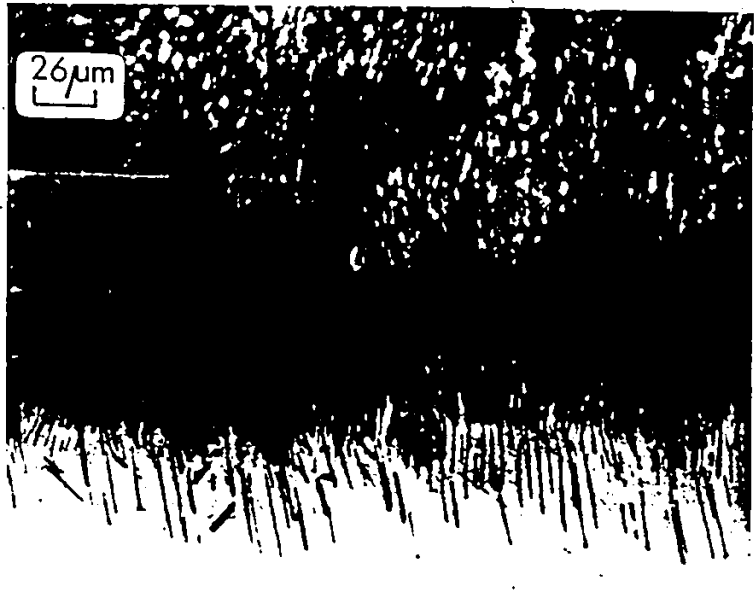


Fig. 5.26. Optical photomicrograph of the interface region between the external scale and alloy at $p_{s_2} = 10$ Pa for Fe-18 Al alloy.

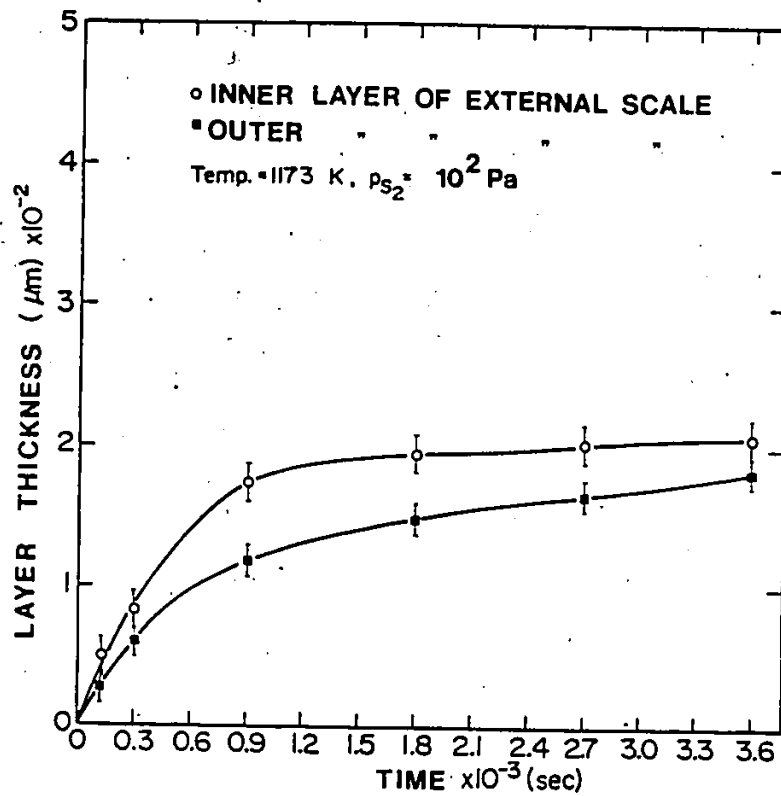


Fig. 5.27(a) Plots of sulfide layer thicknesses vs. time on the Fe-18 Al alloy sulfidized in $\text{H}_2\text{S}-\text{H}_2$ atmospheres.

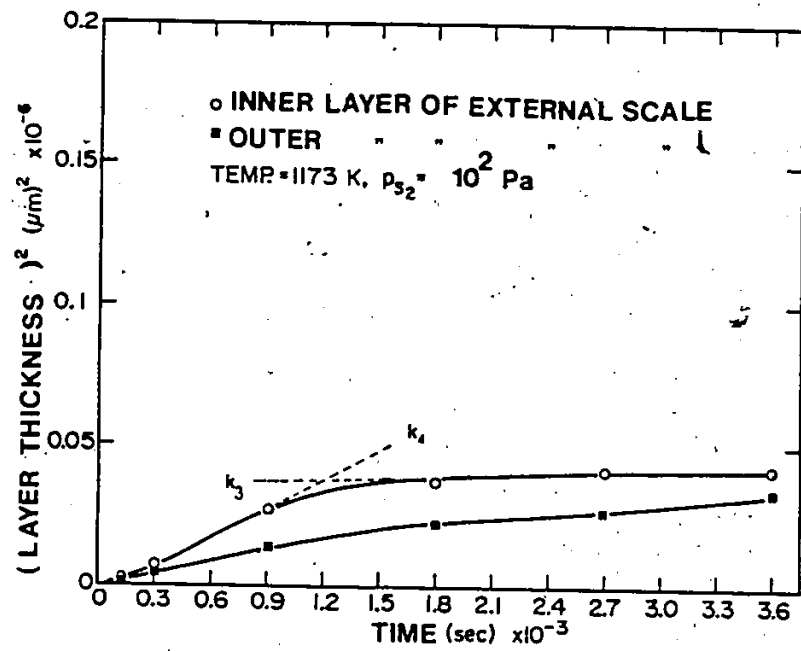


Fig. 5.27(b) Parabolic plots of sulfide layer thicknesses on the Fe-18 Al alloy sulfidized in $\text{H}_2\text{S}-\text{H}_2$ atmospheres.

sites on the alloy surface and some of these sites were located at alloy grain boundaries. Figure 5.28 represents SEM observations of the nodules. These nodules were observed to grow laterally and vertically and finally coalesce to form continuous sulfide layer as shown in Fig. 5.29.

Scale cross-sections were etched with dilute HCl acid to reveal the morphology of the inner layer for the Fe-18 Al alloy at $p_{S_2} = 10$ Pa. Figure 5.30 represents a scanning electron micrograph of the inner two-phase layer which is composed of platelet-like precipitates.

5.5 INERT MARKER MEASUREMENTS

Several platinum wire markers of 50 μ m diameter were spot welded by a Hughes VTA-60 spot welding machine on to the alloy surface prior to making a diffusion couple. These alloy samples were embedded in FeS and then compressed in the die. Such couples were annealed for 5h in evacuated quartz capsules. An optical photomicrograph of the sample taken in cross-section is shown in Fig. 5.31. The markers are seen to rest in between the FeS and the sulfidation zone. This result substantiates the preceding observations of sulfidation in that the internal sulfidation zone has formed by the inward diffusion of sulfur in the alloy.

In the experiments with H_2S-H_2 atmospheres, several platinum markers were welded to the surfaces of several alloy specimens prior to sulfidation. Figures 5.32 (a) and (b) show

Fig. 5.28 SEM observations of the nodular sulfide formation on Fe-18 Al alloys at $p_{S_2} = 10$ Pa in H_2S-H_2 atmospheres.

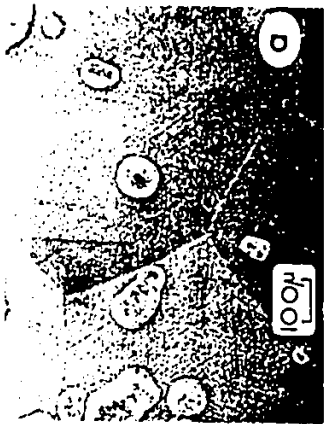
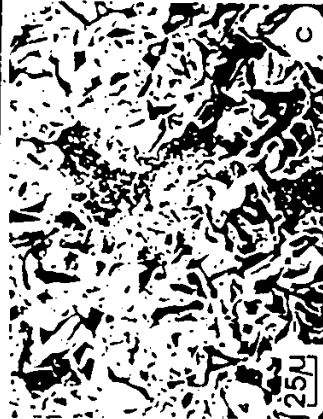
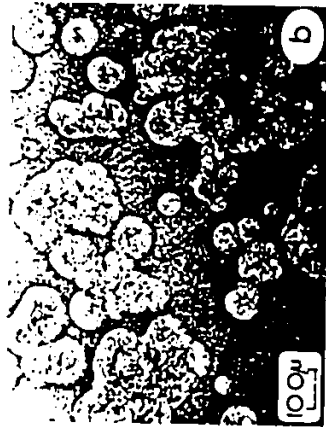
Fig. 29 Optical photomicrographs of the cross-sections of the sulfide nodules.

(a), (c) and (d) at $p_{S_2} = 10^2$ Pa

(b) at $p_{S_2} = 10$ Pa.

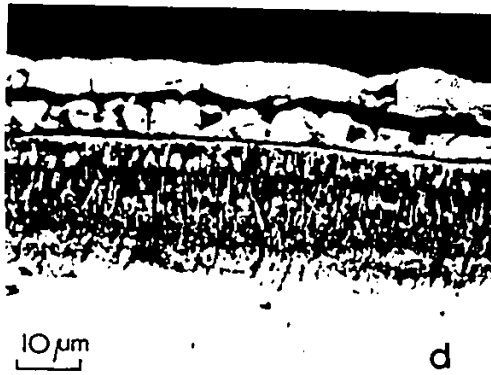
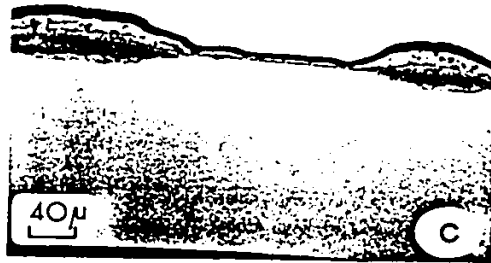
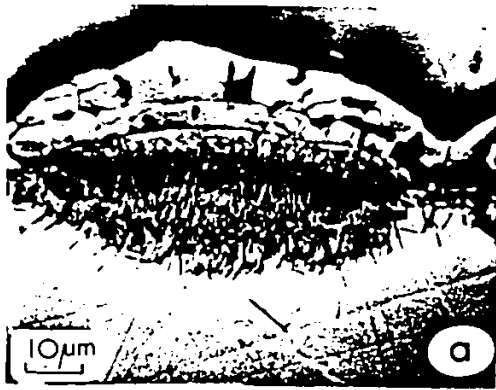
Fig. 5.30 Fe-18 Al alloy sulfidized at $p_{S_2} = 10$ Pa.

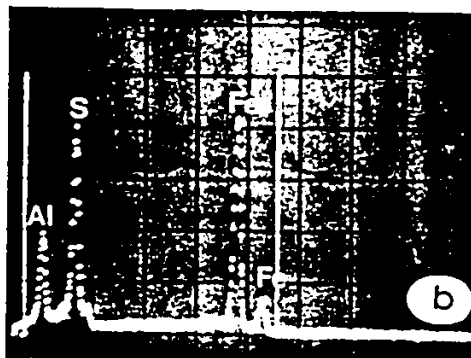
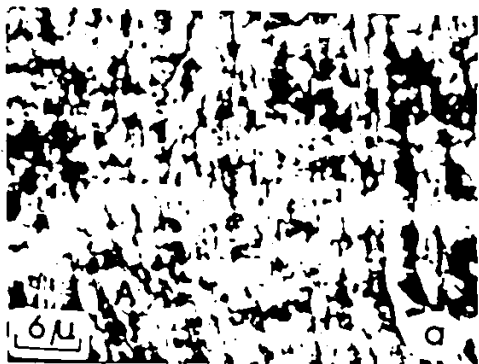
- a) Cross-section of the inner two-phase layer of the external scale.
- b) EDAX analysis on a point A (dark phase) in (a).
- c) SEM observation of the inner layer after etching with dilute HCl acid for 60 s.
- d) Platelet shaped $FeAl_2S_4$ precipitates were completely etched leaving behind respective holes.
- e) Etched $FeAl_2S_4$ precipitates in the inner layer.
- f) Etched $FeAl_2S_4$ precipitates in the inner layer.



POOR PRINT
Epreuve illisible

170





Point A

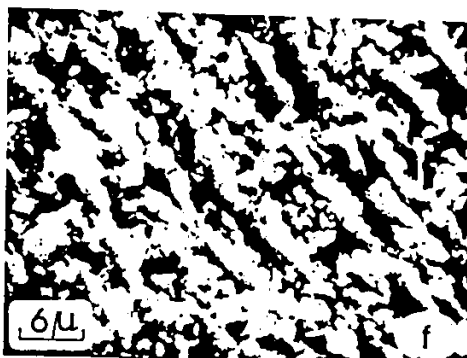
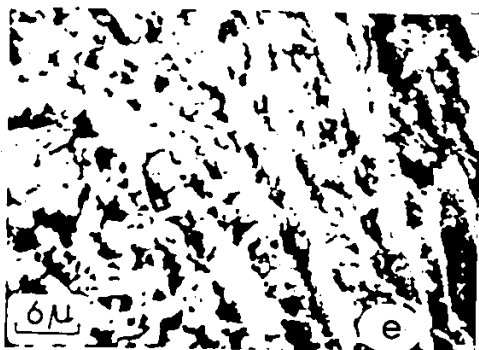
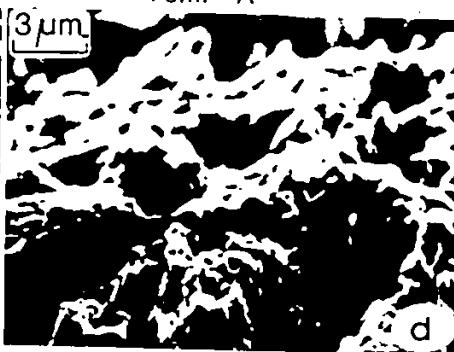


Fig. 5.31 Optical photomicrograph showing the position of a 50 μm Pt marker residing above the sulfidation zone of Fe-9 Al alloy in the FeS/alloy diffusion couple.

Fig. 5.32 Optical photomicrographs showing the position of a 25 μm Pt marker residing at the outer and inner layer interface for Fe-9 and 18 Al alloys at $p_{\text{S}_2} = 10^{-1}$ Pa and 10 Pa respectively.

POOR PRINT
Epreuve illisible

172

↑
FeS



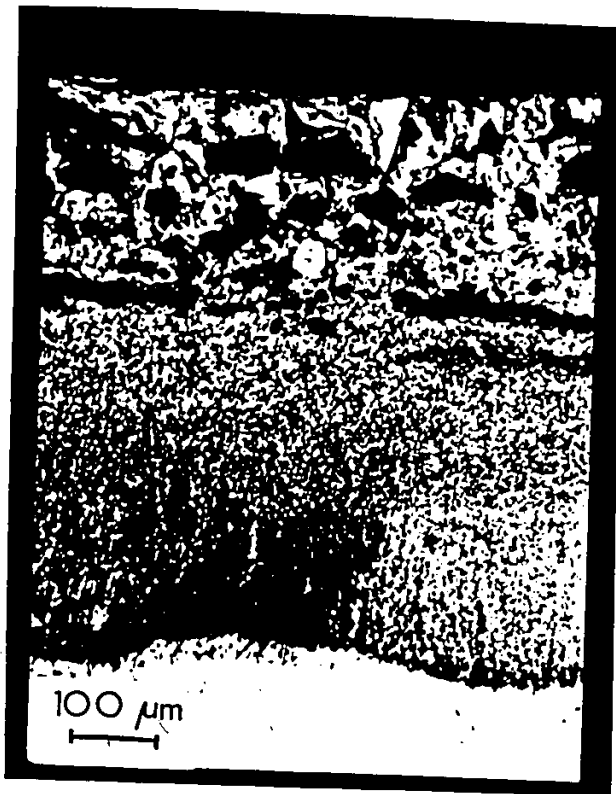
Alloy Sulfidation
Zone



50 μm

POOR PRINT
Epreuve illisible

173



a.



b.

the results of such experiments. The markers are seen to rest in between the inner and outer layer of the scales on both Fe-9 a/o Al alloys (a) and Fe-18 a/o Al alloys (b). These findings indicate that the outer layer grew by the outward diffusion of iron and that the inner layer grew by the inward migration of sulfur.

5.6 PHASE IDENTIFICATION

The phases present in the sulfide scales were identified by means of electron probe microanalyses, X-ray diffraction and energy dispersive X-ray analyses.

5.6.1 Electron Probe Microanalyses

Microanalysis was performed at various parts of the scale using a Cameca MS-64 electron microprobe. Spot counting procedure at an operating voltage of 20 KV was used to determine the composition of the phases. Because of the fine dispersion of two phases in the internal sulfidation zone and loss of optical contrast due to carbon coating, the point counting method was considered inadequate to ascertain the composition of these sulfide precipitates. Therefore, a qualitative estimate of the constituents of each phase was obtained by scanning the electron-probe beam over the sample.

Figure 5.33 shows microprobe traces of various elements across the sulfidation zone formed on the Fe-9 Al alloy diffusion coupled with FeS for 1500 seconds at 1173K. Figure 5.33(a) shows typical line scans for iron and aluminum whereas Fig.

COLOURED PICTURES
Images en couleur

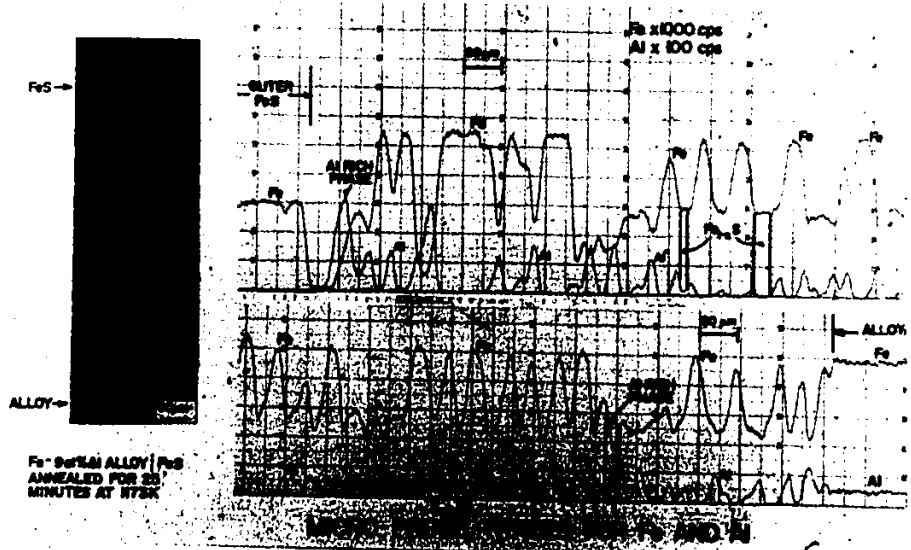


Fig. 5.33 a) Microprobe traces for iron and aluminum in FeS/Fe-9 Al alloy diffusion couple.

5.33 (b) shows line scans for iron and sulfur across the sulfidation zone. Similar analyses have been made for other diffusion couples with Fe-6 Al, Fe-18 Al and Fe-28 Al alloys. In Fig. 5.33(a), aluminum counts arise from the double sulfide (FeAl_2S_4) phase which is distributed non-uniformly in the sulfide bands. Low count rates of Fe, Al and S K_α radiation were occasionally obtained because during the metallographic preparation some of the sulfides were pulled out, giving rise to voids. The aluminum solubility in FeS is determined to be less than 1 a/o. The fine particle size of the double sulfide phase made it quite difficult to estimate its exact composition. However, towards the external FeS/sulfidation zone region the double sulfide particle size was coarse enough for representative microanalyses. It was estimated from these measurements that the double sulfide composition was closer to FeAl_2S_4 . As seen by the elemental scans in Fig. 5.33(a), the alloy bands were depleted of aluminum. A small aluminum depletion zone was observed in the alloy beneath its interface. This depletion was more prominent in higher aluminum content alloys. In some instances, the counts of Fe, Al, S K_α radiation were recorded simultaneously during line scanning to determine the distribution of these elements in the sulfidation zone. This method, however, was unsuccessful due to the periodicity of the sulfide bands. Notwithstanding, a larger distribution of FeAl_2S_4 was found from such measurements towards the FeS/sulfidation zone region supporting the evidence obtained from optical microscopy observations.

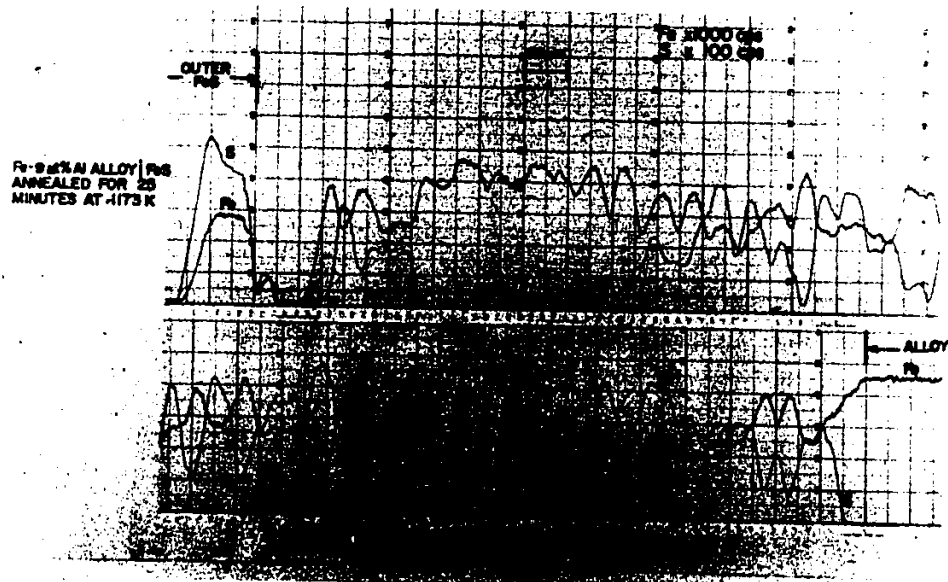


Fig. 5.33(b) Microprobe traces for iron and sulfur in FeS/Fe-9 Al alloy diffusion couple.

Alloys containing 6 a/o Al showed internal sulfidation when sulfidized in S_2 vapour corresponding to the decomposition pressure of FeS. The Fe-9 Al alloy also sulfidized internally and, in addition formed very thin external scales at isolated sites. The Fe-18 Al alloy sulfidized internally and formed a continuous external scale. These sulfidized alloys were investigated in order to determine the compositions of the sulfides in the internal sulfidation zones and in the external scales. It was difficult to ascertain the composition of internal sulfide precipitates because their size was much smaller than the probe diameter. Figure 5.34 shows microprobe traces for Fe and Al across the internal sulfidation zone in the Fe-9 Al alloy. The alloy is depleted locally near the alloy/internal sulfidation zone interface causing a slight enrichment of Al in the sulfidation zone. The internal sulfide precipitates have compositions corresponding to $FeAl_2S_4$ in the Fe-6 Al alloy and to $FeAl_2S_4 + Al_2S_3$ in alloys containing 9 and 18 a/o Al. In particular, the Al_2S_3 precipitates were found towards the alloy/internal sulfide interface. In the case of the Fe-18 Al alloy, the internal sulfidation zone of $FeAl_2S_4 + Al_2S_3$ was overgrown by a $FeAl_2S_4$ external scale. The external slow growing sulfide layer on the Fe-28 Al alloy was determined to be Al_2S_3 . Since Al_2S_3 and $FeAl_2S_4$ hydrolyzed in moist air, precautions were taken to isolate the specimens from air when preparing the samples for microprobe analyses.

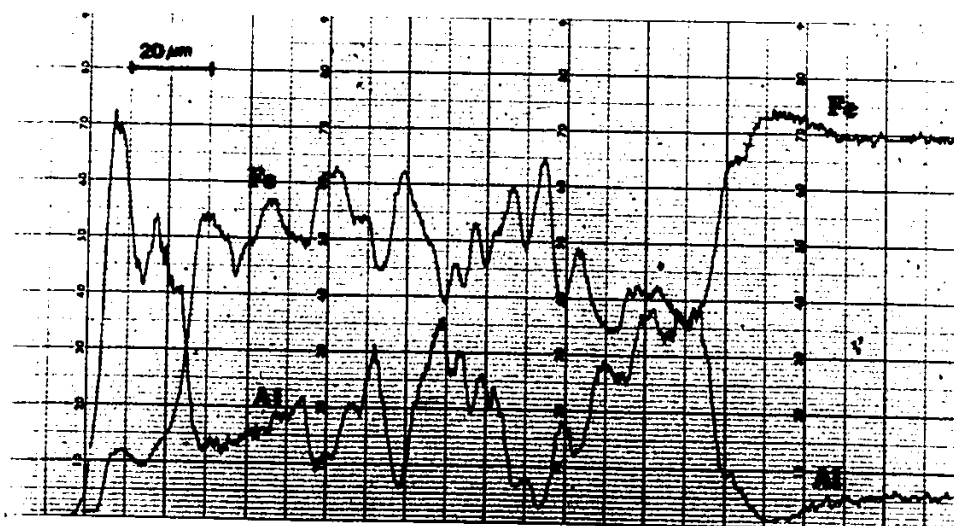


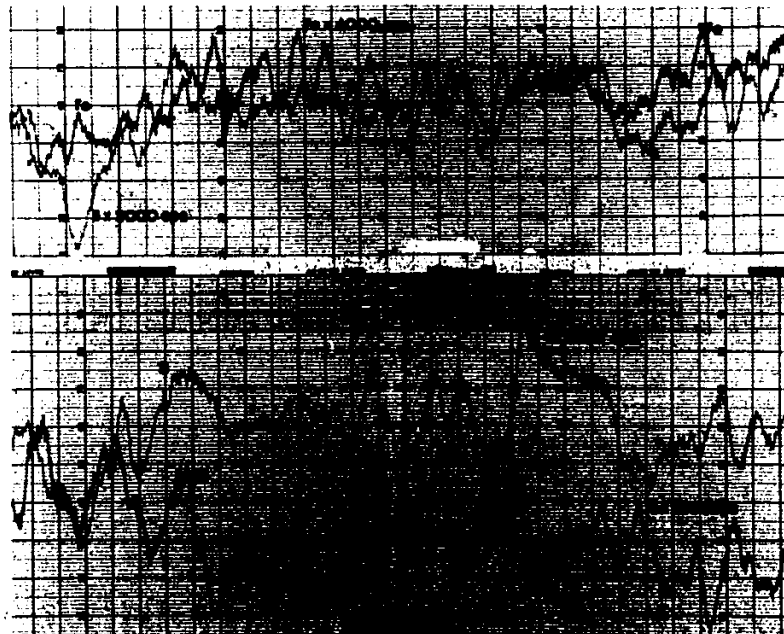
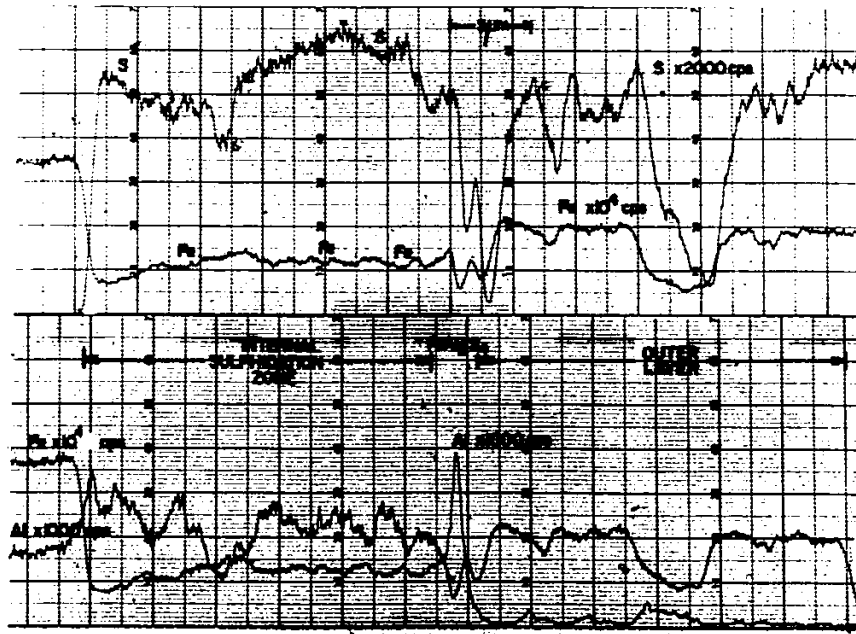
Fig. 5.34 Microprobe traces for iron and aluminum in the sulfidation zone of Fe-9 Al alloy sulfidized in S_2 vapour.

Compositions of sulfide phases present in the reaction product layers at higher sulfur activities in H_2S-H_2 atmospheres corresponding to $p_{S_2} = 10^2$ Pa and 10 Pa were investigated by microprobe analyses. Figure 5.35 shows microprobe traces of various elements across a nodule formed on the alloy containing 18 a/o Al at 1173K and $p_{S_2} = 10^2$ Pa during the initial period (5 minutes) of the reaction. The inner layer of a nodule is constituted of an intense localized internal sulfidation zone as previously shown (Fig. 5.29). The outer layer is FeS doped with Al. In the internal sulfidation zone, peaks of Al correspond to troughs of Fe and peaks of sulfur. Figure 5.36 shows the distribution of Fe, Al and S in the inner scale layer formed on the Fe-18 Al after exposure of 900 seconds at $p_{S_2} = 10^2$ Pa. From these measurements, the inner layer is predicted to be a mixture of FeS, $FeAl_2S_4$ and Al_2S_3 with Al_2S_3 concentrated at the scale/alloy interface.

A complete line scan across the scale formed on the Fe-18 Al at $p_{S_2} = 10$ Pa after 10800 seconds of exposure is presented in Fig. 5.37. There is an increase in Al concentration as the scale/alloy interface is approached. At the scale/alloy interface, peaks of Al, S and a trough of Fe indicate the presence of Al_2S_3 . Beneath this Al and S rich zone, several line scans were taken across the dark sulfide platelets. Such microprobe scans are presented in 5.38(a) and (b). The precipitates are seen to be rich in Al and S and are probably constituted of Al_2S_3 .

Fig. 5.35 Microprobe scans across the scale on the Fe-18 Al alloy at $p_{s_2} = 10^2$ Pa.

Fig. 5.36 Microprobe scans across the inner two-phase layer of the external scale on Fe-18 Al alloy at $p_{s_2} = 10^2$ Pa.



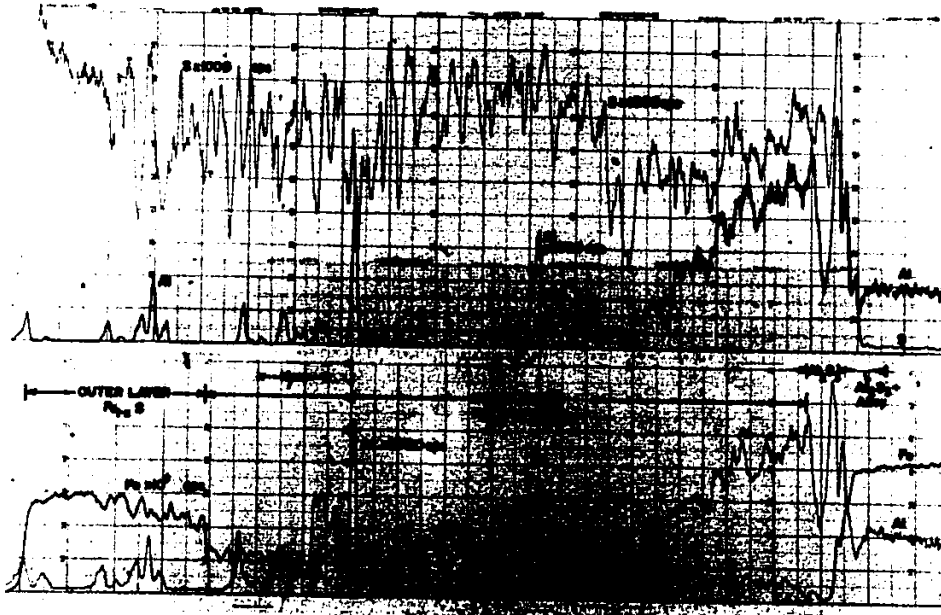


Fig. 5.37 Microprobe scans across the scale on Fe-18 Al alloy at $p_{s_2} = 10^2$ Pa.

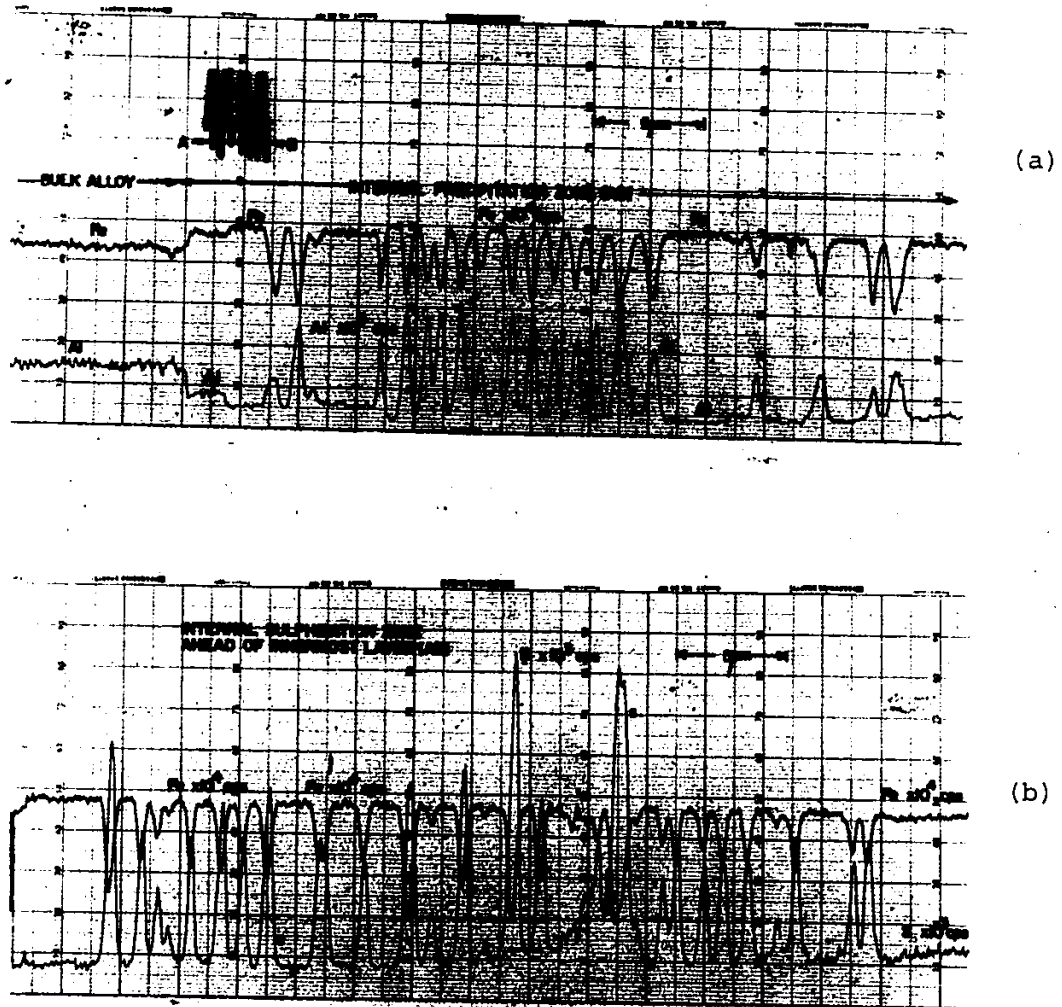


Fig. 5.38 Microprobe traces for (a) Fe, Al and (b) Fe, S in the internal sulfidation zone ahead of the innermost layer of Fe-18 Al alloys at $p_{S_2} = 10 \text{ Pa}$.

In summary, various microprobe scans and spot analyses made on the reaction product layers formed at 1173K, $p_{S_2} = 10^2$ Pa and 10 Pa indicate the formation of an outer FeS layer and an inner layer consisting of FeS and $FeAl_2S_4$. The innermost layer at the scale/alloy interface was essentially Al_2S_3 from which Al_2S_3 platelets or needles extended into the alloy.

5.6.2 X-ray Analyses

X-ray powder analyses of the sulfide reaction products were performed in an attempt to substantiate the structure of phases formed. The diffraction patterns of various samples were chart recorded. The intensity of peaks and their positions on the chart (angle 2θ) were recorded to evaluate the 'd' spacings from the relation $\lambda = 2d\sin\theta$ ($\lambda = 15.406$ nm for CuK_α radiation). The intensities of peaks were normalized with respect to the highest peak obtained in the system. Tables 5-11, 5-12 and 5-13 represent standard values of 'd' in nm and the corresponding relative intensities ($I/I_1 \times 100$) for FeS, $FeAl_2S_4$ and Al_2S_3 respectively.

The internal sulfidation zones of the diffusion couples were completely scraped from the alloy and then ground to powder. To identify the various phases present, the X-ray results were tabulated as 'd' spacings with 2θ and I/I_1 ratio. The intensity of lines at various diffracted angles (2θ) were plotted on graphs (Figs. 5.39(a), (b), (c) and (d)). Since the samples contained more than one phase, the analysis described

Table 5-11

Intensity, d spacings and (hkl) indices of Fe_{1-x}S

Peak No.	'd' in $\text{nm} \times 10^2$	Relative Intensity ($I/I_1 \times 100$)	(hkl) Indices	Peak No.	'd' in $\text{nm} \times 10^2$	Relative Intensity ($I/I_1 \times 100$)	(hkl) Indices
1	34.5	3	100	10	13.26	9	402
2	29.81	30	200	11	12.99	4	204
3	28.79	4	002				
4	26.53	40	201				
5	20.72	100	202				
6	17.24	25	220				
7	16.14	6	203				
8	14.45	4	401				
9	14.46	10	004				

Table 5-12

Intensity, d spacings and (hkl) indices of FeAl_2S_4

Peak No.	'd' in $\text{nm} \times 10^2$	Relative Intensity ($I/I_1 \times 100$)	(hkl) Indices	Peak No.	'd' in $\text{nm} \times 10^2$	Relative Intensity ($I/I_1 \times 100$)	(hkl) Indices
1	119.36	30	00.3	11	18.232	18	11.0
2	60.00	4	00.6	12	16.937	30	00.21
3	40.08	100	00.9	13	16.608	7	11.9
4	31.55	6	10.2	14	15.064	5	
5	30.49	15	10.3	15	14.576	4	00.24
6	30.054	15		16	13.222	4	00.27
7	27.978	30	10.5	17	12.427	6	20.17
8	24.086	11	00.15	18	12.058	4	00.30
9	21.79	23	10.12				
10	19.163	17	10.15				

Table 5-13
Intensity, d spacings and (hkl) indices of Al_2S_3

Peak No.	'd' in nm×10	Relative Intensity (I/I ₁ ×100)	(hkl) Indices	Peak No.	'd' in nm×10	Relative Intensity (I/I ₁ ×100)	(hkl) Indices
1	5.3	13	101	15	1.86	66	300
2	4.7	23	102	16	1.74	20	208
3	3.47	13	104	17	1.69	33	119
4	3.22	100	110	18	1.6	33	220
5	2.95	27	006	19	1.56	33	306
6	2.82	83	113	20	1.5	27	218
7	2.66	13	202	21	1.4	10	226
8	2.54	20		22	1.31	20	
9	2.47	13					
10	2.37	13					
11	2.18	13	116				
12	2.19	7					
13	2.07	33	212				
14	1.99	20					

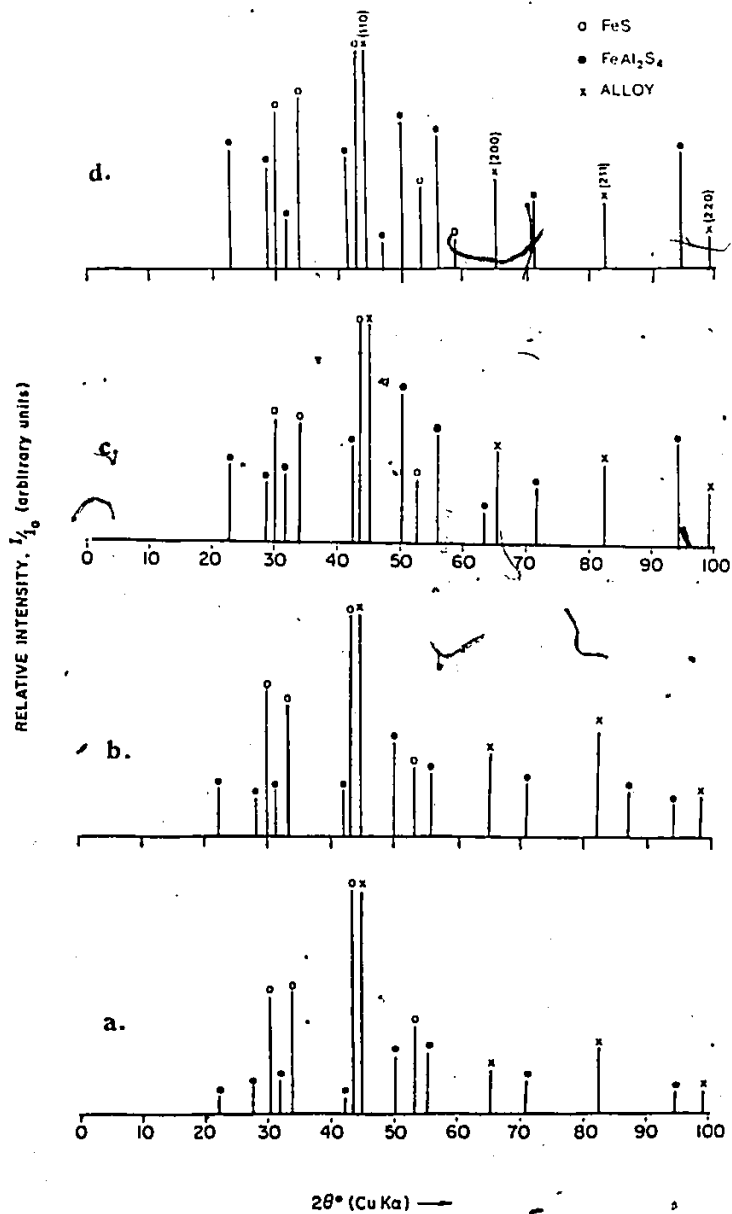


Fig. 5.39 X-ray diffraction pattern of sulfides and alloy from the sulfidation zone of FeS/(a) Fe-6 Al, (b) Fe-9 Al (c) Fe-18 Al and (d) Fe-28 Al alloy diffusion couples.

by Cullity⁽¹⁵⁹⁾ was used. In this method, a known highest intensity line of a phase present in the mixture is taken as I_1 and the rest of the diffraction intensity peaks are normalized with respect to it. Then the relative intensities of the known phase are separated from the mixture and the remaining lines in the pattern are again normalized with respect to the highest intensity. Using this method for the results given in Fig. 5.39(a) to (d), the phases present in the sulfidation zone were identified as alloy, FeS and FeAl_2S_4 for diffusion couples consisting of Fe-6, 9, 18 and 28 Al alloys.

X-ray investigations were carried out for alloys sulfidized in S_2 vapour at the dissociation pressure of FeS. Fe-6 and 9 a/o Al alloys sulfidized internally. The diffraction pattern obtained from the internal sulfidation zone of the Fe-9 Al alloys corresponded to the presence of FeAl_2S_4 as shown in Fig. 5.40(a). The Fe-18 Al alloy exhibited diffraction patterns containing FeAl_2S_4 from the external scale and FeAl_2S_4 +alloy from the internal sulfidation zone. The internal precipitates towards the alloy and internal sulfidation zone interface were found to be Al_2S_3 for Fe-9 and 18 a/o alloys. The external scale on the Fe-28 Al alloy was identified to be Al_2S_3 (Fig. 5.40(b)).

Scales formed on the Fe-18 Al alloy at high sulfur pressures $p_{\text{S}_2} = 10^2$ and 10 Pa were analyzed by a similar method. Samples were obtained from various parts of the scales.

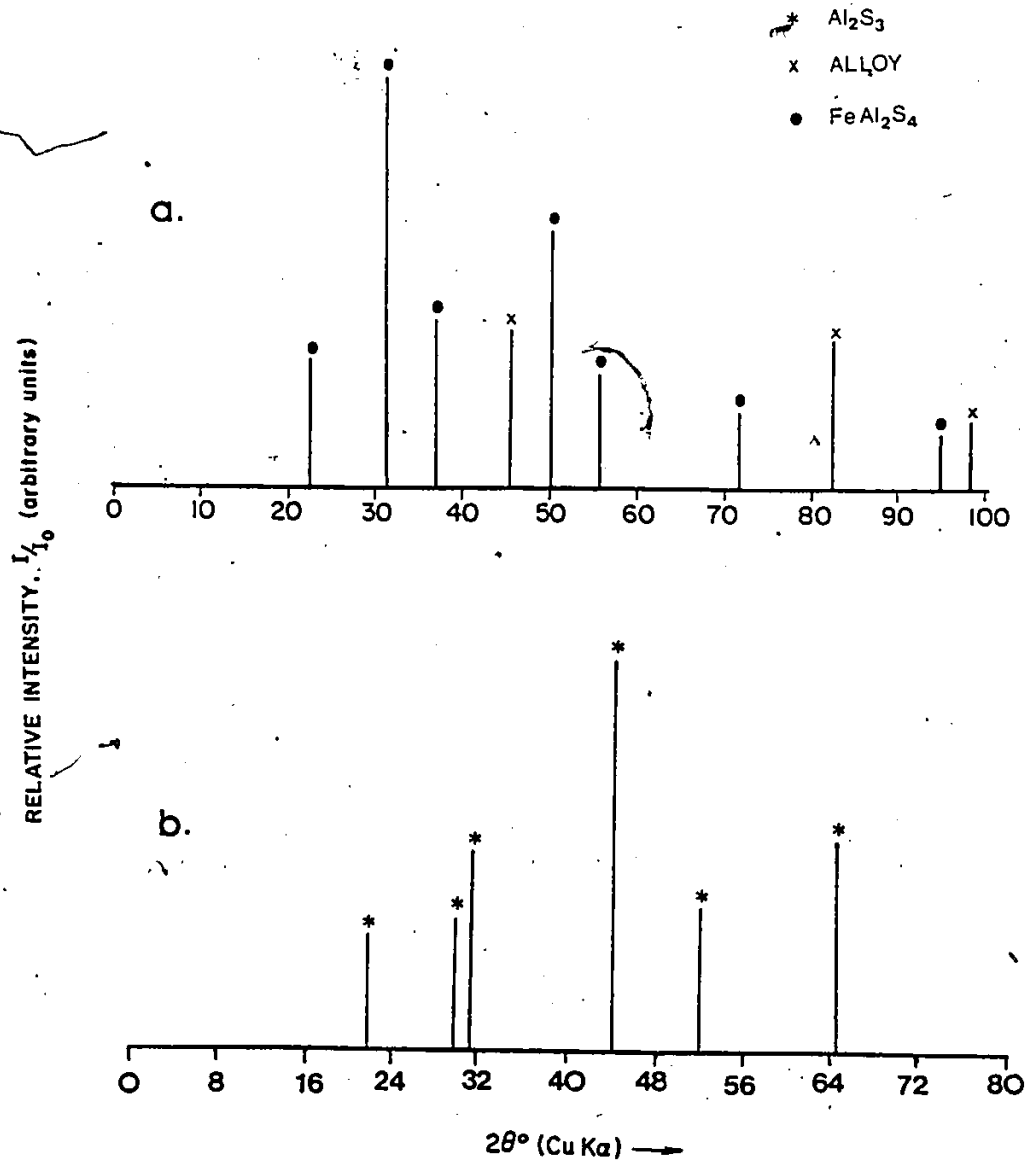


Fig. 5.40 X-ray diffraction of sulfides from (a) internal sulfidation of Fe-9 Al alloy and (b) external scale on the Fe-28 Al alloy in S_2 vapour.

Typical diffraction patterns are shown in Figs. 5.41(a), (b) and (c). The analyses suggest that the reaction product layers on the Fe-18 Al alloy consist of an outer FeS layer, an inner layer consisting of a mixture of FeS+FeAl₂S₄ and a layer adjacent to the alloy-scale interface containing a mixture of FeAl₂S₄ and Al₂S₃.

5.6.3 X-ray Energy Dispersive Analyses

Some of the samples were analyzed qualitatively to supplement the previous quantitative analyses, by using the KEVEX X-ray energy dispersive analyzer attached to the SEM. In this system X-rays are generated upon scanning the electron beam across the specimen surface. Also a spot, the size of the stationary electron beam (~ 50 nm), can be analyzed for inclusions of various phases. The X-rays which are given off the sample being collected by the detector are counted each second. To obtain relative results from one part of the sample to the next, 1000 counts/second was maintained. The X-rays are then located in the spectrum on the oscilloscope screen depending on their energies. This X-ray energy spectrum is then analyzed by a teletype computer. In the output, CENTROID is the number to look up on the energy spectrum chart to indicate the element. FWHM is the number of channels at the full-width-half-maximum point. AREA is the total number of counts within peak limits which is proportional to the concentration of the element. To obtain representative results, flat and polished samples were

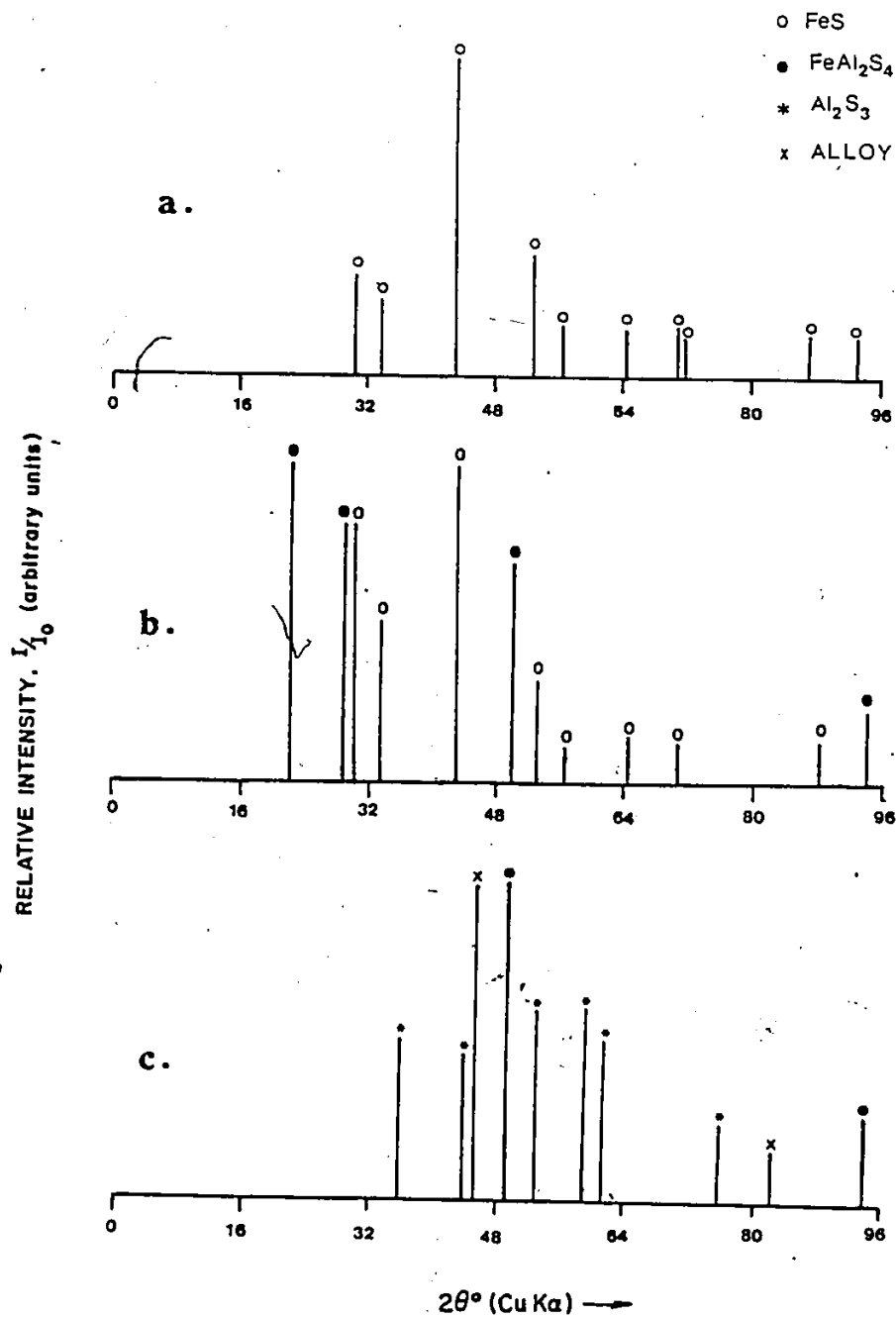


Fig. 5.41 X-ray diffraction pattern of sulfides from Fe-18 Al alloy sulfidized in H₂S-H₂ atmospheres at $p_{S_2} = 19$ Pa; (a) outer FeS layer (b) inner FeS+FeAl₂S₄ layer (c) innermost FeAl₂S₄+Al₂S₃ layer near the alloy.

used. During such analyses it was established that X-rays generated by the sample possessed a free path to the detector.

Tables (5-14) and (5-15) show some results of point analyses obtained on Fe-Al alloys. Tables (5-16) and (5-17) show point analyses taken from the sulfidation zone of FeS/Fe-9 Al alloy diffusion couple. The presence of S, Fe (Table 5-16) and Al, S and Fe (Table 5-17) at different points in the sulfide bands support the previously presented evidence that these sulfide bands are indeed composed of FeS and FeAl_2S_4 .

The external scale formed on the Fe-18 Al alloy in S_2 vapour was identified to be FeAl_2S_4 . Generally, it was difficult to detect the sulfur counts from FeAl_2S_4 because of its nature to undergo hydrolysis in moist air, particularly during specimen preparation. The internal sulfides which appeared platelike in these alloys at times showed low sulfur counts due to this hydrolysis effect. Tables (5-18), (5-19) and (5-20) illustrate these considerations based upon the analyses of the external scale and of internal sulfidation zone.

EDAX analyses were also applied to identify the various sulfide phases formed on the Fe-Al alloys at higher sulfur pressures. Figure 5.30(b) shows a spectrum obtained from the point A in the inner layer suggesting the composition FeAl_2S_4 . Similar analyses performed on other parts of the scale supported the quantitative results obtained by EPMA analyses.

Table 5-14

EDAX Point Analysis on Fe-6 a/o Al Alloy

No.	Centroid	FWHM	Area	Element
1	1.46	0.10	516.16	Al
2	6.43 ^A	0.15	3327.98	Fe
3	7.09	0.15	4095.49	Fe

Table 5-15

EDAX Point Analysis on Fe-9 a/o Al Alloy

No.	Centroid	FWHM	Area	Element
1	1.46	0.10	852.55	Al
2	6.44	0.15	31656.45	Fe
3	7.10	0.16	3680.00	Fe

Table 5-16

EDAX Point Analysis on a sulfide band in
FeS/Fe-6 Al diffusion couple

No.	Centroid	FWHM	Area	Element
1	2.27	0.13	14088.97	S
2	6.22	0.15	18879.96	Fe
3	6.83	0.15	2187.12	Fe

Table 5-17

EDAX Point Analysis on a sulfide band in
FeS/Fe-9 Al diffusion couple

No.	Centroid	FWHM	Area	Element
1	1.46	0.11	2423.79	Al
2	2.27	0.11	2698.12	S
3	6.22	0.15	26359.49	Fe
4	6.83	0.15	3375.72	Fe

Table 5-18

EDAX Analysis on the external scale formed on
Fe-18 a/o Al alloy in S₂ vapour

No.	Centroid	FWHM	Area	Element
1	1.47	0.11	12043.99	Al
2	6.22	0.15	17011.46	Fe
3	6.83	0.15	2058.12	Fe

Table 5-19

EDAX Analysis in the internal sulfidation
zone of Fe-9 a/o Al alloy in S₂ vapour

No.	Centroid	FWHM	Area	Element
1	1.47	0.12	3264.02	Al
2	2.27	0.11	9039.00	S
3	6.22	0.15	22537.48	Fe
4	6.83	0.16	2803.47	Fe

Table 5-20

EDAX Analysis in the internal sulfidation
zone in Fe-9 a/o Al alloy in S₂ vapour

No.	Centroid	FWHM	Area	Element
1	1.47	0.10	2728.28	Al
2	2.27	0.12	9472.00	S
3	6.22	0.15	22853.45	Fe
4	6.83	0.16	2701.50	Fe

5.6.4 Summary

Sulfide phases present in the diffusion couples of Fe-6, 9, 18 and 28 a/o Al alloys coupled with FeS consists of FeS and FeAl_2S_4 . Solubility of Al in FeS was determined to be less than 1 a/o. The scales formed on these alloys in S_2 vapour at the decomposition pressure of FeS were composed of FeAl_2S_4 and Al_2S_3 . Alloys containing 6 a/o Al sulfidized internally, 9 and 18 a/o Al alloys sulfidized both externally and internally forming FeAl_2S_4 and $\text{FeAl}_2\text{S}_4 + \text{Al}_2\text{S}_3$, respectively. The Fe-28 Al alloy sulfidized externally to yield a slow growing Al_2S_3 film. In $\text{H}_2\text{S}-\text{H}_2$ atmospheres at p_{S_2} ranging from 1 to 10^3 Pa, the Fe-9 and 18 a/o Al alloys formed an external scale consisting of an outer FeS layer and an inner two-phase layer of $\text{FeS} + \text{FeAl}_2\text{S}_4$ accompanied with an internal sulfidation zone containing $\text{FeAl}_2\text{S}_4 + \text{Al}_2\text{S}_3$ precipitates. In addition, the Fe-18 Al alloys formed a continuous layer of Al_2S_3 at the external scale/alloy interface.

5.7 PHASE EQUILIBRIA IN THE Fe-Al-S SYSTEM AT 1173K

Several overall compositions were chosen for this study (Fig. 5.42). The Al/Fe ratio was varied from 8.33×10^{-2} to 85.71×10^{-2} . The composition of sulfur was kept fixed (35 a/o). Well equilibrated pellets were mounted for metallography, microprobe and X-ray analyses.

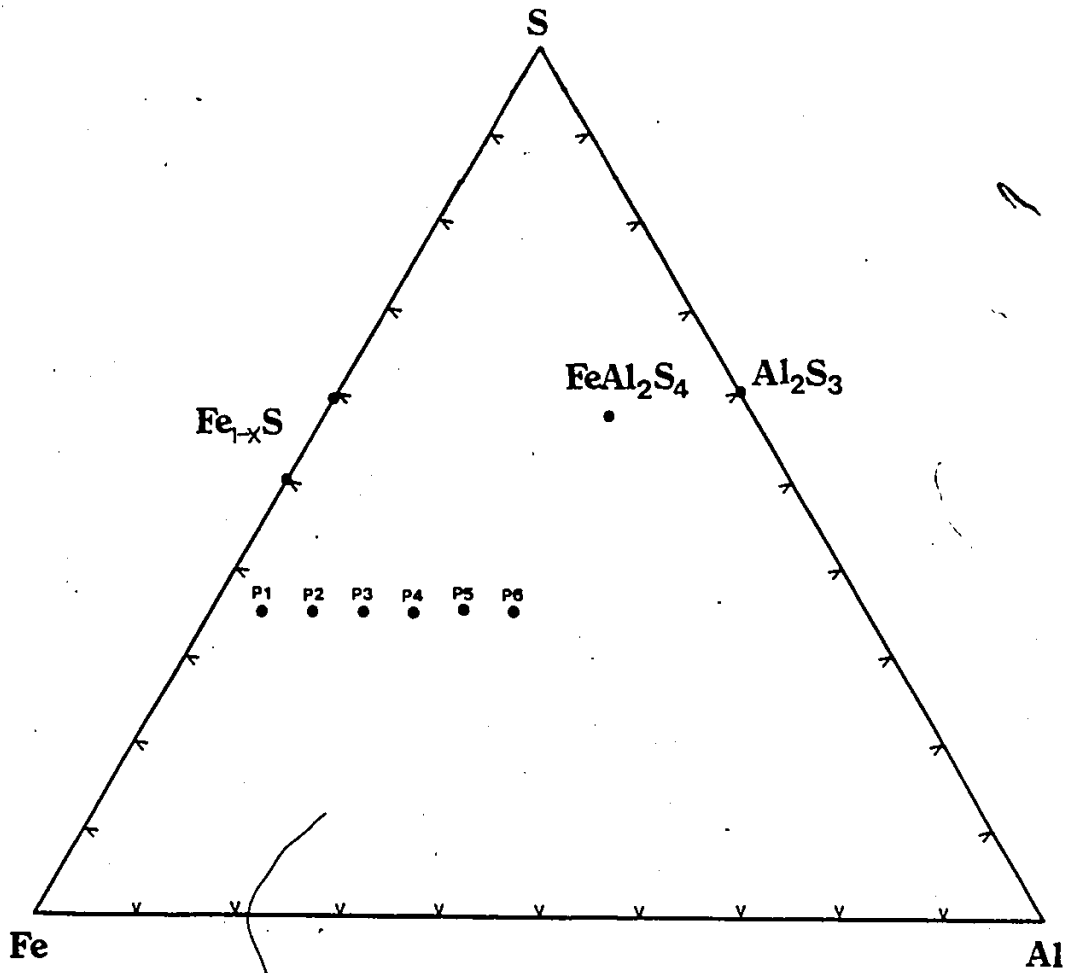


Fig. 5.42 Overall compositions of Fe, Al and S (P1-P6) considered for the analysis of Fe-Al-S isotherm at 1173K:

5.7.1 Metallography

Polished specimens were observed under the optical microscope. Figure 5.43(a) shows a three phase equilibrium between alloy, FeS and FeAl_2S_4 . The bright, grey and dark phases are respectively alloy, FeS and FeAl_2S_4 . Figure 5.43(b) shows a two-phase equilibrium between FeAl_2S_4 and alloy whereas Figs. 5.43(c) and 5.44(d) show three-phase regions (alloy+ FeAl_2S_4 + Al_2S_3) and two-phase regions (alloy+ Al_2S_3) respectively. Table (5-21) summarizes the metallographic observations.

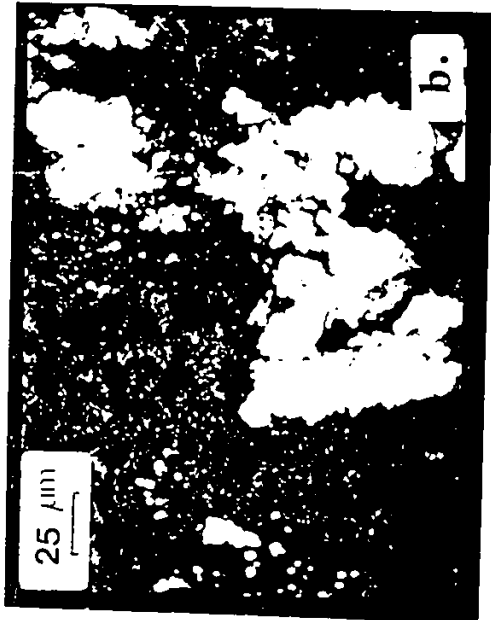
Table 5-21

Summary of metallographic observations in equilibrium experiments.

Points on Isotherm	Overall composition			Inference
	S	Al	Fe	
P1	35	5	60	3 phase region: alloy, FeS and FeAl_2S_4
P2	35	10	55	3 phases: alloy+FeS+ FeAl_2S_4
P3	35	15	50	2 phase region: alloy+ FeAl_2S_4
P4	35	20	45	2 phase region: alloy+ FeAl_2S_4
P5	35	25	40	3 phase region: alloy+ Al_2S_3 + FeAl_2S_4
P6	35	30	35	2 phase region: alloy+ Al_2S_3

- Fig. 5.43 a) Three-phase; FeS , FeAl_2S_4 and alloy equilibrium.
- b) Two-phase; FeAl_2S_4 and alloy equilibrium.
- c) Three-phase; FeAl_2S_4 , Al_2S_3 and alloy equilibrium.
- d) Two-phase; Al_2S_3 and alloy equilibrium.

POOR PRINT
Epreuve illisible



5.7.2 X-ray Analyses

The phases in the Fe-Al-S system were identified using the powder X-ray diffraction method using Ni filtered CuK_α radiation. The X-ray intensity plots vs. the diffraction angle 2θ for the pellets 1 through 5 are shown in figures 5.44(a) through 5.44(e). These X-ray results support the inferences drawn from the metallographic observations.

5.7.3 Electron Probe Microanalyses

To determine the compositions of the equilibrated phases, the spot counting procedure was used. Annealing of the pellets was carried out for two different times, 140 and 240h. Microprobe analyses of the adjacent phase composition did not change for the two annealed batches of samples demonstrating equilibrium between various phases.

Al-K_α , Fe-K_α and S-K_α radiation signals were used to determine phase compositions quantitatively. Alloy standards were used to calculate the composition of alloy in the equilibrated samples (Table 5-22). The intensities of X-ray signals after subtracting the background counts for Fe, Al and S obtained from the equilibrated phases in the Fe-Al-S system are tabulated in Table 5-23. Each intensity value is the average of 20 values taken at different spots of a phase. FeS and FeAl_2S_4 prepared separately were used as standards to measure the composition of Fe, S, and Al in the sulfides. Atomic number and absorption corrections were applied when determining the compo-

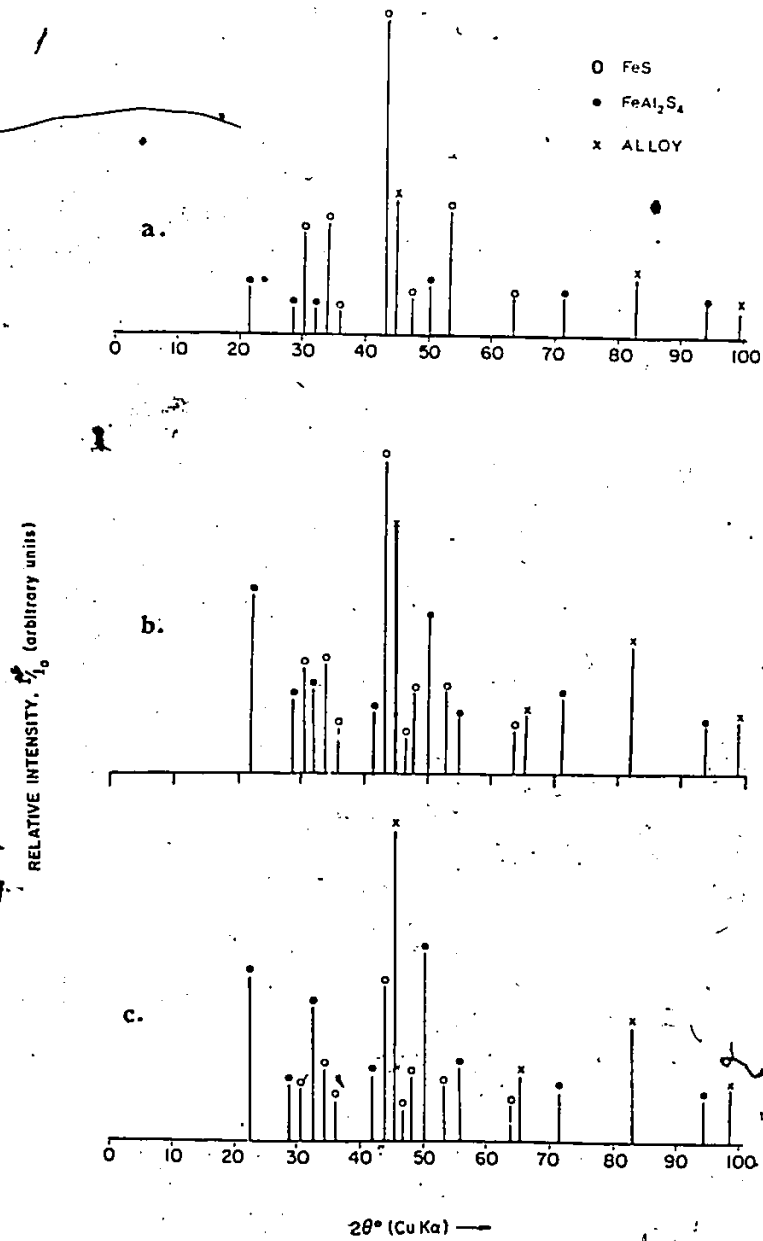


Fig. 5.44 X-ray diffraction pattern of various phases in the equilibrated pellets of overall compositions (a) P1, (b) P2, (c) P2, (d) P5, (e) P6 as shown in Fig. 5.42.

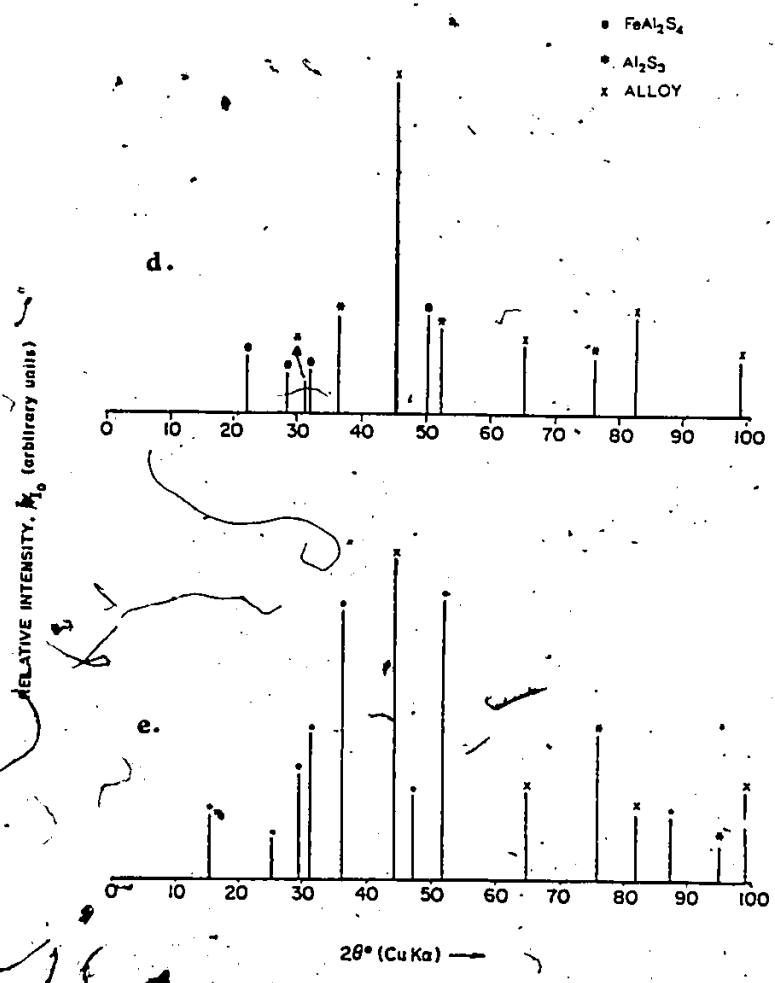


Fig. 5.44 cont'd.

Table 5-22
Electron probe microanalyses of the Fe-Al alloys

Nominal Composition		Intensity Ratio		Weight Percent		Atom percent	
Al (w/o)	Fe (w/o)	Al	Fe	Al	Fe	Al	Fe
0.5	99.5	0.0021	0.992	0.4	99.5	0.8	99.1
3.0	97.0	0.0120	0.945	2.9	97.0	5.8	94.1
4.5	95.5	0.0181	0.929	4.3	95.7	8.5	91.5
10.0	90.0	0.0396	0.879	9.8	91.2	18.2	81.8
15.0	85.0	0.0594	0.830	15.4	84.4	27.4	72.4

Table 5-23
 Electron probe microanalysis of equilibrated phases in Fe-Al-S system

Sample	X-ray intensity from standards		Phase	X-ray Intensity from sample			Al and Fe a/o in the alloy	Chemical formula of the sulfide
	Pure Al	Pure Fe		Al	Fe	S		
Pellet-2	87156	125771	Alloy	178	124764	-	0.84 99.15	-
	87156	125771	Fe sulfide	250	78698	53159	-	(Fe _{0.96} Al _{0.012})S
	87156	125771	Double sulfide	15775	36747	33146	-	(Fe _{1.24} Al _{1.618})S ₄
Pellet-3	87612	126694	Alloy	468	128014	-	2.73 96.54	-
	87612	126694	Double sulfide	16399	33706	34773	-	(Fe _{1.14} Al _{1.653})S ₄
Pellet-4	87612	126694	Alloy	641	120323	-	3.42 96.54	-
	87612	126694	Double sulfide	17861	32746	42178	-	(Fe _{1.10} Al _{1.846})S ₄

Table 5-23 cont'd

Sample	X-ray intensity from standards		Phase	X-ray Intensity from sample			Al and Fe a/o in the alloy		Chemical formula of the sulfide
	Pure Al	Pure Fe		Al	Fe	S	Al	Fe	
Pellet-5	87612	126694	Alloy	1012	118294	-	5.86	94.11	
	87612	126694	Double sulfide	18856	29304	41424	-	-	$(\text{Fe}_{0.99}\text{Al}_{1.910})\text{S}_4$
	87612	126694	Al sulfide	30478	681	30188	-	-	$(\text{Fe}_{0.015}\text{Al}_{1.955})\text{S}_3$
Pellet-6	86976	124605	Alloy	3972	106527	-	20.92	79.01	
	86976	124605	Al sulfide	30687	452	30505	-	-	$(\text{Fe}_{0.009}\text{Al}_{1.982})\text{S}_3$

sition of each phase (Table 5-23). The electron probe results obtained in this investigation for Fe-Al-S system indicated the following:

- a) Iron sulfide in equilibrium with the double sulfide and an alloy containing 0.84 a/o Al dissolves 0.61 a/o Al at 1173K.
- b) The double sulfide phase in equilibrium with iron sulfide and the Fe-0.84 Al alloy is rich in iron and its iron content decreases as the double sulfide equilibrates with higher aluminum containing alloys.
- c) The solubility of iron in Al_2S_3 equilibrated with the double sulfide and alloy containing 5.86 a/o Al is found to be 0.3 a/o.
- d) Iron-aluminum alloys equilibrate with aluminum sulfide containing a small concentration of iron ions in its lattice. The solubility of iron in Al_2S_3 was found to decrease with increasing Al contents of the alloy. The iron content of aluminum sulfide in equilibrium with the Fe-19.53 Al alloy is 0.28 a/o.

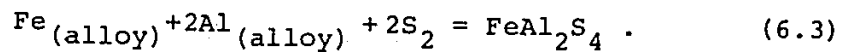
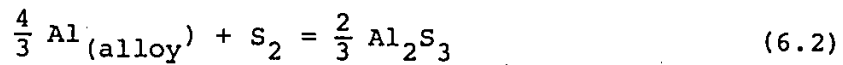
CHAPTER 6

ANALYSIS AND DISCUSSION OF EXPERIMENTAL RESULTS

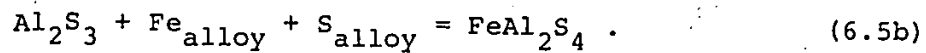
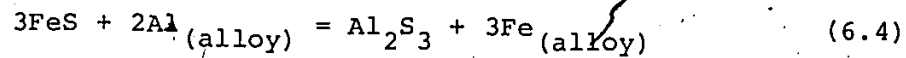
6.1 INTRODUCTION

In Chapter 5 the experimental results were presented according to the three methods of sulfidizing the Fe-Al alloys: FeS/alloy diffusion couples, by S_2 vapour at the dissociation pressure of FeS, and in H_2S-H_2 atmosphere with $1 \leq p_{S_2} \leq 10^3$ Pa. A similar format will be used in this chapter to analyze and discuss the experimental results.

When Fe-Al is exposed to sulfur containing atmospheres at 1173K, several sulfides can form according to the following reactions:



Also, FeS would be converted to the more stable sulfides Al_2S_3 or $FeAl_2S_4$ via the following reactions.



Initially, the sulfides may not be in equilibrium with the alloy in view of their rapid formation. The early stage, which is referred to as "transient sulfidation", is sensitive to surface preparation and the method of exposure to the sulfidizing atmosphere. Eventually, if sulfidation becomes diffusion controlled, the concentrations of the diffusing species at the alloy/scale interface assume fixed values which are determined by alloy bulk composition and the interplay between the diffusion processes in the alloy and sulfide phases. Only sulfides, which are thermodynamically stable with respect to the steady state alloy interfacial concentration, continue to grow.

Construction of the Fe-Al-S ternary isotherm at 1173K is required for the application of ternary diffusion formalism. No Fe-Al-S ternary isotherm has been reported in the literature to the present. This diagram is constructed using the results of phase equilibria in Fe-Al-S system from the previous chapter (section 5.7) and the thermochemical data in the literature. Following this, the experimental results are interpreted in terms of thermodynamic and diffusion data for the Fe-Al-S system. Scale and subscale growth models are proposed to rationalize the experimental observations.

6.2 THERMOCHEMISTRY OF Fe-Al-S SYSTEM AND ITS TERNARY ISOTHERM AT 1173K

A ternary Fe-Al-S isotherm can be constructed for 1173K as shown in Fig. 6.1 using binary phase extents (from Figs. 3.1, 3.4 and 3.9) and other additional results from this investigation.

Pure iron and aluminum dissolve up to 0.05 and 5 a/o sulfur, respectively. These concentrations and the solubility in the alloy are presented by a dotted line on the isotherm shown in Fig. 6.1. From the microprobe results reported in section 5.7.3, Table 5-23, the solubility of Al and Fe, respectively, in Fe_{1-x}S and Al_2S_3 was determined to be 0.6 a/o and 0.3 a/o where each of these phases was equilibrated with alloy and FeAl_2S_4 . The phase field of FeAl_2S_4 was obtained from the microprobe analyses. The construction of two-phase regions containing alloy+ FeAl_2S_4 , alloy+ Al_2S_3 and three-phase triangles consisting of alloy+ Fe_{1-x}S + FeAl_2S_4 , alloy+ FeAl_2S_4 + Al_2S_3 were made using the compositions of the appropriate equilibrated phases. The tie lines (dotted) shown in the two-phase regions are those determined experimentally. Dotted lines in the upper portion of the isotherm are also schematic. The limiting compositions of the metallic phases are taken from the Fe-Al equilibrium diagram.

The aluminum activity values in solid Fe-Al alloys over the range 5-80 a/o Al at 1173K were determined by Elridge and Komarek⁽⁸⁹⁾ as reported in chapter 3 and their values are recorded in Table (6-1). Thermochemistry of iron and aluminum sulfides is reported in Appendix I.

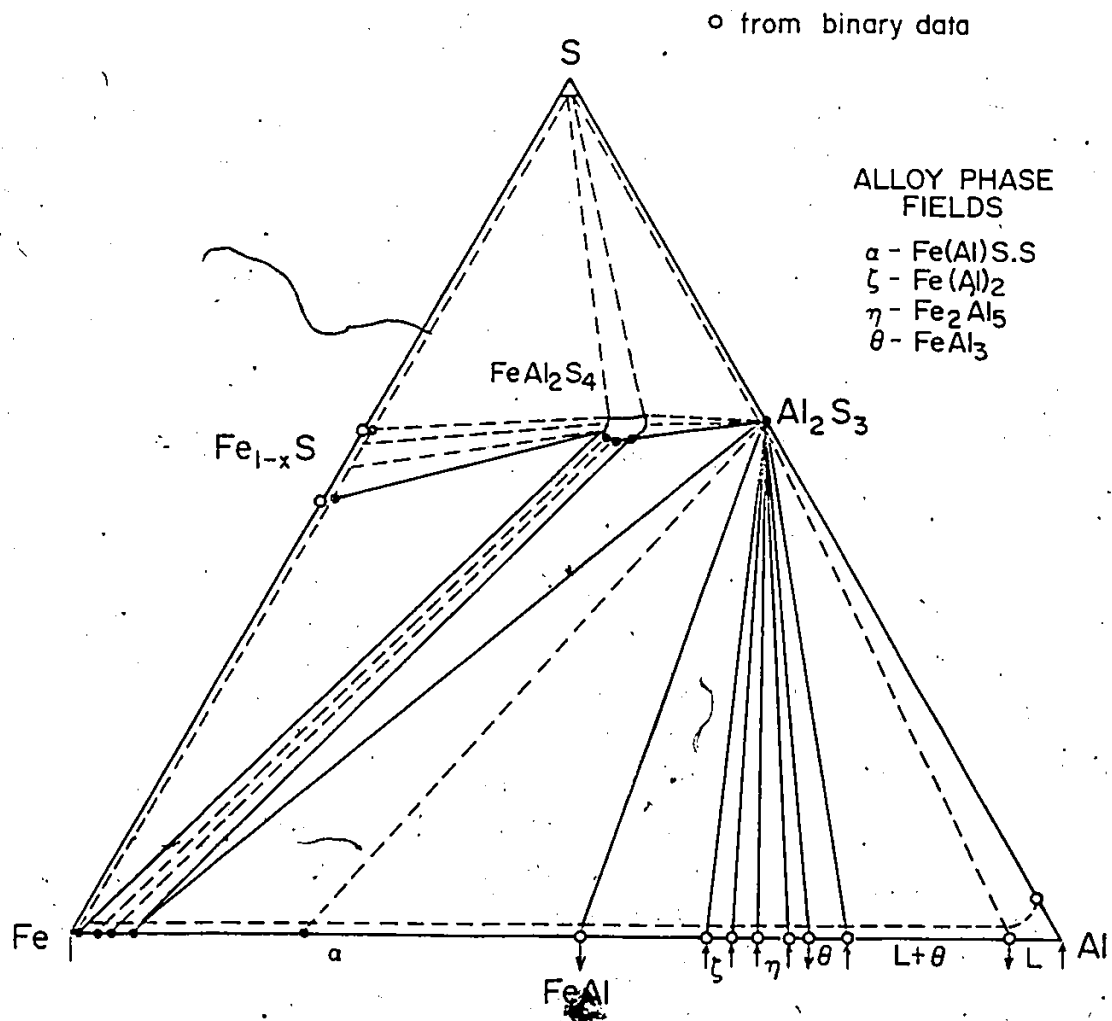
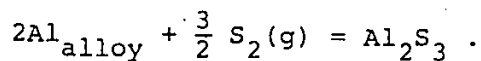


Fig. 6.1 Experimentally determined ternary Fe-Al-S isotherm at 1173K.

The sulfur activity upon equilibrating Al_2S_3 with alloys containing from 6 a/o Al to 80 a/o Al were calculated as follows. Equilibrium between aluminum in an alloy and Al_2S_3 can be expressed as:



$$\text{Equilibrium constant } K = \exp -\frac{\Delta G_f^\circ}{RT} = \frac{a_{\text{Al}_2\text{S}_3}}{a_{\text{Al}}^2 P_{\text{S}_2}^{3/2}}$$

Assuming $a_{\text{Al}_2\text{S}_3} \approx 1$, the sulfur pressure relationship is given by

$$\log p_{\text{S}_2} (\text{Pa}) = \frac{2}{3} \left(\frac{\Delta G_f^\circ(\text{Al}_2\text{S}_3)}{2.303RT} - 2 \log a_{\text{Al}} \right) + \log(101300) \quad (6.6)$$

Substituting the values for $\Delta G_f^\circ(\text{Al}_2\text{S}_3)$, the sulfur activity is calculated as

$$\log a_{\text{S}} = \frac{1}{2} [\log(p_{\text{S}_2} (\text{Pa})/10^5 \text{ Pa})] = -7.54 - \frac{2}{3} \log a_{\text{Al}} \quad (6.7)$$

The sulfur activity for the alloy- Al_2S_3 equilibrium is then calculated as given in Table (6-2) using the Al activity values from Table (6-1).

At equilibrium between the alloy, FeAl_2S_4 and Al_2S_3 , Al atom fraction in the alloy was determined to be 0.059 corresponding to an activity of 3.9×10^{-4} . The corresponding sulfur activity was calculated to be 5.35×10^{-6} using the equilibrium constant for Al_2S_3 .

Atomic Percent of Al	Aluminum Atom Fraction	a_{Al} at 1173K
5	0.05	3.8×10^{-4}
10	0.10	8.1×10^{-4}
15	0.15	1.5×10^{-3}
20	0.20	2.45×10^{-3}
25	0.25	3.7×10^{-3}
30	0.30	5.5×10^{-3}
35	0.35	8.3×10^{-3}
40	0.40	1.35×10^{-2}
45	0.45	2.6×10^{-2}
50	0.50	5.5×10^{-2}
52	0.52	9.8×10^{-2}
60	0.60	9.8×10^{-2}
67	0.67	1.3×10^{-1}
70	0.70	1.3×10^{-1}
75	0.75	4×10^{-1}
80	0.80	7×10^{-1}
100	1	1

Table 6-1 The thermodynamic activity of Al in Fe-Al alloys (89,90).

a/o Al	$\frac{\eta_{Al}}{\eta_{Al} + \eta_{Fe}}$	$-\log a_s$
6	0.06	5.27
10	0.10	5.47
15	0.15	5.65
20	0.20	5.79
25	0.25	5.91
30	0.30	6.026
40	0.40	6.28
45	0.45	6.47
50	0.50	6.69
52	0.52	6.86
60	0.60	6.86
65	0.65	6.86
67	0.67	6.94
70	0.70	6.94
75	0.75	7.26
80	0.80	7.42
100	1.0	7.54

Table 6-2 Sulfur activity for the alloy- Al_2S_3 equilibrium.

Figure 6.2 shows the sulfur activity diagram for the Fe-Al-S system at 1173K. This diagram is semi-schematic and it has been compiled insofar as possible from the results of this investigation and the data given in Table 6-2.

The sulfur activity decreases from 1.2×10^{-4} which is imposed by the Fe-Fe_{1-x}S coexistence to a lower value (not determined) associated with the invariant alloy-Fe_{1-x}S-FeAl₂S₄ equilibrium. The atom fraction of aluminum $\epsilon_{Al} = n_{Al}/n_{Al} + n_{Fe}$ in each phase of the alloy-FeS-FeAl₂S₄ coexistence is 0.0084, 0.012 and 0.566, respectively. These latter values are those determined in the Fe-Al-S isotherm proposed previously in this section.

The sulfur activity in equilibrium with the alloy-FeAl₂S₄-Al₂S₃ coexistence was determined to be 5.35×10^{-6} . The Al atom fraction of each phase is 0.059, 0.658 and 0.992, respectively. FeAl₂S₄ equilibrated with alloys containing from 0.84 up to 5.86 a/o Al. The results available indicate that Al₂S₃ only exists with alloys containing greater than 5.86 a/o Al.

Sulfur activity decreases with increasing Al contents of the alloy until it reaches, at 1173K, 2.9×10^{-7} corresponding to that of Al-Al₂S₃ equilibria. Iron contents of Al₂S₃ in equilibrium with alloys containing up to 22.28 a/o Al were determined and these values range from 0.28 a/o to 0.09 a/o Fe and are given in Table 5-23.

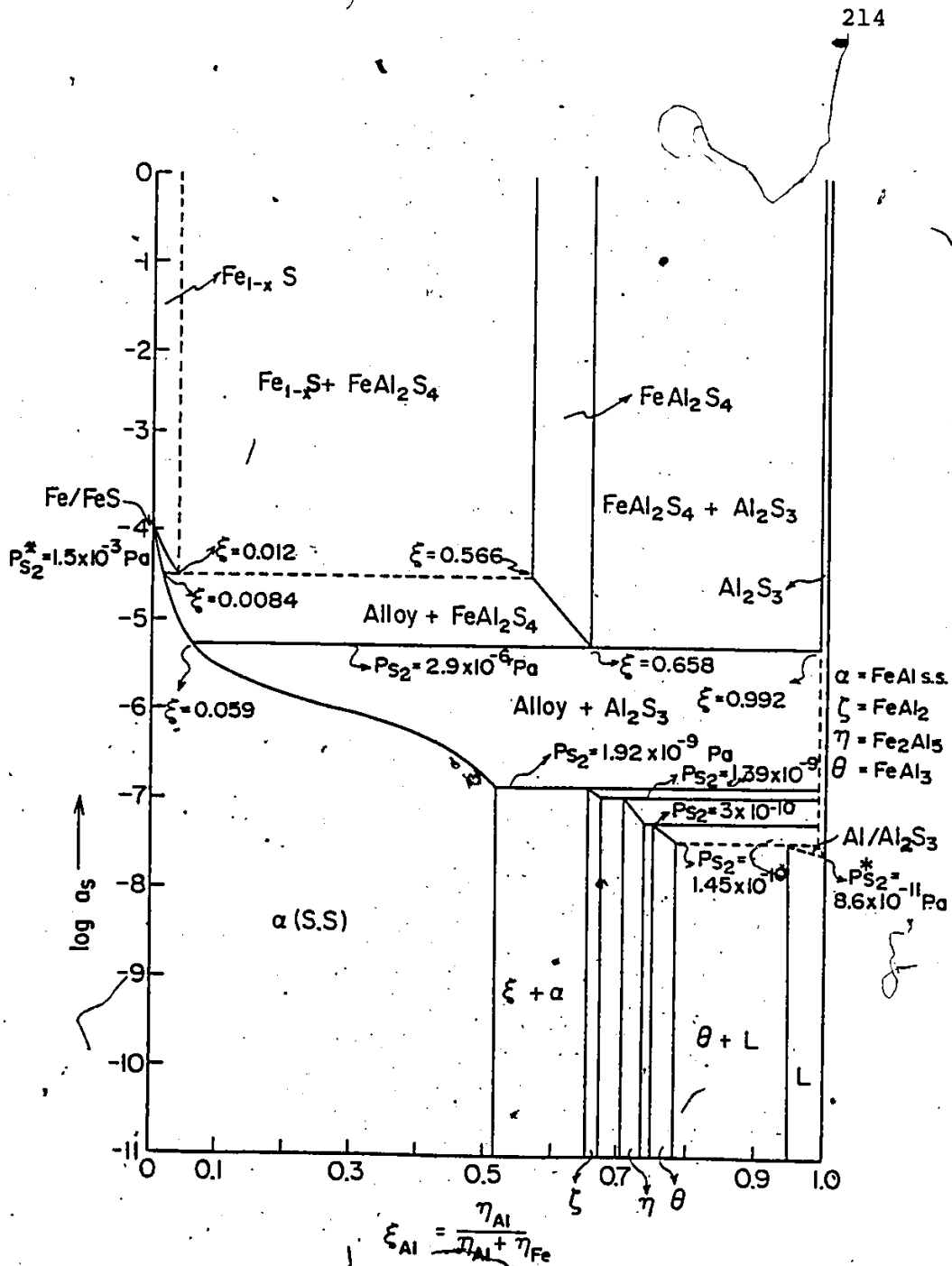


Fig. 6.2 Plot of sulfur activity as a function of aluminum atom fraction at 1173K.

6.3 PERIODIC PRECIPITATION OF SULFIDES IN FeS/Fe-Al ALLOY DIFFUSION COUPLES

6.3.1. Introduction

The Fe-Al alloys containing 6, 9, 18 and 28 at/o Al in the FeS/alloy diffusion couples formed a sulfidation zone consisting of alternate layers of sulfide and metal bands. The sulfidation zone thickened according to a parabolic relation. The rate of sulfidation of these alloys increased with increasing Al content in a linear manner. The individual sulfide layers, which formed parallel to the original alloy/FeS interface, contained a mixture of Al-doped FeS and FeAl_2S_4 . The metal bands were alloy depleted of Al. No change in orientation of these sulfide and metal bands was observed from one alloy grain to the other.

Results from the FeS/Fe-Al alloy diffusion couple studies in the present work differ from the literature on Liesegang periodic precipitation in the following manner.

(i) In the classical description of periodic precipitation, diffusion of the active reactant (either As, Ga, H or O as the case may be) is assumed to not be hindered by the discontinuous precipitate bands. In the present case, sulfur diffusion is blocked by the sulfide ($\text{FeS} + \text{FeAl}_2\text{S}_4$) bands since these sulfides grow predominantly by metal migration. Sulfur diffuses only in the metal bands and alloy substrate.

(ii) The distance between consecutive precipitation zones increases with depth in the Liesegang type of precipitation.

This relationship also applies to precipitation of the sulfidation zones in the FeS/alloy diffusion couples but the individual metal band thicknesses remained constant irrespective of depth for a particular alloy.

(iii) Thicknesses of precipitate bands have been actually ignored in the classical description of Liesegang phenomenon advanced by investigators since they have found insignificant growth of the layers of precipitate with time. Sulfide layers in the FeS/Fe-Al alloy diffusion couples, nevertheless, show considerable increase in their thicknesses, particularly towards the sulfidation zone/alloy interface. This behaviour suggests that a diffusional growth mechanism is responsible for thickening of the sulfide phases by sulfidation of the metal bands.

In view of these differences, it is evident that the available mathematical analyses of periodic precipitation cannot be used directly in the Fe-Al-S system to precalculate the Jablczynski's spacing coefficient or the parabolic rate constants as expressed by Eqns. (2.60) and (2.61). Instead, a diffusion analysis is made in the following section to calculate the inward precipitation distance of the first line of precipitates from the FeS/Fe-Al alloy interface, which form by the mode of internal sulfidation. This calculated precipitation distance is compared where possible with the experimentally observed distance in several alloys. In a later section, a diffusion model is then presented to account for the diffusional growth of the sulfide bands containing $\text{FeS} + \text{FeAl}_2\text{S}_4$.

6.3.2 Calculation of the First Precipitation Distance in the Alloy and Mechanism of Periodic Precipitation

To calculate the first precipitation distance in the FeS/alloy diffusion couples, it is essential to calculate the distance at which the activity product ($a_S^3 a_{Al}^2$) achieves a maximum value when sulfur is diffusing from the FeS/alloy interface into the Fe-Al alloy for Al_2S_3 precipitation. Auxiliary calculations in Fe-Al-S system using available methods to determine ternary solution thermodynamic parameters like ϵ_S^{Al} show that these interaction terms exhibit values close to zero for Henrian solution behaviour. Therefore a diffusional analysis can be carried out in terms of concentrations rather than activities. Accordingly, the concentration product is defined as

$$K_n = N_{Al}^2 \cdot N_S^3 \quad (6.8)$$

where N_S and N_{Al} are the concentrations of sulfur and aluminum in atom fractions.

The assumption of Al_2S_3 precipitation in these calculations is reasonable, since the Fe-Al-S ternary isotherm presented in section 6.2 demonstrates that the alloys containing more than 0.058 atom fraction of Al equilibrate with Al_2S_3 . The calculation is carried out assuming that no precipitation has occurred. The concentrations $N_S(x,t)$ and $N_{Al}(x,t)$ of S and Al, respectively, are given by the well known error function solutions to Fick's second law (Eqns. 2.26 and 2.29) with the initial and boundary conditions given by

$$N_S = N_S^0 \quad \text{for } x=0 \quad \text{at } t > 0 \quad (6.9)$$

$$N_S = 0 \quad \text{for } x > 0 \quad \text{at } t = 0 \quad (6.10)$$

for $N_S(x, t)$, and

$$N_{Al} = 0 \quad \text{for } x=0 \quad \text{at } t > 0 \quad (6.11)$$

$$N_{Al} = N_{Al}^0 \quad \text{for } x > 0 \quad \text{at } t = 0 \quad (6.12)$$

for $N_{Al}(x, t)$. Hence,

$$N_S(x, t) = N_S^0 \operatorname{erfc}\left(\frac{x}{2\sqrt{D_S t}}\right) \quad (6.13)$$

$$N_{Al}(x, t) = N_{Al}^0 \operatorname{erf}\left(\frac{x}{2\sqrt{D_{Al} t}}\right) \quad (6.14)$$

where D_S and D_{Al} are the diffusion coefficients of sulfur and aluminum respectively. The concentration product is given by

$$K_n = N_{Al}^0{}^2 N_S^0{}^3 \left[\operatorname{erf} \frac{x}{2\sqrt{D_{Al} t}}\right]^2 \left[\operatorname{erfc} \frac{x}{2\sqrt{D_S t}}\right]^3 \quad (6.15)$$

A maximum value of the concentration product can be obtained by differentiating the concentration product and equating to zero. That is

$$\frac{dK_n}{dx} = 0 \quad (6.16)$$

and the following expression is obtained upon substituting Eqn. (6.16) in (6.15).

$$\frac{3}{2} \left[\operatorname{erf} \frac{x}{2\sqrt{D_{Al}t}} \cdot \exp\left(-\frac{x^2}{4D_S t}\right) \right] = \left(\frac{D_{Al}}{D_S}\right)^{\frac{1}{2}} \left[\operatorname{erfc}\left(\frac{x}{2\sqrt{D_S t}}\right) \exp\left(-\frac{x^2}{4D_{Al}t}\right) \right] \quad (6.17a)$$

Equation (6.17a) was solved numerically by the method of iteration for known values of D_S and D_{Al} to obtain a value for $\frac{x}{\sqrt{t}}$. For $D_S = 1.2 \times 10^{-9} \text{ cm}^2/\text{s}$, $D_{Al} = 2 \times 10^{-10} \text{ cm}^2/\text{s}$

$$\frac{x}{\sqrt{t}} = 3.18 \times 10^{-6} \text{ cm/s}^{\frac{1}{2}} \quad (6.17b)$$

Substituting Eqn. (6.17b) in (6.15) the maximum concentration product is obtained as

$$K_n^{\max} = 5 \times 10^{-15} \quad (6.17c)$$

This value of K_n^{\max} is compared with the solubility product data from the equilibrium constant determined from the free energy of formation of Al_2S_3 at 1173K (Appendix I).

$$K_{S_P}^{\text{Al}_2\text{S}_3} = \frac{K}{\gamma_{Al}^2 \gamma_S^3} = \frac{2.46 \times 10^{-23}}{\gamma_{Al}^2 \gamma_S^3} \quad (6.18)$$

From the binary Fe-Al alloy data at 1173K, the activity coefficient of Al, γ_{Al} , is 5.6×10^{-3} . The activity coefficient of sulfur in liquid Fe-Al alloys at 1823K has a value of 3.2 but its variation with temperature or type of condensed alloys is not known. Nevertheless, a value of 7.8×10^{-19} is obtained for the solubility product of Al_2S_3 at 1173K, upon substituting the value of γ_{Al} and assuming $\gamma_S = 1$ in Eqn. (6.18). Moreover, as shown in Appendix I, there is a large divergence in values

of the free energy of formation of Al_2S_3 in the literature ranging from $-368,456$ J to $-782,131$ J/mole of Al_2S_3 at 1173K.

This variation for the free energy of formation gives rise to a variation of the $K_{\text{sp}}^{\text{Al}_2\text{S}_3}$ value from 6×10^{-18} to 1.9×10^{-31} .

A comparison, accordingly, cannot be made of the ratio $K_n^{\text{max}}/K_{\text{sp}}^{\text{Al}_2\text{S}_3}$ to determine the degree of supersaturation for Al_2S_3 precipitates.

To obtain the first precipitation distance, concentration profiles of sulfur and aluminum were calculated using Eqns. (6.13) and (6.14) for various periods of time as shown in Fig. 6.3(a). Their values are presented on a logarithmic scale to present sulfur and aluminum concentrations on the same graph. Plots of the corresponding concentration product of aluminum and sulfur are shown in Fig. 6.3(b) as a function of distance for various periods of time. It is evident from Fig. 6.3(b) that the concentration product goes through a maximum. When this maximum exceeds the calculated maximum concentration product (K_n^{max}) of 5×10^{-15} at a given time, precipitation is assumed to occur at the distance where the concentration product has exceeded K_n^{max} . This distance is obtained from Fig. 6.3(b) as $1.3 \mu\text{m}$ to $1.5 \mu\text{m}$.

The mechanism of precipitation and growth of the sulfide layers in Fe-6, 9, 18 and 28 Al alloys can be illustrated using schematic concentration profiles for sulfur and aluminum as shown in Fig. 6.4. Figure 6.4(a) shows the concentration profiles of S and Al in an alloy before-onset of internal

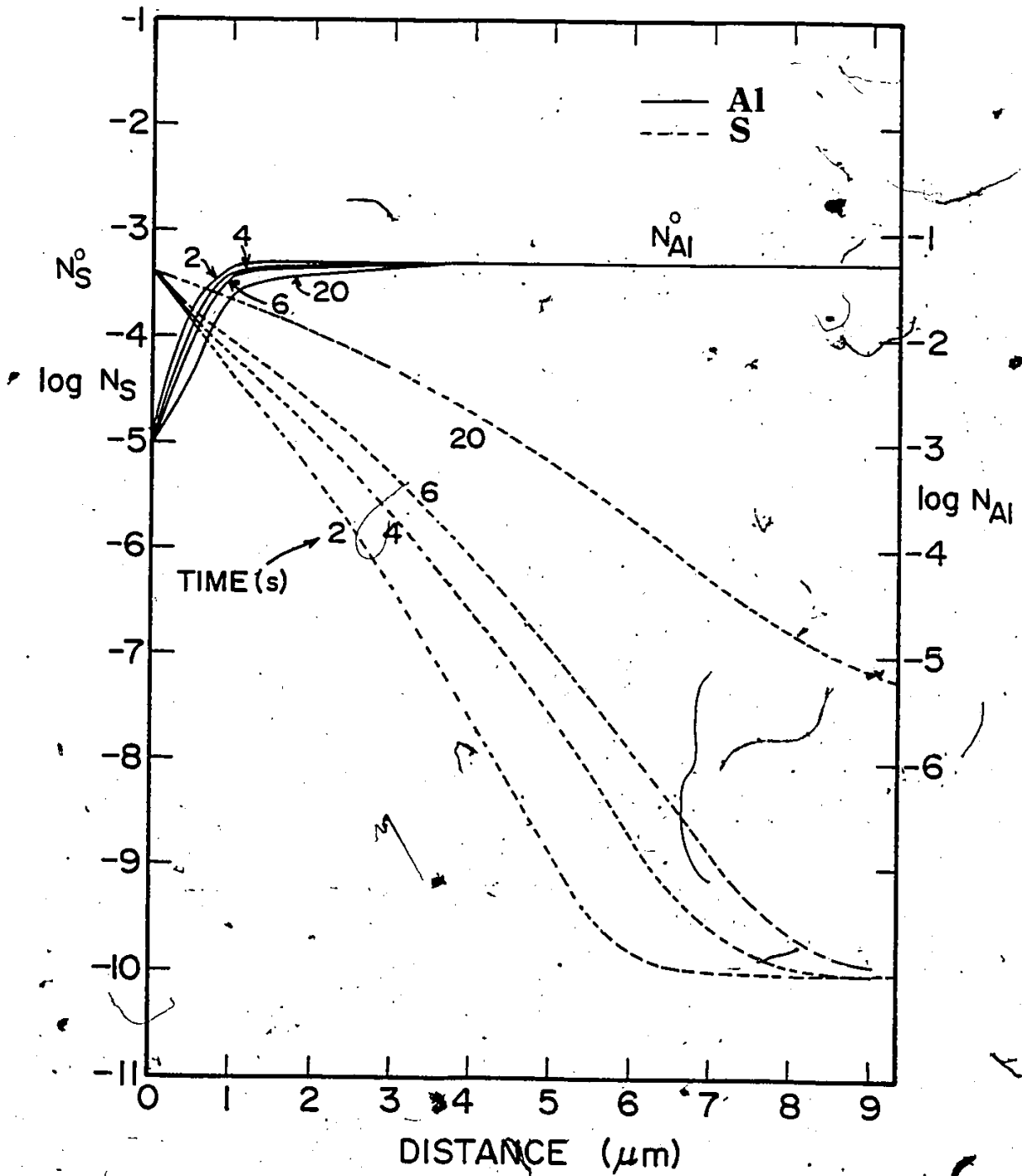


Fig. 6.3a) Concentration profiles of aluminum and sulfur in Fe-6 Al alloy for various time periods.

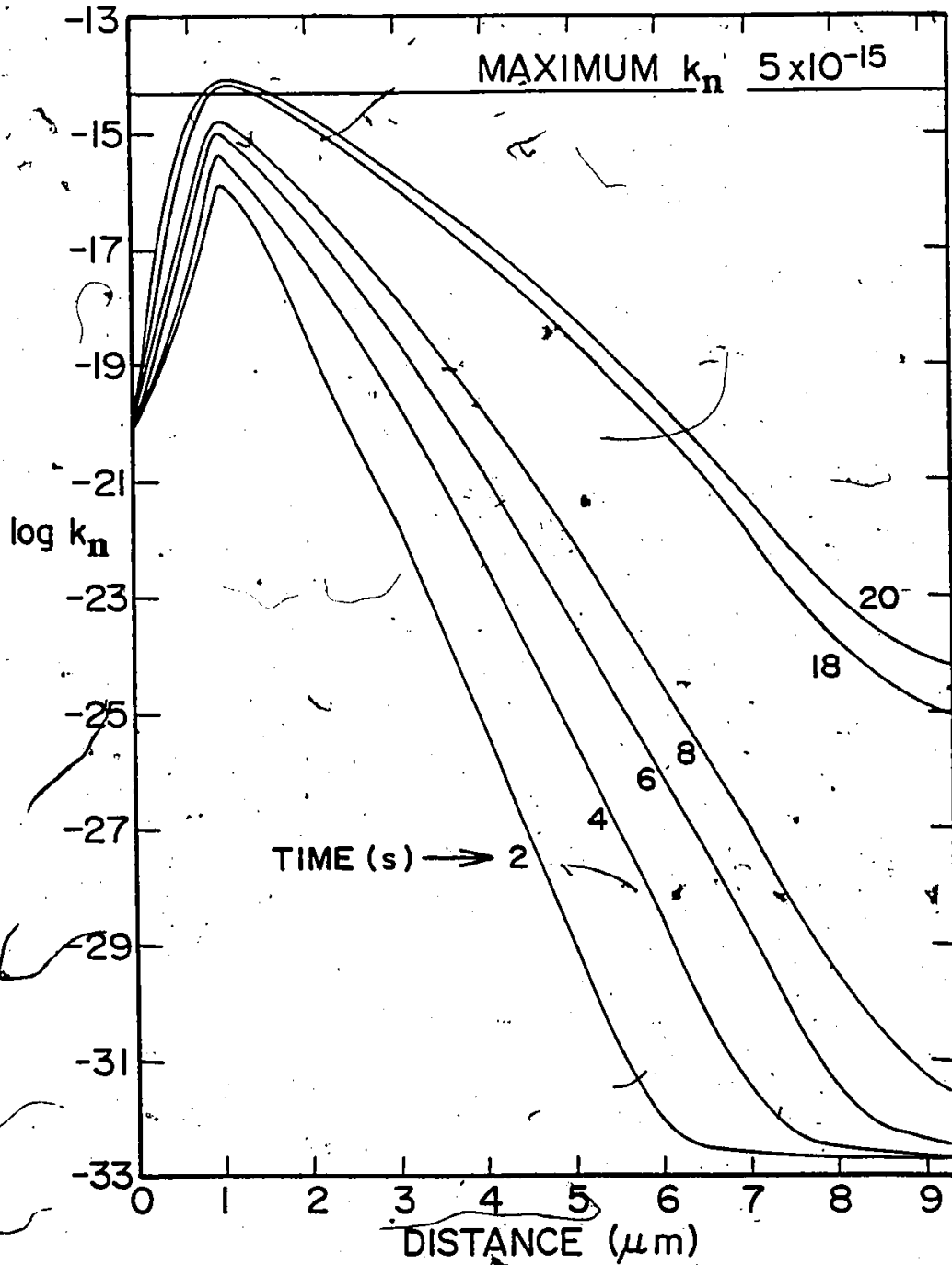


Fig. 6.3b) Plots of concentration product of aluminum and sulfur by Eqn. (6.17) in Fe-6 Al alloy for various periods of time.

sulfide precipitation. After about 18 seconds (Fig. 6.3 (b)), precipitation of Al_2S_3 takes place at a distance of x_1 from the FeS/alloy interface since the concentration product $N_{\text{Al}}^{*2}N_{\text{S}}^{*3}$ exceeds its maximum value. After Al_2S_3 precipitation, the concentration profiles are of the shapes shown in Fig. 6.4(b). The change in slope in the sulfur concentration profile reflects the portion of sulfur continually consumed by aluminum arriving by diffusion and causing continued growth of the Al_2S_3 precipitates at x_1 . As the sulfidation reaction proceeds, Al_2S_3 is converted to FeAl_2S_4 via reaction 6.5(b) and FeS containing a maximum of about 1 a/o Al continue to grow around the FeAl_2S_4 precipitates. The concentration profiles around the precipitates during these stages of reaction are schematically shown in Figs. 6.4(c) and (d). Since FeS is a fast growing phase, its continued growth by iron and aluminum diffusion leads to the development of a continuous band containing FeS and FeAl_2S_4 , the latter being embedded as precipitates in the FeS phase. At this stage of the reaction, this two-phase sulfide band co-exists with remnants of the internal sulfidation zone containing isolated sulfide precipitates as depicted in Fig. 6.4(e). Once the internal sulfide precipitates have been entirely converted to a sulfide band, further sulfur for diffusion into the alloy is supplied by the dissociation of FeS at the sulfide band/alloy interface. This sulfidation stage is shown in Fig. 6.4(f).

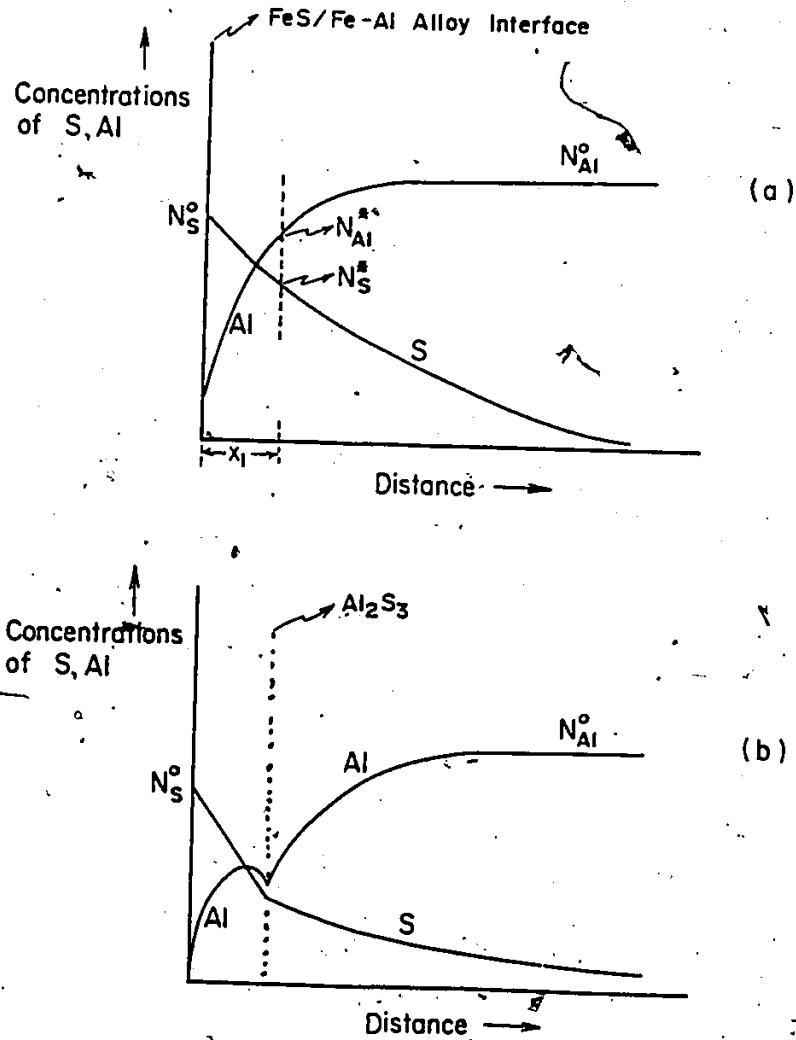


Fig. 6.4 Schematic concentration profiles of Al and S (a) before and (b) after precipitation of aluminum sulfide.

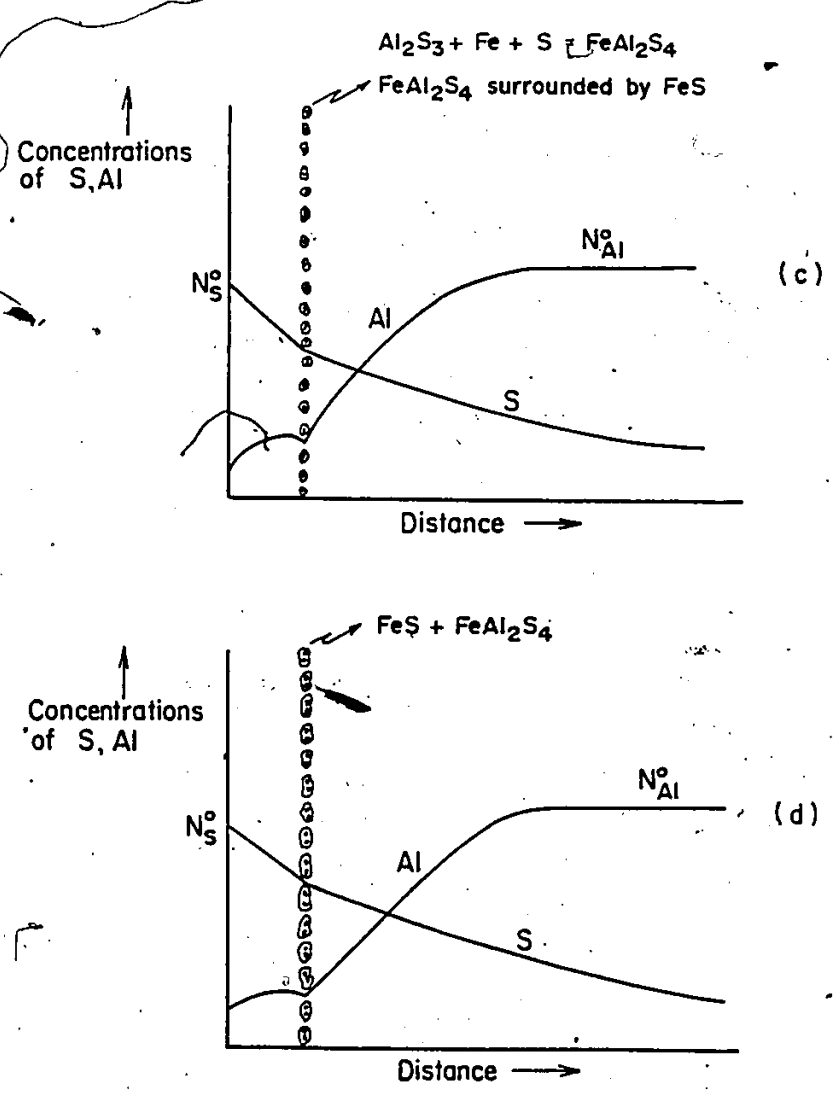


Fig. 6.4 cont'd ..
(c) and (d). Schematic profiles of Al and S in the vicinity of precipitation zone.

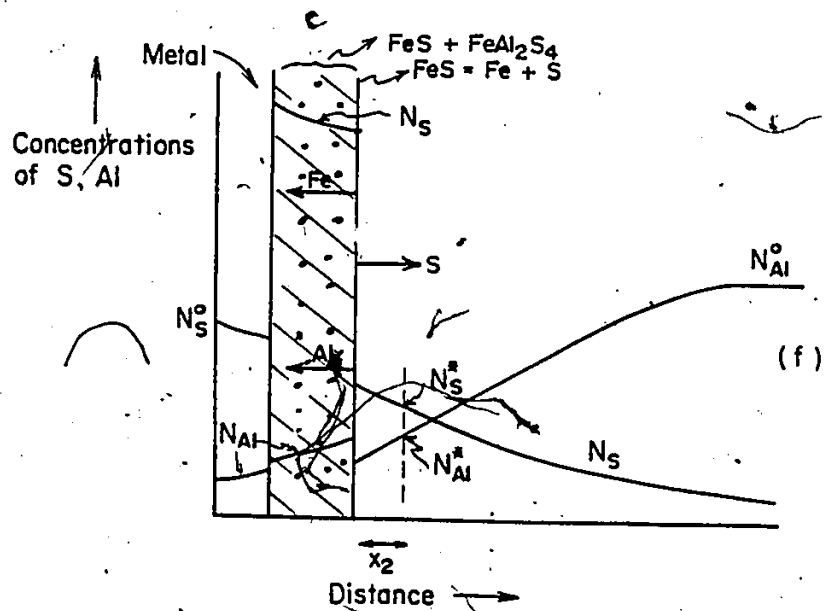
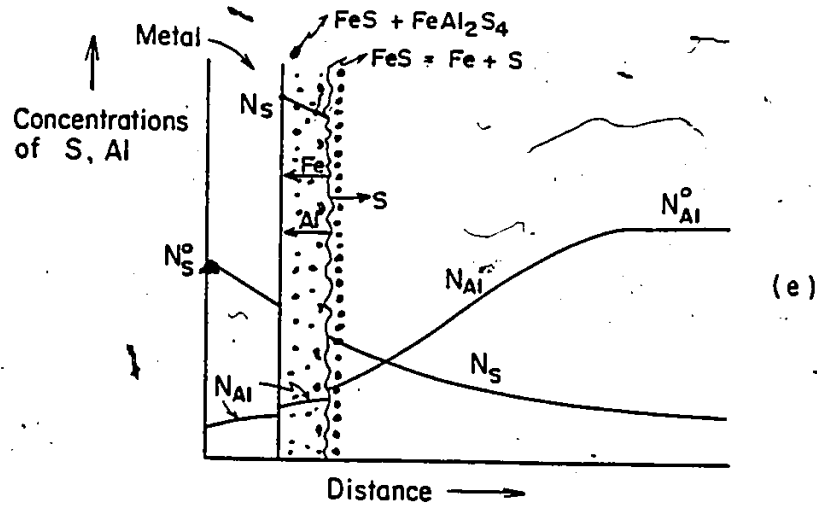


Fig. 6.4 cont'd ..

(e) and (f) Schematic concentration profiles of Al and S in the vicinity of a growing sulfide band.

With increase in time, the aluminum concentration of the sulfide band/alloy interface falls to a very small level, $\ll 1$ a/o. The concentrations of aluminum and sulfur are then inadequate to support the continued growth of any of the sulfide phases as shown by the schematic concentration profiles in Fig. 6.4(f). Therefore, the reaction front ceases to advance. Further precipitation would then only occur at a distance ahead of the complete band when the concentration product $N_{Al}^2 \cdot N_S^2$ exceeds its maximum value for precipitation of Al_2S_3 . Upon precipitation of all the three sulfides Al_2S_3 , $FeAl_2S_4$ and FeS , growth of the latter two sulfides leads to the beginning of a new sulfide band, the growth of this sulfide band continuing for a longer time as compared to the preceding band. This gives rise to an increase in sulfide band thicknesses with depth as observed in the experimental measurements (Figs. 5.7 and 5.9). Since, sulfur and aluminum diffusivities differ within an order of magnitude in Fe-Al alloys (Table 6-3), periodic changes in concentrations are expected in this system as found in other systems exhibiting periodic precipitations (Table 2-1).

Within assigned standard deviation values, no noticeable difference was observed between the consecutive average metal band thicknesses in the sulfidation zones. It is commonly observed in the Liesegang phenomenon, however, that the distance between consecutive precipitation zones increases with depth. In the present case, it was not possible to ascertain this

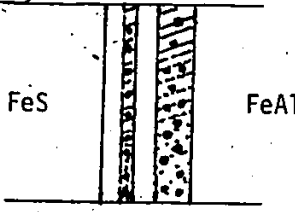

Couple	Outer Reactant	Inner Reactant	Precipitates	Diffusion Parameters
	S	Al	 FeS and FeAl ₂ S ₄	$D_S = 1.2 \times 10^{-9} \text{ cm}^2/\text{s}$ $D_{Al} = 2 \times 10^{-10} \text{ cm}^2/\text{s}$ $\frac{D_S}{D_{Al}} = 6.$

Table 6-3. Diffusion parameters and mode of precipitation in FeS/Fe-Al alloy diffusion coupled at 1173K.

effect. The mitigation of this effect can be possibly associated with metal consumption giving rise to continuous sulfide bands of larger thickness with depth into the alloy.

The effect of aluminum concentration of the parabolic sulfidation rate of Fe-6 to 28 Al alloys was presented in Fig.

5.2. A linear increase in the penetration rate of the sulfidation zone was observed ($k_s = 0.265 N_{Al}^0$). The spacing coefficient k was found to be independent of alloy aluminum concentration (Fig. 6.10). Considering Eqns. (5.1), (5.2) and (5.3), the following relationships can be obtained.

$$\Delta \text{SULF}_n^{\text{max}} = 0.265 N_{Al}^0 (k-1) \sqrt{t_n} \quad (6.19)$$

where, $\Delta \text{SULF}_n^{\text{max}}$ is the sulfide band thickness at maximum depth x_n^{max} , time t_n and N_{Al}^0 is the bulk atom fraction of aluminum in the alloy. Therefore,

$$\Delta \text{SULF}_n^{\text{max}} = k_1 N_{Al}^0 \quad (6.20)$$

where, $k_1 = 0.265(k-1)\sqrt{t_n}$ is a constant. This linear dependence of sulfide thickness at maximum depth x_n^{max} on the alloy aluminum concentration is verified in Fig. 6.5 from the data presented in Table 5-7, yielding a correlation coefficient of 0.98.

In addition, alloys of higher aluminum concentration exhibited a greater number of sulfide bands. The increase in aluminum concentration, accordingly, leads to a smaller precipitation distance in the alloy (smaller values of x_1 in Fig. 6.4(a))

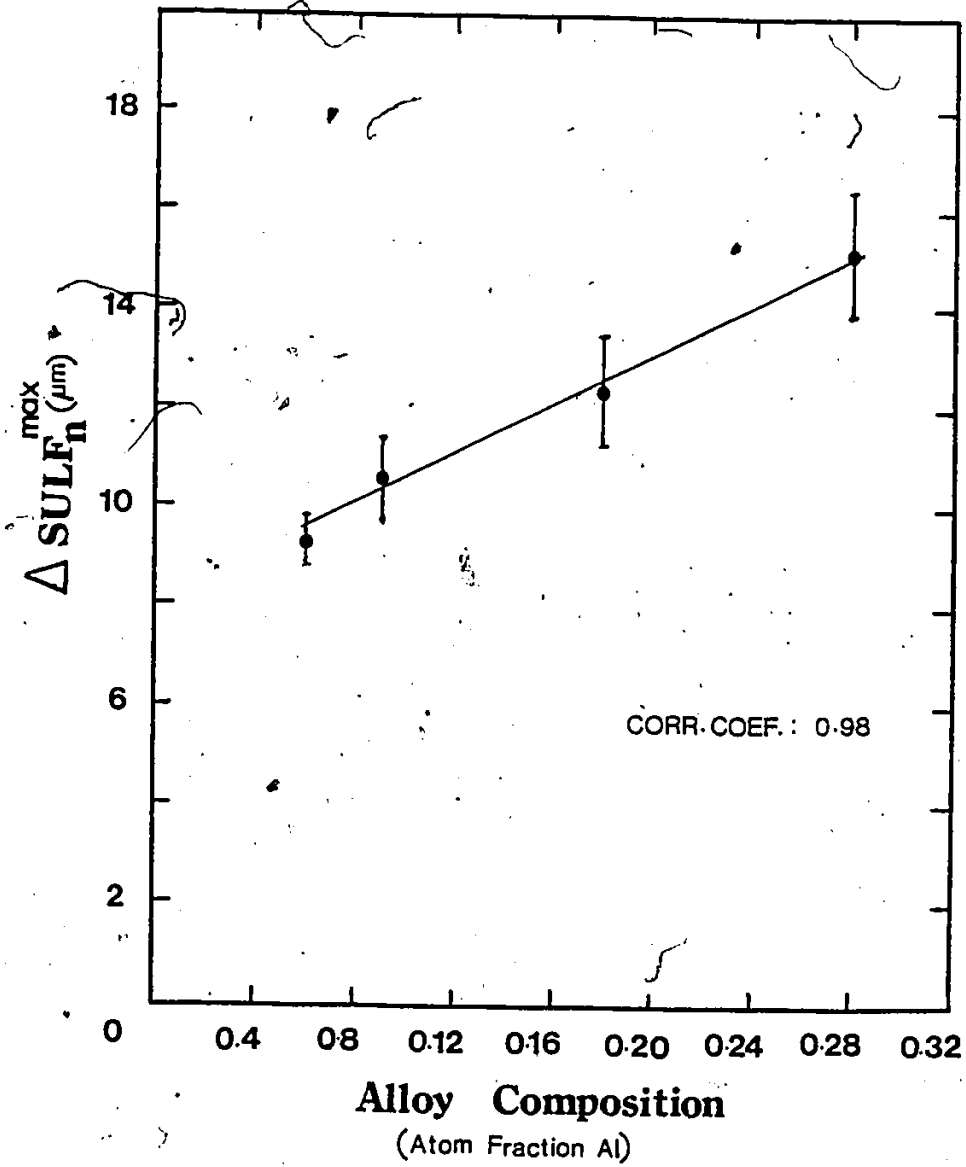


Fig. 6.5 Verification of relationship (6.20) between sulfide thickness vs. alloy composition.

and hence smaller metal band thicknesses. Because of the experimental difficulties in measuring the metal band thicknesses at brief exposures such as 18 to 20 seconds, the average metal band thicknesses after a time of 1500s was compared. Micrographs illustrating the onset of periodic internal sulfidation behind the innermost metal band for the Fe-6 and 18 Al alloys is shown in Fig. 6.6(a) and (b) respectively. The dimension of the metal bands corresponds to $4 \sim 5 \mu\text{m}$ to $3 \sim 4 \mu\text{m}$ for Fe-6 Al and Fe-18 Al alloys respectively. The interfacial aluminum alloy concentration in front of the sulfide band (Fig. 6.4(f)) in alloys of high aluminum concentration falls below $\ll 1 \text{ a/o}$ at longer times. This increase in time required for aluminum depletion and stabilization of FeS consequently gives rise to higher sulfide thicknesses with increase in aluminum content in the alloy (Fig. 6.5).

6.3.3 Diffusion Model for the Growth of a Sulfide Band

A diffusion model is now advanced to account for the growth of sulfide bands in FeS/Fe-6, 9, 18 and 28 Al alloy diffusion couples. Since FeS is the predominant phase in the sulfidation zone of these alloys, order of magnitude calculations demonstrate that diffusional growth of the sulfide bands by metal migration is responsible for their observed sulfidation rates. For example, Fe diffuses in FeS at the rate of $10^{-5} \text{ cm}^2/\text{s}$ at 1173K whereas sulfur diffuses in the metal at the rate of $10^{-9} \text{ cm}^2/\text{s}$.

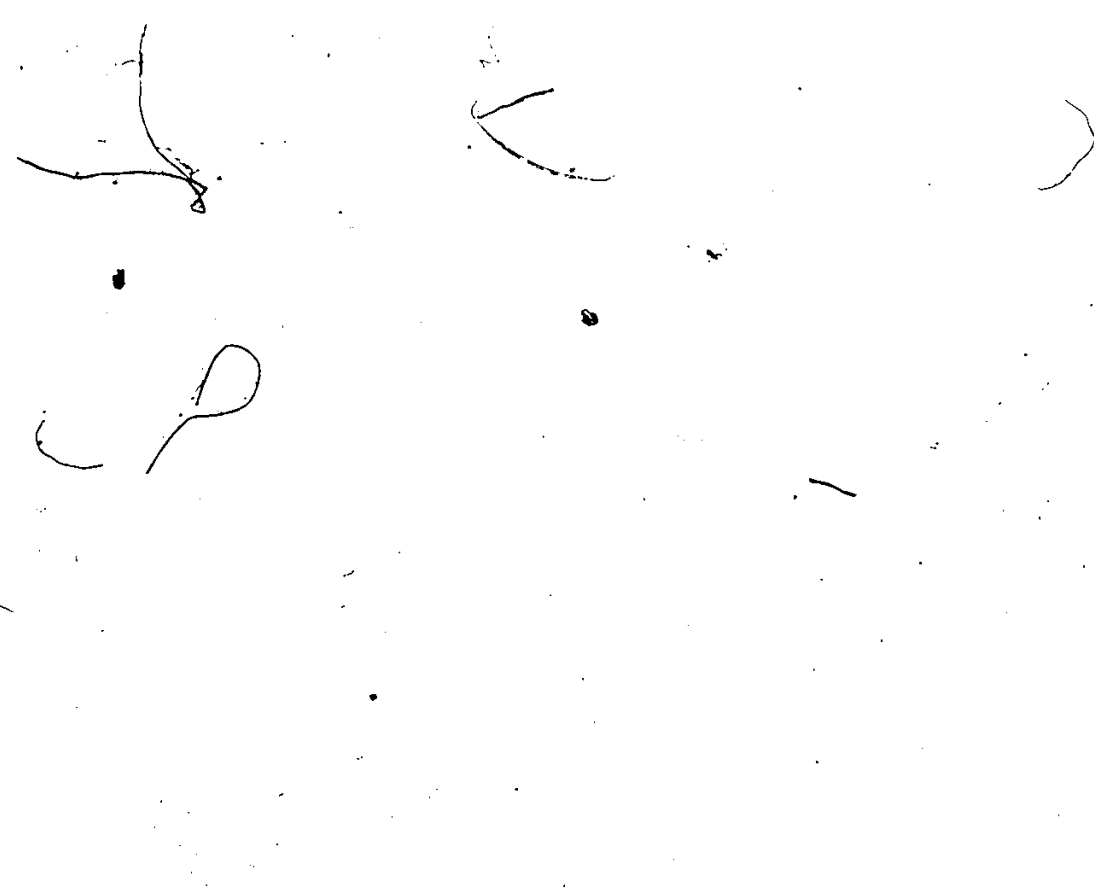
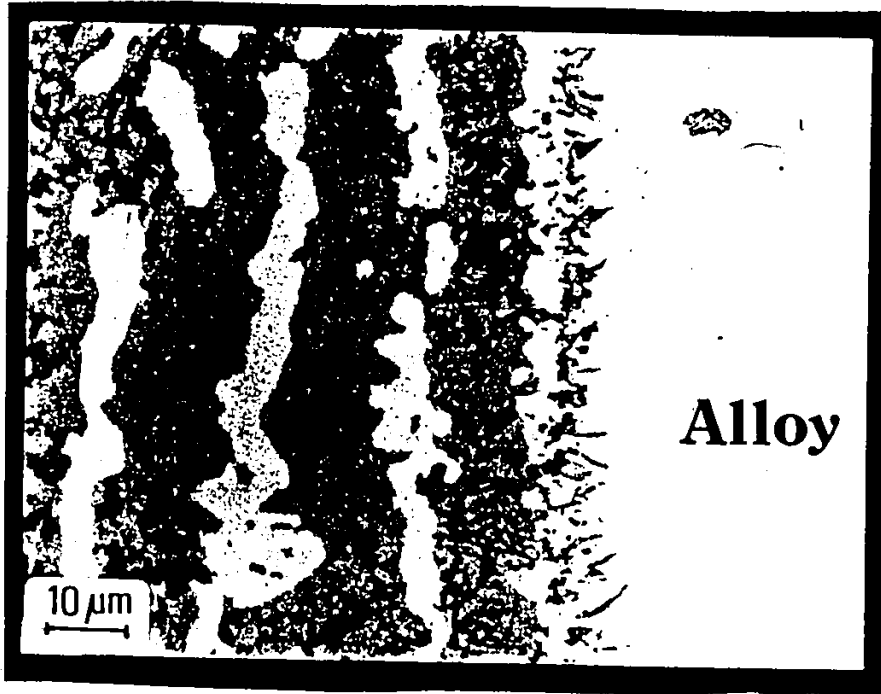
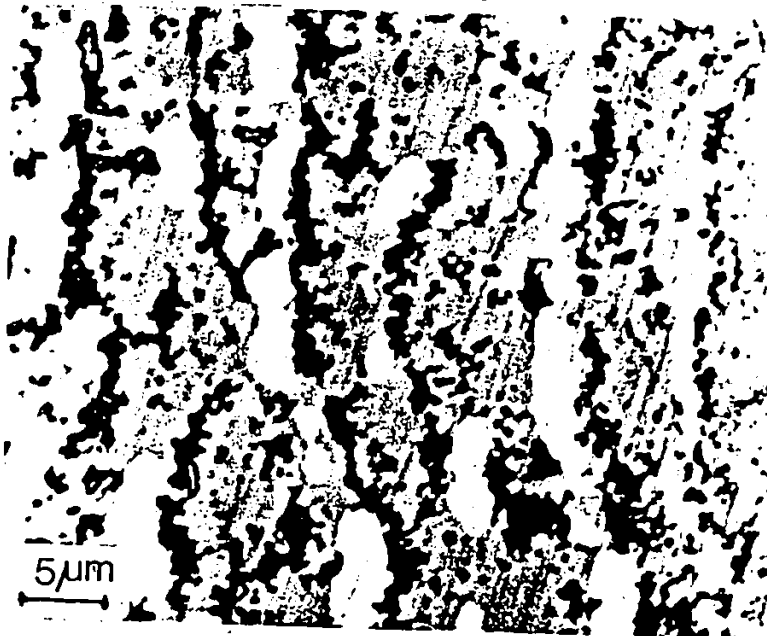


Fig. 6.6 Optical photomicrographs of the cross-section of the sulfidation zone during the precipitation and growth of sulfide phases for (a) FeS/Fe-6 Al and (b) FeS/Fe-18 Al diffusion couples.



a.



b.

A diffusional model is considered in Fig. 6.7, where the growth of the sulfide layer is expressed by a parabolic rate relationship

$$z^2 = 2k_p' t + C \quad (6.21)$$

Here, z is the sulfide thickness at time t , k_p' is the parabolic rate constant for the growth of the sulfide layer and C is a constant. In this model, for simplicity, the FeAl_2S_4 precipitates will be considered not to interfere with the diffusion of Fe and Al in the sulfide. The sulfide thickness z can be expressed in terms of the alloy consumption thickness y as follows:

$$z = y \cdot \frac{M_{\text{FeS}} \rho_{\text{alloy}}}{\rho_{\text{FeS}} M_{\text{alloy}}} \quad (6.22)$$

where M and ρ are molecular weights and densities respectively. Differentiation of Eqn. (6.21) and substituting the M and ρ values in Eqn. (6.22), gives the following pair of equations

$$\frac{dz}{dt} = \frac{k_p'}{(2k_p' t + C)^{1/2}} \quad (6.23)$$

$$z = 2.57 y \quad (6.24)$$

Using Fick's law for diffusion of Al in the alloy phase

$$\frac{\partial N_{\text{Al}}}{\partial t} = D_{\text{Al}}^{\text{alloy}} \frac{\partial^2 N_{\text{Al}}}{\partial x^2} \quad (6.25)$$

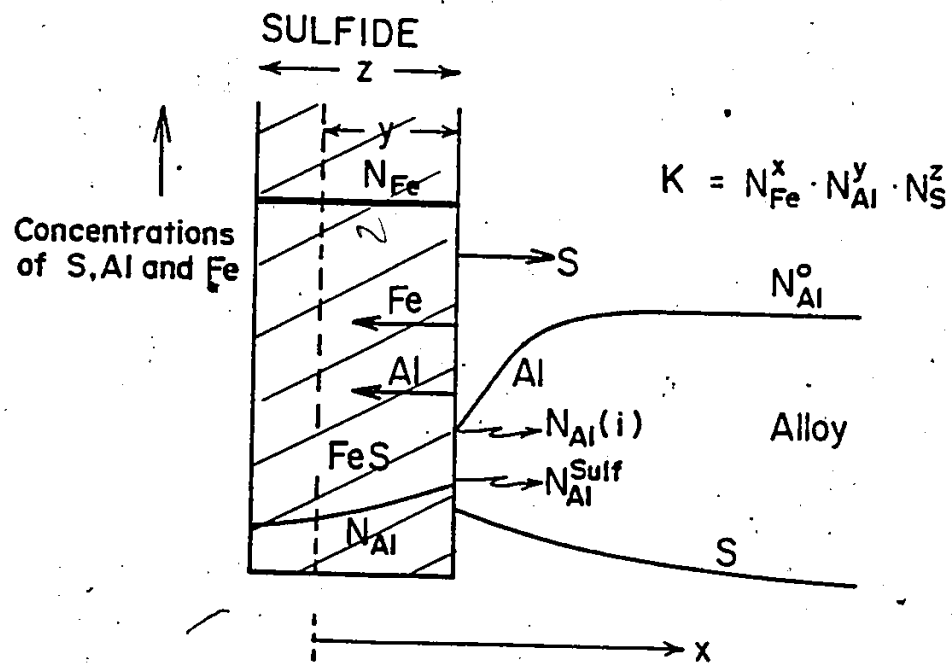


Fig. 6.7 Schematic model for the growth of a sulfide band. Concentration profiles of Fe, Al and S are shown in the growing sulfide band and the adjacent alloy.

where D_{Al}^{alloy} is the alloy interdiffusion coefficient assumed to be independent of composition. The initial condition for Eqn. (6.25) is

$$N_{Al} = N_{Al}^0 \quad \text{at all } x, \quad t = 0 \quad (6.26)$$

In a small increment of time, dt , the alloy/sulfide interface is displaced by a distance, dy , and the sulfide increases in thickness by dZ . This movement of the alloy/sulfide interface releases $N_{Al}^{(i)} \cdot dy$ amount of aluminum into the sulfide. However, the sulfide receives $N_{Al}^{sulf} \cdot dZ$ of Al during this time and a part diffuses away into the sulfide from the interface to assist in the growth of $FeAl_2S_4$ precipitates. Thus the effective Al flux from the alloy is

$$N_{Al}^{sulf} \cdot \frac{dZ}{dt} + D_{Al}^{sulf} \left[\frac{\partial N_{Al}}{\partial x} \right]_{x=y}^{sulf} - N_{Al}^{(i)} \cdot \frac{dy}{dt}$$

This is equated to the concentration gradient at the alloy surface;

$$D_{Al}^{alloy} \left[\frac{\partial N_{Al}}{\partial x} \right]_{x=y}^{alloy} = N_{Al}^{sulf} \cdot \frac{dZ}{dt} + D_{Al}^{sulf} \left[\frac{\partial N_{Al}}{\partial x} \right]_{x=y}^{sulf} - N_{Al}^{(i)} \frac{dy}{dt} \quad (6.27)$$

where D_{Al}^{sulf} is the diffusivity of Al in the sulfide. Upon re-arranging (6.23), (6.24) and (6.27),

$$0.39k_p'(2k_p't+C)^{-\frac{1}{2}}N_{Al}^{(i)} + D_{Al}^{alloy} \left[\frac{\partial N_{Al}}{\partial x} \right]_{x=y}^{alloy}$$

$$= \frac{D_{Al}^{sulf} \cdot N_{Al}^{sulf}}{\sqrt{\pi D_{Al}^{sulf} t}} + N_{Al}^{sulf} k_p'(2k_p't+C)^{-\frac{1}{2}} \quad (6.28)$$

or

$$\alpha \cdot N_{Al}^{(i)} + \beta \cdot \frac{\partial N_{Al}}{\partial x} = \gamma \quad \text{at } t > 0 \quad (6.29)$$

where $\alpha = 0.39 k_p'(2k_p't+C)^{-\frac{1}{2}}$

$$\beta = D_{Al}^{alloy}$$

and $\gamma = \frac{D_{Al}^{sulf} \cdot N_{Al}^{sulf}}{\sqrt{\pi D_{Al}^{sulf} t}} + N_{Al}^{sulf} k_p'(2k_p't+C)^{-\frac{1}{2}}$

Thus, solution of equations (6.25), (6.26) together with (6.29) will give the concentration profiles of aluminum in the alloy as a function of time.

Equation (6.25) was solved numerically for the aluminum concentration profile in front of the growing sulfide band, using Eqns. (6.26) and (6.29) for initial and boundary conditions respectively. These concentration profiles are plotted in Fig. 6.8. It is observed from this figure that with increase in sulfidation time, the depth of Al depletion increases and the aluminum concentration gradient decreases. The interfacial concentration value of Al decreases slowly with time. Ultimately, the sulfide band stops growing when the concentration product

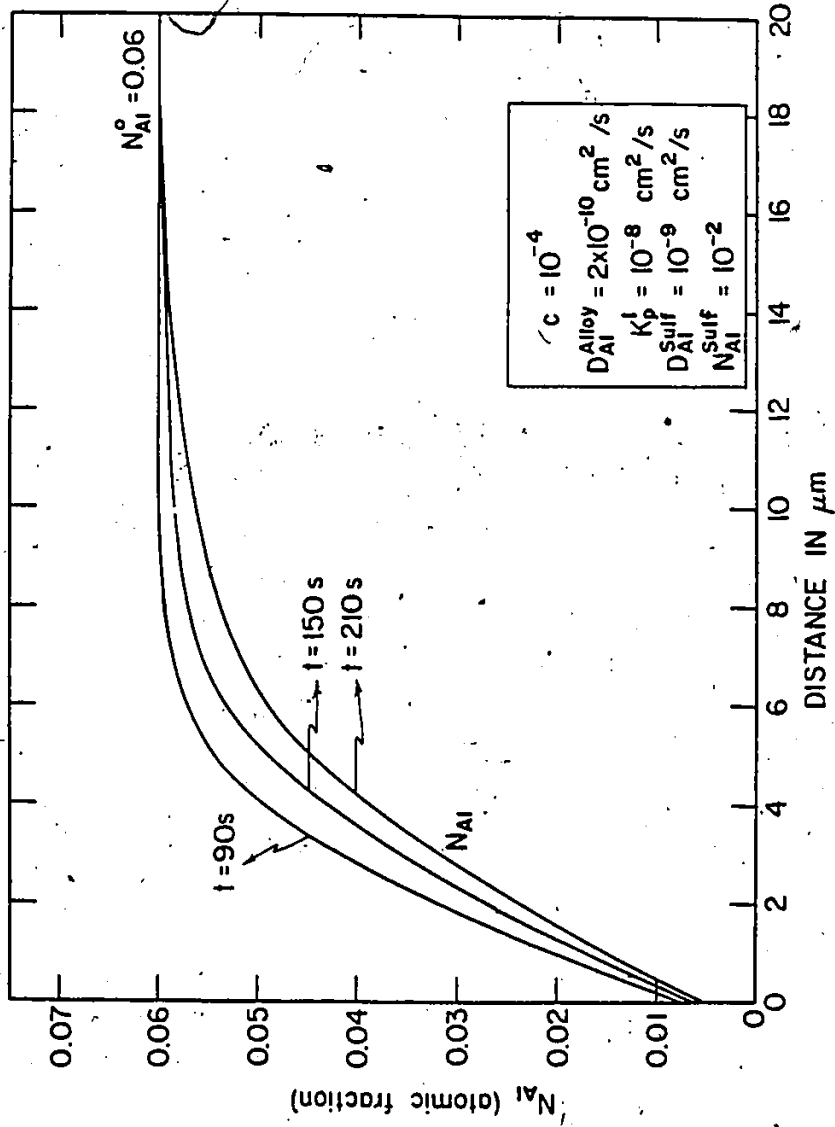


Fig. 6.8 Concentration profiles of Al in front of a growing sulfide band for various time periods according to Eqns. (6.27), (6.28) and (6.31) at 1173K.

$N_{Fe}^x N_{Al}^y N_S^z$ at the sulfide/alloy interface falls below the maximum value that is required for the precipitation of any of the three sulfide phases. Then, the respective concentration profiles of sulfur and aluminum in front of the sulfide band can be represented as in Fig. 6.4(f). A subsequent band then forms at a distance x_2 (Fig. 6.4(f)) where the concentration product for the precipitation Al_2S_3 is again satisfied.

6.3.4 Conclusions

(i) Sulfidation of Fe-6 to 28 a/o Al alloys by diffusion coupling with FeS at 1173K, results in periodic precipitation of $FeS+FeAl_2S_4$ in the alloy. These sulfides appear as layers alternating with metal bands parallel to the original FeS/alloy interface. The metal bands are alloy depleted of aluminum.

(ii) The sulfidation rate of these alloys as measured by the thickness measurements of the sulfidation zone, increase with increasing aluminum alloy content.

(iii) In the sulfidation zone, the ratio of distances of successive sulfide bands, from the original FeS/alloy interface is found to be a constant, in accordance with the Jablczynski's relationship for Liesegang type of precipitation processes. Using the Jablczynski's spacing coefficient, a relationship is derived and verified in which the sulfide thickness increases with depth.

(iv) The metal band thicknesses remained approximately constant with depth, within a sulfidation time of 10800s (3h).

(v) Increasing the aluminum concentration in the alloy, results in higher sulfidation rates and larger number of sulfide layers. The sulfide thicknesses at the greatest depth ($\Delta \text{SULF}_n^{\text{max}}$) increased with increasing aluminum alloy content but the average metal band thickness decreased as the aluminum alloy content increased.

(vi) The initial stage of sulfide layer formation is explained by a model involving precipitation of Al_2S_3 . This precipitated sulfide is subsequently converted to FeAl_2S_4 .

(vii) It is suggested that growth of FeS in a sulfide layer takes place as a result of rapid diffusion of iron within this phase. Aluminum diffusion in FeS assists the growth of FeAl_2S_4 . A diffusion model is advanced for the growth of a sulfide layer, in which, it is suggested that aluminum depletion in front of the layer ultimately leads to its cessation of growth. Further sulfide precipitation then occurs at a distance ahead of the sulfide layer where the concentration product $K = N_{\text{Al}}^2 \cdot N_{\text{S}}^3$ exceeds its maximum value. The steps described in (vi) and in the above when repeated several times give rise to a periodicity in the arrangement of alternate sulfide and metal bands.

6.4 SULFIDATION OF Fe-Al ALLOYS IN S₂ VAPOUR AT THE DISSOCIATION PRESSURE OF FeS

6.4.1 Introduction

Sulfidation behaviour of the Fe-Al alloys containing 6, 9, 18 and 28 a/o Al in sulfur vapour at 1173K established by equilibrium of Fe+FeS was presented in section 5.3.

The sulfidation kinetics of these alloys were obtained by measuring the uniform depths of internal sulfidation zones as well as the sulfur uptake. The kinetics were parabolic. The Fe-6 Al alloy exhibited internal sulfidation with acicular FeAl₂S₄ precipitation. The Fe-9 and 18 Al alloys exhibited internal sulfidation with acicular sulfide precipitates of FeAl₂S₄+Al₂S₃, accompanied by an external scale of FeAl₂S₄. In the internal sulfidation zone of these alloys, Al₂S₃ was precipitated first and then converted to FeAl₂S₄ via reaction 6.5(b). A small zone containing Al₂S₃ precipitates was found in the Fe-9 and 18 Al alloys in the advancing front of the sulfide precipitates. The Fe-28 Al alloy sulfidized with the formation of an external Al₂S₃ scale without any internal sulfidation. The depths of internal sulfidation in the Fe-9 Al alloys after corresponding exposures were lower than Fe-6 Al. Fe-18 Al alloy exhibited the highest depth of internal sulfidation.

In the following, the mode of internal precipitation of FeAl₂S₄ and Al₂S₃ in the Fe-6 to 18 Al alloys and the formation of a protective Al₂S₃ scale on the Fe-28 Al alloy will be discussed. A diffusion model will be presented to represent the growth of acicular sulfides.

6.4.2 Internal Precipitation of FeAl_2S_4 and its Formation in the External Scale

Sulfidation of Fe-6, 9 and 18 Al alloys in S_2 vapour, at the dissociation pressure of FeS, showed extensive internal sulfidation. Sulfidation of Fe-9 and 18 Al alloys produced internal sulfides of $\text{FeAl}_2\text{S}_4 + \text{Al}_2\text{S}_3$ and an external scale consisting of FeAl_2S_4 . The internal acicular sulfide precipitates appeared as platelets parallel to the growth direction with widths ranging from 10 to 20 μm and thicknesses ranging from 0.5 to 2 μm . In order to present a diffusion model for the growth of these precipitates, a comparison of the permeabilities ($N_S^{(S)} \cdot D_S$) is made for various alloys using the classical model of internal sulfidation.

Permeabilities of sulfur in Fe-Al alloys were calculated using the experimental penetration depths of internal sulfidation with the help of limiting Eqns. (2.36) and (2.42) where sulfur as well as aluminum diffusion are considered important for the rate of advancement of the internal sulfidation zone.

Estimates of D_{Al}/D_S and $N_S^{(S)}/N_{\text{Al}}^0$ in the Fe-Al alloys at 1173K, show that

$$\frac{N_S^{(S)}}{N_{\text{Al}}^0} \ll \frac{D_{\text{Al}}}{D_S} \ll 1 \quad (6.30)$$

Therefore, the depth of internal sulfidation zone is given by

$$\xi = \frac{N_S^{(S)}}{\sqrt{N_{\text{Al}}^0}} (\pi \phi D_S t)^{1/2} \quad (6.31)$$

in the absence of an external scale, where v is the ratio of sulfur to Al in the stoichiometric precipitates. Equation (6.31) can be written in the form

$$N_S^{(S)} \cdot D_S = \xi \cdot v \cdot N_{Al}^0 \left(\frac{D_{Al}}{\pi t} \right)^{1/2} \quad (6.32)$$

The depth of internal sulfidation zone under an external scale, with the same condition as (2.27), is given by Eqn. (2.42). The $N_S^{(S)} D_S$ product accordingly, can be written as

$$N_S^{(S)} \cdot D_S = [\xi(\xi - \xi')]^{1/2} v \cdot N_{Al}^0 \left(\frac{D_{Al}}{\pi t} \right)^{1/2} \quad (6.33)$$

where ξ' is the position coordinate of the metal-scale interface at time 't'. In calculating these permeabilities* v was assumed to be 2 in the sulfidation zone. D_{Al} and D_S values were obtained from literature. Values of this apparent permeability for several alloys are tabulated in Table (6-4) and plotted as a function of aluminum alloy contents in Fig. 6.9. An increase in the apparent permeability is observed with increase in Al content.

* In subsequent text, the product $N_S^{(S)} D_S$ will be termed as the apparent permeability.

Table 6-4

Apparent permeabilities as a function
of Al content in the alloy

Alloy	Apparent $N_S^{(S)} D_S$	From Equation
Fe-6 Al	5.7×10^{-10}	(6.32)
Fe-9 Al	9.7×10^{-10}	(6.33)
Fe-18 Al	18.3×10^{-10}	(6.33)

A model involving enhanced sulfur diffusion within the internal sulfidation zone along the incoherent boundaries between the sulfide and the alloy matrix will be presented and verified using the results obtained in this investigation. In order to understand this apparent increase in permeability with increase in aluminum content in the Fe-Al system, it is appropriate to consider the morphology of the internal sulfide precipitates. Since the precipitates show considerable elongation in the growth direction and the internal sulfidation kinetics can not be explained using values for sulfur and aluminum lattice diffusivities alone, possibilities must be considered of enhanced sulfur diffusion along the incoherent interface between the internal sulfide particles and the alloy. Recently Whittle et al. (62) have considered the enhanced diffusion of oxygen in the internal oxidation of Ni-Al alloys and obtained a good agreement between the theory advanced and experiment.

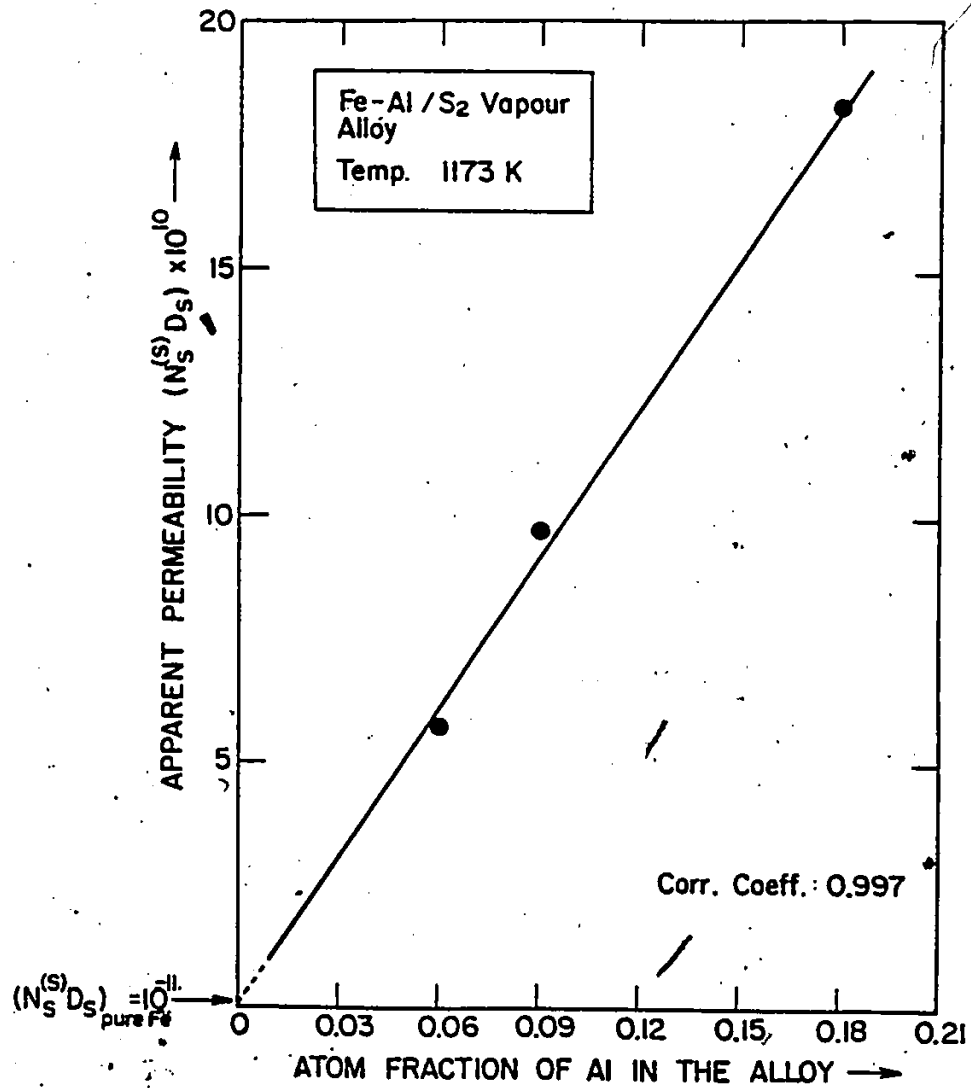


Fig. 6.9 Plot of apparent permeability vs. Al alloying content.

6.4.3 Internal Sulfidation Model

The effective sulfur flux through the internal sulfidation zone is expressed as the sum of fluxes of sulfur through the alloy lattice, J_l , the internal sulfide/alloy interface, J_i , and the internal sulfide particles, J_{sulfide} as shown schematically in Fig. 6.10. Thus,

$$J_{\text{eff}} = J_l A_l + J_i A_i + J_{\text{sulf}} A_{\text{sulf}} \quad (6.34)$$

where, A_l , A_i and A_{sulf} are the area fractions of alloy phase, of alloy/sulfide interfaces and of sulfide in a unit cross-section cut parallel to the external surface. Sulfur diffusion in the sulfide may be neglected in comparison to diffusion in the alloy lattice and along the interfaces. Assuming a common sulfur concentration gradient along the interfaces and in the alloy and considering a uniform concentration at any distance x from the external surface, the effective sulfur diffusion coefficient in the internal sulfidation zone is given by

$$D_{s,\text{eff}} = D_{s,l} A_l + D_{s,i} A_i \quad (6.35)$$

where $D_{s,l}$ is the lattice diffusion coefficient for sulfur and $D_{s,i}$, the interfacial or boundary diffusion coefficient, assuming both independent of composition.

The area fractions A_l and A_i are calculated as follows. The thickness and width of the platelets are designated as d and w respectively (Fig. 6.10) and it is assumed that they extend

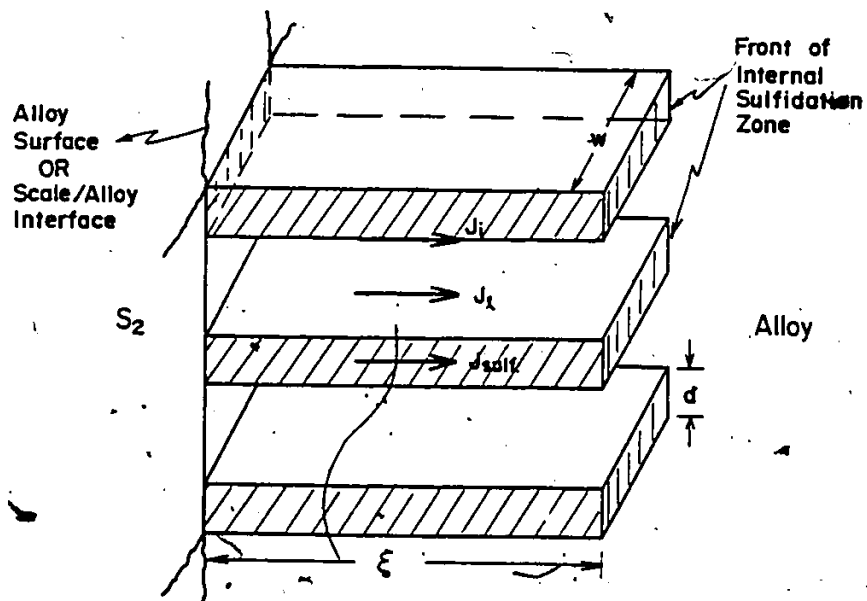


Fig. 6.10. Schematic internal sulfidation model of Fe-Al alloys in S_2 vapour at the dissociation pressure of FeS.

continuously through the internal sulfidation zone which extends up to a depth ξ below the surface or external scale/sub-scale interface. Since Al_2S_3 precipitates first in the alloys, its mole fraction is expressed as N_{AlS_v} relative to the total number of moles of alloy constituents within the internal sulfidation zone. Considering a volume of internal sulfide zone of thickness ξ and unit cross-sectional area, the number of sulfide platelets, z , may be calculated to be

$$\frac{N_{\text{AlS}_v} \xi}{v_{\text{alloy}}} = z \frac{w d \xi}{v_{\text{sulfide}}} \quad (6.36)$$

where v_{sulfide} and v_{alloy} are the molar volumes of sulfide and alloy phases, respectively. If the volume expansion due to internal sulfide precipitation is neglected,

$$z = \frac{v_{\text{sulfide}}}{v_{\text{alloy}}} \frac{N_{\text{AlS}_v}}{w d} \quad (6.37)$$

The fractional area of the interface becomes

$$A_i = 2(w+d)z b_i \approx 2wz b_i \quad (6.38)$$

since $d \ll w$ for thin plates and b_i is the width of the interface. Therefore, the lattice fractional cross-section area available for diffusion is,

$$A_l = 1 - A_i - A_{\text{sulfide}} = 1 - 2wz b_i - z w d \quad (6.39)$$

Substituting Eqns. (6.37) to (6.39) in (6.35) gives

$$D_{s,eff} = D_{s,l} \left[1 - \frac{v_{\text{sulfide}}}{v_{\text{alloy}}} N_{\text{AlS}_v} \left(1 + 2 \frac{b}{d} \right) \right] + 2D_{s,i} \frac{v_{\text{sulfide}}}{v_{\text{alloy}}} N_{\text{AlS}_v} \frac{b}{d} \quad (6.40)$$

On rearrangement,

$$\frac{D_{s,eff}}{D_{s,i}} = 1 + \left[2 \frac{b}{d} \frac{D_{s,i}}{D_{s,l}} - \left(1 + 2 \frac{b}{d} \right) \right] \frac{v_{\text{sulfide}}}{v_{\text{alloy}}} N_{\text{AlS}_v} \quad (6.41)$$

Since $D_{s,i} \gg D_{s,l}$

$$\frac{D_{s,eff}}{D_{s,i}} = 1 + \left[2 \frac{b}{d} \frac{D_{s,i}}{D_{s,l}} - 1 \right] \frac{v_{\text{sulfide}}}{v_{\text{alloy}}} N_{\text{AlS}_v} \quad (6.42)$$

Thus, the effective diffusion coefficient in the internal sulfidation zone is a linear function of the mole fraction of the internal sulfide precipitate which is proportional to the original atom fraction of Al in the alloy N_{Al}^0 . Eqn. (6.42) can be expressed as

$$\frac{N_S^{(S)} \cdot D_{s,eff}}{N_S^{(S)} D_{s,l}} = 1 + \left[2 \frac{b}{d} \frac{D_{s,i}}{D_{s,l}} - 1 \right] \frac{v_{\text{sulf}}}{v_{\text{alloy}}} \cdot \alpha \cdot N_{\text{Al}}^0 \quad (6.43)$$

where α is the enrichment factor as defined by Eqn. (2.38).

It is usually accepted in this type of internal sulfidation problem that the sulfur solubility at the interface would not be dependent on the presence of Al in the alloy since the alloy matrix becomes virtually pure due to the relative sulfidation of the alloying element. The ratio on the left-hand side of Eqn. (6.43), consequently, corresponds to the ratio of the

apparent $N_S^{(S)} D_{(S)}$ product obtained by extrapolating to pure Fe. A plot of Eqn. (6.43) is shown in Fig. 6.11; a linear fit is obtained with 0.997 correlation coefficient. The slope of the linear plot in Fig. 6.11 corresponds to

$$\left(2 \frac{D_{s,i}}{D_{s,l}} \frac{b_i}{d} - 1\right) \frac{v_{\text{sulfide}}}{v_{\text{alloy}}} \cdot \alpha = 1030 \quad (6.44)$$

The ratio $\frac{D_{s,i}}{D_{s,l}}$ was calculated using Eqn. (6.44) to examine whether the parameters in Eqn. (6.43) are physically reasonable. If one assumes that all the internal sulfide particles were converted to FeAl_2S_4 , $v_{\text{sulfide}} = 8 \times 10^{-5} \text{ m}^3$, $v_{\text{alloy}} = 7.2 \times 10^{-6} \text{ m}^3$, $\alpha = 2$, $b_i = 1 \text{ nm}$ and the thickness of the internal sulfide precipitates to range from $0.5 \text{ }\mu\text{m}$ to $2 \text{ }\mu\text{m}$, the calculated $D_{s,i}/D_{s,l}$ ratio has values in the range 1.2×10^4 to 4.8×10^4 . These values compare well to a calculation of the ratio using literature values for sulfur grain boundary⁽¹⁵⁶⁾ and lattice (Table 3-2) diffusion in pure iron.

$$D_s^{\text{gb}} = D_0' \exp\left(-\frac{135240\text{J}}{RT}\right) \quad (6.45a)$$

where, $D_0' = 9.55 \text{ cm}^2/\text{s}$ for $b_i = 1 \text{ nm}$.

At 1173K, $D_s^{\text{gb}} = 9.9 \times 10^{-6} \text{ cm}^2/\text{s}$

and

$$\frac{D_s^{\text{gb}}}{D_{s,l}} = \frac{9.9 \times 10^{-6}}{1.2 \times 10^{-9}} = 8.3 \times 10^3 \quad (6.45b)$$

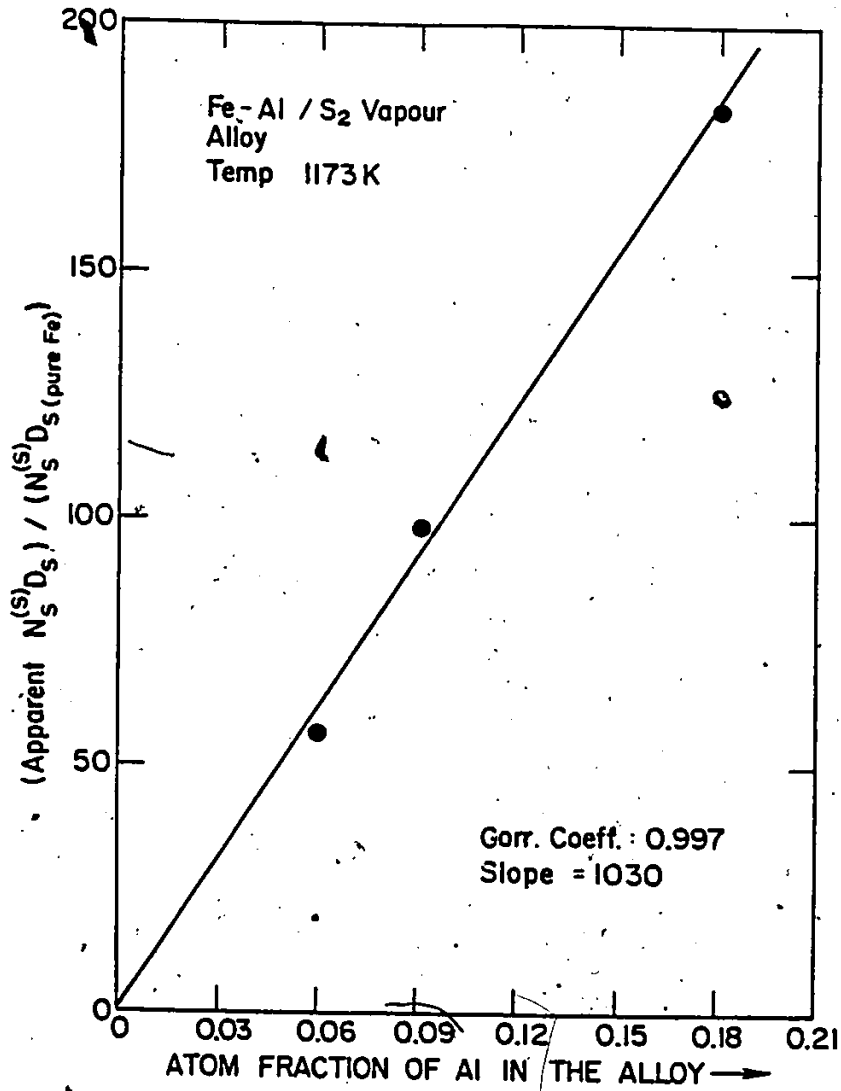


Fig. 6.11 Plot of the ratio of apparent permeability to that in pure Fe as a function of alloying content.

Since the increase in the apparent $N_S^{(S)} D_S$ product as a function of alloying content is attributed to the internal sulfide morphology, it is appropriate here to discuss briefly the factors which may affect this morphology. According to Böhm and Kahlweit⁽⁴⁶⁾, there is a competition at the internal sulfidation front between the growth of existing precipitates and the nucleation of new particles, both processes resulting in advance of the sulfidation front. Nucleation of new particles depends on the degree of supersaturation in advance of the existing particles and is determined by the relative magnitude of the sulfur and solute fluxes at that point. A high sulfur flux, such as occurs when the zone of the internal sulfide is thin, results in repeated nucleation of relatively small individual particles. On the other hand, when the sulfur flux diminishes as the internal sulfidation zone grows thicker, the existing particles tend to grow in size, often elongating in the growth direction. Thus, the individual sulfide particles in the case of general precipitation for a given exposure condition vary in size from the alloy surface to the interior of the alloy.

The dependence of precipitate size with distance into the alloy involving sulfide platelet growths cannot be quantitatively assessed. In each alloy investigated the internal sulfides tended to elongate in the growth direction giving rise to sulfide platelet precipitates. The spacing between sulfide platelets decreased with increase in alloying content as summarized in Table (5-9). The intersulfide spacing decreased from

7.9±0.5 μm for Fe-6 Al alloy to 2.6±0.5 μm for Fe-18 Al alloys. It is not possible, however, to analytically account for this diverse internal sulfidation phenomena.

6.4.4 Growth of Protective Al₂S₃ Scales

The Fe-28 Al alloy sulfidized at 1173K in S₂ vapour at the dissociation pressure of FeS formed only an external Al₂S₃ scale. Internal sulfidation was not observed. The scale grew at the rate of $7.2 \times 10^{-2} \text{ } \mu\text{m/s}^{\frac{1}{2}}$ and it spalled from the alloy substrate on cooling (Fig. 5.20). Due to this slow growth rate it was impossible to determine the active migrating reactant species using a Pt marker. No results are available in the literature on the parabolic growth of Al₂S₃ for comparison. Aluminum sulfide melts at 1373K, therefore its potentially protective effect is being lost beyond 1273K as observed by Strafford et al. (157). At low temperatures 773 to 973K, aluminum addition to iron has been found to be extremely useful for offering corrosion resistance (153,157).

Using the criteria for no internal sulfidation (without any interaction between aluminum and sulfur, i.e. $\epsilon_S^{\text{Al}} = 0$), Eqn. (2.47) was used to calculate the minimum concentration of aluminum in the alloy needed for an external Al₂S₃ scale formation.

$$N_{\text{Al}}^{*0} = \frac{F(u) + \frac{1}{v} \left(\frac{D_S}{D_{\text{Al}}} \right)^{\frac{1}{2}} \cdot u \cdot \pi^{\frac{1}{2}}}{1 + \frac{1}{v} \left(\frac{D_S}{D_{\text{Al}}} \right)^{\frac{1}{2}} \cdot u \cdot \pi^{\frac{1}{2}}}$$

$$\text{where, } u = \left(\frac{k_P}{2D_{Al}} \right)^{\frac{1}{2}} = \left(\frac{1.9 \times 10^{-12}}{2 \times 5.8 \times 10^{-10}} \right)^{\frac{1}{2}} = 4.02 \times 10^{-2}$$

$$\frac{D_S}{D_{Al}} = \frac{1.2 \times 10^{-9}}{5.8 \times 10^{-10}} = 2.07$$

$$F(u) = \pi^{\frac{1}{2}} \cdot u \cdot \exp(u)^2 \cdot \text{erfc}(u) \\ = 6.8 \times 10^{-2}$$

$$N_{Al}^* = 0.1274$$

In comparison with the experiment, the alloy which exhibited an external scale of Al_2S_3 had a composition of Fe-28 a/o Al (0.28 atom fraction). Therefore, a positive interaction between aluminum and sulfur in the alloy must be considered (since negative interactions tend to decrease this critical alloying concentration as shown in Fig. 2.7(a)). In the present case, considerations were made to check the validity of Eqn. (2.59), since the off-diagonal diffusion coefficient D_{OB} expressed in Eqn. (2.50) is valid for cases where the oxidant diffuses interstitially. In Fe-Al alloys where sulfur diffuses substitutionally, the off-diagonal diffusion coefficient D_{SAl} can be expressed as⁽¹⁶⁰⁾:

$$D_{SAl} = D_{SS} N_S \left[\epsilon_S^{Al} - \left(\frac{N_S}{N_{Al} D_{Fe}^{Fe}} \right) \cdot (N_{Al} D_{Al}^{Fe} - N_{Al} N_{Fe} D_{Fe}^{Fe}) \right] \quad (6.46)$$

where, N_S , N_{Al} and N_{Fe} are atom fractions of sulfur, aluminum and iron respectively. D_{SAl} is the diffusivity of sulfur in the gradient of aluminum. Using the binary data of Fe-Al and Fe-S

systems, the term $(N_S/N_{Al} D_S^{Fe}) \cdot (N_{Al} D_{Al}^{Fe} - N_{Al} N_{Fe} D_{Fe}^{Fe})$ was calculated to be less than 10^{-3} and therefore neglected. Equation (6.46) can then be approximated to Eqn. (2.50).

The minimum aluminum concentration in the alloy was calculated using Eqn. (2.59) as a function of positive values of interaction parameter and plotted in Fig. 6.12. It is observed from this figure that the critical alloying concentration of aluminum for transition from internal sulfidation to external scale formation increases with increasing values of ϵ_S^{Al} . From Fig. 6.12 for the Fe-18 Al alloy which exhibited an external scale accompanied by internal sulfidation, an interaction parameter value of 9 is obtained whereas for the Fe-28 Al alloy with the only external scale, a value of 15 is obtained. The correct value of ϵ_S^{Al} at 1173K would therefore be in the range 9 to 15. In comparison, the value of ϵ_S^{Al} in liquid Fe-Al-S alloys has been measured to be 6.7⁽¹²¹⁾. The sulfur solubility in alloys exhibiting positive interaction parameters (ϵ_S^B) were shown in Fig. 2.1(b). The solubility of sulfur decreases with increasing alloying concentration in these alloys and the solubility curves do not exhibit a minimum.

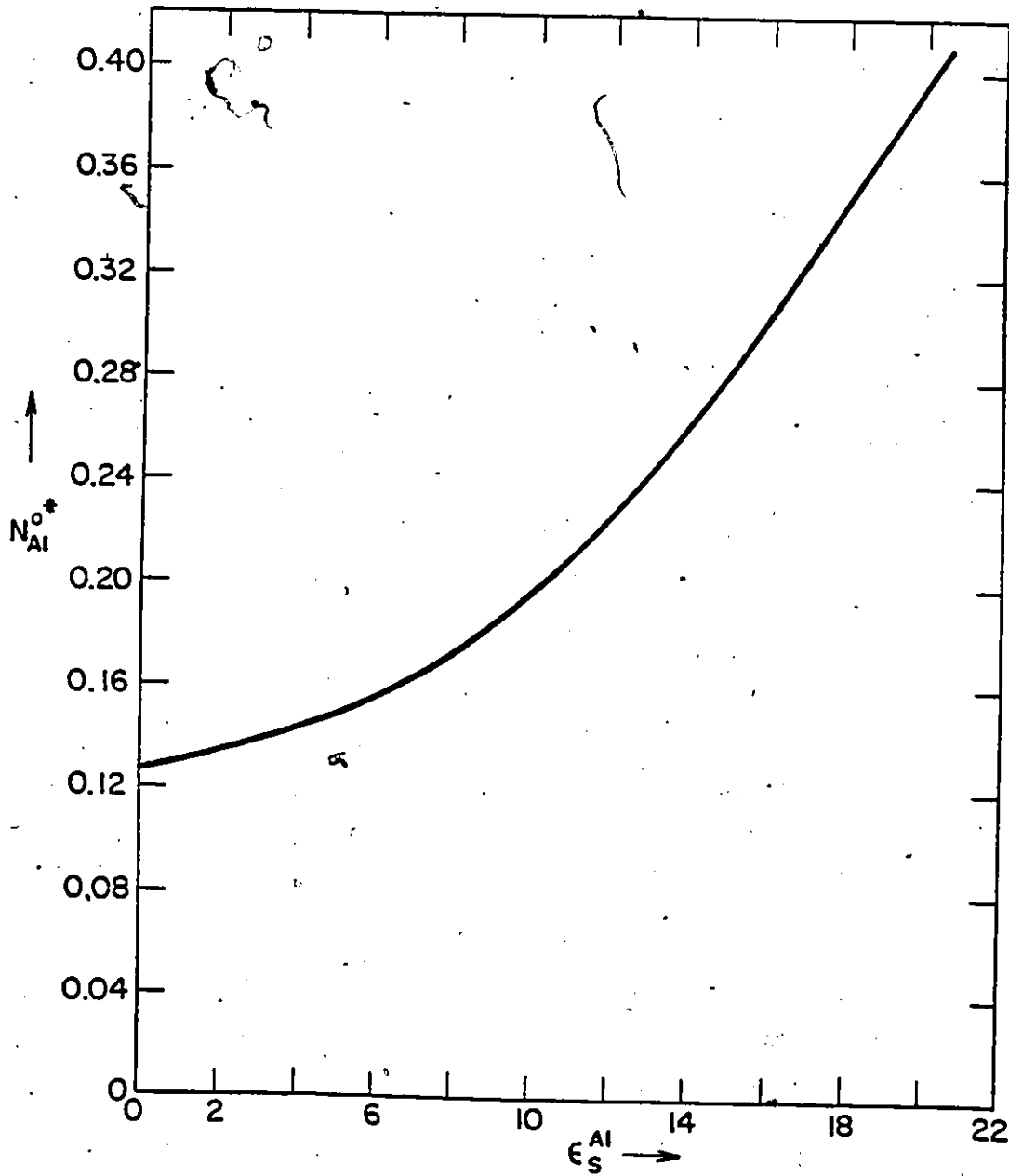


Fig. 6.12 Variation of critical atom fraction of Al in the alloy for transition from internal to external scale formation as a function of interaction parameter.

6.4.5 Conclusions

(i) Fe-6, 9 and 18 Al alloys sulfidized in S_2 vapour at the dissociation pressure of FeS exhibited intense internal sulfidation. The sulfidation kinetics were parabolic as measured by the internal sulfidation zone thicknesses. The acicular sulfide precipitates of $FeAl_2S_4$ and Al_2S_3 showed considerable elongation in the growth direction.

(ii) The Fe-6 Al alloy only exhibited internal sulfidation. The Fe-9 and 18 Al alloys sulfidized forming external scales of $FeAl_2S_4$ and internal sulfidation zones consisting of $FeAl_2S_4$ and Al_2S_3 precipitates.

(iii) The apparent permeabilities ($N_S^{(S)} D_S$) of sulfur in Fe-Al alloys estimated from the internal sulfidation kinetics increased with increasing alloy aluminum content.

(iv) This increase in the apparent permeability was attributed to the enhanced diffusion of sulfur along the incoherent interfaces between the internal sulfides and the alloy matrix. A relationship between the ratio of apparent permeability of sulfur in the Fe-Al alloys to that in pure Fe, and the alloy aluminum content was derived and verified. The ratio of boundary to lattice diffusivities of sulfur in iron was estimated from this work and compared with the value available in the literature with satisfactory agreement.

(v) The intersulfide spacing decreased with increasing the alloy aluminum content.

(vi) The critical alloying atom fraction for the transition from internal sulfidation to external scale formation was

calculated to be 0.127 assuming no interaction between aluminum and sulfur. Experimentally this transition was observed in alloys with aluminum content in between 18 and 28 atom percent. In the presence of an interaction between aluminum and sulfur, ϵ_S^{Al} was calculated to be in between 9 and 15 using the experimentally observed alloying concentrations and corrosion rate constants.

The Al_2S_3 , which is the sole sulfide phase formed on Fe-28 Al alloy, grew as a protective film at the rate of $7.8 \times 10^{-2} \text{ } \mu\text{m/s}^{\frac{1}{2}}$.

6.5 SULFIDATION PROPERTIES OF Fe-Al ALLOYS IN $\text{H}_2\text{S-H}_2$ ATMOSPHERES

6.5.1 Introduction

Sulfidation of alloys containing 9 and 18 Al were investigated in $\text{H}_2\text{S-H}_2$ atmospheres, at 1173K, and a total pressure of 10^5 Pa. The Fe-9 Al was exposed at $p_{\text{S}_2} = 10^{-1}$ Pa and the Fe-18 Al alloy was exposed at sulfur pressures $10^3 \text{ } p_{\text{S}_2} \geq 1$ Pa.

The scale formed on the Fe-9 Al alloy at $p_{\text{S}_2} = 10^{-1}$ Pa consisted of two layers, an outer layer consisting of FeS and an inner layer containing a mixture of $\text{FeS+FeAl}_2\text{S}_4$. There was also a narrow internal sulfidation zone containing $\text{FeAl}_2\text{S}_4+\text{Al}_2\text{S}_3$ precipitates. The corrosion rate of this alloy followed parabolic kinetics.

The corrosion mechanism of the Fe-18 Al alloy was investigated in most detail. After an initial period of 2000s, the corrosion rate was approximated by the limiting values k_1 ,

k_2 , k_1' , k_2' for the parabolic reaction rate constant (Fig. 5.22) at $p_{S_2} = 10^2$ Pa and 10 Pa, respectively, by limiting tangents at distinct sections of the reaction curves. During the first stage of parabolic sulfidation, there was growth of a duplex scale containing an outer FeS layer and an inner layer containing a FeS and $FeAl_2S_4$ conglomerate. The second parabolic stage led to growth of a continuous Al_2S_3 film below the sulfide conglomerate layer. Once the Al_2S_3 film covered the alloy surface, further sulfidation proceeded at a rate approximately an order of magnitude less than the initial rate (Table 5-10).

Nodular scale growth was observed on the Fe-18 Al alloy in the p_{S_2} range 10^2 to 10 Pa during initial exposures up to 2000s. The Al_2S_3 film produced on the alloy surface was highly defective containing a number of leakage paths where $FeAl_2S_4$ and FeS nucleated to grow as nodules with a circular base and mushroom shape. FeS grew at the fastest rate. At 673K the growth rate of FeS is 10^4 times faster than the growth rate of Al_2S_3 ⁽⁸⁾. These nodules spread laterally and grew vertically and coalescence with one another finally led to growth of a continuous duplex scale with outer FeS scale and inner FeS+ $FeAl_2S_4$ layer. The outer FeS layer exhibited extensive porosity (Fig. 5.29).

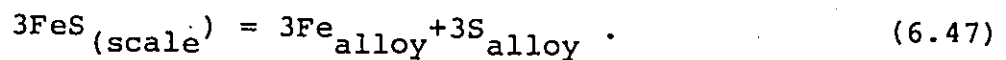
In subsequent sections, sulfidation behaviour of the Fe-9 and 18 Al alloys will be discussed and sulfidation models will be presented. These diffusion models are shown to be consistent with predictions from the Fe-Al-S isotherm.

6.5.2 Sulfidation Mechanisms and Models

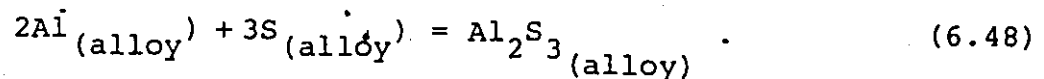
The model for the scale growth on the Fe-9 Al alloy at $p_{S_2} = 10^{-1}$ Pa is shown in Fig. 6.13. The outer layer of the scale grows by outward iron diffusion and the inner layer by inward diffusion of sulfur resulting from the dissociation of iron sulfide. No attempt has been made to show the presence of a small volume fraction of porosity (Fig. 5.23) in this schematic model. The $FeAl_2S_4$ phase in the inner layer is in the form of plates with an average spacing of 2 μm aligned normal to the alloy/scale interface.

The mechanism for the growth of the inner layer of the external scale containing $FeS+FeAl_2S_4$ is as follows:

The source of sulfur supply as suggested by the marker measurement (Fig. 5.32) is from the dissociation of FeS at the FeS/alloy interface. The reaction at the FeS/alloy interface is given by



Inward diffusion of sulfur through the alloy or boundaries between Al_2S_3 /alloy in the internal sulfidation zone to react with sulfur at the precipitation front can be represented as



Addition of reactions (6.47) and (6.48) gives the net displacement reaction of type (6.49).

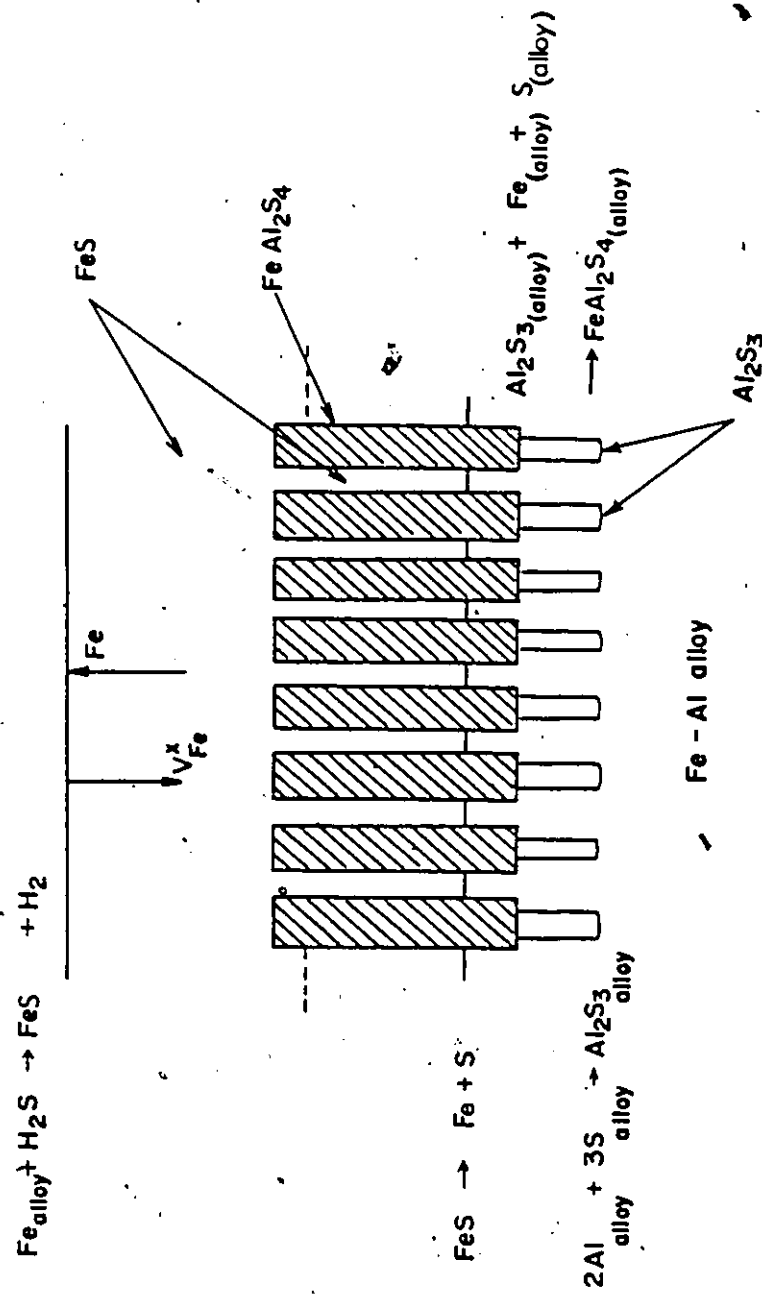
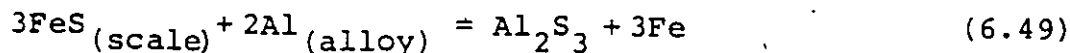
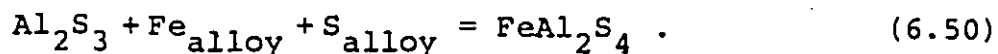


Fig. 6.13 Schematic model for scale growth on Fe-9 Al alloys, $P_{\text{S}_2} = 10^{-1}$ Pa in $\text{H}_2\text{S}-\text{H}_2$ atmospheres.



where the resultant Fe diffuses outward through the scale to react with the H_2S atmosphere. The aluminum solubility in FeS is about 1 a/o. The Al_2S_3 precipitates are then converted to FeAl_2S_4 either by reaction 6.5(a) or 6.5(b).

The FeAl_2S_4 part of the platelike precipitate was mainly confined to the inner conglomerate layer of the external scale. Al_2S_3 in the region of the scale/alloy interface can be converted to FeAl_2S_4 by solid state reactions. Since the scale retained intimate contact with the receding alloy surface during all stages of sulfidation, these reactions involved diffusion processes. The FeAl_2S_4 plates continue to penetrate inwards as a result of solid state reaction of Al_2S_3 with iron and dissolved sulfur in the alloy as follows:



The alloy in between the FeAl_2S_4 or Al_2S_3 precipitates is sulfidized gradually by the sulfur released from the dissociation of FeS. The overall reaction rate at this stage decreases because the effective area for diffusion of iron is reduced due to the limited supply of iron through FeS in the inner conglomerate layer of the external scale.

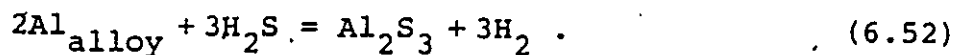
Models describing evolution and growth of the sulfide scale on the Fe-18 Al alloy at $10 \text{ Pa} \leq p_{\text{S}_2} \leq 10^2 \text{ Pa}$ are illustrated in Fig. 6.14. During the initial stage, a defective Al_2S_3

layer containing leakage paths is formed rapidly as illustrated in Fig. 6.14(a). FeAl_2S_4 and FeS then nucleate and grow at these defective sites (or leakage paths) to form well defined mushroom shaped nodules exhibiting whiskers and plates of pyrrhotite. The alloy beneath these nodules was simultaneously sulfidized internally producing Al_2S_3 precipitates. Following the initial nodular growth period, as illustrated in Figs. 6.14(b) and (c), a continuous scale containing outer and inner layer formed over the entire alloy surface (Figs. 5.29 and 6.14(d)) as a result of coalescence of the nodules.

Growth of FeS in the inner and outer scale layers involves iron diffusion through iron vacancies. Since FeS is a metallic conductor at temperatures above 411K, adsorption of sulfur as a result of reaction (6.51) on FeS



produces a neutral iron vacancy in the sulfide lattice and growth of scale takes place by the diffusion of iron through iron vacancies. Considering the free energy of formation of FeS and Al_2S_3 (appendix I), Al_2S_3 is also formed during the initial reaction period,



The initial iron sulfide layer exhibited whiskers and plates (Fig. 5.28(e)) supplying a large surface area for the subsequent

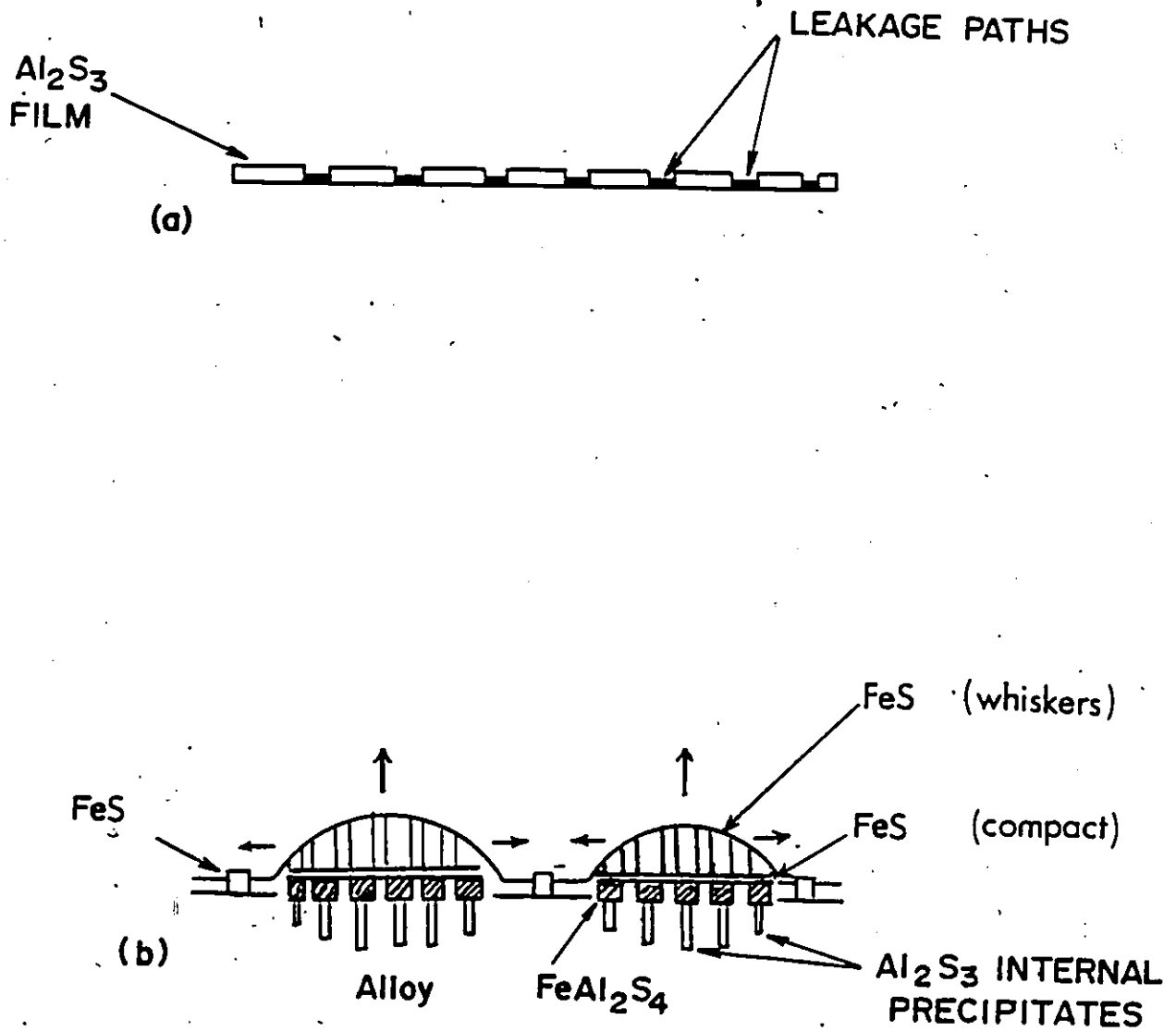


Fig. 6.14 a) Initial stage of sulfidation.
 b) Lateral coverage of nodules.

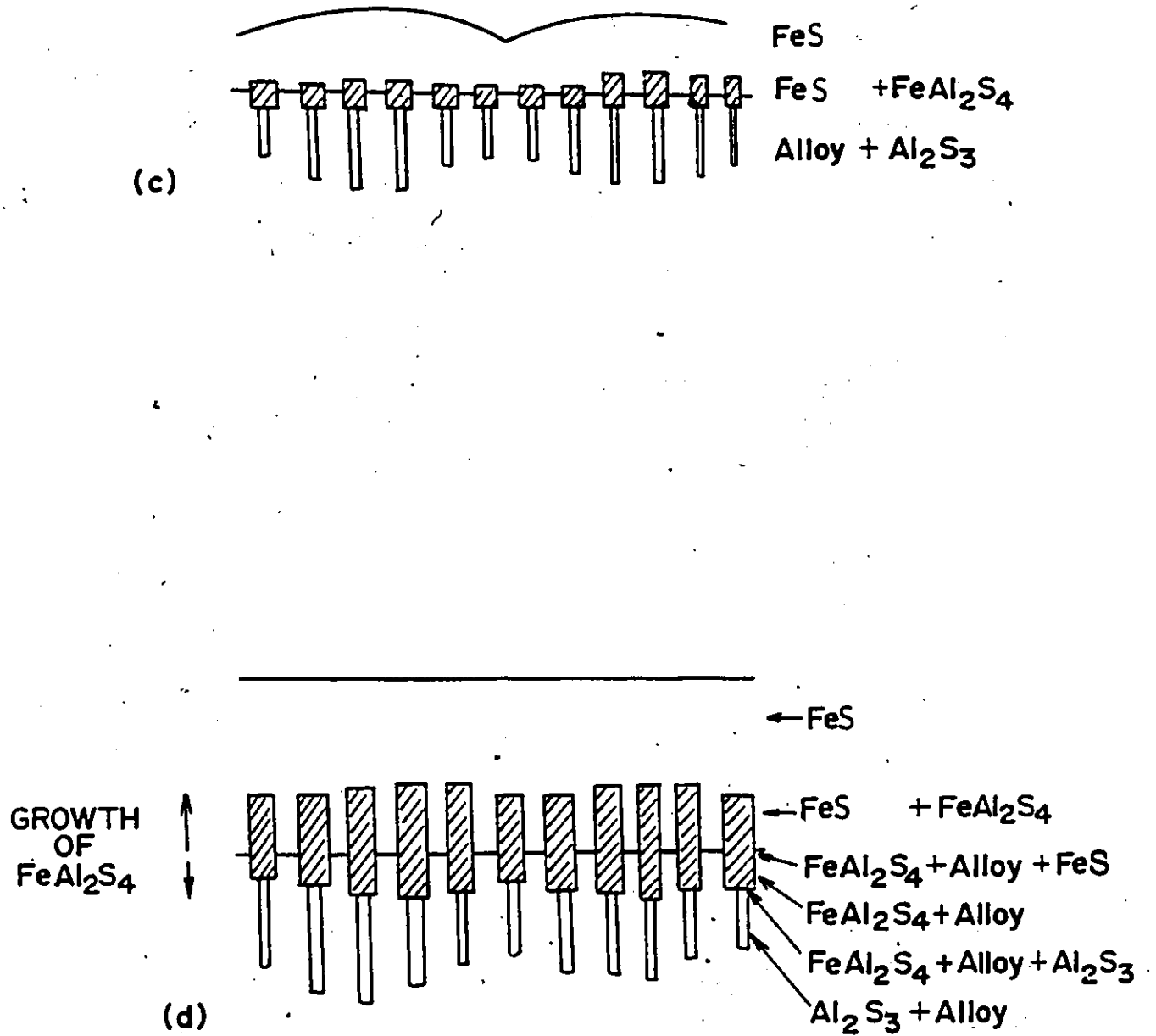


Fig. 6.4 c) Coalescence of two nodules.
d) Continuous external scale formation.

adsorption of sulfur in comparison to a compact FeS layer. The outer layer of FeS is doped with aluminum but very high levels of aluminum were found by the microprobe analyses in localized regions (Fig. 5.37). This is perhaps associated with the conversion of the Al_2S_3 film sections buried underneath the growing FeS phase to FeAl_2S_4 via reactions of type 6.5(a). The mechanism for the growth of the inner layer is similar to that presented for the Fe-9 Al alloys. A quantitative description relating the parabolic rate constant to sulfur pressure could not be made because several factors lead to a complicated reaction mechanism such as double sulfide (FeAl_2S_4) formation and microporosity growth in the inner layer of the external scale and internal sulfidation in the alloy.

Growth of the inner $\text{FeS}+\text{FeAl}_2\text{S}_4$ layer as plotted in Fig. 5.27(b) decreases to very low scaling rate ($2.1 \times 10^{-8} \text{ cm}^2/\text{s}$) after 1800s of sulfidation at $p_{\text{S}_2} = 10^2 \text{ Pa}$ for Fe-18 Al alloys. This phenomenon initially occurs at isolated sites near the external scale/alloy interface after first 1800s and is attributed to the formation of FeAl_2S_4 and Al_2S_3 film sections. The preferential sites for Al_2S_3 formation at the interface could not be ascertained in the present work. It took approximately 3h for the Al_2S_3 film to appear throughout the scale/alloy interface, thereby decreasing the corrosion rate by an order of magnitude (Table 5-10). Figure 6.14(e) shows a schematic presentation of the situation where localized Al_2S_3 film growths occur beneath

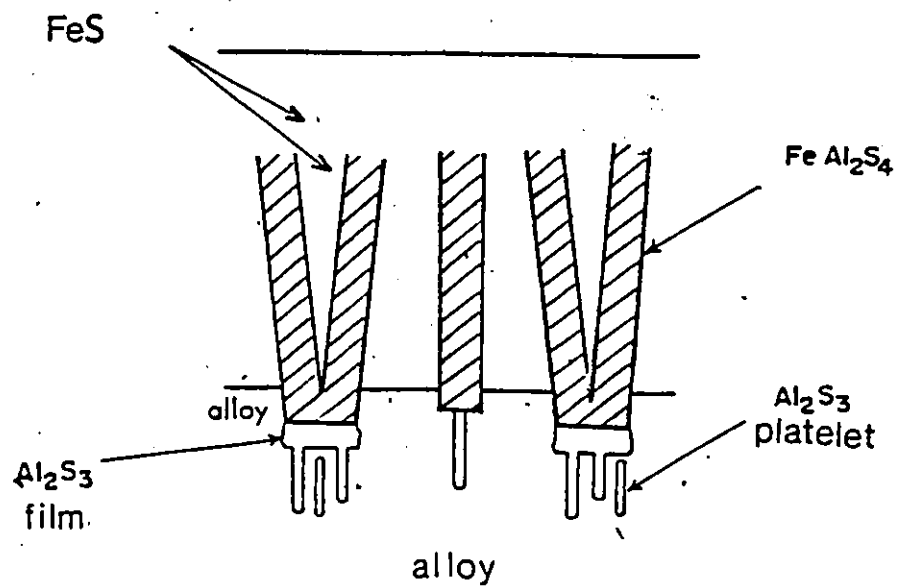


Fig. 6.14(e) Schematic presentation of the situation where the Al_2S_3 film is formed beneath two favourably oriented FeAl_2S_4 platelets.

two favourably oriented FeAl_2S_4 platelets. As sulfidation progressed, lateral growth of these films at such sites gave rise to a completely continuous Al_2S_3 film over the scale/alloy interface. The scale growth model for the final reaction stage is shown in Fig. 6.14(f). The lateral growth of the Al_2S_3 film would involve the simultaneous growth of a FeAl_2S_4 layer on its upper surface in accordance with the following reaction 6.5(a). Careful compositional and structural analyses demonstrated the occurrence of this FeAl_2S_4 layer (Fig. 5.41(c)). It was not possible, however, to distinguish the relative thicknesses of FeAl_2S_4 and Al_2S_3 in the innermost sulfide layer.

The Al_2S_3 film appeared to act as an effective diffusion barrier permitting at most only a very small supply of iron from the alloy to support scale growth. The Al_2S_3 layer was always associated with a layer of FeAl_2S_4 formed by reaction 6.5(a) which separated Al_2S_3 from the $\text{FeS}+\text{FeAl}_2\text{S}_4$ heterophase layer. The final parabolic reaction stage, accordingly, proceeded in the presence of a complete Al_2S_3 layer at the alloy/scale interface as shown in Fig. 6.14(f). This continuous Al_2S_3 layer and the internal sulfidation zone beneath it is clearly seen in Fig. 5.26. Growth of Al_2S_3 platelets or needles would take place by inward diffusion of sulfur as well as outward diffusion of aluminum as observed in internal sulfidation experiments (section 6.4). The average width of Al_2S_3 platelets or needles beneath the Al_2S_3 film ranged from 0.8 to 1 μm . They generally grew in a direction normal to the original alloy surface and to the reaction front.

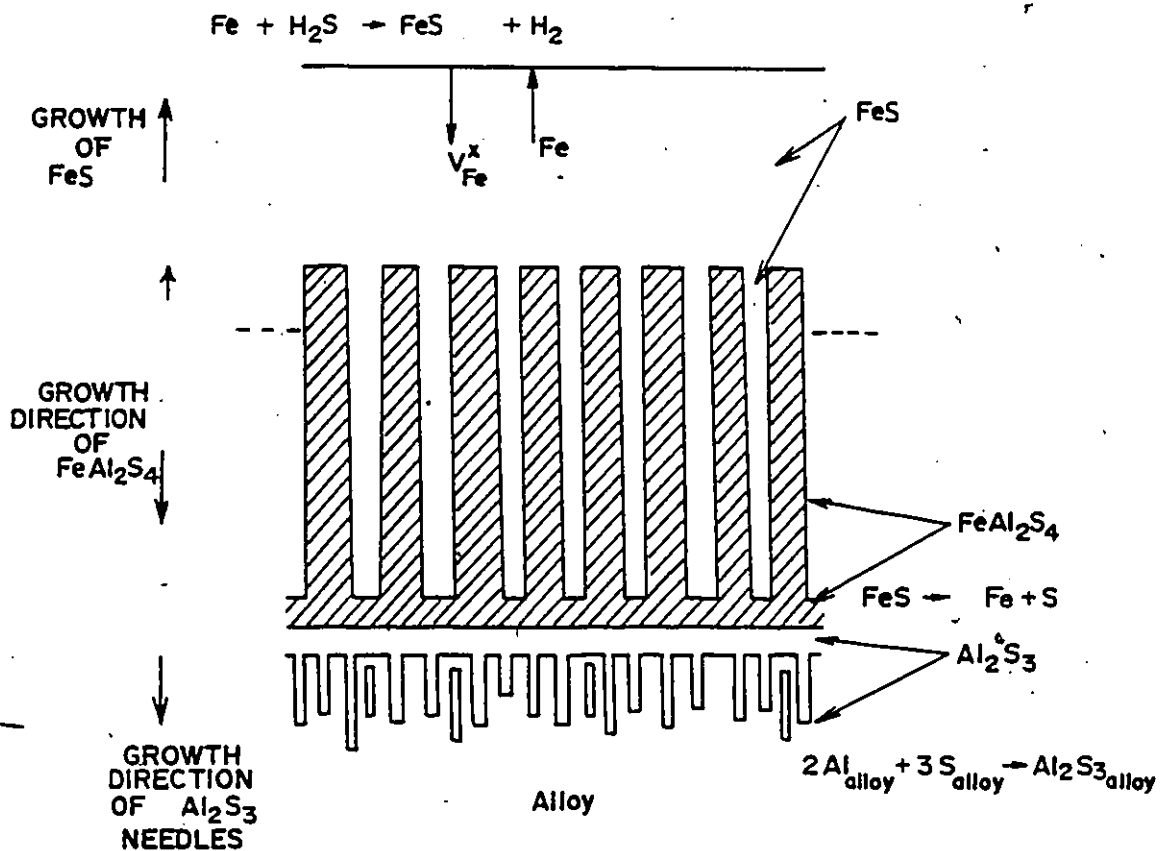


Fig. 6.14(f) . Schematic model for the scale growth on the Fe-18 Al alloys at $10 \leq p_{\text{S}_2} \leq 10^2$.

It is possible that Al_2S_3 needles or platelets beneath the continuous Al_2S_3 film have formed as a result of both morphological breakdown of the Al_2S_3 /alloy interface and internal sulfidation. These features are suggested by the morphologies shown in Fig. 5.26 where precipitates of Al_2S_3 are shown to emerge from the Al_2S_3 layer into the alloy and also as isolated needle or platelet precipitates in the alloy. In the former case, the tips of the alloy in between two Al_2S_3 precipitates become spheroidized and gave rise to isolated alloy particles (rich in Fe) embedded in the continuous Al_2S_3 scale (Fig. 5.26). In the latter case, growth of Al_2S_3 internal precipitates proceeded by inward diffusion of sulfur in the alloy and lateral diffusion of aluminum from the alloy.

6.5.3 Correlation of the Sulfidation Scaling Models to the Fe-Al-S Isotherm

The isothermal diffusion controlled growth of a sulfide scale of uniform thickness on the planar surface of a binary alloy can be considered as a three-phase (gas-solid-alloy) ternary diffusion couple. The corresponding diffusion path can be calculated using Eqn. 2.23(c) and then plotted on the appropriate ternary isotherm as illustrated in Fig. 6.15. Two possible⁽³⁸⁾ configurations are shown in this figure. In the first case (dotted line MN), a region of supersaturation isolated from the AS/alloy interface is indicated by the calculated diffusion path. This leads to the precipitation of sulfide within the alloy phase upon relief of supersaturation and is referred to as internal sulfidation. In the second case, solid line MN, a region

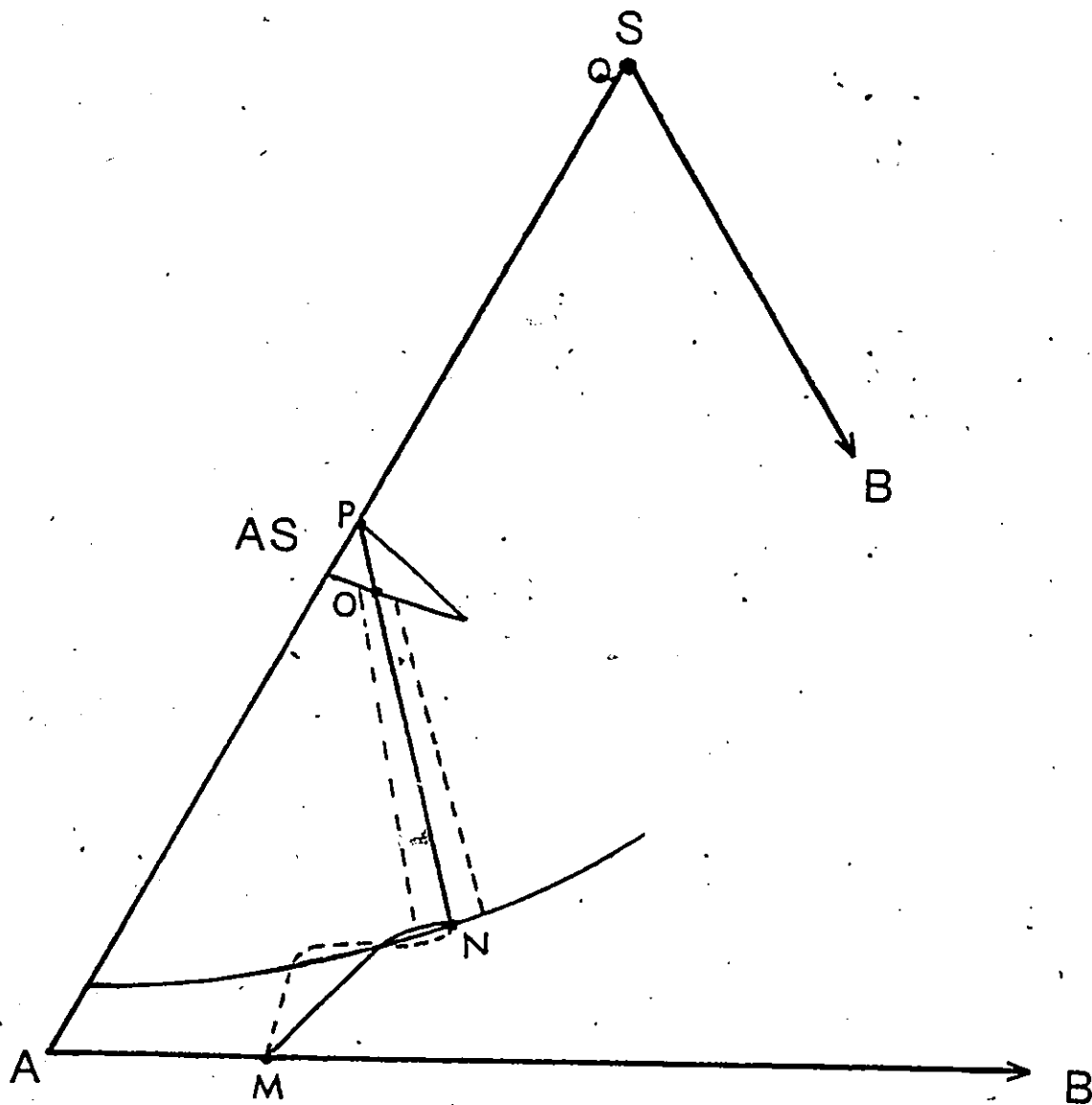


Fig. 6.15 Isothermal section of a phase diagram ABS relevant to alloy sulfidation. The lines MNO PQ and MNO P Q are two possible calculated diffusion paths corresponding to uniform sulfidation of a binary alloy AB of composition given by a point M to form a sulfide AS.

of supersaturation in contact with the interface can relieve supersaturation through a transition from planar to non-planar morphology by the growth of Al_2S_3 precipitates emerging from the Al_2S_3 scale. If the calculated diffusion path associated with the second possibility, cuts into the two-phase field, internal sulfidation as well as morphological breakdown will result.

Sulfidation of the Fe-Al alloys leads to complicated morphologies which evolved to final structures containing multi-layer scales and internal sulfidation zones. The two virtual diffusion paths x and l for Fe-9 Al and Fe-18 Al alloys, respectively, are shown on the ternary isotherm in Fig. 6.16. Because of the regions of virtual supersaturation, the tie lines are cut by the virtual diffusion path leading to precipitation. The diffusion path for Fe-9 Al is given by path x ($A_1B_1C_1D_1E_1F_1G_1H_1I_1$) in Fig. 6.16. This path enters into two phase alloy+ Al_2S_3 field and then passes through several three phase and two phase regions and ultimately exits through FeS and FeS+S₂ phase zones to the gaseous sulfur phase. The diffusion path for Fe-18 Al is given by path l ($A_1B_1C_1D_1E_1F_1G_1H_1I_1$) in Fig. 6.16. This path enters well into the two phase field (alloy+ Al_2S_3) at an angle to the tie lines and exists coincident with one of them. The two-phase zone contains isolated needles and/or plates of Al_2S_3 due to internal sulfidation and non-isolated plates of Al_2S_3 rooted in the present phase (Al_2S_3 layer in Fig. 5.26) due to morphological breakdown of the Al_2S_3 /alloy interface.

Alloy A_x Fe-9 at%Al
 Alloy A_1 Fe-18at%Al

• from binary data

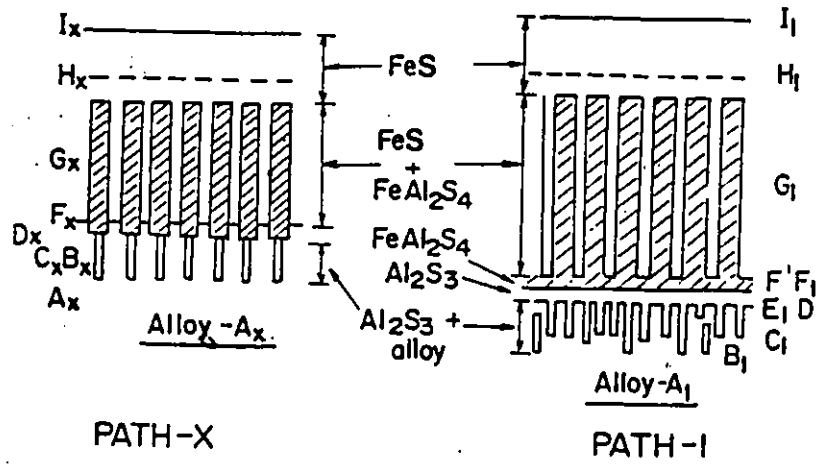
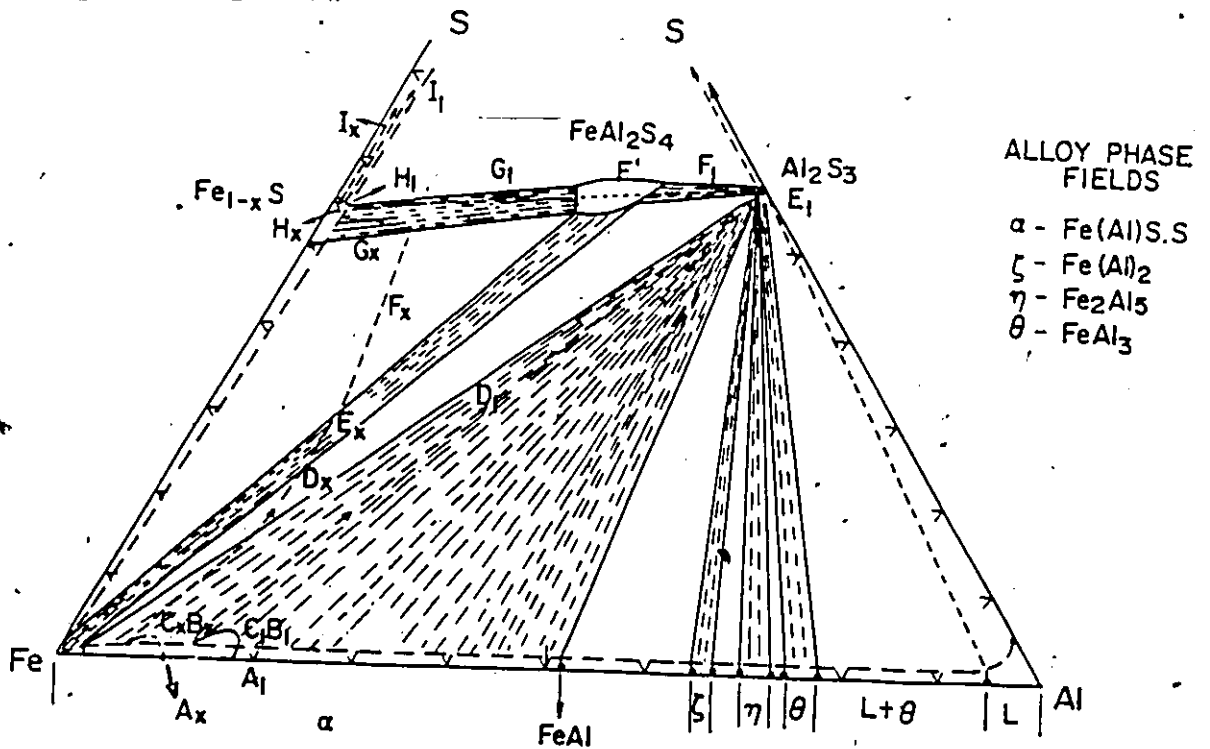


Fig. 6.16 Diffusion paths and corresponding schematic scale microstructures on Fe-9 and 18 Al alloys.

6.5.4 Conclusions

(i) The sulfidation kinetics of Fe-9 and 18 Al alloys at 1173K in H_2S-H_2 atmospheres are slower than pure iron at all sulfur pressures (10^{-1} Pa to 10^3 Pa). The kinetics approximated to parabolic sulfidation behaviour and increased with increasing sulfur partial pressure.

(ii) The Fe-9 Al alloy sulfidized parabolically with an external scale consisting of an outer FeS layer and an inner FeS+FeAl₂S₄ layer. A narrow zone of internal precipitation of Al₂S₃ was observed at the external scale/alloy interface.

(iii) The Fe-18 Al alloy sulfidized by a two-stage kinetics at $10 \leq p_{S_2} \leq 10^2$ Pa. During the initial period of sulfidation a thin layer of Al₂S₃ was formed on the alloy by selectively dissolving the thin residual oxide film on the metallographically polished alloy specimens. FeS+FeAl₂S₄ nodules nucleated at defective sites (leakage paths) of the Al₂S₃ film and grew (by the migration of Fe through Fe vacancies in FeS) laterally and vertically. The alloy beneath the nodule was sulfidized internally by the precipitation of Al₂S₃ in the alloy matrix.

(iv) The initially formed internal sulfidation zone was converted to a FeS+FeAl₂S₄ layer by further sulfidation giving rise to a slow growing film containing layers of FeAl₂S₄ and Al₂S₃ at the alloy/scale interface.

(v) The sulfidation rate of the Fe-18 Al alloy during the slower reaction stage was dependent on several factors, such

as: dissociation of FeS in the inner scale layer and several growth and diffusion processes taking place in the FeS/FeS+ FeAl₂S₄/Al₂S₃ zones. Therefore a rate controlling reaction step could not be suggested.

(vi) Virtual diffusion paths were placed on the ternary Fe-Al-S isotherm to describe the microstructures of scales which grew by parabolic reaction kinetics and to demonstrate the consistency of the proposed mechanisms for sulfide layer and precipitate growths with thermodynamic sequences.

CHAPTER 7

SUMMARY

The sulfidation properties of Fe-Al alloys containing 6, 9, 18 and 28 a/o Al were investigated by sulfidizing these alloys in alloy/FeS diffusion couples, in sulfur vapour at the dissociation pressure of FeS and in H_2S+H_2 atmospheres at 1173K.

These alloys exhibited periodic precipitation of sulfide layers containing $FeS+FeAl_2S_4$ spaced laterally and alternately to metal bands when sulfidized in the modes of FeS/alloy diffusion couples. The internal sulfidation rates of the alloys increased with alloy aluminum content. In each alloy, the sulfide layer thickness increased with depth whereas the metal band thickness remained approximately constant. The initial stage of sulfide layer formation was explained by a model involving precipitation of Al_2S_3 . This precipitated sulfide was subsequently converted to $FeAl_2S_4$. It was demonstrated that growth of FeS in a sulfide layer takes place by rapid diffusion of iron in this phase and aluminum diffusion in FeS accounted partially for the growth of $FeAl_2S_4$.

A diffusion model was advanced for the growth of a sulfide layer, in which it was suggested that aluminum depletion in front of the layer ultimately leads to its cessation of growth.

New sulfide precipitation was then described to occur at a distance ahead of the sulfide layer where the concentration product for the formation of Al_2S_3 was again satisfied.

The sulfidation kinetics of Fe-6, 9 and 18 Al alloys were parabolic at p_{S_2} ($= 1.45 \times 10^{-3}$ Pa) corresponding to the dissociation pressure of FeS. These alloys exhibited intense internal sulfidation. The acicular sulfide precipitates of FeAl_2S_4 and Al_2S_3 were elongated in the growth direction. The Fe-6 Al alloy only exhibited internal sulfidation whereas Fe-9 and 18 Al alloys exhibited external scales of FeAl_2S_4 and internal FeAl_2S_4 and Al_2S_3 precipitate. The apparent permeability ($N_{\text{S}}^{(\text{S})} D_{\text{S}}$) of sulfur in the alloys increased with increasing alloy aluminum content.

A diffusion model was advanced to describe the sulfidation behaviour of Fe-6, 9 and 18 Al alloys in sulfur vapour, involving enhanced sulfur diffusion along the incoherent interfaces between the internal sulfides and alloy matrix. The ratio of boundary to lattice diffusivities of sulfur in iron was estimated from this diffusion model and compared satisfactorily with the literature values.

An external scale of Al_2S_3 was formed on the Fe-28 Al alloy in sulfur vapour and grew as a protective film. Calculation has shown that an alloy of Fe-12.7 Al could be sufficient to form a continuous Al_2S_3 scale without any internal sulfidation under ideal conditions. Using non-ideal solution behaviour,

an interaction parameter for sulfur and aluminum, (ϵ_S^{Al}), was calculated to be in the range 9 to 15 consistent with estimates that can be made from the available literature data.

The reason for the occurrence of periodic precipitation and growth of sulfides as layers in the FeS/Fe-Al alloy diffusion couples as opposed to the acicular platelet morphology of internal sulfides in S_2 vapour could not be ascertained in the present work.

As the sulfur pressure was increased above 10^{-3} Pa using H_2S+H_2 atmospheres, FeS was observed to grow in the external scales of Fe-9 and 18 Al alloys. The sulfidation kinetics, which increased with increase in sulfur partial pressure, were approximated to parabolic behaviour. The Fe-9 Al alloy sulfidized with a duplex layer consisting of an outer FeS and an inner FeS+FeAl₂S₄ layer. A narrow zone of internal precipitation of Al₂S₃ was observed near the scale/alloy interface. The Fe-18 Al alloy sulfidized by two-stage kinetics. In the initial stage, growth of FeS+FeAl₂S₄ nodules was observed accompanied by internal sulfidation beneath these nodules. During later stages, continuous layers of FeAl₂S₄ and Al₂S₃ were formed giving rise to a slower kinetics. Schematic models have been employed to depict these sulfidation phenomena.

The Fe-Al-S ternary isotherm at 1173K was determined experimentally. Virtual diffusion paths were placed on it to describe the scale microstructures which grew by parabolic kinetics consistent with the proposed mechanisms for sulfide precipitation and growth.

REFERENCES

1. Materials Problems and Research Opportunities in Coal Conversion (Columbus, Ohio, April 1974) by Ohio State University: Volume I, pp. 46.
2. R.I. Jaffe: Met. Trans. 10A, 139, February 1979. Metallurgical Problem and Opportunities in Coal Fired Steam Power Plants.
3. W.W. Bodle and K.C. Vyas: Oil and Gas Journal, 73 (1974).
4. C. Samans in High Temperature Metallic Corrosion by Sulfur and Its Compounds: Z.A. Forulis et al., (The Electrochemical Society, Detroit, Michigan, 1970).
5. R.B. Setterland and G.R. Prescott: Corrosion 17, 103 (June, 1961).
6. E.B. Backensto, et al: Corrosion 18, 253t (July, 1962).
7. O. Kubaschewski and B.E. Hopkins: Oxidation of Metals and Alloys (Butterworths, London, 1967), pp. 234, 236.
8. K.N. Strafford and R. Manifold: Oxid. Met. 1(1), 221 (1969); 5(2), 85 (1972).
9. Materials for Petrochemical Industries: International Metals Review, 23, No. 3, 101, 1978.
10. K. Nishida: Trans. ISIJ, 10, 421 (1970).
11. F.J. Burns: Corrosion, 25, 119 (1969).
12. S. Mrowec, T. Werber: Gas Corrosion of Metal, National Centre for Scientific Information, Warsaw, Poland (1978).
13. L. Czerski, S. Mrowec, T. Weber: J. Electrochem. Society, 109, 273 (1962).
14. U.R. Evans: The Corrosion and Oxidation of Metals, Edward Arnold, London (1960), Supplement (1968).
15. Introduction to High Temperature Oxidation of Metals: N. Birks and G.H. Meier, Edward Arnold (Publishers) Ltd., London (1983).

16. K. Hauffe: Oxidation of Metals, Plenum Press, N.Y. (1965).
17. P. Kofstad: High Temperature Oxidation of Metals, Wiley, N.Y. (1966).
18. ASM Seminar Oxidation of Metals and Alloys: American Society for Metals, Metals Park, Ohio (1971).
19. M.S. Seltzer and R. Jaffee, Editors: Defect and Transport in Oxides, Plenum Press, N.Y. (1974).
20. R.C. Logani, W.W. Smeltzer: Can. Met. Quart., 10, 149 (1971).
21. W.W. Smeltzer, D.J. Young: Progress Solid State Chemistry, 10, Part (1), 17 (1975).
22. K.N. Strafford: Metallurgical Reviews, 138, 153 (1969).
23. D.J. Young: Review High Temperature Materials 4, 299 (1980).
24. F.D. Richardson and J.H.E. Jeffes: J.I.S.I., 171, 165 (1952).
25. W.W. Smeltzer and D.P. Whittle: J. Electrochem. Soc., 125, No. 7, 1116 (1978).
26. L.H. Germer and A.U. MacRae: J. Chem. Phys. 36, 1555 (1962).
27. N. Ramasubramanian, P.B. Sewell and M. Cohen: J. Electrochem. Soc., 122, 11 (1975).
28. U.R. Evans: The Corrosion and Oxidation of Metals, Edward Arnold Ltd., London, (1960).
29. C. Wagner: Atom Movements, ASM, Ohio, 151 (1951).
30. W.W. Smeltzer, R.R. Haering and J.S. Kirkaldy: Acta Met. 9, 880 (1961).
31. B.A. Irving: Corrosion Science, 5, 471 (1965).
32. J.M. Perrow, W.W. Smeltzer and J.D. Embury: Acta Met., 16, 1206 (1968).
33. G.C. Wood: J. Oxidation of Metals, 2, 11 (1970).
34. C. Wagner: J. Electrochemical Society, 99, 309 (1952).

35. C. Wagner: J. Electrochemical Society, 103, 11, 627 (1956).
36. C. Wagner: J. Electrochemical Society, 103, 571 (1956).
37. G.L. Wulf, T.J. Carter, G.R. Wallwork: Corrosion Science, 9, 689 (1969).
38. D.E. Coates and J.S. Kirkaldy: Trans. ASM, 62, 426 (1969).
39. D.P. Whittle, D.J. Young and W.W. Smeltzer: J. Electrochemical Society, 123, 1073 (1976).
40. J.S. Kirkaldy: ASM Seminar, Oxidation of Metals and Alloys, Metals Park, Ohio, 101 (1970).
41. J.S. Kirkaldy, L.C. Brown: Can. Met. Quart., 2, 89 (1963); 8, 35 (1969).
42. A.D. Dalvi and D.E. Coates: Oxidation of Metals, 5, 113 (1972).
43. F.N. Rhines: Trans. AIME, 137, 246 (1940).
44. F.N. Rhines, W.A. Johnson, W.A. Anderson: Trans. AIME, 147, 205 (1942).
45. L.S. Darken: Trans. AIME, 150, 157 (1942).
46. G. Bohm and M. Kahlweit: Acta Met., 12, 641 (1964).
47. C. Wagner: J. Electrochemical Society, 63, 773 (1959).
48. R.A. Rapp: Acta Met., 9, 730 (1961).
49. R.A. Rapp, D.F. Frank, J.V. Armitage: Acta Met., 12, 505 (1964).
50. R. Rapp: Review paper, Corrosion, 21, 382 (1965).
51. F. Maak: Z. Metallk., 52, 545 (1961).
52. C. Wagner: Corrosion Science, 8, 889 (1968).
53. A. Atkinson: Report AERE-R9960, AERE Harwell, Oxfordshire, England (1981).
54. W.W. Smeltzer, D.P. Whittle: J. Electrochemical Society, 125, 116 (1978).

55. M.N. Lesychyn: M. Eng. Thesis, McMaster University, Hamilton, Ontario, Canada (1980).
56. F. Gesmundo, F. Viani and V. Dori: Oxidation of Metals, 17, Nos.1/2, 99 (1982).
57. B. Ozturk and G. Simkovich: Chemical Metallurgy, A Tribute to Carl Wagner, N.A. Gokeen, ed., TMS-AIME, Warrendale, PA, 405-417 (1981).
58. H.M. Hindam and W.W. Smeltzer: J. Electrochemical Society, 127, 1116 (1980).
59. D.J. Young, J.S. Kirkaldy and W.W. Smeltzer: J. Electrochemical Society, 123, 1758 (1976).
60. V.S. Bhide and W.W. Smeltzer: J. Electrochemical Society, 129, 902 (1981).
61. F.A. Elrefaie and W.W. Smeltzer: Oxidation of Metals, 17, 407 (1982).
62. D.P. Whittle, Y. Shida, G.C. Wood, F.H. Stott and B.D. Bastow: Phil. Mag. A, 46, No. 6, 931 (1982).
63. Y. Shida, F.H. Stott, B.D. Bastow, D.P. Whittle and G.C. Wood: Oxidation of Metals, 18, No. 3/4, 93 (1982).
64. G.C. Wood, F.H. Stott et al.: Corrosion Science, 23, No. 1, 9 (1983).
65. F.H. Stott, G.C. Wood et al.: Corrosion Science 21, No. 8, 599 (1981); Oxid. of Met., 18, No. 3/4, 127 (1982).
66. Y.S. Shen, E.J. Zdanuk and R.H. Krock: Met. Trans., 2, 2839 (1971).
67. R.E. Liesegang: Naturw. Wschr., 11, 353 (1896).
68. C. Wagner: J. Colloidal Science, 5, 85 (1950).
69. S. Prager: J. Chemical Physics, 25, 279 (1956).
70. K. Jablczynski: Kolloidz., 40, 22 (1926).
71. W. Ostwald: Z. Physik. Chem. 22, 365 (1897).
72. V.A. VanRooijen, E.W. Van Royen, J. Vrijen and S. Radellar: Acta Met., 23, 987 (1975).

73. J.E. Gerrard, M. Hoch and F.R. Meeks: Acta Met., 10, No. 9, 751 (1962).
74. C.F. Chenot: Ph.D. thesis (1964), University of Cincinnati, Cincinnati, Ohio (U.S.A.).
75. R.L. Klueh and W.W. Mullins: Acta Met., 17, 59, 69 (1969).
76. K.N. Strafford and A.F. Hampton: J. Metal Science, 8, 1354 (1973).
77. M. Hansen, K. Anderko: Constitution of Binary Alloys, 2nd. ed., McGraw-Hill (1959), (1968).
78. R. Hultgren, P. Desai, D. Hawkins, M. Gleiser, K. Kelly, Selected Values of the Thermodynamic Properties of Binary Alloys, ASM (1973).
79. V.F. Lihl, H. Ebel: Arch. Eisenhüttenw. 32, 483 (1961).
80. E. Schürman, C. Zellerfeld and H.P. Kaiser: Arch. Eisenhüttenw. 51, 325 (1980).
81. Y.A. Chang and J.P. Neumann: Prog. Solid St. Chem., 14, 221-301 (1982).
82. J.K. Edgar: Trans AIME, 180, 225 (1949).
83. P. Rocquet, G. Jegaden and J.C. Petit: J.I.S.I., 194(2), 222 (1967).
84. A.J. Bradley and A.H. Jay: Proc. Roy. Soc. (London), A136, 210 (1932).
85. J.D. Livingston: J. Crystal Growth, 24-25, 94 (1974).
86. G.F. Bastin, F. Vanloo, J. Vrolijk and L. Wolff: J. Crystal Growth, 43, 745 (1978).
87. P. Gross, D.L. Levi, E.W. Dewing and G.L. Wilson: Physical Chemistry of Process Metallurgy Part I, Interscience Publishers, 403 (1961).
88. S.V. Radcliffe, B.L. Averbach and M. Cohen: Acta Met., 9, March, 169 (1961).
89. J. Eldridge and K.L. Komarek: Trans AIME, 230, 226 (1964).

90. A. Steiner and K.L. Komarek: Trans. AIME, 230, June, 786 (1964).
91. O. Kubaschewski and W.A. Derch: Acta Met., 3, July, 339 (1955).
92. K. Sato: Trans. Japan Inst. of Metals, 4, 121 (1963).
93. K. Hirano and A. Hishinuma: J. Japan Inst. of Metals, 32, 516 (1968).
94. K. Nishida, T. Yamamoto and T. Nagata: Trans. Japan Inst. of Metals, 12, 310 (1971).
95. H.C. Akuezue and D.P. Whittle: Metal Science, 17, No. 1, 27 (1983).
96. V.R. Ryabov et al., Properties of Intermetallic Compounds in the Fe-Al System, Fiz. Metal. Metalloved, 27, No. 4, 668 (1969).
97. P. Fellner, K. Matiasovsky, Surface Technology, 8, 501 (1979).
98. N. Morimoto et al.: Science, 168, 964 (1970).
99. H. Nakazawa et al.: Materials Res. Bull., 6, 345 (1971).
100. K. Niwa and T. Wada: "Physical Chemistry of Process Metallurgy". Part 2, Interscience, New York 8, 495, 1961.
101. M. Nagomori and M. Komeda: Trans. Japan Inst. Met., 9, 187 (1968).
102. J.C. Ward: Solid State Communications, 9, 357 (1971).
103. G.G. Libowitz: "Proceedings of VII International Symposium on Reactivity of Solids", p. 17.
104. H. Rau: J. Phys. Chem. Solids, 37, 425 (1978).
105. David Adler: Review of Modern Physics, 40, No. 4, 714 (1968).
106. H.I. Kaplan, W.L. Worrell, "Chemistry of Extended Defects in Non-metallic Solids", L. Eyring and M. O'Keefe, p. 561 (1970), Elsevier Publishers, N.Y.
107. R.C. Thiel: Phys. Status Solidi, 40, 417 (1970).

108. R.H. Condit, R.R. Hobbins, C.E. Birchenall: Oxid. of Met., 8, No. 6, 409 (1974).
109. Thermodynamic Data for Inorganic Sulfides, Selenides and Tellurides, K.C. Mills, Butterworths, p. 292 (1974).
110. S.M. Ariya: Morozova, Zhur, Fiz. Khim, 40, 1607 (1966).
111. F. Grönvold and E.F. Westrum Jr.: Inorganic Chemistry, 1, 37 (1962).
112. T. Rosenqvist: J.I.S.I., 176, 37 (1954).
113. C.L. McCabe, C.B. Alcock and R.G. Hudson: Trans. AIME, 206, p. 693 (1956).
114. K.T. Jacob, D.B. Rao, H.G. Nelson: Oxid. of Metals, 13, No. 1, 25 (1979).
115. K. Sudo: Sci. Rep. Res. Inst., Tohoku Univ., Ser. A., 2, 312-317 (1950).
116. F.D. Richardson and J.H.E. Jaffes: J.I.S.I., 171, 165 (1952).
117. N.G. Ainslie and A.U. Seybolt: J.I.S.I., March, 341 (1960).
118. W.H. Herrnstein, F.H. Bech, M.G. Fontana: Trans. AIME, 242, June, 1049 (1968).
119. N.G. Ainslie, R.E. Hoffman and A.U. Seybolt: Acta Met., 8, August, 523-538 (1960).
120. J. Swisher: Trans. AIME, 242, No. 12, 2433 (1968).
121. G.K. Sigworth and J.F. Elliot: Metal Science, 8, 298 (1974).
122. E. Turkdogan et al.: J.I.S.I., August, 349 (1955).
123. G. Siebel: Mem. Sci. Rev. Met., 61, No. 6, 413 (1964).
124. I.F. Knonyuk: Fiz. Metal. Metallored., 19, No. 2, 311 (1965).
125. S.J. Wang and H.J. Grabke: Z. Metallkde, 61, 597 (1970).
126. E.M. Fryt, W.W. Smeltzer and J.S. Kirkaldy: J. Electrochem. Soc., 126, No. 4, 673 (1979).

127. A.J. Rosenberg: J. Electrochem. Soc., 107, 795 (1960).
128. M. Danielewski: Ann. Chim. Fr., 4, 187 (1979).
129. T. Narita, K. Nishida: Trans. J.I.M., 15, 314 (1974).
130. A. Dravenicks, Ind. Eng. Chem., 43, 2897 (1951).
131. E.B. Backensto, R.E. Drew and C.C. Stapleford: Corrosion, 12, 22 (1956).
132. K. Hauffe and A. Rahmel: Z. Phys. Chem., 199, 152 (1952).
133. R.A. Meussner and C.E. Birchenall: Corrosion, 13, 677t (1957).
134. E.T. Turkdogan: Trans. AIME, 242, 1665 (1968).
135. K.N. Strafford and R. Manifold: Corrosion Science, 9, 489 (1969).
136. T. Narita and K. Nishida: Trans. Japan Inst. of Metal, 14, 439, 447 (1973).
137. A. Sterten and S. Haugen: Oxidation of Metals, 3, 545 (1971); 7, 45 (1973).
138. S. Mrowec, A. Stolaska and M. Danielewski: Oxidation of Metals, 11, 355 (1977).
139. D.J. Young and W.W. Smeltzer: J. Electrochem. Soc. 123, 229 (1976).
140. E.M. Foyt, V.S. Bhide, W.W. Smeltzer and J.S. Kirkaldy: J. Elec. Chem. Soc., 126, 683 (1979).
141. L. Czerski, S. Mrowec and T. Werber: J. Electrochem. Society, 109, 273 (1962).
142. A. Brückman: Corrosion Science, 7, 51 (1967).
143. S. Mrowec: Corrosion Science, 7, 563 (1967).
144. P.J. Ficalora, J.W. Hastie and J.L. Margrave: J. Phys. Chem., 72, p. 1660 (1968).
145. J. Flahaut: Compt. Rend. 232, 334 (1951).
146. J. Flahaut: Ann. Chim. (Paris), 7, 632 (1952).
147. H. Schafer, A. Weiss: Z. Ang. Chem. 325, 77 (1963).

148. P.C. Donohue: J. Sol. State Chem., 2, 6 (1970).
149. E.E. Hellstrum and R.A. Huggins: Mat. Res. Bull., 14, 127 (1979).
150. K.J. Range: Z. Natur. 288, 353 (1973).
151. M.J. Ferrante, J.M. Stuve, H.C. Ko and R.R. Brown: High Temp. Sc., 14, 91 (1981).
152. F. Jellrek, G. Nickless, Editors: Inorganic Sulfur Chemistry, Elsevier, New York, 1968.
153. K. Nishida and T. Narita: Trans. ISIJ, 12, 422 (1972).
154. K. Nishida, T. Narita: Bulletin of Faculty of Engineering, Hokkaido University, Japan, No. 81, 1976.
155. S. Banya and J. Chipman: Trans. AIME, 245, Jan., 133 (1969).
156. P.L. Gruzin, V.V. Mural, A.P. Fokin: Fiz. Metal. Metalloved. 34, No. 6, 1326-8 (1972).
157. K.N. Strafford and R. Manifold: Oxidation of Metals, 5, No. 2, 85 (1972).
158. P.C. Patnaik: M. Eng. Thesis, McMaster University, Hamilton, Ontario, Canada (1980).
159. B.D. Cullity: Elements of X-ray Diffraction, 2nd. ed., Addison-Wesley Publishing Co., p. 404 (1978).
160. J.S. Kirkaldy: Advances in Materials Research, 4, 55-100, Editor; Herbert Herman, John Wiley and Sons (1970).
161. C.B. Alcock, F.D. Richardson: Nature, 168, 661 (1952).
162. D.R. Gaskell: Introduction to Metallurgical Thermodynamics, McGraw-Hill publications, page 124.
163. P. Sabatier: Ann. Chim. Phys., 22, 5 (1891).
164. I.A. Korshunov: J. Phys. Chem. (USSR), 13, 703 (1939).
165. M. Bloom: Ph.D. Thesis, London University (1947).
166. A.F. Kapustinskii and Y.M. Golutvin: Izvest. Akad. Nauk. Otdel. Khim. Nauk., (1951), 192 (1951).
167. M. Zaheeruddin, I.A. Awan and M.A. Khan: Pakistan J. Sci. Res. 31, 194 (1979).

168. G.R. Laflamme and J.E. Morral, Acta Metallurgica,
26, 1791 (1978).

169. E.K. Ohriner and J.E. Morral, Scripta Metallurgica,
13, No. 1, 7 (1979).

APPENDIX I

1. Thermochemistry of iron sulfide (Fe_{1-x}S)

Between 773 and 1261K the gas ratio H₂S/H₂ for the reaction,



is given by the following expression⁽¹¹²⁾.

$$\log(\text{H}_2\text{S}/\text{H}_2) = -\frac{3100}{T} + 0.179 \quad (\text{I-2})$$

The corresponding Gibb's free energy is given by,

$$\Delta G^\circ = R T \ln\left(\frac{\text{H}_2\text{S}}{\text{H}_2}\right) \quad (\text{I-3})$$

$$\therefore \Delta G^\circ = -59396 + 3.43 T \text{ Joules.} \quad (\text{I-4})$$

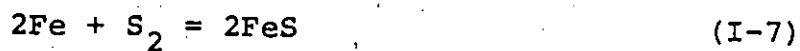
From the work of Richardson and Jeffes⁽¹¹⁶⁾, the free energy for the reaction,



is given as

$$\Delta G^\circ = 180710 + 98.8 \text{ J/mole of S}_2 \quad (\text{I-6})$$

Therefore, the free energy for the reaction



is given by,

$$\Delta G^{\circ} = - 300,000 + 105.7 T (\pm 2900) \text{ Joules/mole of } S_2 \quad (\text{I-8})$$

Other available data are tabulated in Table I-1. The recent paper by Jacob et al. (114) reviews the Fe-S binary system and established the standard free energy for reaction (I-7),

$$\Delta G^{\circ} = - 303,000 + 108.2 T (\pm 3000) \text{ Joules/mole of } S_2 \quad (\text{I-9})$$

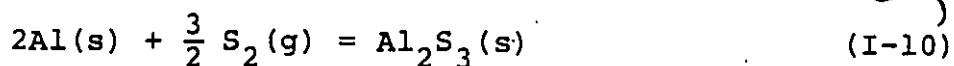
Table I-1

Free energy of formation for $Fe_{1-x}S$

No.	Temp. range (K)	ΔG° in Joules per mole of S_2	Reference
1.	773-1261	$-300,000 + 105.7 T (\pm 2900)$	116
2.	800-1260	$-298,000 + 103 T (\pm 2800)$	115
3.	800-1260	$-300,700 + 105.1 T (\pm 3000)$	161
4.	1073-1373	$-293,000 + 105 T (\pm 2100)$	111
5.	800-1260	$-303,000 + 108.2 T (\pm 3000)$	114

2. Thermochemistry of Aluminum Sulfide (Al_2S_3)

From the thermochemical data by Ferrante et al. (151), the standard enthalpy of formation for the following reaction



was obtained as

$$\Delta H_f^{\circ} \text{ }_{298} = 8.5 \times 10^5 \pm 3800 \text{ J/mole of } Al_2S_3 \quad (\text{I-11})$$

In the following, free energy of formation of Al_2S_3 (reaction I-10) at 1173K is calculated using the heat capacity values, standard heat of formation and standard entropy of formation values from the literature.

$$\begin{aligned} \Delta H_{1173\text{K}}^{\circ} = & \Delta H_{298}^{\circ} + \int_{298}^{1173} C_{P\text{Al}_2\text{S}_3} \cdot dT - 2 \int_{298}^{933} C_{P\text{Al}(s)} dT \\ & - 2 \int_{933}^{1173} C_{P\text{Al}(l)} \cdot dT - \frac{3}{2} \int_{298}^{700} C_{P\text{S}_2(g)} \cdot dT \\ & - \frac{3}{2} \int_{700}^{1173} C_{P\text{S}_2(g)} \cdot dT - \Delta H_{m,\text{Al}}^{\circ} \end{aligned} \quad (\text{I-12})$$

$$C_{P\text{Al}_2\text{S}_3} = 102.24 + 0.036 T \text{ J/K/mole (Ref. 151).}$$

$$C_{P\text{Al}(s)} = 20.68 + 0.0124 T \text{ J/K/mole (Ref. 162).}$$

$$C_{P\text{Al}(l)} = 29.3 \text{ J/K/mole (Ref. 162).}$$

$$\frac{1}{2} C_{P\text{S}_2(g)} = 14.6 + 5.9 \times 10^{-3} T \text{ J/K/mole, } T < 700\text{K}$$

$$= 17.3 + 1.3 \times 10^{-3} T \text{ J/K/mole, } T > 700\text{K}$$

$$\Delta H_{m,\text{Al}}^{\circ} = 10800 \text{ J/mole (Ref. 78).}$$

Substituting these values in Eqn. (I-12) and integrating,

$$\Delta H_{1173\text{K}}^{\circ} = - 839933 \text{ J/mole .} \quad (\text{I-13})$$

Entropy Change Calculation

The entropy change for reaction (I-10) is given by

$$\Delta S_T^{\circ} = S_{T, Al_2S_3(s)}^{\circ} - 2S_{T, Al(s)}^{\circ} - \frac{3}{2} S_{T, S_2(g)}^{\circ} \quad (I-14)$$

Al₂S₃

$$S_{T, Al_2S_3(s)}^{\circ} = S_{298, Al_2S_3}^{\circ} + \int_{298}^{1173} (102.24 + 0.036 T) d \ln T \quad (I-15)$$

$$S_{298, Al_2S_3}^{\circ} = 116.9 \text{ J/K/mole (Ref. 151).}$$

$$\therefore S_{T, Al_2S_3(s)}^{\circ} = 288.6 \text{ J/K/mole} \quad (I-16)$$

Aluminum

$$S_{T, Al}^{\circ} = S_{298, (Al)}^{\circ} + \int_{298}^{933} (20.68 + 0.0124 T) d \ln T + \Delta S_{m, (Al)}^{\circ} + \int_{933}^{1173} C_{p, Al(l)} d \ln T \quad (I-17)$$

$$S_{298, Al}^{\circ} = 28.34 \text{ J/K/mole (Ref. 162).}$$

$$\Delta S_{m, Al}^{\circ} = \frac{\Delta H_{m, Al}^{\circ}}{T_{m, Al}} = \frac{10800}{933} = 11.6 \text{ J/K/mole}$$

$$\therefore S_{T, Al}^{\circ} = 78.04 \text{ J/K/mole} \quad (I-18)$$

Sulfur (gas)

$$S_{T}^{\circ} S_2(g) = S_{298}^{\circ} S_2(g) + \int_{298}^{700} (14.6 + 5.9 \times 10^{-3} T) d \ln T + \int_{700}^{1173} (17.3 + 1.3 \times 10^{-3} T) d \ln T \quad (I-19)$$

$$S_{298}^{\circ} S_2(g) = 228.2 \text{ J/K/mole (Ref. 78)}$$

$$\therefore S_{T}^{\circ} S_2(g) = 276.3 \text{ J/K/mole} \quad (I-20)$$

Substituting (I-16), (I-18) and (I-20) in (I-14),

$$\Delta S_T^{\circ} = - 283.04 \text{ J/K/mole} \quad (I-21)$$

Substituting (I-13) and (I-21) in (I-22) for $T = 1173K$,

$$\Delta G_{1173}^{\circ} = \Delta H_{1173}^{\circ} - T \Delta S_{1173}^{\circ} \quad (I-22)$$

the free energy of formation of Al_2S_3 is obtained as:

$$\Delta G_{1173}^{\circ} = - 508025.5 \text{ J/mole of } Al_2S_3 \quad (I-23)$$

$$= - 338204.9 \text{ J/mole of } S_2 \quad (I-24)$$

Dissociation pressure of Al_2S_3 at 1173K

For reaction (I-10), the equilibrium constant can be expressed as:

$$K = p_{\text{S}_2}^{3/2} \quad \text{assuming } a_{\text{Al}} = 1 \quad (\text{I-25})$$

$$a_{\text{Al}_2\text{S}_3} = 1$$

Also,

$$K = \exp - \frac{\Delta G^\circ}{RT} \quad (\text{I-26})$$

Substituting (I-23) in (I-26),

$$K = 2.46 \times 10^{-23} \quad \text{at } 1173\text{K} \quad (\text{I-27})$$

$$p_{\text{S}_2}^{\text{diss.}} = 8.57 \times 10^{-11} \text{ Pa} \quad (\text{I-28})$$

₁₁₇₃

Other available data for the enthalpy and free energy of formation of Al_2S_3 are tabulated in Table I-2. A wide divergence in these values is observed.

Table I-2

Free energy of formation of Al_2S_3 (Reaction I-10)

No.	ΔH_{298}° J/mole	ΔG_{298}° J/mole	ΔG_{1173}° J/mole of Al_2S_3	Reference
1	- 780456.8	- 696298.1	- 444240.7	163
2	- 701741.2	- 615070.3	- 365525.1	164
3	-1050937.7	- 966778.3	- 715139.6	165
4	- 916534.3	- 828607.3	- 584923.9	166
5	- 844371.2	- 759940.5	- 507883.1	151
6	- 700903.8	- 616326.4	- 368456.0	167